Dissertation zur Erlangung des Doktorgrades
der Fakultät für Chemie und Pharmazie
der Ludwig-Maximilians-Universität München

Structural and biochemical studies of the adhesion protein talin-1

Dirk Lübbert Dedden

Oldenburg, Germany

2019

Erklärung:

Diese Dissertation wurde im Sinne von § 7 der Promotionsordnung vom 28.11.2011 von Herrn Prof. Dr. Reinhard Fässler betreut.

Eidesstattliche Versicherung:

Diese Dissertation wurde selbstständig, ohne unerlaubte Hilfe erarbeitet.

München den 27.06.2019

_____
Dirk Dedden

Dissertation eingereicht am: 27.06.2019

1. Gutachterin / 1. Gutachter: Prof. Dr. Reinhard Fässler

2. Gutachterin / 2. Gutachter: Prof. Elena Conti, PhD

Mündliche Prüfung am: 25.07.2019

Table of Contents

Abbreviations

aa	aminoacid
ABS	actin binding site
ADMIDAS	metal ion-dependent adhesion site
Å	Angstrom
ARP2/3	actin-related protein 2/3
CCD	charge-coupled device
cryo-EM	cryo electron microscopy
CMSC	cortical microtubule stabilization complexes
CHO	chinese hamster ovarys
DAAM1	Disheveled-associated activator of morphogenesis
Dab2	disabled homolog 2
DD	dimerization domain
DLC1	deleted in liver cancer 1
ECM	extracellular matrix
EZH2	enhancer of zeste homolog 2
FA	Focal Adhesion
FAK	focal adhesion kinase
FB	fibrillar adhesion
FERM	4.1-ezrin-radixin-moesin
GEF	guanine nucleotide exchange factor
IBS	integrin binding site
ILK	integrin-linked kinase
Irsp53	Insulin receptor substrate p53
Kank	KN motif and ankyrin repeat domains
kDa	kilodalton
LIM	Lin11-Isl1-Mec3
µm	micrometer
MIDAS	metal ion-dependent adhesion site
nm	nanometer
NA	Nascent Adhesion
NMR	nuclear magnetic resonance
p130CAS	Breast cancer anti-estrogen resistance protein
PH	pleckstrin homology
PIPKIγ90	phosphatidylinositol 4-phosphate 5-kinase Type Iγ 90
pN	piconewton
PSI	plexin-semaphorin-integrin
PTB	phospho-tyrosine binding
PtdIns(4,5)P_2	Phosphatidylinositol-4,5-bisphosphat
RIAM	Rap1–GTP-interacting adapter molecule
ROCK	Rho-associated coiled-Coil containing protein kinase
SAXS	small angle X-ray scattering
Src	Proto-oncogene tyrosine-protein kinase Src
TEM	transmission electron microscope
THATCH	talin/HIP1R/Sla2p actin tethering C-terminal homology
TIAM	T-lymphoma invasion and metastasis-inducing protein
TMD	transmembrane domain
VBS	vinculin-binding site
VASP	vasodilator-stimulated phosphoprotein
YAP	Yes-associated protein

List of Figures

List of Figures

1 Summary

Integrin-mediated adhesions are responsible for the majority of cell matrix-contacts. Their regulation and correct function are vital in development, cell migration and tissue homeostasis. Integrins are class1 transmembrane receptors containing an α- and β-subunit. Their extracellular domain engages with different extracellular matrix (ECM) proteins and their cytoplasmic tail interacts with adaptor proteins, such as talin and kindlin, to establish a link to the actin-cytoskeleton. Thus, they form an anchor for cells to move and sense matrix properties.

As one of the two major integrin adaptor proteins, talin can bind to the integrin cytoplasmic β-tail and activate integrins. Talin is a 270 kDa protein that consists of a small head domain and a large rod domain. The talin head interacts with both integrin and the plasma membrane and can activate integrin's extracellular domain, which enhances its ligand binding capabilities. The talin rod domain binds to F-actin and acts as recruitment platform for further adhesion proteins. Thus, talin functions as the linker between the actin cytoskeleton and integrin. It transmits the force generated by the actomyosin machinery, allowing cells to use the adhesion complex as an anchor for cell migration.

When both its N-terminal head an C-terminal rod domain are bound, talin adopts an elongated conformation, where the N- and C-terminus are more than 80 nm apart from each other. The mechanical tension transmitted over talin, induces the opening of some of its force dependent binding sites for vinculin and other adhesion components. This recruitment enhances the link to the actin cytoskeleton and reinforces the adhesion site.

Since regulation of cell adhesion is of critical importance for many cellular processes, integrin and its adaptor proteins also need to be tightly controlled. Talin was shown to be autoinhibited by interaction between its head and rod domains. This autoinhibited conformation was thought to be mainly present in the cytoplasm. Furthermore, several proteins and factors such as Rap1, PIPKIγ90 and RIAM were discovered to play a role in talin's activation and recruitment to the plasma membrane.

A considerable amount of biochemical and structural research has been performed on talin's 18 different domains; however, so far, no comprehensive model of its full length architecture and its possible autoinhibition conformation has been suggested.

In this study, talin and its interaction with some of its binding partners, such as vinculin, actin and Kank was characterized. Recombinant talin adopts different conformations

between an 80 nm robe-like shape and a 15 nm globular shape *in vitro*, which can be controlled and manipulated. Using cryo electron microscopy (cryo-EM) a 6.2 Å 3D-reconstruction of talin full length in its autoinhibited conformation was generated. Combining the map and the available structural information of individual domains, a model of talin was determined, revealing a general two-state inhibition and how different protein binding sites are buried within the domain arrangement. Further *in vitro* reconstitution showed, talin can bind to vinculin in a force independent manner depending on talin's conformational state. Furthermore, talin acts as a scaffold of focal adhesion by binding to actin. The combination of structural and biochemical experiments gave insights into which of actin binding sites are accessible, depending on its conformational states.

Taken together, my findings suggest how talin's closed conformation inhibits its interaction with its major binding partners actin and vinculin and suggests a mechanism for talin to be recruited and subsequently activated at the membrane.

2 Introduction

2.1 Integrin based adhesions

The ability of cells to adhere to other cells or extracellular matrices has been an important step in the evolution of eukaryotes. Cell to cell and cell to matrix contacts are the two major adhesion classes in metazoan life. Cell to matrix contacts are not only anchors to other tissues, but a machinery for cell migration as well as signaling clusters to probe the cell's environment. Their tight regulation and maintenance are essential in development as well as cell homeostasis. Failure of the system can cause defects in development or uncontrolled cell migration, which can result in cancer formation.

The major class of cell matrix adhesions are integrin mediated adhesions. They have two key functions: the connection of the extracellular matrix (ECM) with the cytoskeleton and the generation of signaling clusters. These clusters sense the cell's mechanical and chemical environment and transmit signals inside the cell to adjust and regulate its behavior.

Integrins are class 1 transmembrane receptors, containing two subunits. They have a large extracellular domain which, when activated, binds to ECM proteins like fibronectin, laminin or collagen. In addition, each subunit has a single transmembrane helix as well as a short cytoplasmic tail where cellular adaptor proteins can bind and connect integrins to the cytoskeleton.

Due to their different roles and their dynamic nature, there are different types of integrin mediated adhesions: Nascent adhesions (NA) are small adhesion plaques at in the lamellopodium with a short lifetime. They are dynamic structures that locate at the leading edge of the cell. Focal adhesions (FA) are the best-studied adhesion structures. They are large protein assemblies that contain hundreds of different adhesion proteins and are connected via large actin cables with the cytoskeleton. FAs have a longer lifetime of several minutes. Fibrillar adhesions appear at locations where the most mechanical tension is exerted. They are matured adhesion complexes that create large actin stress fibers and can secrete their own fibronectin matrices.

Defects in adhesion components or their regulation are at the heart of many developmental and immunological diseases and also cause cancer formation. This makes them highly interesting therapeutic targets (Winograd-Katz et al., 2014). Therefore, the understanding of their interactions, spatial organization and regulation provides vital information for future drug design and development.

2.1.1 Molecular organization of integrin based adhesions

Integrin mediated adhesions are highly dynamic structures, containing hundreds of different proteins. Different proteomic studies each revealed thousands of proteins in various phosphorylation states, depending on the given integrin subtype (Horton et al., 2015; J. D. Humphries et al., 2009; Schiller and Fässler, 2013). A study comparing these different datasets determined a commonly found 'core' of 60 proteins (Horton et al., 2015). This core was determined and named the 'consensus adhesome'. Among them are essential integrin activators like talin and kindlin, signaling proteins such as paxillin and the integrin-linked pseudokinase (ILK)-PINCH-parvin complex (IPP) and those adhesion proteins, that have the highest number of interactions with candidates that are outside of the 'consensus adhesome' like filamin, focal adhesion kinase (FAK) or α-actinin (Horton et al., 2016).

The architecture of FA has been studied in both x/y-direction at the plasma membrane, as well as in z-direction towards the actin cytoskeleton.

Due to recent developments in super-resolution microscopy, the architecture of FA in z-direction is quite well characterized. In vertical direction, FA organization can be divided into 3 distinct layers, with most proteins located to a specific layer (Kanchanawong et al., 2010). The first membrane proximal layer is called integrin-signaling layer and stretches approximately over 23 nm in distance away from the plasma membrane. It contains the integrin cytoplasmic tail and the talin head and is enriched in FAK, paxillin and inhibited vinculin. The second layer, named 'force transduction layer, reaches from 23 nm in to about 50 nm and contains the elongated talin rod and active vinculin (Case and Waterman, 2015). The last 'actin regulatory layer' is enriched in actin binding and crosslinks proteins like zyxin, VASP and α-actinin.

In x/y-direction the structure of focal adhesions less strictly layered. Some of the FA proteins show a polarized distribution at the membrane plane. Phosphorylated paxillin and other tyrosine phosphorylated proteins are enriched at the FA tip (Hu et al., 2015; Zaidel-Bar et al., 2007). In contrast we showed that Kank is enriched at the lateral border of the FA as a belt (Z. Sun et al., 2016). The lateral organization often depends on the highest force exerted on the FA. Using FRET tension sensors, it was observed that the highest ECM tension lies at the center of FAs. Interestingly this correlates well with paxillin localization, but not with talin and vinculin recruitment. However, these talin-tension sensor experiments also show

that the force is directed towards the cell center, which correlates well with the tilted nature of elongated FA proteins like talin and vinculin (Kumar et al., 2018).

Some proteins require a specific orientation within FA. It was shown for talin that in its planar orientation its head is facing the cell periphery whereas its C-terminus is pointed towards the cell center (Margadant et al., 2011). In z-direction, talin's head is located at the plasma membrane and its tail is pointing away at an angle of 15˚ to 25˚ (Paszek et al., n.d.) with an average distance of 97 nm (Liu et al., 2015).

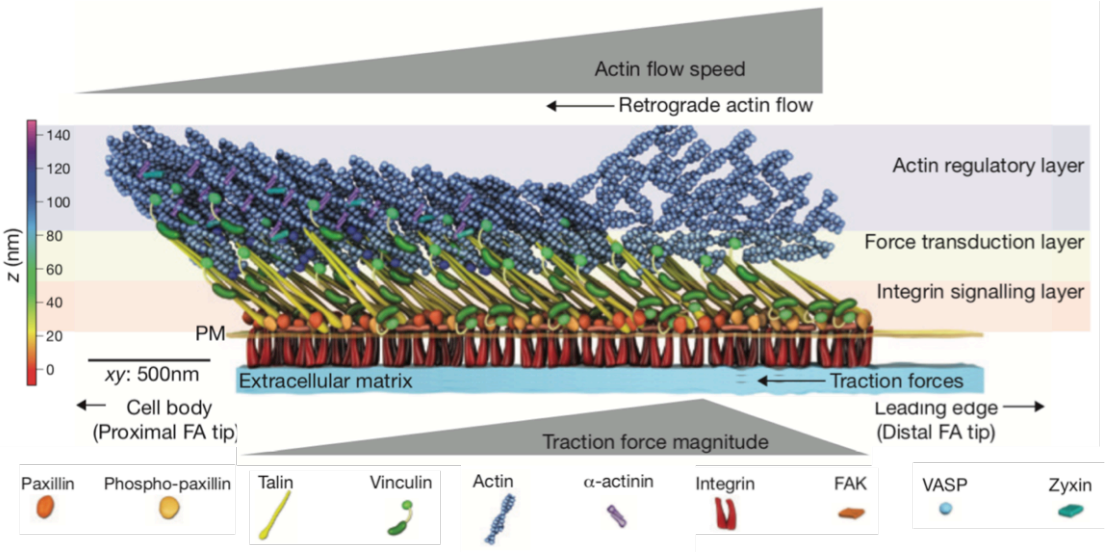

Figure 1: Architecture of integrin based focal adhesions in z-direction

This model was generated from a study using interferometric photoactivated localization microscopy (IPALM) to obtain the positioning of the C- and N-termini from several adhesion proteins in z-direction. The model shows the 3 organization layers: Integrin signaling layer, the force transduction layer and the actin regulatory layer. Forces generated by actin retrograde flow and traction force through ECM are depicted as arrows in grey. Distance from the substrate in z-direction is displayed on the left side in nanometer. Legend of adhesion components located in the study is displayed on the bottom.
(Image is adopted from Case and Waterman, 2015)

It was long debated whether integrins located in the plasma membrane form clusters and whether these are always signs of integrin activation. In 2015 Changede et al. used super resolution microscopy to observe integrin clusters in FA. The study revealed integrin clusters of about 100 nm diameter containing 50 integrins on average (Changede et al., 2015). Clustering was previously associated with active integrins; however, this was challenged in 2018 by a study observing inactive integrin clusters, which were segregated in and out of FAs (Spiess et al., 2018). By the use of single molecule tracking, it was discovered that FA were permeated by freely diffusing as well as immobilized clusters of integrin; with

differences in diffusion behavior according to integrin type (Shibata et al., 2013; Rossier et al., 2012).

In general FAs can be seen as assemblies of archipel-nanoclusters that are anchored by immobile integrins to the membrane, but have components moving unhindered between them. Adhesion components exhibit various recruitment patterns to FAs. Some proteins, such as talin, a-pix and ß-pix are recruited directly from the cytoplasm, whereas others followed a two-stage recruitment; first to the ventral plasma membrane and second in lateral direction towards the FA (Shibata et al., 2013).

2.1.2 Mechanobiology of integrin based adhesions

During development, cells sense their mechanical environment and the topology of their surroundings. These properties have a strong influence on where a cell migrates to, or what type of tissue is developed. Also, in later stages of multicellular life, mechanical properties can still determine cell fate. An example is the human mesenchymal stem cell system. Here, the stem cell differentiation is determined by the cell shape, which in turn is changed by the rigidity of its surrounding matrix (Engler et al., 2006). The bases for all of these processes are the cell-matrix adhesions. For all integrin mediated adhesions mechanosensitivity and mechanotransduction play an important role in maturation and disassembly.

Integrins that bind to RGD motifs on fibronectin can be activated through ligand binding. After this initial binding a 'catch-bond' is formed that further increases the lifetime of the integrin-ligand interaction. Catch-bonds are protein-protein interactions with increased bond-lifetime, due to additional allosteric binding properties that are induced by the application of mechanical force. In the case of α5ß1 an additional binding site for fibronectin in the α-subunit is revealed, upon application of force (W. Chen et al., 2010). This catch-bond formation results in adhesion strengthening and maturation (Benito-Jardón et al., 2017; Friedland et al., 2009; Strohmeyer et al., 2017). Similar force induced activation was also recently reported for αLß2 integrins in migrating T-cells (Moore et al., 2018; Nordenfelt et al., 2017).

Another effect of mechanical force in adhesions is the activation of force-specific binding sites on mechanosensitive adhesion proteins. Some adhesome components such as talin contain buried binding sites for interaction partners that are only available with the application of force. The application of mechanical tension can expose these cryptic sites

and lead to the recruitment of further adhesome components. It was shown for talin that under mechanical tension, additional vinculin binding sites are revealed and vinculin can be recruited (del Rio et al., 2009a). Similar behavior was observed for p130Cas, which was shown to reveal a Src specific phosphorylation site under mechanical tension (Sawada et al., 2006). FAK undergoes a conformational change under force that increases its kinase activity, leading to adhesion strengthening and maturation (Zhou et al., 2016).

In all of these cases the application of mechanical tension leads to increased recruitment and adhesion strengthening, which in turn associates more of the actomyosin machinery to the adhesion. This induces a feedback loop promoting adhesion maturation and growth.

2.1.3 Molecular clutch hypothesis

Cell migration is a complex process required for a multitude of cellular actions. During the cell movement, protrusions are created at the leading edge, which are made of rapidly polymerizing actin filaments. Actin is polymerized in close proximity to the leading edge with its barbed ends pointed towards the membrane. Actin is nucleated by the Arp2/3 complex, which binds to existing actin fibers and nucleates new actin filaments in a 45° angle. This creates a dynamic meshwork of polymerizing and depolymerizing actin filaments called the lamellipodium. The polymerization process of actin creates the force that drives the cell protrusion forward. However, this force can only be utilized if the protrusions are anchored to an immobile object like the ECM. When unanchored, the actin filaments get pushed back towards the cell center, a process called 'actin retrograde flow'.

Integrin mediated adhesions function as anchors and use integrin adaptor proteins to couple actin filaments via integrin to the ECM. The 'molecular clutch' concept, originally proposed by Mitchison and Kirschner in 1988, explains this mechanism. It states that, like an engaged clutch, integrin adhesions coupled to actin flow can propel a cell forward, using the force that is generated by the actin polymerization at the leading edge (Mitchison and Kirschner, 1988).

Integrin has more then one binding partner, that is able to connect the transmembrane receptor to the actomyosin machinery (Brakebusch and Fässler, 2003). With binding sites for both actin and integrin, talin is thought to form initial bonds bearing a low force. Upon stronger engagement of actomyosin with the newly formed adhesion higher forces can be exerted, which may lead to partial talin domain unfolding. This allows the exposure of talin's cryptic binding sites for vinculin, followed by vinculin recruitment and thus further

reinforcement of the clutch. It was shown that vinculin depletion results in excessive actin retrograde flow (Thievessen et al., 2013). Similarly, depletion of talin also leads to higher retrograde flow during initial cell spreading (Zhang et al., 2008).

Odde and colleagues observed, that the model predicts different behavior of the clutch system on different substrates, depending on the substrate stiffness (Chan and Odde, 2008). On hard substrates clutches would engage, but soon reach their braking point. Opposing, on soft substrates a longer loading time for talin to bind integrin would allow more clutches to engage, generating a more stable bond until breakage.

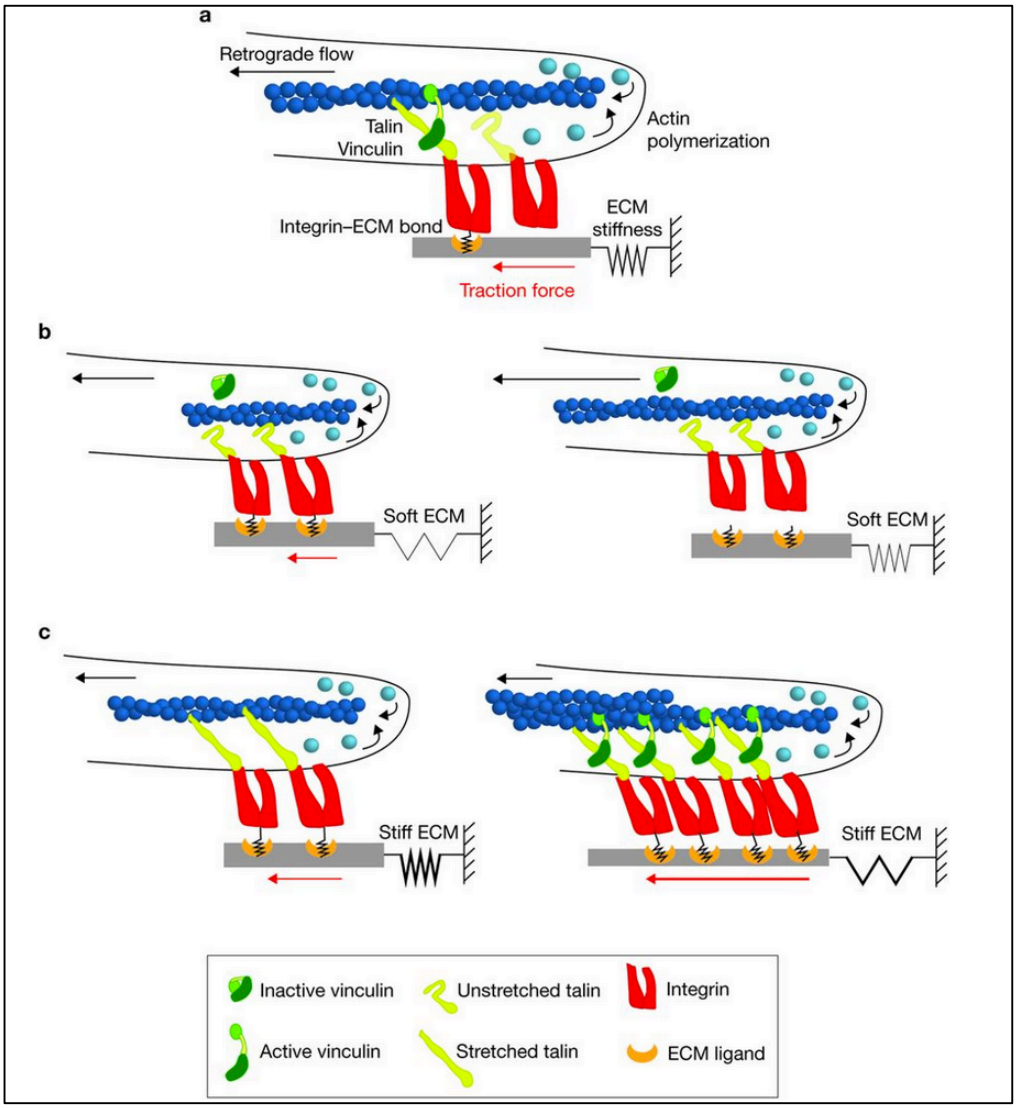

Figure 2: Representation of Roca-Cusachs molecular clutch model

A. actin retrograde flow is created by actin polymerization at the leading edge. Integrin adhesions anchor actin filaments to the ECM, thus acting as clutch and provide cell movement. B. Clutch model on soft substrates: Force is not sufficient to activate talin in time before the lifetime of an integrin-ECM bond runs out. Talin dis not activated and vinculin is not recruited. C. On stiff substrates, force can be generated on talin, vinculin get activated

and binds before the integrin-ECM bond slips, resulting in actin mediated adhesion reinforcement. (Swaminathan and Waterman, 2015)

This model was further evolved by the addition of the effect of talin's force dependent vinculin recruitment and integrin's 'catch bond' formation (Elosegui-Artola et al., 2016). It predicts that the integrin-substrate bond fails on low stiffness ECMs before sufficient force is transmitted to talin for clutch reinforcement through vinculin. However, on high stiffness substrates the integrin ECM bond is reinforced, force gets transmitted and vinculin recruited, thus resulting in increased traction and cell movement (*Figure 2*).

This bi-phasic force response due to substrate stiffness indicates that other integrin adaptors such as kindlin play a role in the integrin-actin linkage (Swaminathan and Waterman, 2017). Furthermore, it is currently discussed that the dimerization capabilities of both integrin adaptors, talin and kindlin could create a network that could prevent a system failure in case single integrin-ligand or integrin-adaptor links break (Klapholz and Brown, 2017).

2.2 Maturation of integrin based adhesions

Motility and dynamic migration are essential for development an need to strictly regulated throughout cell life; therefore integrin adhesion structures are heterogeneous in composition and can undergo drastic morphological changes depending on their mechanical and biochemical activities. Integrin adhesions start as nascent adhesions and mostly disassemble after less than two minutes. However, when engaged with force and with the required signals they can mature into focal adhesions, or even further, into fibrillar adhesions. Both are larger adhesion structures with a longer lifetime that act as more stable cell-matrix anchor (*Figure 3*).

The maturation of integrin adhesion structures is regulated by a multitude of factors. Biochemical processes such as phosphorylation (Choi et al., 2011), proteolysis (Franco et al., 2004) or cytosolic Ca^{2+} level play important roles. In addition, mechanical properties of the surfaces and the forces cells exert on their adhesions are essential for their maturation (Schoen et al., 2013). Upon maturation, changes in protein composition occur, through recruitment of a wide range of adhesome components, as well as reinforcement of the actin cytoskeleton with actin-crosslinker and motor proteins.

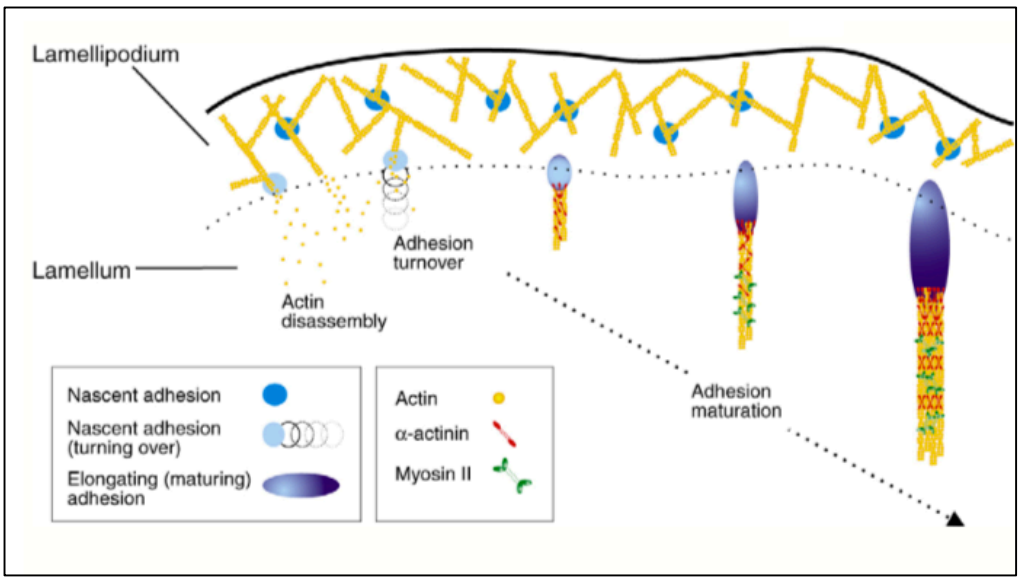

Figure 3: Schematic view of actin based adhesion maturation in the lamellipodium.
Lamellipodium represented as actin network (yellow) with Arp2/3 network intersections and NAs (blue). NA entering the lamellum are either disassembled, together with their actin connections and turned over, or mature force-dependent into elongated focal adhesions. FAs in the lamellum recruit actin bundling proteins such as α-actinin and later force generating myosin-II to mature and enlarge further (adopted from Vicente-Manzanares et al., 2009).

For a moving cell following biochemical signals, it is vital, that adhesions stay dynamic and that ECM anchors at the rear of cell are disassembled. Cells disassemble and internalize their adhesions at the rear end and recycle their components in order to minimize the required energy.

2.2.1 Nascent adhesions

To bring cells into motion, they require a dynamic cycle of assembly and disassembly of their adhesions at the lamellipodium and the rear end of the cell. At the leading edge of the cell the first visible adhesion structures are the short-lived NAs. With a diameter of less than 0.25 µm, they are the smallest visible adhesion structures triggered by integrin activation (Choi et al., 2008; Gardel et al., 2010). Their formation at the edge of the lamellipodium requires a couple of initial steps.

To initiate the NA formation, integrin needs to be activated and bound to a ligand. It is still debated how this activation is precisely achieved. It is thought that integrins can be either activated from the inside by adaptor protein binding (inside-out activation) or that they can be activated via extracellular ligand binding (outside-in signaling). Inside-out

activation is facilitated by the integrin adaptor proteins talin and kindlin. Though it was initially thought that talin binding to the integrin cytoplasmic tail is sufficient, it was later shown that initial NA formation can occur without talin being present and that loss of kindlin is fatal for integrin activation in some cell types (Moser et al., 2009; Zhang et al., 2008; Montanez et al., 2008).

Furthermore, activated integrins need to be clustered in order to form NA. It was shown that in small adhesion structures, integrins are clustered in groups of > 10 within in the plasma membrane (Wiseman et al., 2004). In addition, on the outer membrane site integrins need to be able to bind to at least three RGD nanoclusters in the ECM for a successful NA formation (Cavalcanti-Adam et al., 2007).

For further stabilization and maturation of NAs, force needs to be exerted on integrins bound to the ECM via the actin cytoskeleton. Talin is used as a mechanical linker between integrin and the actomyosin-machinery. It links integrin directly to actin, as well as indirectly via the force sensitive recruitment of vinculin. Talin acts as a clutch in transmitting force generated by the actin retrograde flow to integrin. The importance of mechanical force was shown in experiments, where either vinculin or Arp2/3 complex were knocked out, both resulting in strongly reduced NA maturation (Dang et al., 2013; Thievessen et al., 2013).

During NA formation, different adhesion signaling molecules, such as focal adhesion kinase, p130CAS or Src, are recruited to the adhesion site. Some of them, for example most LIM domain containing proteins, are recruited in a force-dependent manner. Furthermore it was shown that most of the initial adhesion components appear at the NA at about the same time. In 2014, a study by Bachir et al. showed that some of these adhesion components are recruited from and ejected to the cytoplasm in preassembled complexes. This indicates that they are reused for different adhesion complexes, which agrees with the dynamic picture of NAs (Bachir et al., 2014).

NAs can act as anchors between ECM and actin cytoskeleton or as signaling assembly to sense surrounding properties, but eventually, depending on the movement speed of the cell every NA will reach the rear end of the lamellipodium. Here, their fate is decided to either be disassembled or to mature into FAs. Thus, every NA's lifetime and their maturation speed depends on the cell's migration speed.

Dynamic NA assembly is vital for moving cells. On the one hand, it provides them with a fixing point to move the cells lamellipodium forward, through the cycle of actin polymerization and treadmilling. On the other hand, NAs act as mobile signaling centers to

report the biochemical environment and ECM properties, which in turn decides over migration or resting of the cell.

2.2.2 Focal adhesions

An NA that has reached the rear edge of the lamellipodium can mature into a FA. However, for this maturation process the right signals need to be provided. During this maturation the lifetime of focal adhesions increases drastically to up to 20 minutes and its size enlarges to 1 to 5 µm. Located at the inner edge between lamellum and main cell body FAs start connecting to stress fibers and recruit more adhesome components (*Figure 3*). This process requires further integrin clustering, stable integrin-actin linkage and actin bundling.

One of the proteins that is suspected to have a role in some of these events is α-actinin. It was shown to directly bind integrin cytoplasmic tails and to be recruited in clusters with ß1 integrin to growing FAs (Bachir et al., 2014; Roca-Cusachs et al., 2013). Further, α-actinin is able to crosslink F-actin filaments into larger actin bundles. This increases the actin amount at the FA leading to a higher local concentration of actin-bound talin, which in turn ensures more stable integrin-actin linkage (Rossier et al., 2012).

Another process of great impact for FA maturation is mechanotransduction, due to its implications in enabling the access of force-dependent binding sites in adhesome proteins and allowing the recruitment of critical components, such as vinculin recruitment to talin (del Rio et al., 2009b). Proteomic studies have shown that inhibition of myosin-II, a protein that induces mechanical force in the actin cytoskeleton, alters the adhesome protein composition, as the recruitment of some of the adhesome components depends on mechanical tension (Horton et al., 2015; Schiller and Fässler, 2013). It was observed for myosin-II inhibition that the recruitment of critical integrin adaptor proteins, such as kindlin and talin is diminished. In addition, a strong effect was observed for LIM-domain containing adhesome members, such as zyxin and paxillin (Horton et al., 2015). Interestingly, in these myosin-II deficient cells the levels of ß-Pix, an adhesion maturation inhibitor was increased, which lead to increased rates of cell migration (Kuo et al., 2011).

Mechanical tension in FAs has other interesting aspects; as it facilitates for some proteins not only the additional recruitment of binding partners (for example vinculin the in case of talin), but also increased accessibility of tension-dependent phosphorylation sites, thus altering the signaling aspects in FAs. This type of effect was shown in the case of the

focal adhesion kinase and p130Cas, both gaining additional functionalities under mechanical force (Sawada et al., 2006; Zhou et al., 2016).

Another effect of tension is the formation of so-called 'catch-bonds'. It was shown for ß1-integrin that it changes its conformation under force to increase binding to synergy sites on fibronectin, thus strengthening its bond (Friedland et al., 2009). Another catch-bond formation suggested in the field is the interaction between talin and the integrin tail. *In vitro* they show only a weak interaction in the high micromolar range, but they are suspected to increase their bond strength and bond lifetime significantly under tension.

Overall, mechanical force on adhesion components is suggested to lead to increased phosphorylation, followed by further recruitment of adhesion components and actin, thus inducing a feedback loop to further strengthen the adhesion.

2.2.3 Adhesion disassembly

To maintain a constant movement, it is important for cells that the adhesion's tethering to the ECM remains dynamic. Adhesions need to be assembled and reinforced at the leading edge, but also need to be disassembled at the rear end of the cell, or in regions that are not optimal for migration. Adhesion disassembly is the default fate for NAs, if maturation to FA does not occur. In FAs however, this process needs to be tightly regulated.

As FA networks are complex protein assemblies it is unlikely that their disruption follows the inverted sequence of events that are needed for their formation (Ezratty et al., 2005). It is more likely that their disassembly is orchestrated through a disruption of the weakest nodes in the network. While adhesions are diverse and consist of hundreds of different proteins, there are only two integrin adaptor proteins at the core of all adhesion architecture, namely talin and kindlin. The disruption of talin and kindlin's binding to the cytoplasmic integrin tail eventually leads to a reduction of force in adhesions, due to the loss of the cytoskeleton-ECM linkage. Thus, the loss of force in a FA initiates adhesion disassembly, shown by experiments in the presence of blebbistatin or in cells with an inhibited ROCK pathway (Carisey et al., 2013a; Stehbens et al., 2014).

There is little known about how interactions between kindlin's and the cytoplasmic integrin tail could be disrupted. However, several mechanisms were suggested that could destabilize the integrin-talin-actin linkage and initialize adhesion disassembly.

Talin's sequence shows two potential cleavage sites for the calcium-induced protease calpain. Both are at critical positions within the protein; One is located in the linker region between talin's head and rod, the other at talin's C-terminal actin binding site, before its dimerization domain. It was shown that the inhibition of calpain hinders adhesion disassembly in cells (Bhat and Ma, 2002; Franco et al., 2004).

Upon phosphorylation through the MAP4K4 kinase, the FERM domain protein moesin can compete with talin for the interaction with the cytoplasmic integrin tail. Displacement of talin promotes adhesion disassembly (Vitorino et al., 2015). In this context, it was shown in *D. melanogaster* that the MAP4K4 kinase homologue *misshapen* is enriched at the rear end of migrating cells to promote cell migration (Lewellyn et al., 2013).

Interestingly, the histone methyl-transferase EZH2 is able to methylate talin at actin binding site 3 in the C-terminus, thus partly disrupting talin's link to the actomyosin machinery. This leads to adhesion disassembly and was shown to promote higher levels of cell migration for neutrophils and dendritic cells (Gunawan et al., 2015).

A more global mechanism for adhesion disassembly is the internalization of integrin clusters at adhesion sites. It has been observed that microtubules, targeting adhesions structures at the front of the migrating cells tend to induce their endocytosis (Ezratty et al., 2005). Furthermore, cells can induce the clathrin-mediated endocytosis of integrins through adaptor proteins that compete with talin's and kindlin's binding to the NPxY and the NxxY motif on the β-integrin tail (Calderwood et al., 2003). The adaptor proteins Dab2, ARH and Numb were shown to concentrate around adhesion sites and mediate the clathrin-dependent integrin internalization (Ezratty et al., 2009).

Some proteins including FAK, ERK, paxillin and p130Cas (Webb et al., 2004) are shown to have a role in adhesion disassembly, since their absence makes adhesions more stable and increases their lifetime. In the case of p130Cas, it has recently been shown that cells make use of its degradation to enhance the stability of some selected adhesions. In those adhesions p130Cas is actively phosphorylated, which leads to the recruitment of an E3 ubiquitin ligase that induces p130Cas's degradation (Teckchandani and Cooper, 2016). The cell's ability to alter p130Cas levels in adhesions indicates a possible selection mechanism that allows cells to actively maintain or disrupt adhesions, depending on the current requirements.

2.3 Integrin

It is necessary for multicellular organisms that their cells organize by adhering their surfaces and facilitating their cell-cell communication. During their evolution, they developed complex receptor systems, sensing their environment and are able to mediate signals to themselves as well as other cells. The receptor family responsible for interaction and communication with the ECM are integrins.

The integrin receptor family is a highly conserved group of heterodimeric transmembrane receptors, which was first described in the 1980s and named after their function of integrating the ECM with the cytoskeleton (Hynes, 1987; Tamkun et al., 1986). They mediate cell adhesion to different ECM proteins and other cell receptors such as the I-CAM and V-CAM receptor family (Xia and Kanchanawong, 2017)

Integrins are heterodimeric transmembrane receptors composed of two individual proteins the α and β subunit. There are 16 α and 8 β subunits, which form the 24 members of the integrin family. Integrin subunits are usually composed of a large extracellular domain a single transmembrane helix and a short unstructured cytoplasmic tail. Even though integrin receptors are universally expressed in metazoans each family member adopted specific roles and tasks during evolution in the organism development and tissue homeostasis, together with their specific ECM ligand (Johnson et al., 2009).

The correct function of integrin systems is vital for many types of cells. Cells in development need to travel the correct path in order to form organs correctly; leukocytes need to adhere site-specific of engage their designated targets; platelet activation needs to be tightly controlled in order to avoid catastrophic failure of the hematopoietic system. It is clear that integrin-mediated adhesions play a critical role in cancer formation, due to their role in potentially enabling cells to migrate and overcoming tissue homeostasis.

2.3.1 The integrin familiy

The 24 members of the integrin family are heterodimeric class 1 transmembrane receptors. They are composed of non-covalently associated α- and β-subunits, each with a large extracellular domain, a single transmembrane helix and a short cytoplasmic tail (except for β4 integrin). Cells generally express an excess of β-subunits, but present only heterodimeric integrin to the cell surface. Hence, the amount of α-subunits determines the integrin surface concentration (Santala and Heino, 1991).

The average integrin has roughly 1750 aa, where the α-subunit provides 1000 aa and the β-subunit 750 aa. The α-subunit consists of a seven-bladed β-propeller linearly connected to a thigh, a calf1- and calf2-domain followed by the transmembrane domain (TMD) and the short cytoplasmic tail (*Figure 4*). In 9 of the 18 α-subunits the β -propeller contains an additional αI domain between the 2nd and 3rd blade, which in those integrins directs the ligand binding (Larson et al., 1989). This αI domain assumes a Rossman fold and, together with a coordinated Mg2+ ion, forms the metal-ion-dependent adhesion site (MIDAS) (J. O. Lee et al., 1995).

The β-subunits ectodomain is composed of a plexin-sempahorin-integrin (PSI) domain followed by a hybrid domain, a βI domain and four cysteine-rich epidermal growth factors (EGF) repeats. Interestingly the βI domain also contains Mg^{2+} coordinating MIDAS site as well as an adjacent a Mg^{2+} coordinating ADMIDAS (adjacent to MIDAS) site, both within the βI domain.

Both TMD of the α or β subunit are highly conserved. They are single transmembrane helices that reach into the cytoplasm and overlap in a juxtaposed manner in the dimerized state. It was shown that the TMD have two distinct interaction points that are responsible for dimer formation. One lies within the membrane, where the dimerization is mediated via a GxxxG motif on the α-subunit's transmembrane helix. This motif creates the binding pocket for another hydrophobic patch on the β-subunit's transmembrane helix. The other interaction site is called the inner membrane clasp and occurs at a patch of opposing electrostatic charged residues, located at the juxtaposed region on C-terminal site of both TMDs. Through mutation studies, it was shown that in both the inner (R995D/D723R) and outer (G972L/G976L) membrane clasp that disruption of the dimerization interface results in constitutively active integrins (Hughes et al., 1995; Luo et al., 2005). Interestingly at the C-terminal end of both transmembrane helices a so called 'snorkling lysine' followed by a hydrophobic region can be found, which is suspected to be the reason for the tilted arrangement of the transmembrane helixes. These hydrophobic regions are responsible for both tilted and/or straight positions of the TMDs within the membrane, which is thought to play a significant role in the transmembrane signal transduction (Partridge et al., 2005).

Integrins have rather short (30-50 aa) cytoplasmic tails, except for the β4 integrin tail, which has about 1000 aa. It is widely accepted that both the α or β subunit's cytoplasmic domains are unstructured, if not in complex with an integrin binding protein (Campbell and M. J. Humphries, 2011). It was proposed by NMR studies (LFreview6) that α or β cytoplasmic tails could interact via a salt bridge between the GFFKR (α) HDR(R/)E (β) sequences;

however, these interactions seem to be week at best (Legate and Fässler, 2009). Of more importance are two motifs on the β integrin cytoplasmic tail, both of which function as recognition sequences for PTB domain proteins. The membrane proximal NPxY motif and the membrane distal NxxY motif act as binding sites for crucial integrin adaptor molecules such as talin and kindlin.

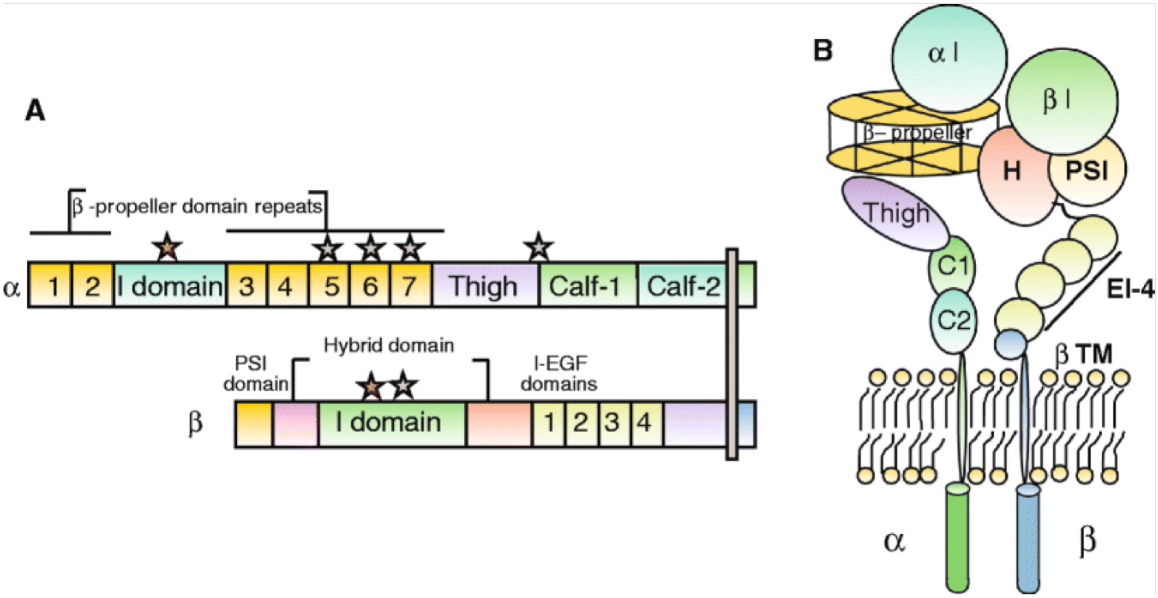

Figure 4: typical domain arrangement of an αI-domain containing integrin family member. *A.: shows the domain arrangement of both heterodimer subunits. Stars indicate the divalent cation-binding sites. Grey bar indicates the transmembrane helix and membrane dimerization sites. B.: Representation of the integrin heterodimer within the plasma membrane. Extracellular domain depicted on the top, transmembrane helixes indicated as stretched ellipsoids across the membrane and cytoplasmic tails represented by cylindric columns at the bottom. (Barczyk et al., 2010)*

The ligand specificity of integrins is usually dictated by the α-subunit but several studies suggest that divalent cations binding to the MIDAS and ADMIDAS sites are of importance as well (J. O. Lee et al., 1995; Springer et al., 2008; Xiao et al., 2004). The integrin family can be classified according to their ligand binding into four subcategories. A third of the integrins (α5β1, α8β1, αIIbβ3 and all αV integrins) recognize the RGD sequence in matrix proteins like fibronectin, vitronectin, fibrinogen and others. The αI-domain containing integrins α1β1, α2β1, α10β1 and α11β1 recognize a GFOGER motif and belong to the collagen and laminin binding integrins. Another group containing α3β1, α6β1, α7β1 and α6β4 binds to laminins, through yet unknown but specific interactions. The last subgroup contains all leukocyte-specific β2 integrins, LDV motif specific integrins (α4β1, α4β7 and α9β1) and αEβ7 integrin that interacts with the αI domains in ICAM, VCAM and E-cadherin (*Figure 5*).

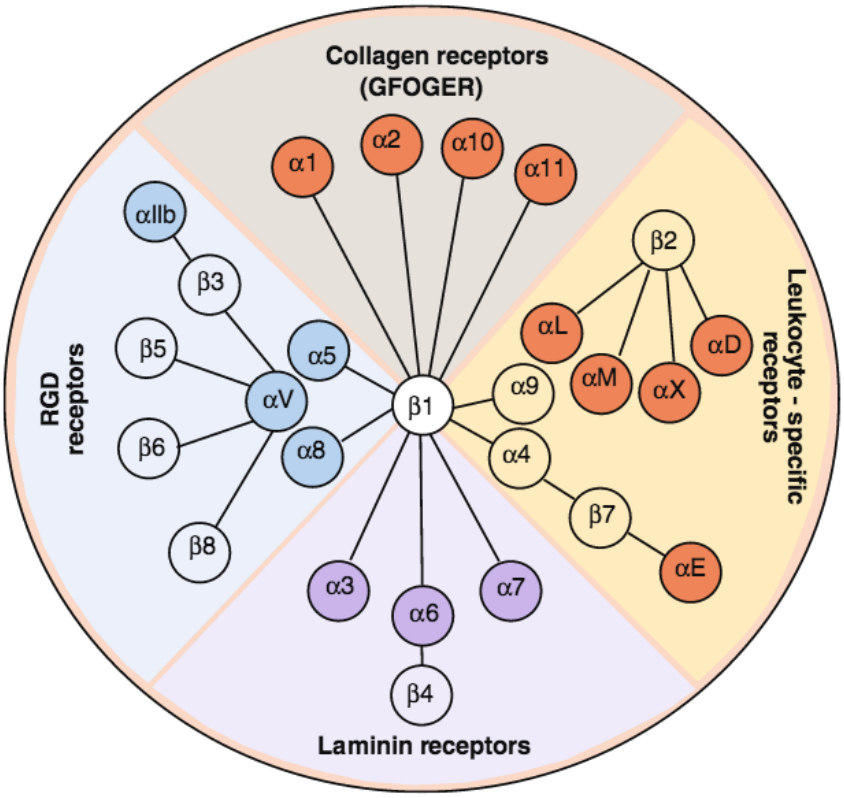

Figure 5: Integrin family overview

Representation of the vertebrate integrin family. The 24 different heterodimers are arranged in different classes, according to their ligand binding capabilities, which is usually defined by the α-subunit (Barczyk et al., 2010)

2.3.2 Integrin activation

The role of integrins in cells is diverse. Not only do they provide a physical link for the actin cytoskeleton to the extracellular matrix, but they can sense the extracellular environment and induce signaling cascades to alter the fate of cells. Integrins do not possess any catalytic activities themselves, but function as transmitters of signals through the plasma membrane. For this they can adopt different conformations as response to inside and outside signals. Through structural studies it was shown that that integrins have at least 3 different states (Luo et al., 2007a) (Springer and Dustin, 2012).

It was shown in a X-ray crystal structure that αVβ3 integrins ectodomain adopts a bent conformation with the N-terminal ligand binding domain facing downwards next to the crossed α- and β-subunits leg domains (Xiong et al., 2001). This 'bent' conformation is referred to as the inactive state, since the ligand binding domain is facing towards the plasma membrane.

In 2002, an electron microscopy study on αVβ3 showed that integrin can adopt an extended open conformation upon Mn2+ addition in which both subunits legs are separated from each other and the head domain is pointing away from the membrane. In 2010 it was shown that a similar conformational change after addition of the talin head domain on αIIbβ3 in lipid nanodiscs (Ye et al., 2010). In addition, it was shown that the movement of integrin's ectodomain positions the ligand binding site ~19 nm away from the membrane, thus increasing the reach of integrin receptors in a membrane potentially surrounded by large glycosalix structures.

The third conformation named 'extended closed' is a transition between 'bent' and 'extended open', where the ectodomain is extended, but its leg domains and the TM domains are still closed. This conformation was suggested by negative staining electron microscopy studies (Takagi et al., 2002). It is yet unclear if there are more transition states between these three steps that remain to be uncovered.

A recent paper hinting at those dynamic short-lived states shows a cryo-EM structure of the head domain of αVβ8 integrin, where the headpiece conformation is stabilized by the β-subunits leg. The study also shows that within its extended closed conformation the integrin undergoes a dynamic 'sunflower like' movement, where the head domain is able to shift and rotate on the joint of the closed leg domains(Cormier et al., 2018).

It was further observed in an X-ray crystallography study, where crystals containing the integrin extracellular domain were soaked with ligand, that during the transition between the three main conformations the βI MIDAS domain is reshaped by a piston-like movement of the α7 helix. This causes the hybrid domain to pivot by 60° and finally resulting in a swingout movement of ~75 Å by the β-subunit's leg domain away from the α-subunit (*Figure 6*). Since this drastic movement results in a separation the α- and β-cytoplasmic tail potential integrin adaptors can bind and subsequently force can be applied to the extended β-ectodomain (J. Zhu et al., 2013).

The structural information about integrin's conformational changes is mostly derived from platelet integrins. However, it is expected that due to the high amount of sequence homology between different integrin family members this information remains true for other integrin family members.

The precise steps during the events of integrin ligand binding and head piece extension are still unclear; different models have been proposed and are highly debated.

The 'switchblade' model predicts that ligand binding can only occur after the integrin head piece is extended (Luo et al., 2007b). This extension is induced by ligand binding of

talin and probably kindlin to the integrin cytoplasmic tail (Inside-out signaling). In contrast, the 'deadbolt model' hypothesizes that ligand binding to the extracellular domain induces the head piece extension and the leg-swingout and subsequently allows adaptor proteins to bind (Outside-In signaling) (Xiong et al., 2003).

Anther model that is recently discussed is based on the kinetic energy needed to maintain the integrin in its extended open conformation. In the thermodynamic landscape the transition between bent-closed and open-extended integrin requires a high amount of activation energy. Since, the simple binding of talin and/or kindlin is probably not sufficient to provide this energy, an additional effect is needed. It is predicted that small mechanical forces of 1-3 pN are needed to keep the extended-open conformation stable (J. Li and Springer, 2017). The model predicts, that a through application of small forces the conformational equilibrium is shifted towards the extended open conformation. Hence ligand binding and small forces provided through adaptor proteins can induce and maintain the extended open conformation (Z. Sun et al., 2018).

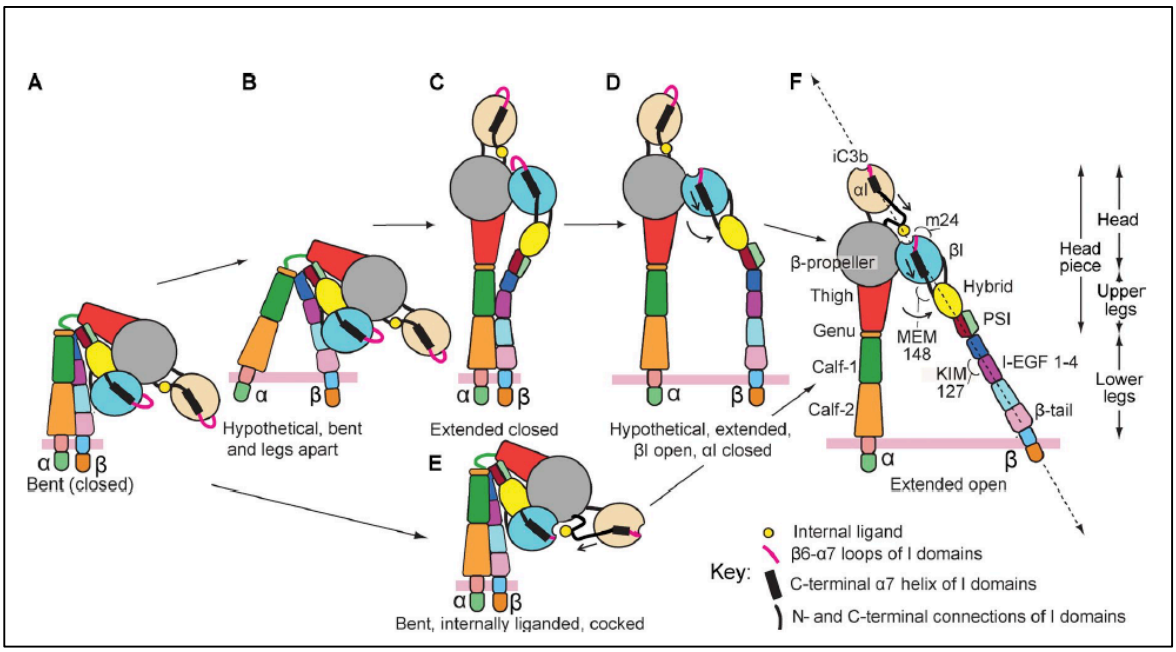

Figure 6: Illustration of an α-I domain integrin during activation and ligand binding.

The integrin activation either by external ligand binding (A-F except E) in 5 steps, or 3 steps by internal ligand binding to β-integrins βI-domain (A,E and F). B and D are hypothetical stages, A,C,E and F were observed in electron microscopy or crystal structures. F. Forces applied by actin cytoskeleton over integrin are depicted in dashed lines. (Sen et al., 2013)

2.3.3 Integrin adaptor proteins talin and kindlin

Integrin activation can be induced in multiple ways. Whereas a ligand binding from the outside can induce the piston like movement of the β-subunit and separate the TM domains, it is believed that a similar motion can be initiated from the cytoplasm. Integrins cytoplasmic tail has many interaction partners, among them talin was first discovered to play a critical role in integrin activation. It was shown in chinese hamster ovaries (CHO) that talin can activate normally inactive integrin (Calderwood et al., 2002; Horwitz et al., 1986). Further knockout and knockdown experiments showed that talin is key in regulating integrin's affinity and ligand binding. Talin orthologs were subsequently found in all multicellular eukaryotes and in vertebrates two talin isoforms were detected (Calderwood et al., 1999; Monkley et al., 2001a). Talin is organized in two main parts, a head and a rod domain and it was shown that the F3 subdomain of the FERM like head domain interacts with integrins membrane proximal NPxY motif. Despite the head domain being of importance for the integrin activation (Ye et al., 2010), the rod domain in needed for correct adhesion and cell spreading (Zhang et al., 2008).

In 2008 siRNA studies in mice showed that kindlin is another important integrin adaptor protein essential in integrin activation (Montanez et al., 2008; Moser et al., 2009; 2008; Ussar et al., 2008). Kindlins are structurally similar to talin head in that they are FERM domain proteins, though they have an additional pleckstrin homology (PH) domain inserted in the F2 domain. Their family has 3 members; kindlin-1 is expressed in epithelial cells, kindlin-2 is widely expressed, kindlin-3 is expressed mainly in hematopoietic cells. It was subsequently discovered that kindlin is needed for correct integrin activation (Moser et al., 2008; Theodosiou et al., 2016).

Whereas talin mainly binds to the membrane proximal NPxY motif on the integrin β-subunit tail, kindlin's F3 domain was found to interact with the membrane distal NPxY motif (Harburger et al., 2009). It is unclear if both proteins bind the integrin tail simultaneously of if the interaction happens in tandem.

Kindlin functions as protein interaction hub and is able to bind and recruit the complex of ILK-PINCH-parvin (IPP) to the cytoplasmic integrin tail, as well as paxillin and the arp2/3 complex (Böttcher et al., 2017; Fukuda et al., 2014; Theodosiou et al., 2016).

A crystal structure of kindlin-2 without its PH domain revealed, that kindlin similar to talin is able to dimerize, though with very slow kinetics, giving rise to the hypothesis that kindlin plays a role in integrin clustering (H. Li et al., 2017).

Interestingly, it was found that kindlin can bind actin directly, thus would be able to connect

the actin cytoskeleton directly to integrin. However, unlike talin there was so far no report on kindlin bearing any forces *in vivo* (Bledzka et al., 2016).

2.4 Talin

Discovered in 1983 as a protein that localizes to adhesion sites, talin was shown to be an integrin adaptor protein binding to cytoplasmic integrin tail. Shortly afterwards, it was shown that talin could also bind to F-actin. (Burridge and Connell, 1983) (Horwitz et al., 1986; Muguruma et al., 1990). Thus, talin was seen as adaptor molecule that could act as a direct link between integrin and the actin cytoskeleton. Talin's sequence is highly conserved throughout metazoan life. Interestingly mammals acquired two isoforms of talin: talin1 and talin2, which have different tissue specificity (Gough and Goult, 2018a; Kopp et al., 2010a; Monkley et al., 2001b). Whereas talin1 is expressed in all tissues, talin2 expression is more variable as it is for example highly expressed in heart muscle cells and neurons. Both isoforms seem to complement each other as it was shown that a knockout of talin1 in mouse fibroblast could be compensated by upregulation of talin2 (Kopp et al., 2010b). However, a knockout of talin1 in mice is embryonic lethal (Monkley et al., 2000). These and other genetic studies in mice, drosophila and *C. elegans* show that talin is essential for flawless integrin function.

2.4.1 Talins structural organization

As one of the most important integrin activators talin is a large (~2500 aa) protein in the cytosol of the cell. It consists of two main parts, the N-terminal 4.1-ezrin-radixin-moesin (FERM) domain (~400 aa) known as the talin head and the C-terminal rod domain (~2000 aa), which are connected, via a 82 aa unstructured linker region.

FERM domains are found in many different proteins and typically consist of 3 subdomains (F1 – F3), which have membrane binding properties (Tepass, 2009). However, talin's FERM domain is atypical as it has an additional subdomain (F0), which has a similar sequence to first subdomain (F1). Both, F0 and F1 domains share an ubiquitin like fold, whereas subdomain F3 shows a phosphotyrosine-binding (PTB) fold. It was shown that the F0 domain interacts with Rap1, which could play a role in talin's membrane recruitment

(Bromberger et al., 2018). The F2 and F3 domains contain basic amino acid patches mostly made of lysine, acting as lipid binding sites for charged lipids. It was shown that these lipid binding sites are especially specific to phosphatidylinositol-4,5-bisphosphat (PtdIns(4,5)P_2) (Chinthalapudi et al., 2018a). In addition, there is a ~40 aa loop region in the F1 domain containing several positive residues binding to negatively charged lipids. Further the F2 and F3 domain harbors actin binding site 1 (ABS1), which was recently shown to have an actin capping function while bound to the integrin tail (Ciobanasu et al., 2018).

The F3 domain also contains a conserved binding site that directly engages integrin at the membrane proximal NPxY motif on the cytoplasmic integrin tail. It was shown that both talin 1 and 2 have different specificity to different integrin tails, based on the charges of the conserved aa in the F3 domain (Gingras et al., 2010b). In addition to those binding sites it was reported that the F3 domain is able to bind different other proteins sharing the same motif. One of them is the PIPKIγ90, which is a source of PtdIns(4,5)P_2. Further interaction partners associated with talin regulation, such as RIAM, FAK, TIAM, layilin and Gα13 were reported to bind to this F3 interface as well. These multiple interaction partners make the binding interface in the F3 domain probably the most important regulation checkpoint for talin's activity. This is supported by the crystal structure, showing an autoinhibition of talins F3 domain though binding of talins R9 domain (4F7G)(Song et al., 2012a).

The talin rod connected to the head domain via an 82 aa unstructured linker region, sensitive to calpain cleavage (Franco et al., 2004). The 2000 aa rod is constituted of 62 alpha helixes organized into 13 rod domains and a single alpha helical dimerization domain at the C-terminus. Of the 13 rod domains 9 rod domains (R1,R5,R6,R7 and R9 -R13) are arranged as bundles of 5 helixes arranged one after another in a linear fashion, due to their N- and C-terminus located at opposite ends of the bundle (*Figure 7*). The other 4 rod domains (R2,R3,R4 and R8) are organized as 4 helix bundles with N- and C-terminus located side by side. Due to this, R2 - R4 form a distinct region at the N-terminus of the talin rod. The 4 helix bundle of R8 is inserted in between the 5 helix bundle of R7, forming a unique fold within talin (*Figure 7*)(Gingras et al., 2010b).

There are numerous interaction sites for different proteins along the rod (*Figure 7*). It was suggested that there are 11 potential vinculin binding sites in the talin rod, however all of them are buried in different helix bundles and are not directly accessible (Gingras et al., 2005; Kuo et al., 2011). Due to their N- and C-terminus location 4 helix bundle rod domains are more force sensitive and have a higher tendency to display their buried vinculin binding sites. An exception to this is the R8 rod domain. It is force resistant, due to its embedded

location within the R7 domain, this helps to retain its binding interface for its multiple interactors.

The rod further contains 2 actin binding sites (ABS2 and ABS3). ABS2 is located between the domains R4 – R8 and with the current understanding responsible for the main tension bearing actin connection (Atherton et al., 2015). ABS3 on the other side seems to act as initial actin binding point to provide force to talin and make the mechanosensitive vinculin binding site in R3 accessible.

In addition to the Integrin binding site 1 (IBS1) at the F3 domain, there is a secondary IBS in the R11 domain, though its function is not yet fully understood. It is discussed that it could play a role in integrin clustering and talin network formation at the membrane (Klapholz and Brown, 2017). The same motif in R11, as well as the rod domain R8 were shown to contain binding sites for RIAM. Rod bundle R8 acts as a binding motif for multiple other adhesion proteins, such as LIM domain containing paxillin, α-synemin and the DLC-1 receptor (H.-S. Lee et al., 2009; G. Li et al., 2011; N. Sun et al., 2008).

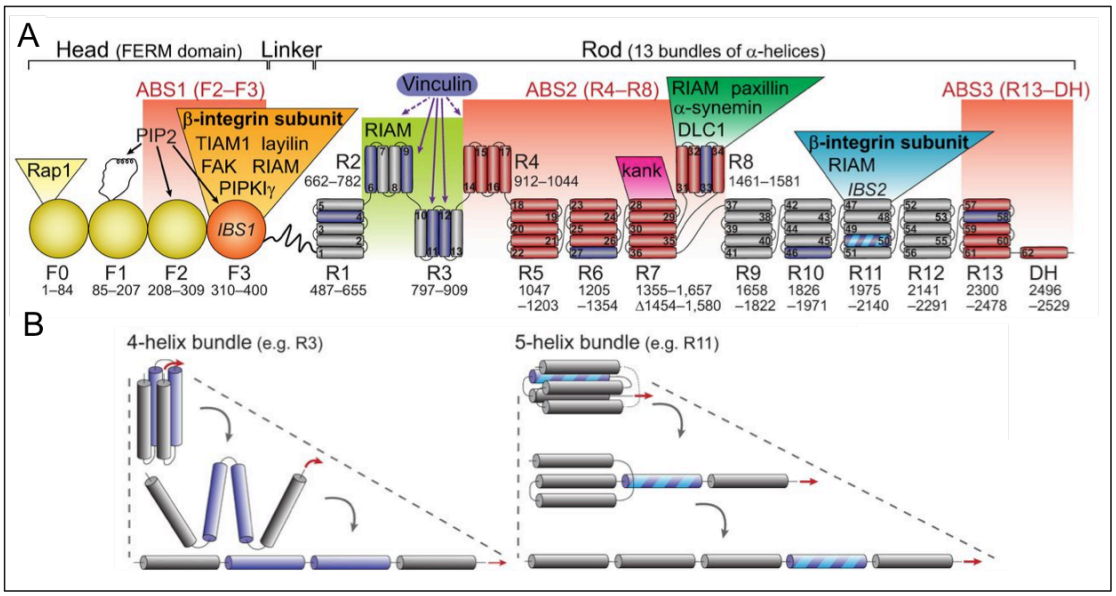

Figure 7: Talin-1 domain organization and mechanical domain unfolding

A. Domain organization and amino acid annotation of human talin-1. FERM domain indicated with its binding sites in yellow and orange, rod helixes in grey, helixes involved in actin binding (red) and helixes with VBS (purple). Further different protein interaction sites indicated on top. Lower panel shows model of the domain unfolding of a 4 and 5 helix rod domain through force (red arrow) and display of the cryptic VBS (purple). (adopted from Klapholz and Brown, 2017)

In our study, we could show that Kank is binding to talin's R7/R8 domains via its N-terminal KN motif and that it has several functions at the adhesion site that are talin related. It is able to activate talin *in vitro* and subsequently enhance integrin activation. In addition,

the recruitment of Kank to actin associated talin reduces the amount of actin that is bound via talin (Z. Sun et al., 2016). It was confirmed in another study, that the interface for Kank binding on the talin rod is the R7 domain (Bouchet et al., 2016).

At the very C-terminus of the rod is the dimerization domain, consisting of a single helix, which can dimerize with its counterpart in an antiparallel manner (Gingras et al., 2008). It was suggested that talin can dimerize as a homodimer, where both rod domains are wrapping around both talin heads and form a globular structure (Goult et al., 2013a). Another EM study showed, that talin's R13 and dimerization domain can form dimers on actin fibers (Gingras et al., 2008).

In our study we determined the structure of recombinantly purified full length talin with cryo-EM. We confidently placed 15 of the 18 domains of talin and identified it as a monomer. Via biochemical and biophysical experiments, the talin monomer was characterized in both active and inactive state. However, the position of the dimerization domain was not visible with certainty in the structure. Thus, is still an open question whether the dimerization plays a role in molecular organization of talin (unpublished data).

2.4.2 Autoinhibition and activation

Despite the most common depiction of talin as elongated chain of alpha helical bundles (*Figure 7*), talin also exists in an autoinhibited conformation in the cytoplasm. Since talin is required for integrin activation it is expressed in high amounts in some cell types (Calderwood et al., 1999; Tadokoro et al., 2003), which in turn makes the regulation of its activity critical. First hints for an autoinhibition function appeared from a study showing, that overexpression of talin's head domain to have a stronger effect for integrin activation compared to the overexpression of talin full length (Goksoy et al., 2008; Song et al., 2012a).

In 1997 it was shown that talin adopts a globular structure in lower ionic strength (Winkler et al., 1997). In 2013 a cryo-EM structure showed a globular talin and fitted with SAXS models of the individual talin domains suggesting a possible architecture for the autoinhibition (Goult et al., 2013a).

Talin's primary autoinhibition is facilitated by the interaction of the R9 with the F3 domain (Goksoy et al., 2008). This interaction surface is highly conserved and a mutation of a glutamic acid to alanine at position 1770 showed reduced wound healing in mice (Haage et al., 2018). Interestingly, it was also shown that breaking this interaction is not sufficient to

recruit all cytosolic talin to the plasma membrane (B. A et al., 2012), indicating that there are multiple layers of inhibition in talin's architecture (Gough and Goult, 2018b).

A model in the flied is the 'push and pull' model, which describes how the inhibition between the F3 and R9 domain could be relieved by charge; Upon binding of negatively charged lipids to the patches of basic residues on the F3 domain, acidic patches on the R9 domain would be repelled from the membrane, leading to the dissociation of the F3 – R9 link (Wang, 2012). Though, how talin is recruited to the membrane and if there are protein interactions acting in support with this mechanism is unclear. There are different candidates that play a role in talin activation.

Integrin activation studies in CHO cells suggested RIAM, the effector of the GTPase Rap1, to be a talin activator (H.-S. Lee et al., 2009). RIAM is able to bind to two regions (R8 and R11) in the talin rod domain, however it was also shown to recruit talin to the membrane and bind to a shielded region in the F3 domain of the talin head. It was suggested to then activate talin, by breaking its F3 – R9 interaction and promote integrin β3 activation (H.-S. Lee et al., 2009). Platelets however lack RIAM expression, indicating that there are different mechanisms how talin can be activated in different cell types.

In combination of *in vivo* (platelets) and *in vitro* NMR studies, it was shown that Rap1 binds to talin F0 domain and recruit talin to the plasma membrane, where talin is thought to activate platelet integrins (Bromberger et al., 2018; L. Zhu et al., 2017) (*Figure 8*). Recently, another study confirmed these results and proposed an additional Rap1 binding site with low affinity in the F1 domain of the talin head (Gingras et al., 2019).

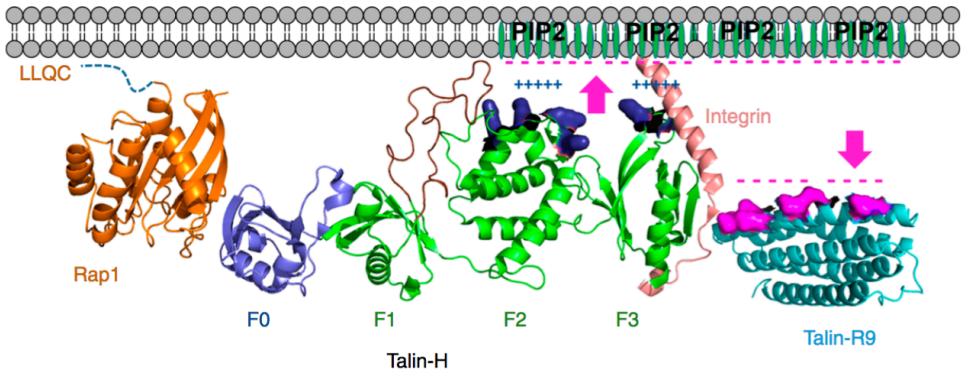

Figure 8 : Model talin recruitment via Rap1 and activation through Push and Pull

Model shows talin head bound to the PtdIns(4,5)P_2 rich membrane, via clusters of positively charged residues (darkblue, surface representation) The F0 domain is bound to Rap1 (orange), the F1 flexible loop is shown in brown. The β-integrin tail (coral) is bound to the F3 domain and the R9 domain (cyan) is repelled from the neg. charged membrane through its patches of negatively charged residues (magenta, surface representation). Margenta arrows indicate forces binding and repelling from the membrane (Push and Pull model). (adopted from Bromberger et al., 2018)

A study provided by Schiemer et al. in platelets found that the G-protein subunit $G\alpha_{13}$ binds directly to talin and is thereby able to modulate the activity of platelet integrin αIIbβ3. They used FRET studies to show that upon $G\alpha_{13}$'s binding to the F3 domain in the talin head the conformation of the full talin molecule alters (Schiemer et al., 2016).

Another possible molecule suggested to be critical for the activation of talin is the PIPKIγ90. This kinase is involved in the synthesizes of PtdIns(4,5)P_2 in the plasma membrane and shows a nanomolar interaction with talin's F3 domain. The loss of talin's interaction with PIPKIγ90 leads to reduced vinculin and talin recruitment and lower ECM attachment (Anthis et al., 2009; Legate et al., 2011).

In our study, we showed that Kank has the ability *in vitro* to increase talin binding to integrin, thus breaking talin's inhibition (Z. Sun et al., 2016). Kank binds at the R7 domain of talin via its KN-motif, however how precisely this resolves the inhibition is not clear.

Furthermore, we solved a cryo-EM structure of the full length talin molecule where we observed that talin's autoinhibition is mediated via two sites. In addition to the F3 – R9 interaction we found an interaction between the R12 domain and the F2/F3 head domain. Here the R12 domain shields several lysines, responsible for PtdIns(4,5)P_2 binding. This interaction was observed to be unstable, allowing phospholipids to disrupt it and potentially induce talin's activation (unpublished data).

Once talin's primary inhibition is relieved, some of talin's functions, such as actin binding site at the C-terminus and the lipid binding surface in the F2, F3 domain, become available. It is thought that talin can now bind to integrin and the membrane with its F2 and F3 domains and to F-actin with its C-terminal domain. This puts the rod domains under mechanical force and relieves the buried vinculin binding sites (*Figure 12*). Furthermore, talin's central ABS2 gets separated from its inhibitory domains R3 and R9 to bind actin with high affinity and reinforce the stability of the adhesion (Atherton et al., 2015).

2.4.3 Mechanism of talin's integrin binding

There are two general mechanisms of integrin activation; ligand based outside-in activation and inside-out activation. Outside-in activation is achieved by ligands of the ECM binding to integrin's extracellular domain, whereas inside-out activation is accomplished by adaptor proteins, like talin and kindlin, binding to the cytoplasmic integrin tail. Via crystal structures and NMR studies it has been shown, that talin binds to integrin at two positions on the cytoplasmic tail with its F3 domain (Anthis et al., 2009; Lau et al., 2009).

The first binding occurs at the NPXY motif of the integrin tail and potentially disrupts the salt bridge between integrin's α- and β-transmembrane domain (Kalli et al., 2011). The following conformational change in integrin repositions the β-subunit's transmembrane helix, which makes the Asp759 (ß1, Asp723 in ß3) available for talin binding (Lau et al., 2009). This direct interaction is supported by an interaction of a patch of basic residues on talin heads F2 and F3 domains as well as the F1-loop of the talin head, with acidic phospholipids such as PtdIns(4,5)P_2 in the membrane (*Figure 9*) (L. Zhu et al., 2017). This lipid binding helps to orient talin head and further supports the talin-integrin interaction (Elliott et al., 2010).

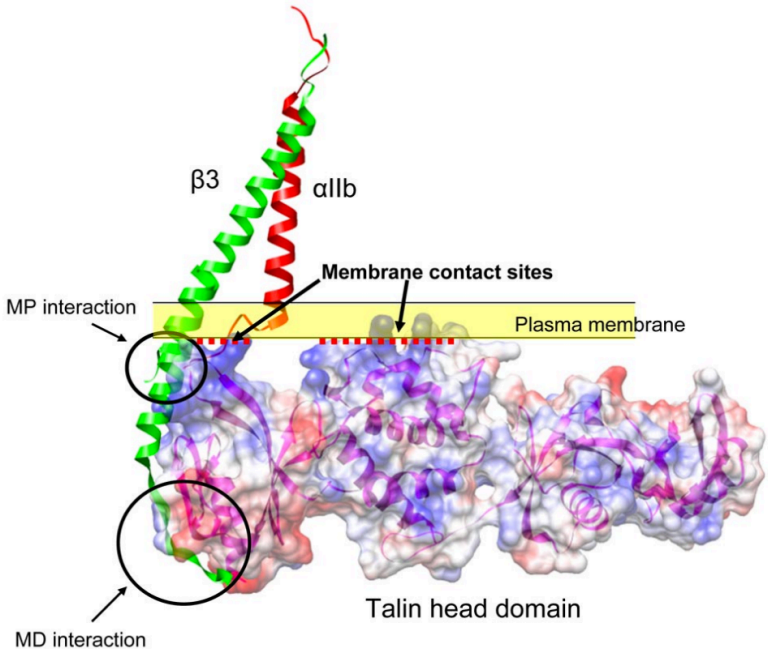

Figure 9: Model of integrin binding of talin head domain.
Talin head domain binds the β3 integrin tail (PDB 2K9J) at two sites, the membrane proximal binding site and the membrane distal NPxY motif. The dotted red lines represent the cluster of basic residues of talin head that are binding to the plasma membrane. The model of talin head is represented in surface view, showing its charge distribution (red = negative, blue = positive) (PDB 3IVF). (Ye 2012 blood)

It was shown that kindlin is needed for efficient integrin activation through talin (Montanez et al., 2008; Moser et al., 2008; Theodosiou et al., 2016). However, it is not clearly understood how talin and kindlin enable integrin activation synergistically. An important question to ask is whether talin and kindlin can bind simultaneously on the β-integrin tail or whether they act in tandem. Another supporting role of kindlin might be the formation of integrin clusters via dimerization and recruitment of further adhesion proteins

like IPP, Paxillin and even the Arp2/3 complex (Böttcher et al., 2017; Theodosiou et al., 2016).

A question of great interest is the role of talin's catch-bond formation with integrin. It was shown *in vitro* that the affinity for the interaction of talin with different β-integrin tails lies in the low micromolar range (Anthis et al., 2010). The catch-bond formation through mechanical tension strengthens the lifetime of the talin-integrin bond. Furthermore, exerted forces on integrin possibly lead to its activation via mechanical force. However, no detailed mechanism for this catch-bond formation was presented so far.

It was shown that talin is of critical importance for the activation of platelets (Lefort et al., 2012) and leukocytes (J et al., 2011; Petrich et al., 2007). Interestingly, overexpression of talin head is enough to increase integrin activation in cells. In contrast, overexpression of full length talin has a less potent effect on integrin activation, indicating the presence of talin's inhibited conformation in cells (Goksoy et al., 2008; Song et al., 2012b).

In addition to its IBS1 in the F3 domain, talin has another IBS in the R11-R12 domain. Even though the importance of this IBS is well established in flies (Ellis et al., 2011), neither its role nor its binding mechanism in mammals has been clarified so far.

2.4.4 Talin as mechanosensitive signaling hub

Mechanical forces are critical for the maturation of adhesion structures in cells; for example, nascent adhesions for example require forces in order to mature into focal adhesions. In recent years, research on mechanical forces at adhesion sites received more attention, and it was shown that talin functions as a mechanosensor and force-dependent binding platform for adhesion proteins. In its function as linker between integrin and actin, talin is exposed to forces generated by the retrograde flow of the actin cytoskeleton.

Talin's chain-like domain organization makes it an ideal binding platform for other adhesion proteins. Interestingly, most of talin's rod domains are sensitive to force and unfold once they are exposed to forces of at least 5 pN (del Rio et al., 2009a). It was shown that talin's R3 domain, due to its threonine-rich core, especially sensitive to forces (Goult et al., 2013). It unfolds at 5 pN and allows vinculin to bind the cryptic binding sites within the domain. It was shown that the binding site of vinculin within the R3 domain is mutually exclusive to its RIAM binding site. Thus, binding of vinculin displaces RIAM, which leads to a reinforcement and maturation of small adhesion complexes, located in so called 'sticky fingers', into nascent adhesions (Lagarrigue et al., 2016). Similar unfolding events are

observed at higher forces for the other rod domains and their vinculin binding sites (Yao et al., 2016). The rod domain R8, however, is a unique case. In its folded state, it is a binding partner of various proteins (RIAM, DCL1, paxillin or actin). Thus, to retain its function even under higher forces, R8 is located within the 5 helix bundle R7, making it very resistant to unfolding by force.

Other interesting aspects are actin binding sites 2 and 3 of talin. It is generally accepted that, during initial assembly, ABS3 connects first with actin and thus provides an initial link, which keeps talin elongated and through which force can be transmitted over the talin rod. In the second step the provided force relieves the R3/R9 inhibition and lets ABS2 engage with actin to provide a more stable cytoskeleton linkage (Atherton et al., 2015). It is unclear whether both ABS domains can be utilized at the same time or if there are further actin-talin organization modes (Goult et al., 2018).

2.4.5 Membrane binding of talin

Talin's FERM domain contains many different interaction sites for proteins, but also several surfaces that interact with phospholipids. Subdomain F2 and F3 both contain patches of basic residues capable of binding negatively charged lipids, specifically PtdIns(4,5)P_2. In addition, F1 contains an unstructured loop, untypical for FERM domains, that was shown to enable further lipid binding (Goult et al., 2010a). Membrane binding of talin is suggested to play a role in three major processes; first, the recruitment from the cytoplasm, second it plays a role in the activation of talin and third a strengthening of talin's weak interaction with the cytoplasmic ß-integrin tail.

The F3 domain is the only part of the talin head that interacts with the integrin tail; however isolated F3 domains were shown to be not very efficient in integrin activation. It was shown that rather the full talin head is needed to maintain active integrins (Bouaouina et al., 2008). The other head subdomains provide an additive effect, which is achieved by their interaction with PtdIns(4,5)P_2 in the plasma membrane. Both F2 and F3 have patches of basic residues, which are directed towards the plasma membrane, when bound to integrin.

In addition, the 30 amino acid long loop in F1 contains several positively charged residues, which were shown to be essential for PtdIns(4,5)P_2 interaction and thus integrin activation (Goult et al., 2010b).

In 2018, Chinthalapudi and colleagues presented a crystal structure of talin head bound to PtdIns(4,5)P_2 via a cluster of lysines (K272,K316,K324 and K343). They further showed that

disrupting the binding pocket by mutations affects integrin activation and FA formation in cells (Chinthalapudi et al., 2018b).

Furthermore, it was recently shown that talin's F0 and F1 domain both contain an interaction site for Rap1. This interaction could function as an initial recruitment step for talin to the membrane (Bromberger et al., 2018; L. Zhu et al., 2017). Disrupting the interaction of Rap1 with talin F1 by mutating R118E was shown to reduce integrin activation in a CHO platelet model system (Gingras et al., 2019) and disrupting the binding sites on both F0 and F1 was shown to be lethal in mice (unpublished data). Recruitment of talin to the membrane via the F0/F1-Rap1 interaction could subsequently be followed by talin activation and integrin binding as predicted by the so-called 'push and pull' model (*Figure 8*).

Interestingly talin is also able to interact via its F3 domain with PIPKIγ90 with high affinity (de Pereda et al., 2005). The recruitment of PIPKIγ90 by talin stimulates PtdIns(4,5)P_2 generation in FA, which induces a feedback loop that could enlarge FA (Di Paolo et al., 2002). However, despite these results indicating an important role for the PIPKIγ90-talin interaction, it was shown that a PIPKIγ90 knockout in mouse fibroblasts does not dramatically impair FA formation (Legate et al., 2011).

2.5 Other direct interactors of talin

2.5.1 Vinculin

Like talin and integrin, vinculin was discovered about 40 years ago and it was found to play a role in adhesion formation (Geiger, 1979; Geiger et al., 1980; Kuo et al., 2011). Indeed vinculin is one of the important adhesion proteins that not only takes a key role in integrin mediated cell-matrix adhesions, but also is essential for cadherin mediated cell-cell adhesions (Zemljic-Harpf et al., 2007). Vinculin itself does not have any enzymatic activity, but it acts in as reinforcement in integrin mediated adhesions, where it binds to actin and talin.

In mammals there are two vinculin isoforms, vinculin and the splice variant meta-vinculin with a 69 aa insertion. The structural organization of vinculin is quite well understood. It consists of 1066 aa, which were crystalized in full length (Bakolitsa et al., 2004) and truncations in complex with several binding partners. Vinculin is comprised of 8 anti-parallel α-helical domains, which organize in two regions. Domains D1-D3 form the larger region with 95 kDa from 116 kDa, which is called the vinculin head. They are arranged in a tri-lobar

way with a diameter of ~80 A (*Figure 10*) (Bakolitsa et al., 2004). The head domain can bind to talin, α-actinin, α- and ß-catenin and IpaA (Carisey and Ballestrem, 2010). The vinculin head is connected to the second region, called the vinculin tail, via a proline rich 61 aa linker, which binds different actin related proteins, such as VASP, vinexin, ponsin and the Arp2/3 complex. Finally, the vinculin tail consists of 30 kDa 5 α-helix bundle, which has a binding site for f-actin, paxillin, different phospholipids and importantly the vinculin head (Izard et al., 2004).

An important feature of vinculin is its autoinhibition, which is mediated through a sub-nanomolar interaction between the vinculin tail and head. FRET experiments showed that the inhibited form of vinculin is located in the cytoplasm, whereas the activated vinculin was found already recruited to adhesion sites (H. Chen et al., 2005). However, since the autoinhibition is strong, it is an open question how the autoinhibition of vinculin is released in the cell.

Initially, it was thought that the interaction with α-actinin is sufficient to release the inhibition, but these studies were performed with isolated domains. It was shown later, that the inhibition in the full length molecule is much stronger (Cohen et al., 2005), thus it seems unlikely that a single interaction is able to break the head to tail binding. Recent studies suggested that phosphorylation (of residues Y100, S1033, S1045 and Y1065) could activate vinculin (Golji and Mofrad, 2010; Golji et al., 2012). Another suggestion is that similar to talin, force could be the key to open vinculin's talin and actin binding sites. This notion is supported by the observation that a loss of force in adhesions causes vinculin to inactivate (Carisey et al., 2013b; Grashoff et al., 2010). The last model suggests, that acidic phospholipids, especially PtdIns(4,5)P_2, might regulate vinculin's functions. The PtdIns(4,5)P_2 binding at the vinculin tail could trigger a conformational change and allow talin binding via the vinculin head domain (Diez et al., 2008; Wirth et al., 2010). Interestingly it was also observed that F-actin and PtdIns(4,5)P_2 binding promote vinculin to form dimers and even other oligomers. Overall, the exact mode of vinculin regulation and activation needs further investigation.

In adhesions vinculin is located in the signaling layer and upon further activation migrates into the actin binding layer (Case et al., 2015). Here Vinculin plays a key role in reinforcing and rearranging adhesions. In cell migration an adhesions lifetime stretches from early focal complexes in protrusions to focal adhesion disassembly. Vinculin localizes to early adhesion complexes and promotes their maturation to NAs by recruitment of Arp2/3. Furthermore, it regulates talin by replacing talin bound RIAM and induce NA maturation to

FA (Goult et al., 2013b). Cells deficient of vinculin lack Arp2/3 recruitment and lamellipodial protrusion (DeMali et al., 2002). In FAs vinculin stabilizes the actin-talin-integrin connection, transducing mechanical force and thus promoting integrin clustering and FA enlargement.

Most of vinculin's functions in cell-matrix adhesions depend on its actin binding and manipulating properties. Studies showed that it can not only bind to actin filaments, but nucleate their formation, bundle multiple filaments and cap actin filaments (Jannie et al., 2015; Le Clainche et al., 2010; Shen et al., 2011; Wen et al., 2009). In addition, vinculin can recruit multiple actin modifiers, such as Arp2/3 or VASP. However, how these functions are regulated and how vinculin matures adhesion complexes will be focus of many future studies.

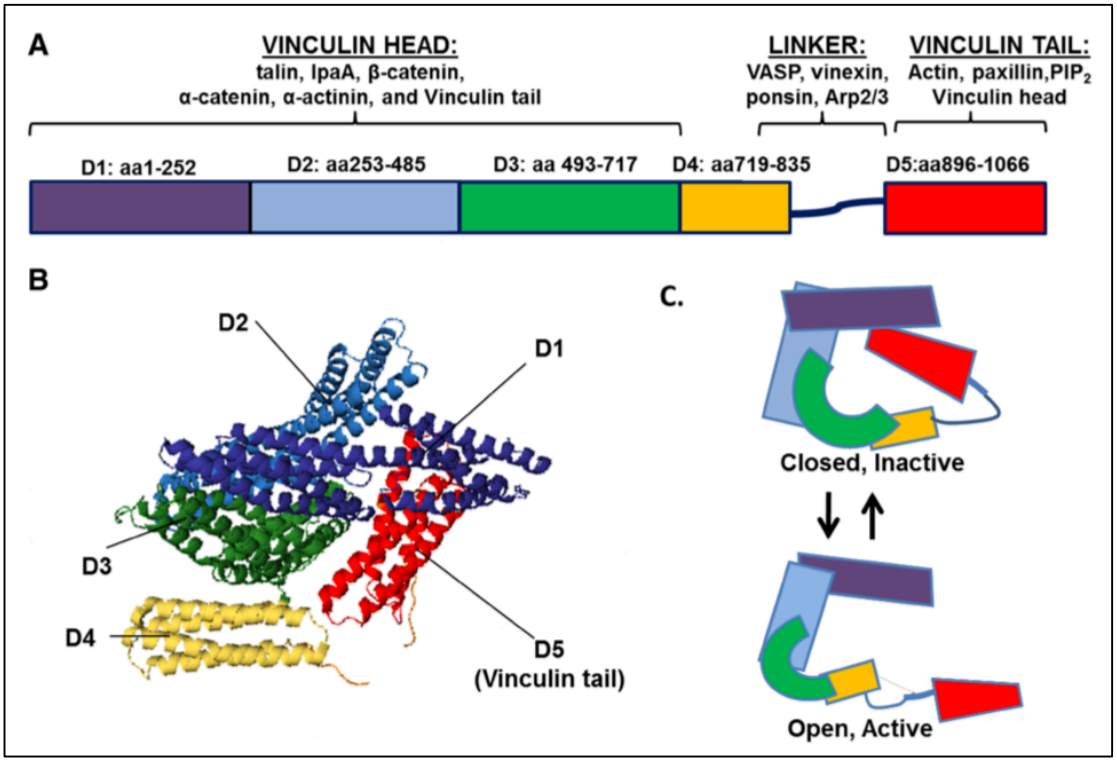

Figure 10: Vinculins domain organization with aminoacid annotations

Vinculin head (D1-D3 domain), linker region (D4 and unstructured) and vinculin tail (D5 domain) interaction partners are listed below the subdomains. B. Ribbon representation of the autoinhibited full-length human vinculin crystal structure with domain annotations (PDB 1TR2). C. Schematic model of vinculin in inhibited and active conformation and the probable changes in domain positioning. (Bays and DeMali, 2017)

2.5.2 Kank

The Kank protein family consists of 4 members in mammals (Kank1,2,3 and Kank4) and is evolutionary conserved up to *C. elegans* with Kank homologue VAB-19, which was initially found in 2002 (Sarkar et al., 2002). The family name Kank stands for kidney ankyrin repeat-containing protein.

The domain architecture of all family members consists of an N-terminal KN-motif followed by a coil-coil domain and a C-terminal ankyrin-repeat domain. Though the KN-motif as well as the ankyrin-repeat domain are conserved in each of the 4 family members, the coil-coil domain contains varying number of helices or is even missing in Kank4. The high similarity between the family members and the fact that both *C. elegans* and *D. melanogaster* have only one Kank homologue gave rise to the notion that gene duplication in higher mammals was responsible for its diversification (Hensley et al., 2016).

Initially, the function of *C. elegans* homologue VAP-19 was connected to adhesions. VAP-19 mutants have defects in muscle attachment and VAP-19 was described to stabilize integrin-mediated cell adhesions between uterine and vulval tissues (Matus et al., 2014). Surprisingly, it was also shown that a knockout of the only Kank homologue *CG10249* in *D. melanogaster* does not lead to developmental defects, the flies suffer from defects in nephrocyte function (Gee et al., 2015). Nonetheless, through recent work in higher mammals the kank family has been suggested to be a key regulator of adhesion dynamics for two processes:

First, during fibroblast migration Kank was observed to initially locate at the tip of FAs. Later it starts to encircle and form belt around the whole adhesion structure. After completed FA encircling, Kank relocates towards the FA center, which leads to a adhesion disassembly. Kank can induce a process called adhesion sliding. This effect is frequently observed in stationary fibroblasts (Smilenov et al., 1999). Adhesion plaques can translocate towards the cell center, sliding over the substratum without getting disassembled. To slide without turnover the intergrins of an adhesion need to be; loosely connected to their ligands via ‘slip bonds’, stabilized in active extended conformation and maintained in clusters.

In our study, showed that Kank2 is recruited to the FA through its N-terminal KN-motif and binds to talin’s R7/R8 rod domains. This was later confirmed by a crystal structure of Kank’s KN-motif in complex with the R7 domain of talin (Bouchet et al., 2016). Upon binding, Kank2 can activate talin and interfere with its actin binding, probably via ABS2, which is located between R4 and R8. This destabilization possibly leads to the disruption of integrin-talin catch bond and subsequently to the destabilization of the actomyosin link, resulting in adhesion sliding (Z. Sun et al., 2016).

The second important role of Kank proteins is the guidance of microtubules to adhesion sites. Microtubules are very dynamic structures that constantly grow and shrink, but show a tendency to grow towards FA. When microtubules reach the plasma membrane, they connect with their tip to it via so called cortical microtubule stabilization complexes (CMSCs). In close vicinity to FAs, microtubules can get linked in two ways to them: First, they can be directly linked to actin, via the microtubule-actin crosslinking factor 1 (MACF1). Second, they can be indirectly linked to talin by an interaction of Kank's coil-coil domain with the CMSC component limprin-ß1. Subsequently, the kinesin-4 family member kif21a gets recruited through Kank's ankyrin-repeat domain to the CMSC and further directs microtubule growth towards the lamellipodium. It was shown that cells deficient of either Kank1, Kif21a or MACF1 show reduced cell polarity due to disorganized microtubule growth (C. Li et al., 2011; van der Vaart et al., 2013).

It was further shown that Kank's coil-coil domain is able to recruit additional F-actin regulating proteins, such as Irsp53 and DAAM1, which is a potential RhoA activator, to the FA (Roy et al., 2009; Suzuki et al., 2017). In addition, Kank1 knockdown in NIH3T3 fibroblasts shows higher RhoA activity, indicating that Kank might play an indirect role in RhoA signaling.

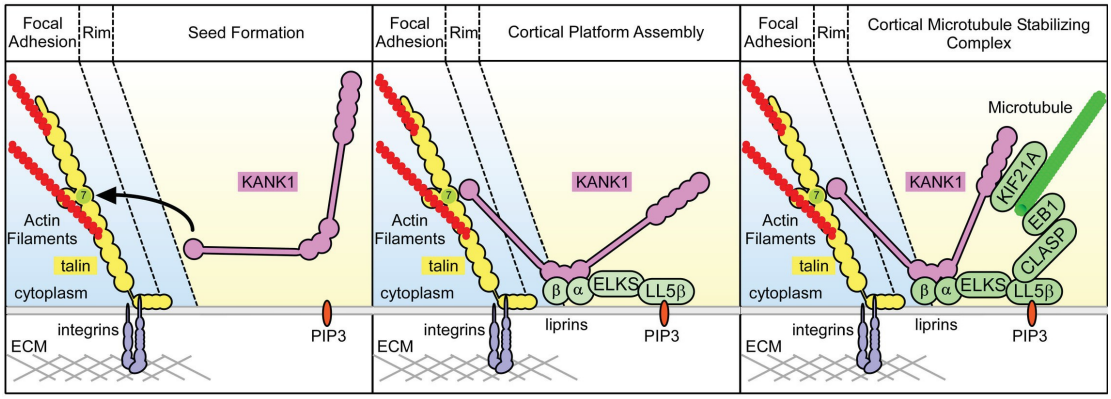

Figure 11: Model of the recruitment of microtubules to FAs in three steps:
1. Recruitment of Kank1 by binding of its KN motif to the R7 domain of engaged talin in FA. 2. The initiation of a CMSC complex through Kank's binding to liprin-b1 with its coil-coil domains. 3. The completion of the CMSC complex and subsequent association of microtubules, by clustering of ELKS, CLASP and Kif21a. (adapted from Bouchet et al., 2016)

Despite the fact that the knockout of the kank homologue in *D. melanogaster* does not show a distinct phenotype, genes of Kank family proteins have been connected to several rare human diseases. A large gene deletion resulting in the loss of the Kank1 gene was connected to a neurodegenerative disease called 'type2 spastic quadriplegic cerebral palasy'

and different mutations in Kank1, 2 and 4 have been connected to human nephrotic syndromes (Gee et al., 2015).

Despite recent *in vitro* and *in vivo* studies the precise function of the Kank family members during adhesion is not fully elucidated.

2.5.3 Actin binding sites of talin

It was discovered that talin can bind both G-actin and F-actin *in vitro* (Goldmann and Isenberg, 1991; Schmidt, 1999). Furthermore, it was later identified that talin has at least three different ABS (Hemmings et al., 1996).

ABS1 is located in the F2 and F3 domain of talin and was found to bind actin at pH 7.0 or lower (H.-S. Lee et al., 2004). It was recently shown that that ABS1 has an actin capping function *in vitro* (Ciobanasu et al., 2018).The proposed actin binding surface is shared with the residues responsible for membrane binding of the talin head, therefore the role of ABS1 in the physiological context is unclear.

ABS2 was first determined at R7/R8 (Gingras et al., 2010a), but later discovered to work in conjunction with R4. Furthermore, it was shown in *in vitro* studies with talin fragments that the presence of the R3 or the R9 domain has an inhibiting effect on ABS2 (Atherton et al., 2015).

ABS3 is the most studied of the three ABS. It is located in R13 and the dimerization domain and called THATCH (talin/HIP1R/Sla2p actin tethering C-terminal homology) domain. The actin binding to ABS3 is dependent on a dimer formation between two dimerization domains of talin. Thus, two talin's are bound on an actin filament in a V-shape formation (Gingras et al., 2008). It is speculated that the flexible linker between R13 and the dimerization domain allows for different talin-actin geometries within focal adhesions (Golji and Mofrad, 2014).

In addition to its three ABS, talin has the ability to connect to actin indirectly via one or more of its numerous VBS. There are 11 cryptic binding sites for vinculin distributed throughout the talin rod (Gingras et al., 2005). If unlocked and bound to vinculin, they can make an additional connection to actin via the actin binding site on the vinculin tail.

It has still been unclear, how the sequential hierarchy among the talin ABS looks like, or which role they play in enabling the recruitment of vinculin to the revealed VBS in talin.

One model suggests that the cryptic vinculin binding sites can be accessed by force transduced via actin bound to either ABS2 or ABS3. It was shown that the deletion of ABS3 only causes a slight reduction of force across talin, still allowing vinculin recruitment. In contrast, the mutation or deletion of both ABS2 and ABS3 greatly reduces the force over talin and blocks vinculin recruitment to FA (Austen et al., 2015; Kumar et al., 2016). This highlights the role of ABS2 as major force bearing site in talin. However, this model might not be applicable to all cell types (Klapholz and Brown, 2017).

It was shown that deletion of ABS2 and ABS3 of talin2 in both mouse and fly does not block vinculin recruitment but rather leads to talin retaining most of its normal actin binding function through vinculin (Austen et al., 2015; Klapholz et al., 2015).

Another study by Atherton and colleagues showed that upon deletion of ABS3, cells either lack adhesions or have only small adhesions with low vinculin amounts. This indicates that ABS3 is important for force activation of cryptic adhesion sites, but that it also can be bypassed (Atherton et al., 2015). Deletion of ABS2 has no effect on initial adhesion formation but blocks maturation of nascent adhesions into focal adhesions. This leads to another model, which states that initial force is generated through actin binding at ABS3, opening VBS in R3 and allowing vinculin recruitment. This in turn relieves ABS2, where actin is bound, further reinforcing the adhesion and allowing maturation (*Figure 12*).

Though the exact role of talin's ABS may depend on cell type and isoform, they are important for talin's function as mechanosensor and binding hub for adhesion assembly.

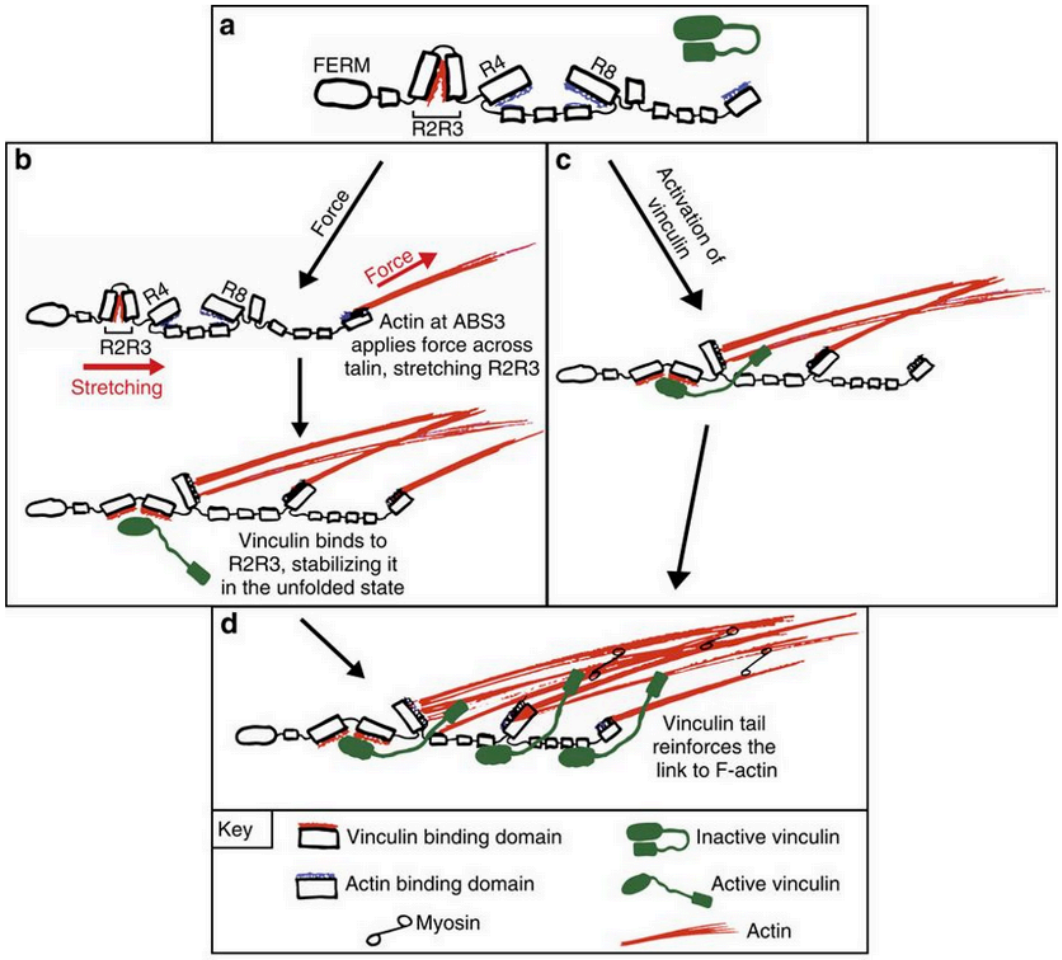

Figure 12: Schematic representation showing talin's actin binding in two different models

Talin's initial state: VBS in R2 and R3 are cryptic (red), ABS2 in R4-R8 is inhibited (blue). Vinculin (green) is in its inhibited state. B. Force-dependent activation: Actin binds to ABS3, generating tension on talin, stretching VBS in R2 and R3. This in turn allows vinculin binding, stabilizing R2/3 and activating ABS2. C. Vinculin-driven pathway: activated vinculin binds to VBS in R2 and R3, activating ABS2 without the need on force generated by actin binding to ABS3. D. Final engagement state of talin: ABS2 and ABS3 are bound to actin. VBS in R2 and R3 as well as further cryptic VBS along the talin rod are engaged, stabilizing the talin-actin link. (Atherton et al., 2015)

2.6 Methods of structural biology

Techniques of structural biology aim to provide information about the spatial positioning of each atoms of a protein in three-dimensional space. This information can be used to understand the nature of protein interactions or mechanisms that are based on structural changes or ligand binding.

There are three prevalent methods used in structural biology: X-ray crystallography, nuclear-magnetic-resonance (NMR) spectroscopy and cryo-electron microscopy (cryo-EM). Each method has its specific strengths and limitations:

In X-ray crystallography, a monochromatic high-energy X-ray beam is shot at protein crystal to collect diffraction signals. The repetitive architecture of the crystal allows the collection of regularly spaced reflections. During the acquisition the crystal is rotated to obtain reflections of different angles. These are combined into a three-dimensional spectrum containing the amplitude information of the protein crystal. However, the phase information is missing. To solve this problem, X-ray crystallography uses different techniques, such as heavy metal soaking or molecular replacement to obtain phase information and calculate an electron density map. X-ray crystallography can be used for samples of all sizes and is able to achieve high resolution structures. However, large amounts of sample are needed and the protein needs to crystalize.

NMR spectroscopy uses a strong magnetic field to observe the local magnetic field around atomic nuclei. For protein NMR spectroscopy isotope-labeled protein samples are used to reduce the range of signals to detect. Although different specific techniques exist in NMR spectroscopy, it is limited to samples of about 35 kDa. However, it is the only structural technique that allows the observation of unstructured proteins and dynamic changes upon protein interactions.

Lastly, cryo-EM uses a high-energy electron beam that is aimed at a thin film of vitrified sample. A camera collects the scattering electron signals. Due to low signal to noise ratio thousands of images are usually collected. From these images, the scattering information is combined and processed to obtain a three-dimensional reconstruction of the protein. Cryo-EM can be used for much larger proteins and protein complexes and requires only a small amount of sample. Proteins can be observed in their native aqueous solution, but by vitrification they are fixed in their conformational state.

The spatial information that is generated by these methods is usually saved in a coordinate file and deposited in the protein data bank (PDB). Today, about 90 % of

structures deposited in the PDB are derived from X-ray crystallography and less then 8 % from NMR experiments [1]. However, in recent years the number of entries and high-resolution structures from cryo-EM studies has increased dramatically.

2.6.1 Cryo electron microscopy

The most commonly used methods of structural biology are X-ray crystallography, NMR spectroscopy and cryo electron microscopy (cryo-EM). While X-ray crystallography is the most widespread and commonly used method, it requires high amounts of pure sample to obtain protein crystals. Since these conditions are difficult to achieve for bigger macro-molecule assemblies or endogenous complexes that are usually available only in small amounts, cryo-EM has emerged as an alternative method to study those challenging projects in the recent years. In single particle cryo-EM small amounts of sample are used to obtain high resolution structures. Recent developments in hardware, as well as software improved the potential to attain structures at high resolutions, allowing even atomic modeling in electron-microscopy density maps.

To obtain high resolution structures of biological samples, a couple of obstacles have to be overcome: First, samples needed to be stable in the high vacuum of a transmission electron microscope (TEM). Second, the radiation damage on samples hit by high energy electrons needed to be reduced and third, the low contrast of biological samples in TEMs needed to be overcome. Initially, protein samples were fixated and stained with heavy metal solutions such as uranyl acetate or tungsten, but this lead to distortion of the biological samples and loss of resolution due to grain size. In the 1980's, Dubochet and colleagues found a method to vitrify samples in their native environment by plunging them into cryogens, such as liquid ethane or propane (Dubochet et al., 1982). Though these vitrified samples suffered from low contrast, due to their biological components scattering signal being similar to the signal of the surrounding water atoms, they were natively preserved and largely protected from radiation damage.

In Cryo-EM, a TEM is used to obtain 2D projections of protein samples. These images contain hundreds of 2D projections from different directions. These can be computationally combined into a 3D reconstruction of the macromolecule that was imaged, a process that was started as far back as 1968 by De Rosier and Klug (De Rosier and Klug, 1968) but has come a long way since.

[1] rcsb.org (25.05.2019)

The low contrast of TEM images set the requirement for the high amounts of 2D particles needed to obtain a 3D model of the sample. Before the invention of direct detectors in 2012, millions of particles were often needed to obtain a sub-nanometer structure of a sample. Since the development of direct detectors, it is now possible to obtain short movie stacks with up to 10 frames per second instead of a single TEM image. This allows to correct for an effect called 'beam-induced-motion', in which the initial electron hits cause the sample to move in the vitrified condition. A 'motion correction' software aligns the single image frames and thus reduces the movement of particles within the image (Brilot et al., 2012; X. Li et al., 2013). Since over longer imaging time the sample is exposed to radiation damage, which results in a loss of high-resolution signal, a method called 'dose weighting' is used to extract the high-resolution information. It weights by taking into account the signal on single image frames in regard to the amount of electron radiation. The new direct detectors can detect electrons directly, which improves the signal over noise ratio dramatically, compared to the previously used charge-coupled device (CCD) cameras, which first needed to convert the electrical charges into photons before these arrived at the camera (Ruskin et al., 2013).

Altogether, these developments combined with higher image throughput, resulting from automatization of the image acquisition and processing steps, led to an increase of structures below <4 Å. These advances in the cryo-EM field allow the observation of heterogeneous complexes and different complex transition states, such as the different stages in the translation machinery (Loveland et al., 2017).

Recent years not only showed progress in hardware development, but also new reconstruction strategies and algorithms: maximum-likelihood classification, GPU based modeling or single particle CTF determination, to name some of them. In general, a typical 3D reconstruction flow is as follows: Raw frames are aligned to be combined to single images, then the contrast-transfer function is determined and then particles to be selected are determined either by using cross correlation to a template, or according to the size of the particles. The selected particles are extracted into small boxes. These boxed, low contrast images are then sorted into groups, on the basis of similar orientation, by 2D classification and combined into particle stacks (Scheres, 2014). Each particle stack then represents a view of an unknown orientation of the final 3D model (*Figure 13*). To determine the orientation within the final structure, the particles are compared to a crude initial model in fourier space. Since the initial model is crude, this process is used iteratively and a newly computed model from the input particles replaces the initial model at the end of each cycle.

New strategies, such as multi-body refinement (Nakane et al., 2018) make it possible to look for heterogeneities and flexibility in parts of larger macromolecular complexes. This allows insights in dynamic processes in complex formation or substrate handling of large protein machineries.

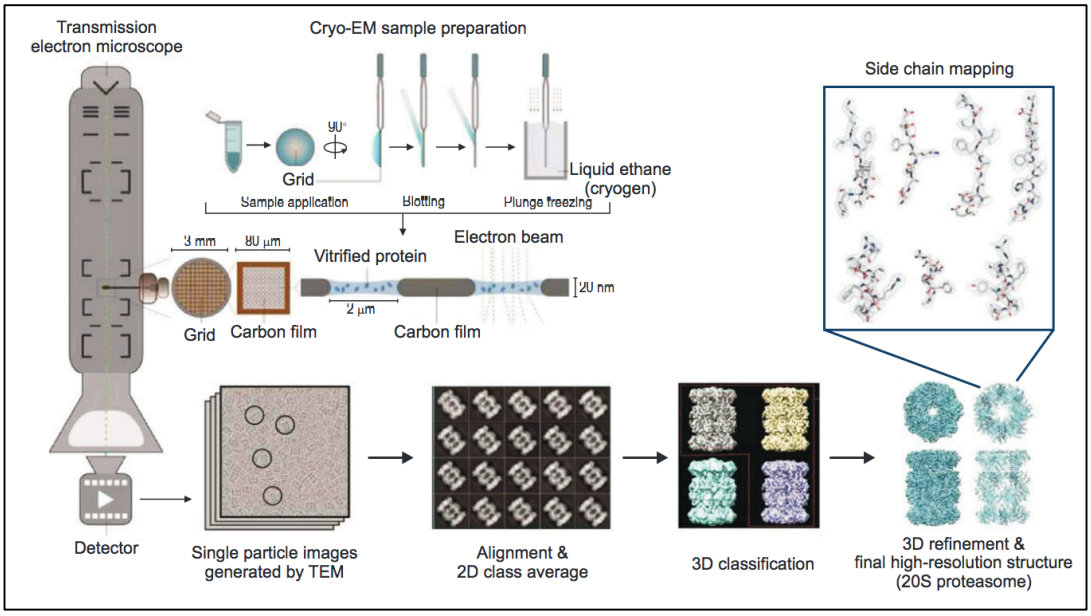

Figure 13: Scheme of a typical cryo-EM workflow.
Purified sample is applied to a grid and plunge-frozen in liquid ethane. Protein particles are vitrified in small µm sized holes to be observed in a TEM. Images are recorded and protein particles are picked. Particles are classified regarding to their orientation and averaged into 2D classes. The different views are aligned and they are further classified in 3D. From the best 3D class a high-resolution EM density map is generated and the structure can be refined. With sufficient resolution (<3.5 Å) an atomic model can be built into the EM density. (Relion workflow of 20S proteasome) image adapted from Chung and Kim, 2017

3 Aim of the thesis

Talin is an important player of the early adhesion complex, thus its regulation and interactions are of great interest. Many studies have been conducted on the structure, interactions and physical properties of talin. However, most of these studies use single domains or largely truncated constructs. So far, there is only limited information on how talin works in full length context.

In my study I aimed to recombinantly prepare full-length talin and biochemically characterize talin to gain insights into the activation mechanism of talin, which is critical for understanding of the events during early adhesion formation. I purified full length talin from two different organisms (mouse and human) and studied its interaction with the adhesion components vinculin, F-actin, as well as the integrin tail.

Talin's regulation and inhibition is of great importance during the correct formation and disassembly of adhesions. Therefore, I opted to use structural methods to study the architecture of full length talin in its autoinhibited state. I used cryo-EM to resolve inhibited talin to a resolution of 6.2 Å and built an atomic model based on available X-ray crystallography and NMR structures of talin's individual domains.

During autoinhibition talin adopts a compact state. Many of talin's binding sites are not available, while others are accessible and play a role in the activation of talin. In order to understand talin's domain-domain interplay, I used biochemical and biophysical methods to characterize full length talin, truncations and different mutation constructs as well as their interactions with some of talin's binding partners. Based on the results obtained in this study, I proposed a model how talin can be recruited and activated on the membrane, before engaging with the actomyosin machinery and directing adhesion growth.

4 Manuscript 1

4.1 The architecture of talin reveals an autoinhibition mechanism

Dirk Dedden, Stephanie Schumacher, Charlotte F. Kelley, Martin Zacharias, Christian Biertümpfel, Reinhard Fässler, Naoko Mizuno
(manuscript in revision)

In this study, we used recombinantly purified talin-1 and identified the molecular architecture with cryo-EM. We solved the structure of the full length protein in its autoinhibited state as a monomer to a resolution of 6.2 Å. The domain arrangement of the autoinhibited structure reveals two distinct inhibition sites. Not only could we show the importance of the inhibition site between the F3 and R9 domain in full length context, but in addition a novel inhibition site, where R12 covers the membrane binding site of the F2 and F3 domain. The structure further reveals that talin's actin binding sites are hidden within a 15 nm globular domain arrangement of rod domains, which prevents actin and vinculin binding. We demonstrated that upon opening of the rod domains, talin unfolds into a 70 nm string-like conformation, in which its vinculin and actin binding sites are accessible. Our data shows that talin in its open conformation is able to bind vinculin in a force-independent way in 1 to 1 stoichiometry. Vinculin binding takes place in the R1 to R3 domains and can help to stabilize talin in its open conformation. Our study provides a model for how talin conformation can switch between globular and open state and suggests how talin's activation-states could play a critical role in adhesion maturation.

The architecture of talin1 reveals an autoinhibition mechanism

Authors: Dirk Dedden[1], Stephanie Schumacher[1], Charlotte F. Kelley[1], Martin Zacharias[2], Christian Biertümpfel[1], Reinhard Fässler[3], Naoko Mizuno[1*]

Affiliations:

[1] Department of Structural Cell Biology, Max Planck Institute of Biochemistry, Am Klopferspitz 18, D-82152 Martinsried, Germany

[2] Physics Department (T38), Technical University Munich, James-Franck-Str. 1, D-85748 Garching, Germany

[3] Department of Molecular Medicine, Max Planck Institute of Biochemistry, Am Klopferspitz 18, D-82152 Martinsried, Germany

*Correspondence and lead contact: mizuno@biochem.mpg.de

Summary

Focal adhesions (FAs) are protein machineries essential for cell adhesion, migration and differentiation. Talin is an integrin-activating and tension-sensing FA component directly connecting integrins in the plasma membrane with the actomyosin cytoskeleton. However, its regulation is poorly understood. Here, we show a cryo-EM structure of full-length talin1 revealing a two-way mode of autoinhibition. The actin-binding rod domains fold into a 15-nm globular arrangement that is further interlocked by the integrin-binding FERM head. In turn, the rod domains R9 and R12 shield access of the FERM domain to integrin and the phospholipid PIP2 at the membrane. This mechanism ensures synchronous inhibition of integrin-, membrane- and cytoskeleton-binding. We also demonstrate that compacted talin1 reversibly unfolds to a ~60-nm string-like conformation, revealing interaction sites for vinculin and actin. Our data explains how fast switching between active and inactive conformations of talin could regulate FA turnover, a process critical for cell adhesion and signaling.

Keywords

Talin, Focal Adhesion, cryo-EM, actin, structure, vinculin, cytoskeleton, signaling, mechanosensor

Introduction

Focal adhesions (FA) are intracellular protein assemblies that serve as tension-sensing, anchoring points to link cells to the extracellular environment (Geiger et al., 2009; Parsons et al., 2010). FAs not only tether cells to the extracellular matrix (ECM), but also facilitate intracellular reorganisation, resulting in dynamic changes of cell functions and cell morphologies (Geiger et al., 2009; Legate et al., 2009; Parsons et al., 2010). FAs consist of hundreds of proteins in a layered arrangement that closely regulate each other (Kanchanawong et al., 2010). The first layer consists of integrin-signaling components at the plasma membrane, the second of force-transduction components, the third of actin-regulatory factors, and the fourth layer is made up of actin fibres. Several key proteins act to coordinate the individual functions of each layer, mediate crosstalk between layers, and to connect these layers with integrin receptors, the master-controller that links cytoplasmic FA complexes to the ECM (Bachir et al., 2014).

FA-mediated cellular processes are facilitated by alternating states of activation and inactivation of integrins. In migrating cells, integrin activation initiates vast FA formation, allowing cells to attach to the extracellular environment, whereas integrin inactivation, followed by disassembly of FAs, detaches cells. This cycling of on/off states allows cells to continuously change anchoring points, facilitating cellular movement. Talin is a key component in FAs, responsible for activating integrins and mediating both inside-out and outside-in signaling (Tadokoro et al., 2003) (Harburger and Calderwood, 2009; Nieswandt et al., 2007). Talin activates integrin by associating with the cytosolic tail of integrin beta-subunits. Once engaged, talin can assume an elongated conformation up to 100 nm in length (Liu et al., 2015), directly linking the beta-integrin subunit in the first layer of the FA to actin bundles in the fourth layer (Kanchanawong et al., 2010). By spanning all four layers of the FA, talin is in a unique position to act as a structural scaffold, greatly contributing to the overall composition and organization of FA complexes (Calderwood et al., 2013). In addition to its role as an integrin activator, talin also acts as a mechanosensor; it stretches like a spring and transmits tension between the ECM and the actomyosin machinery within the FA (Austen et al., 2015; Kumar et al., 2016), a process which is essential for regulating FA maturation and stability. As such, the transition between active and inactive talin likely plays a key regulatory role in FA dynamics, similar to the activation and inactivation of integrins.

Talin is a large, 270 kDa protein with 18 domains comprising a ~50 kDa globular head, a long rod made of 62 helices forming 13 helical bundle (rod) domains (R1-R13) (Calderwood et al., 2013; Goult et al., 2013), and a dimerization (DD) motif at the C-

terminus (Gingras et al., 2008). A unique conformational change of talin facilitates its spring-like behavior, through which talin can unfold into a linearly elongated 60–100 nm rod-like shape (Liu et al., 2015; Molony et al., 1987; Winkler et al., 1997). This allows it to bind to at least 11 different FA components including vinculin and actin (Goult et al., 2018). The talin head contains a 4.1-ezrin-radixin-moesin (FERM) domain with four subdomains (F0-F3), which is a common structural feature of several integrin tail-binding proteins (Elliott et al., 2010; Garcia-Alvarez et al., 2003; Goult et al., 2010; Rees et al., 1990). The FERM domain contains the integrin-binding site IBS1 (Tanentzapf and Brown, 2006; Wegener et al., 2007) and phosphatidylinositol-4,5-bisphosphate (PIP_2) recognition site, allowing talin to attach to the membrane surface in a regulated way. The force-mediated stretching of talin is thought to follow (Atherton et al., 2015; Margadant et al., 2011), resulting in the exposure of up to 11 cryptic binding sites for vinculin (Fillingham et al., 2005; Gingras et al., 2005; Izard et al., 2004; Papagrigoriou et al., 2004). The binding of vinculin to talin is proposed to reinforce FA strength, as vinculin facilitates binding to actin, resulting in a cable-like configuration of F-actin and the FA(Case et al., 2015; Kanchanawong et al., 2010; Liu et al., 2015) (Carisey et al., 2013; Humphries et al., 2007) and triggering the maturation of the FA (Zaidel-Bar et al., 2003).

While the active form of talin is well characterized, the critical state of the inhibited form of talin is scarcely understood. The importance of talin inhibition is highlighted by the fact that failure in proper talin inhibition leads to morphogenetic defects during fly development (Ellis et al., 2013) and it has been implicated in the migration of metastatic cancer cells (Desiniotis and Kyprianou, 2011; Fang et al., 2016; Haining et al., 2016). In its autoinhibited state, talin has a compact conformation (Goldmann et al., 1994; Goult et al., 2013; Winkler et al., 1997), with domains folded into each other, so as to occlude the interaction sites for binding partners such as integrin, membrane, vinculin and F-actin. Although individual, truncated fragments of talin have been well characterized, the regulation of full-length talin and the interplay among its domains are largely unknown on a molecular level. For example, a truncated fragment of the FERM domain (F3) was shown to interact with the R9 rod domain (Song et al., 2012); however, the overall mechanism is unclear because of the lack of information about the full-length architecture of talin.

Here, we report a cryo-EM structure of the autoinhibited form of recombinantly produced full-length talin1. The structure reveals charge-based interactions among the 13 rod domains of the talin1 monomer that entangle the protein into a compact 15 nm globular architecture, which is further secured by respective interactions between the

F2 and F3 FERM subdomains and the R12 and R9 rod domains. Interestingly, the PIP_2-binding surface of the FERM domain is completely covered by the rod domain R12 to occlude access to the plasma membrane. The integrin-binding site is located at the deepest part of the autoinhibition pocket. The closure of the rod domains impedes binding to vinculin and to actin via the actin-binding site 2 (ABS2), although it does not occlude the other actin-binding site, ABS3. By mimicking talin activation, we facilitated talin1 binding to F-actin and vinculin. On the basis of these results, we propose a molecular model that explains how talin activation is controlled at a PIP_2-enriched membrane surface and how the protein transitions from a 15 nm globular structure to a 100 nm extended structure. Our results have wide-ranging implications for the mechanistic understanding of FA and protein activation.

Results

The full-length, autoinhibited talin1 structure shows molecular closure of the rod domains by the FERM domain.

Talin is thought to adopt open and closed conformational states (Figure 1A). While open talin is amenable to further stretching by its interacting partners, the globular state is likely to take on an autoinhibited conformation that hinders access to many of talin's binding sites, restricting interactions with other FA proteins. The autoinhibited form is thought to be the cytosolic state of talin that does not engage in FA assembly. It has been a challenge, however, to obtain a molecular view of the autoinhibited conformation. We successfully purified recombinantly expressed talin1 and pursued a full structural and biochemical characterization.

The cryo-EM analysis of full-length talin1 (talin-FL) in the autoinhibited conformation (Figure 1B, Figure S1 and S2, Table S1) revealed an intertwined architecture. Although the intrinsic flexibility of talin limited the resolution of the structural reconstruction to a global resolution of 6.2 Å (Figure S2A-C, Table S1), the clear connectivity of the rod domains within the density map facilitated robust fitting of available structures of the 13 individual rod domains and the F2 and F3 subdomains of the FERM domain (Figure 1C and S3). We performed further refinement using a flexible fitting scheme by the restraint molecular dynamics (Salomon-Ferrer et al., 2013). Our results show that the rod domains are entangled with each other, resulting in a compact organization, and the FERM domain closes the assembly via two anchoring points on rod domains R9 and R12, respectively, acting as a lid to secure the closure of the talin architecture (Figure 1D). At the first anchoring point, located in the deepest groove of the autoinhibition pocket (Figure 1E), the interacting surface between R9 and F3 agrees well with a previously reported crystal structure of isolated F3 and R9 fragments (Song et al., 2012) (Figure S4), which are necessary for talin inhibition in cells. At the second anchoring point (Figure 1E), located at the critical connecting point for the closure of talin1, K272 and K274 in F2 contacted E2288, and D2297 at the C-terminus of R12, respectively (Figure 1D).

While the F2 and F3 FERM subdomains revealed interactions necessary for talin1 autoinhibition, the densities corresponding to the F0 and F1 FERM subdomains were not visualised in our structure (Figure 1E). F0 serves as an interaction surface for the small GTPase Rap1 (Zhu et al., 2017), which acts as a recruiting factor to promote talin engagement with the plasma membrane (Goult et al., 2010; Plak et al., 2016) (Figure 1F). While these subdomains are missing from our structure, the corresponding fragments were identified by mass spectrometry (Figure S3B). This indicates that the

F0-F1 subdomains are flexibly attached to the talin core structure, presumably by a long, 30 amino-acid linker between F1 and F2 (Figure 1E). Hence, F0 and F1 are likely not part of the inhibited structure, which suggests that talin can be recruited to the membrane surface via Rap1 without a requiring that the rod domains disentangle from each other or disruption of the FERM domain interaction with R9 and R12 (Figure 1E-F).

The closed talin configuration occludes the integrin-binding site and the membrane-binding surface on the FERM domain.

The talin FERM domain was shown to interact with PIP_2 (Chinthalapudi et al., 2018; Orłowski et al., 2015; Song et al., 2012). Specific residues responsible for this interaction were recently identified including K272 of F2 and K316, K324, E342 and K343 of F3 (Chinthalapudi et al., 2018). We mapped their locations to understand the geometrical relationships among them in full-length talin (Figure 1D). In the autoinhibited talin structure, the PIP_2-binding surface was mostly covered by the rod domains, particularly by a region at the C-terminus of R12, ensuring that the binding site was inaccessible to PIP_2 (Figure 1D and 1G). This region, containing the negatively charged amino acids E2288, E2294 and D2297 (Figure 1D), provides an acidic interface to complement the basic PIP_2-binding surface. Furthermore, to understand the arrangement of integrin and the plasma membrane with respect to talin in the open and closed configurations, we superimposed the available structure of the integrin cytosolic tail in complex with F3 (Anthis et al., 2009; Wegener et al., 2007) (Figure 1G). The integrin tail was shown to locate on the surface of the truncated F3 (Song et al., 2012), where R9 also binds in our autoinhibited structure, showing that the integrin-F3 interaction and the F3-R9 autoinhibitory interaction are mutually exclusive. Moreover, the integrin transmembrane helix directly precedes the integrin tail, indicating that F2 and R12 would have to separate to enable F2 and F3 to bind the inner face of the plasma membrane (Figure 1G). We also noted that the interaction surface of F3 for R9 has been reported to be a key interface for talin-binding partners, such as riam (Yang et al., 2014) and laylin (Wegener et al., 2008), which are likely involved in talin activation (Figure S4).

The talin1 folding unit is a monomer in the autoinhibited form.

The last 50 amino acids at the C-terminus of talin1 have been crystalized as a coiled-coil in a dimeric structure (Gingras et al., 2008) (termed DD domain), suggesting the possibility that talin is capable of dimer formation. Furthermore, talin has been separately observed as a dumbbell-shaped dimer (Goldmann et al., 1994) when

interacting with actin and as entwined dimers forming a globular assembly (Goult et al., 2013), keeping the question open as to whether or not talin dimerization is necessary for its autoinhibition. Our cryo-EM structure clearly showed that talin1 monomers are capable of achieving the autoinhibited architecture.

The DD domain, which follows R13, was not clearly visible in our structure because of its high flexibility, which in turn indicates that it is not engaged in the autoinhibited conformation. Indeed, a truncated talin construct that lacked the DD domain (talin-ΔDD) (Figure S3A) was still capable of assuming the autoinhibited conformation (Figure 2A), and analysis by size-exclusion chromatography coupled with multi-angle light scattering (SEC-MALS; Figure 2B) showed that both talin-FL and talin-ΔDD behave as monomers. Therefore, the DD domain appears to be inactive or not strong enough to hold talin-FL dimers together when talin is in the autoinhibited state. We further tested if we could find talin dimers as a minor component in the molecular population. Sucrose-gradient centrifugation of talin-FL in the presence of a concomitant gradient of the cross-linker glutaraldehyde (GraFix (Stark, 2010)) showed a minor population of talin that migrated differently in solution as well as on SDS-PAGE (Figure 2C), suggesting the presence of a talin-FL dimer, in agreement with the previous report (Goldmann et al., 1994). In contrast, talin-ΔDD did not display the corresponding minor band and showed only a single monomeric population, indicating that DD is the only domain in talin that is capable of facilitating dimerization.

Weak interactions among rod domains maintain the compaction of talin.

To explore how the molecular opening of talin is regulated, we varied the ionic environment and tested if and how the conformation was changing. When we raised the ionic environment to 500 mM salt (NaCl or KCl), the conformation of full-length talin changed from the globular, closed architecture to the open, strand-like conformation (Figure 3A and 3B) with a length of 560 Å (standard deviation [SD] = 170 Å) (Figure 3C), which fits well with the reported length of talin in a cell (Kanchanawong et al., 2010; Margadant et al., 2011). We looked for evidence of the conformational change as a function of the salt concentration using dynamic light-scattering (DLS; Figure 3D) and the results fit well with a two-state model of protein folding-unfolding. At an ionic strength of 234 mM salt, the two states were equally populated and at a physiological salt concentration of 150 mM, 81 % of talin had a compact conformation. We also tested that this conformational change was reversible across fluctuating salt concentrations (Figure 3E).

Furthermore, we tested the importance of the inter-domain interactions for autoinhibition by creating point mutations as well as truncated talin constructs lacking the key domains for the interaction of F2-R12. We created a C-terminal truncation N-R11 lacking R12 and the C-terminus (Figure S3A), one of the two contact points necessary for the FERM-rod interactions, as well as N-R12 (Figure S3A). The DLS experiments showed the conformational changes of both constructs in response to the increase of salt concentration (Figure 3F). Point mutants of talin-FL altering the charge at the key interacting points on R12 (talin-FL-5K: E2288K/E2294K/D2297K/E2299K/D2300K and talin-FL-2K: E2288K/E2294K) revealed a compact conformation at 75 mM salt and underwent a conformational change similar to full-length, wild type talin upon change of the salt concentration (Figure 3I). These experiments led us to hypothesize that the rod domains themselves interact with each other to keep a compact formation.

The rod domains contain several binding sites for critical FA components. Those sites include the F-actin-binding sites ABS2 and ABS3 on R4-R8 and R13-DD, respectively (Hemmings et al., 1996). We observed additional contacts among rod domains, as shown by the mapping of neighboring domains (Figure 4A). Particularly, R4 is placed at the 'core' of the globular architecture and shielded by several rod domains (Figure 4B). We therefore tested the overall interactions among the rod domains by using a truncation construct that lacks the FERM domain (R1-C). DLS showed the change of the conformation in response to salt concentration (Figure 4C). Negative-stain EM images of R1-C showed a mixed population of open and not well-defined, but nevertheless compact, conformations (Figure 4D). These indicate that there is an internal interaction within the rod domains, however, it is not strong enough to keep the conformation for observation under negative-stain conditions. To visualize the nature of the interaction, we calculated the electrostatic surface potential of each of the individual rod domains surrounding R4 and estimated the interaction energies of those domains to R4 (Figure 4A and Figure S5). The calculated energy landscape for the domain-domain interaction indicated that the binding is rather weak (Figure S5B), resulting in an overall marginal stability. The rod domains may not rigidly bind to one another without cooperative, multi-module packing, as induced by the overall arrangement of the full-length protein. This explains the observation that the talin architecture is highly sensitive and how its conformation can rapidly change in response to salt.

The closed conformation of talin prevents vinculin binding, whereas the open conformation binds vinculin with 1:1 stoichiometry.

Vinculin is a major talin-binding partner that facilitates crosstalk between talin and actin through its talin-binding head domain (V-head) and its actin-binding tail domain (V-tail) (Borgon et al., 2004; Johnson and Craig, 1994). Sequence-based analysis identified 11 potential vinculin-binding sites (VBSs) in talin (Gingras et al., 2005). Experiments using combinations of talin rod fragments indicated that R3, containing two VBSs, is a potent binding site for vinculin. It has been proposed that the unfolding of the helical bundle in R3 exposes the otherwise hidden binding domain to vinculin (Izard et al., 2004; Yao et al., 2014). Our truncation experiments supported that notion, as the talin fragments R1-R8 and R1-R3 formed complexes with V-head, whereas R4-R8 did not (Figure S6). It was unclear, however, how those observations would be reflected in the context of full-length talin.

To test the binding of vinculin to talin-FL, we performed reconstitution assays using SEC (Figure 5A) at 75mM KCl, where talin shows a compact architecture. While truncated talin including R3 readily bound to vinculin (Figure S6), most of talin-FL did not form complexes with full-length vinculin, V-head, or the vinculin mutant (V-mut, N773, E775A (Cohen et al., 2005)), which exposes the talin interaction site by deregulating the autoinhibition of vinculin (Figure 5A, first row). These findings suggest that the opening of the R3 helical bundle is hindered by steric constraints in the autoinhibited form of talin. The root of R3 is connected to R4, which is buried in the core of autoinhibited talin. Therefore, we attempted to reconstitute the talin-vinculin complex with talin at 500 mM KCl where talin shows an open conformation. SEC revealed that talin and vinculin formed stable complexes with the V-mut (Figure 5A, second row). Talin formed a complex with V-head as well (Fig. 5A and 5B). SEC-MALS showed that the corresponding chromatographic peaks were monodisperse with a molecular mass of 339 kDa, corresponding to a complex comprising one talin-FL and one vinculin molecule (Figure 5C). Interestingly, the talin-FL-2K and talin-FL-5K mutants, which are designed to weaken the interactions between F2 and R12 domains, were able to form a complex with V-head at 75 mM KCl (Figure 5D and 5E). This indicates that the disruption of F2-R12 leads to a partial access of vinculin, while these mutants employ compact conformations under this condition (Figure 3I).

The compact talin can retain vinculin head as a complex but induces the dissociation of full-length vinculin.

To test the conformational change of talin in complex with vinculin, we exposed the reconstituted talin-V-head complex to low ionic strength conditions. We found that the retention volume of the SEC peak of the complex shifted from 1.27 mL (500 mM salt) to 1.31 mL (75 mM salt) (Figure 5A, Figure S7A and S7E), suggesting a possible compaction of the complex. DLS experiments of the preformed talin-FL-V-head complex indeed showed a conformational change upon variation in salt concentration, similar to talin-FL alone (Figure S7B-D). We also observed the conformational change of the complex of V-head with talin-FL-2K as well as talin-FL-5K, altogether pointing to the ability of talin to change its conformation in complex with vinculin head (Figure S7B-C).

The closed talin-V-head complex displayed a globular assembly that was similar to the closed morphology of talin alone (Figure S7F), although the talin-V-head complex had a slightly larger size (100 Å × 230 Å) than talin alone (~100 Å × 150 Å). Two-dimensional class averages of the talin-vinculin complex revealed a 60 Å protrusion from the ~100 Å globular head (Figure S7F, top panel). By combining available crystal structures of the talin VBS3 peptide bound to the vinculin N-terminal rods (N-terminal part of the vinculin head)(Izard et al., 2004), a full-length vinculin (Borgon et al., 2004), and our cryo-EM full-length talin in the autoinhibited form, we assembled a structural model of V-head binding to talin at the R3 domain with the talin helical bundle unfolded (Izard et al., 2004; Yao et al., 2014) (Figure S7G). This model matched well with the shape of the averaged talin-V-head complex (Figure S7F), indicating that the 60 Å protrusion on the talin-vinculin complex likely corresponds to vinculin binding to R3. However, when we attempted to re-close talin in complex with the V-mut including the vinculin tail, vinculin was induced to be displaced from the complex (Figure S7A). This observation suggests that the vinculin tail competes with the talin R3 domain for binding to the vinculin head.

F-Actin binding is enhanced by the opening of talin

Another major binding partner of talin is F-actin, which is located at the base of the FA. Acting as tension-generating machinery, actomyosin is thought to ensure the opening of talin by binding to two sites located at R4-R8 (ABS2) and R13 (ABS3; Figure 6A). Cell-based experiments with talin rod-deletion mutations suggested that ABS3 plays a role in recruiting talin to actin at the FA to activate talin, while ABS2 is critical for the maturation or growth of the FA (Atherton et al., 2015). Combining our structural findings, we hypothesized that the opening of talin is correlated with the engagement of talin to actin, and we tested the binding of various truncated talin variants to F-actin by co-sedimentation assays.

First, we tested the truncated construct N-R12 for binding to F-actin. In the tested condition at 75 mM KCl, N-R12, like talin-FL, employed an autoinhibited compact form (Figure 3F and H) that did not form a complex with vinculin (Figure 6B, Figure S7H). Reflecting the fact that N-R12 lacks ABS3, the binding of F-actin to N-R12 was reduced compared to talin-FL (Figure 6C-D). Next, we tested the C-terminal truncation construct N-R11, which lacks the R12 domain. Without R12, talin N-R11 compaction is weak enough for vinculin to associate (Figure 6B, Figure S7I). In contrast to N-R12, N-R11 bound F-actin with even higher amounts than talin-FL (Figure 6C-D), despite the fact that it lacks ABS3. Those results indicate that loosening the autoinhibitory lid (R12) of talin was directly correlated with the activation of the F-actin-binding of ABS2 as well as with vinculin binding. We also tested the truncation of the N-terminal FERM domain (R1-C) in the same way. R1-C showed binding similar to that of N-R11, although the described F-actin-binding activity of ABS1 at the FERM domain was missing from the fragment. R1-C was also capable of binding to the vinculin head (Figure 6B, Figure S7J); however, it displayed no significant enhancement of F-actin binding.

Discussion

Mechanism of talin regulation.

In cellular environments, the concentration of talin can be as high as 50 μM (Zeiler et al., 2014; Zhu et al., 2017), making talin one of the most abundant components in cells. The activation of talin within FAs is essential; however, it is also critical that the adhesion components can be properly switched off to control cell attachment and migration. Therefore, the autoinhibited state of talin is essential (Ellis et al., 2013). Information is available about interactions among individual talin fragments (Goult et al., 2013; Song et al., 2012); however, the molecular architecture and the mechanism of talin's autoinhibition have been unknown in the regulatory context of full-length talin. We uncovered how talin can be folded to ensure its autoinhibition. A network of polar interactions keeps the 13 rod domains tangled into a compact globular architecture with the R4 domain buried in the core, thus shielding R4 and the actin-binding site ABS2 against actin binding. The compact architecture was further locked down by contacts between the F2 and F3 subdomains of the FERM head and the R12 and R9 rod domains, respectively. The PIP_2 binding FERM domain was masked by the R12 domain inhibiting the interaction of talin to the inner leaflet of the plasma membrane. The densities of R11-R13 are not well defined and show flexibility in the 3D classification (Figure S1C). This suggests that the connection between R12 and FERM domain F2 is loose. The break of this interaction may be sufficient to grant an access to binding partners such as

vinculin, whose binding, however cannot open the molecule completely. The conformational change of talin can be seen as an ensemble of open and closed states, which can be shifted dynamically by the change of salt concentration *in vitro*. The open conformation of talin likely mimics the activated talin stabilized by the actomyosin machinery during FA initiation.

Talin-vinculin complex formation during autoinhibition

We observed that one vinculin-binding site is readily available when full-length talin is released from the autoinhibited state without the application of any active force. Intriguingly, talin is able to reverse back to the closed conformation while vinculin-head is still bound to R3, but only in the absence of the vinculin tail. We speculate that this may hint at a mechanism to release vinculin when talin is inactivated and no longer engaged in the FA assembly. The closure of talin and concomitant folding of R3 may weaken the interaction of vinculin head to R3. In turn, the competition of vinculin tail for the head domain becomes more effective, resulting in the inactivation of vinculin and release from the complex in the autoinhibited form. It will be interesting to structurally map the interaction surface and find out which of the talin-binding partners can bind to the autoinhibited form of talin. Such an analysis will shed light on the functional role of talin in the cytosol and help to determine if there are preformed complexes that act as precursors of FA-related complexes. Along the same line, it is possible that talin dimerization might also occur upon talin activation and elongation. Binding to actin further expands the footprint of talin and exposes the C-terminal dimerization domain, as suggested previously (Goldmann et al., 1994), while dimerization appears dispensable when talin is autoinhibited. Talin dimerization offers an additional layer of regulation and the possibility for larger complexes to be assembled from preformed FA subcomplexes. Further structural analysis of full-length talin in its active, elongated form in comparison with its autoinhibited form will provide a comprehensive view of talin function during FA initiation and maturation.

The topological positioning of talin is a key step in FA activation.

Our talin structure showed that the globular rod domains occlude the membrane-binding plane of the FERM domain. On the other hand, the N-terminal FERM F0-F1 subdomains and the C-terminal DD domain were not involved in maintaining the structural organization of the autoinhibited form of talin, indicating that those domains are freely accessible and not inhibited when talin is closed. In particular, F0 has been

shown to be a key binding domain for Rap1, the binding of which has been suggested as the first step in the recruitment of talin to the cell-membrane surface (Zhu et al., 2017).

In addition, talin has a 30 amino-acid flexible linker between the F1 and F2 subdomains that separates F0-F1 from the globular autoinhibited structure (F2-DD). This separation may allow F0-F1 to "search" for cofactors. Our findings, together with previous results, suggest a model of how talin is recruited and correctly positioned at the membrane surface (Figure 7, model). Autoinhibited talin is recruited to the membrane via its freely accessible F0 subdomain in a Rap1-assisted manner. Thus, the FERM domain orchestrates the binding of Rap1 on the one hand (Zhu et al., 2017), while on the other it accesses the exposed, negatively charged plasma membrane via the flexible loop inserted in the F1 subdomain (Goult et al., 2010). This recruitment process increases the local concentration of PIP_2, due to the recruitment of PIPK1γ90 by the F3 subdomain (Di Paolo et al., 2002; Ling et al., 2002). PIP_2 may bind to talin, opening the R12 lid, thus shifting the conformational ensemble towards open structures. The F3-R9 interaction may then be abrogated (Figure 7, step3), allowing the integrin tail to interact with F3.

This rearrangement releases the rod domains from the head domain (Figure 7, step3), activating the interaction sites for various talin-binding proteins. The rod domains themselves can be readily approached by vinculin and actin (as shown in Figure 6), which could lead to the initiation of FA formation (Figure 7, step 4). Our actin co-sedimentation assays with truncated talin revealed that ABS2 is inhibited while talin is closed. This shows that the initial pulling of talin ABS3 by the actomyosin machinery aids the opening of talin to enable the accessibility of ABS2 as well as vinculin, as also shown in a previous report (Atherton et al., 2015) . Finally, actin binding would enable actin retrograde force to exert tensile force on talin, enabling mechanical force to also stabilize talin opening (Sun et al., 2019). Our structure provides a mechanistic basis to understand the inhibition and activation of talin. Although our model is coherent, further testing is needed to validate key events. Furthermore, other yet-unknown activating factors may be involved to tightly regulate the inhibition and activation of talin or to modulate individual functions of talin.

Author Contributions

Conceptualization, N.M.; Methodology, D.D., M.Z., C.B. and N.M.; Investigation, D.D., S.S. C.K. M.Z. and C.B.; Writing N.M. and D.D.; Resources N.M., R.F.; Funding Acquisition N.M.; Supervision N.M.

Acknowledgements

We thank Carsten Grashoff and Giovanni Cardone for assistance at various stages of the project, Elena Conti, Wolfgang Baumeister and the biochemistry- and cryo-EM core facilities for resources and infrastructure (Max Planck Institute of Biochemistry). NM acknowledges the Max Planck Society, Boehringer Ingelheim Foundation Plus 3 Program, and the European Research Council (ERC-CoG, 724209) for funding. NM is a recipient of the EMBO Young Investigator award. CK is supported by an EMBO long-term fellowship (EMBO ALTF 450-2017) and an Alexander von Humboldt research fellowship for postdoctoral researchers.

Declaration of interests

The authors declare no competing interests.

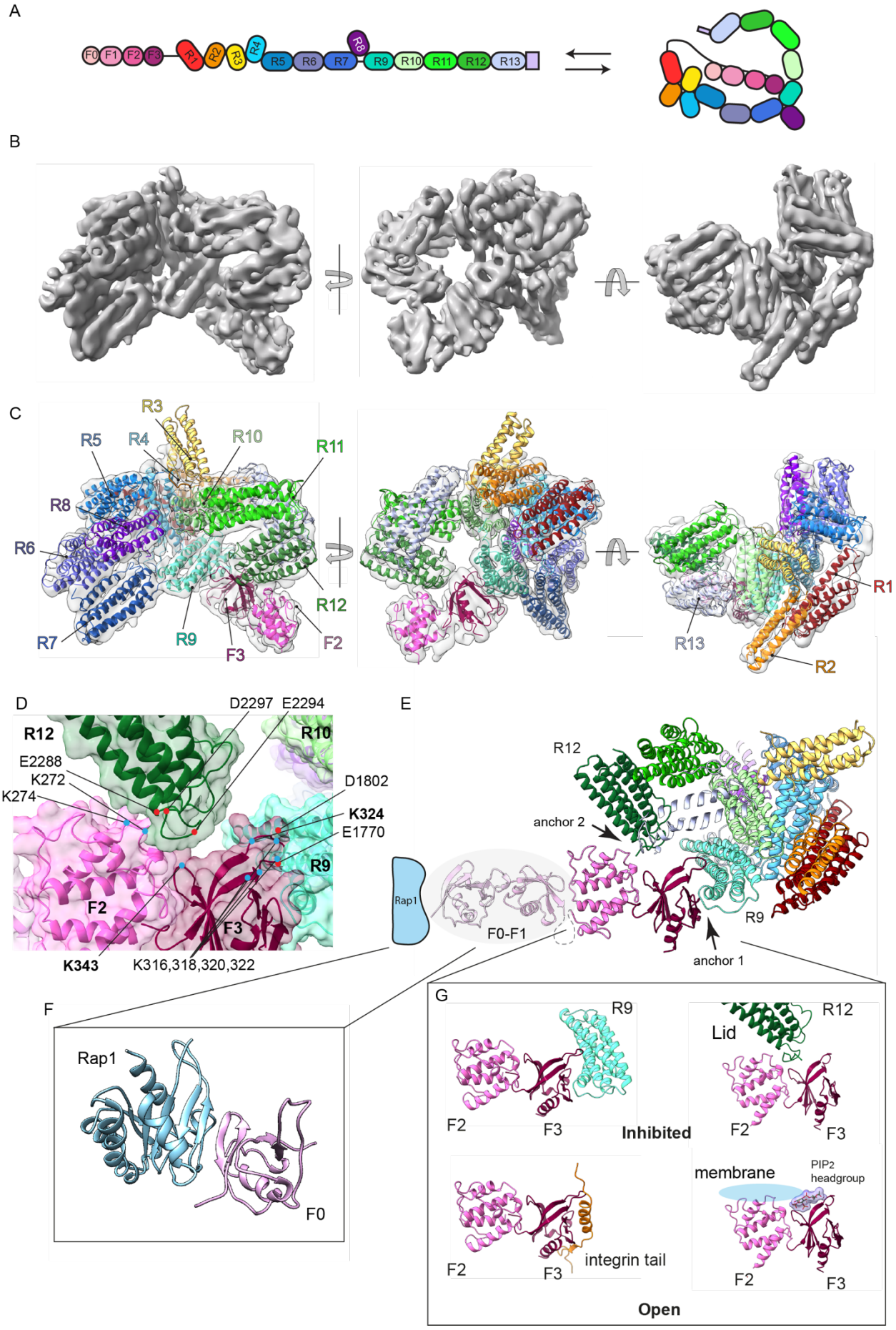
A
F0
F1
F2
F3
R1
R2
R3
R4
R5
R6
R7
R8
R9
R10
R11
R12
R13
B
C
R3
R5
R4
R10
R11
R8
R6
R12
R7
R9
F3
F2
R1
R13
R2
D
D2297
E2294
R12
R10
E2288
K272
K274
D1802
K324
E1770
R9
F2
F3
K343
K316,318,320,322
E
R12
anchor 2
Rap1
F0-F1
R9
anchor 1
F
Rap1
F0
G
R9
R12
Lid
F2
F3
Inhibited
F2
F3
membrane
PIP2
headgroup
F2
integrin tail
F3
F2
F3
Open

Figure 1 Structure of full-length talin.

A: Schematic of the domain organization of talin in the open form (left) and the closed, autoinhibited form (right). **B**: Three views of the structure of full-length talin. **C**: Molecular fitting of talin fragments (PDB codes: 3IVF, 1SJ8, 2L7A, 2LQG, 2L7N, 2L10, 5IC1, 2KVP, 3DYJ, 2JSW) to the EM density map. **D**: The molecular closure of talin achieved by F2-R12 and F3-R9 interactions and the charged amino acids surrounding the interaction interface**.** Bold highlighted numbers match previously published PIP_2-recognition residues. **E**: Superimposition of the F0-F1 subdomains of the talin FERM domain structure (overlaid with grey shadow, PDB: 3IVF) onto our cryo-EM talin model. The F0 and F1 subdomains were not visualized in our structural analysis because of the flexibility of the F1-F2 linker. The small GTP Rap1-binding site on F0 is mapped in blue and labelled "Rap1". **F**: The NMR structure of F0-Rap1 (PDB: 6BA6). **G**: Comparison of the F3-R9 and F2-R12 autoinhibition sites in the closed structure with the F3-integrin tail (PDB: 2H7D) and F2-F3-PIP_2 (PDB: 6MFS) as well as with the membrane-interaction sites of the FERM domain (Anthis et al., 2009), highlighting the mechanism of the autoinhibition of talin. In the inhibited form R12 forms a 'lid' covering the PIP_2-binding site on F2-F3. See also Figure S1-S5.

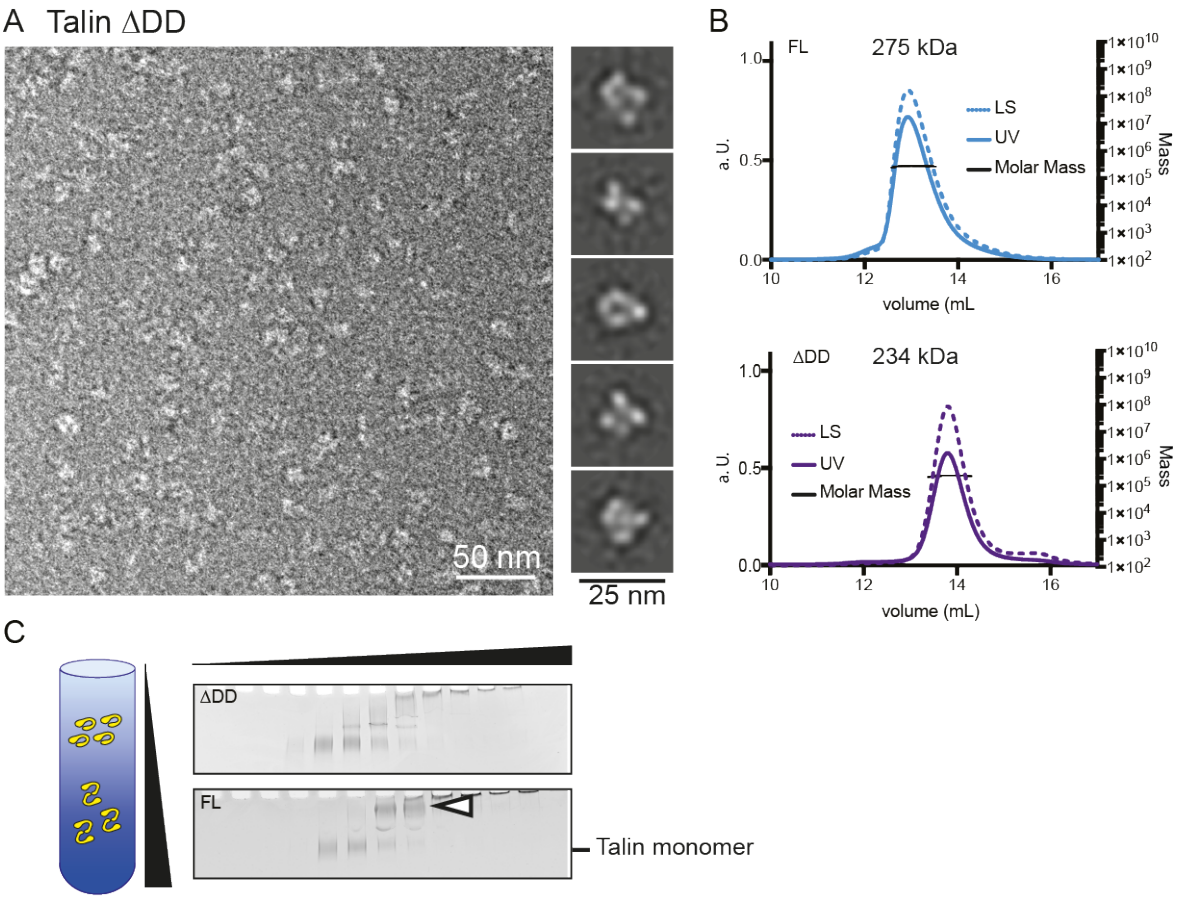

Figure 2. The dimerization domain is not necessary for the closure of talin.

A: Negative-stain EM image of talin-ΔDD lacking the dimerization domain at 75 mM KCl, and 2D averages of the particles (right), showing a morphology similar to that of full-length talin. **B:** Size-exclusion chromatography coupled with multi-angle light-scattering profile of full-length talin (FL) and talin-ΔDD at 75 mM KCl, showing molecular weights corresponding to monomers. LS: light scattering, normalized, UV: absorbance. **C:** Centrifugation profiles of talin-ΔDD and talin-FL using the GraFix method. Full-length talin has an extra band in the fraction with higher sucrose density (open arrowhead). Black triangles depict the gradient of sucrose concentration.

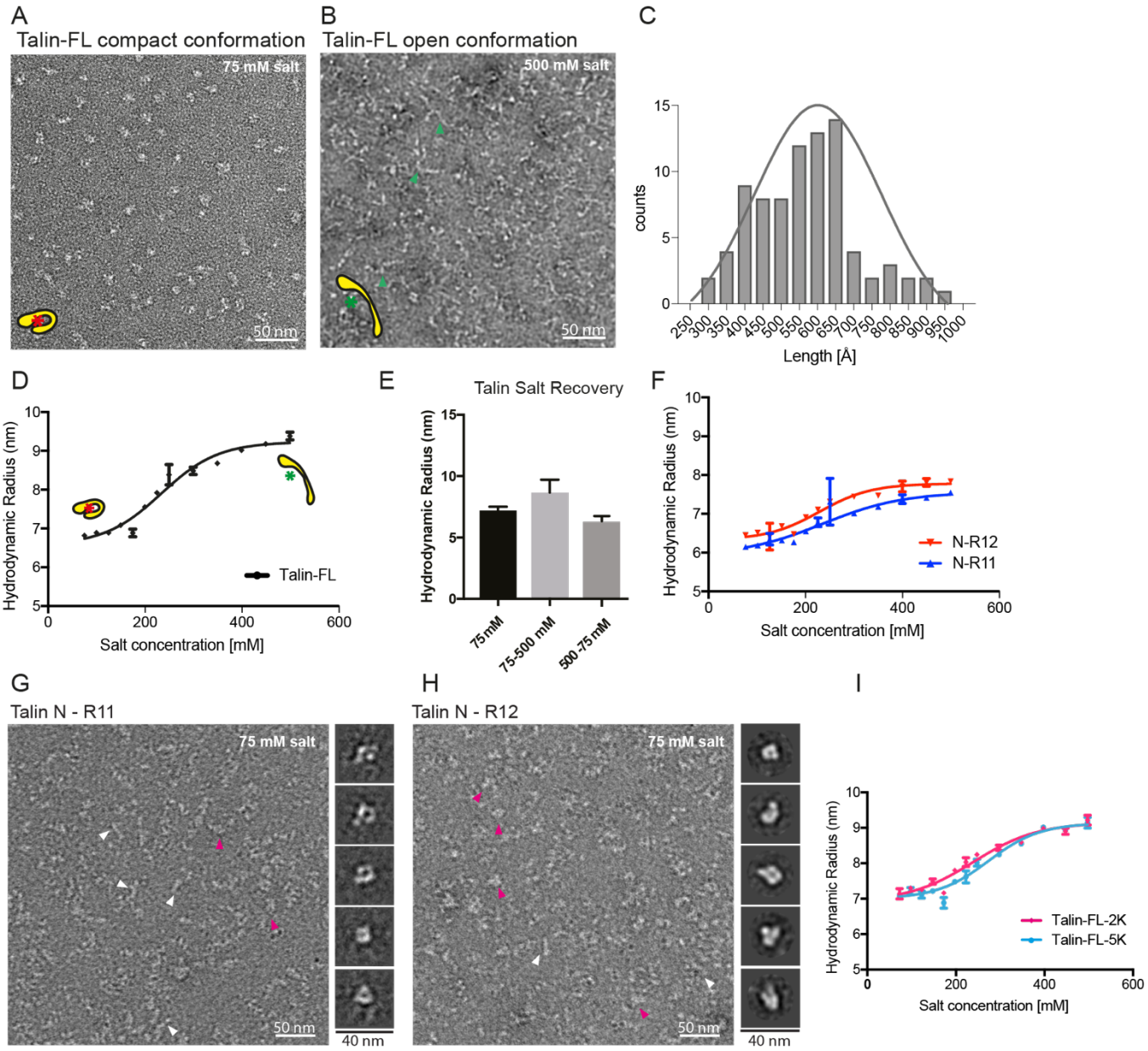

Figure 3 Two-state conformational ensemble of Talin.

A: Negative-stain EM image of full-length talin in the compact conformation at 75 mM KCl. **B:** Full-length talin in the open conformation in the presence of 500 mM KCl. Green arrowheads indicate examples of the open talin. **C**: Distribution of the lengths of the open talin molecules from B (560 ± 170 Å, mean ± S.D. N=89). **D:** Dynamic light-scattering (DLS) measurements of the hydrodynamic radius of full-length talin under various salt concentrations, showing the conformational change of talin as a function of salt concentration. The fitted curve indicates that talin adopts both conformations at an equal ratio at a salt concentration of 234 mM. At a physiological salt concentration of 150 mM, 81% of talin employs the compact formation. **E:** Reversible conformational change of talin depending on the salt concentration as determined by DLS. Left: Talin

employs a closed conformation at an ionic strength of 75 mM. Center: Talin opens and increases its size when the ionic strength is increased to 500 mM. Right: Talin closes again when the ionic strength is lowered back to 75 mM, showing that the shape change of talin is reversible. **F:** DLS measurements of the hydrodynamic radius of N-R11 and N-R12 under various salt concentrations, showing a conformational change comparable to talin-FL with a lower amplitude. The data point at 250 mM was removed as the measurement was outside of the dynamic range of the detector. **G**: Negative-stain EM images of N-R11 at 75 mM KCl, revealing mixed populations of the open (white arrowheads) and the compact (red arrowheads) form, however, it is dominated by open conformations. 2D averages of the compact entity show a globular average (right panel). **H:** Negative-stain EM image of N-R12 and the 2D averages of the compact entities (right panel). Magenta arrowheads indicate examples of the compact molecules. White arrowheads indicate open or deformed molecules. **I:** DLS measurements of point mutants of talin-FL-2K and talin-FL-5K, also showing conformational changes dependent on salt concentration.

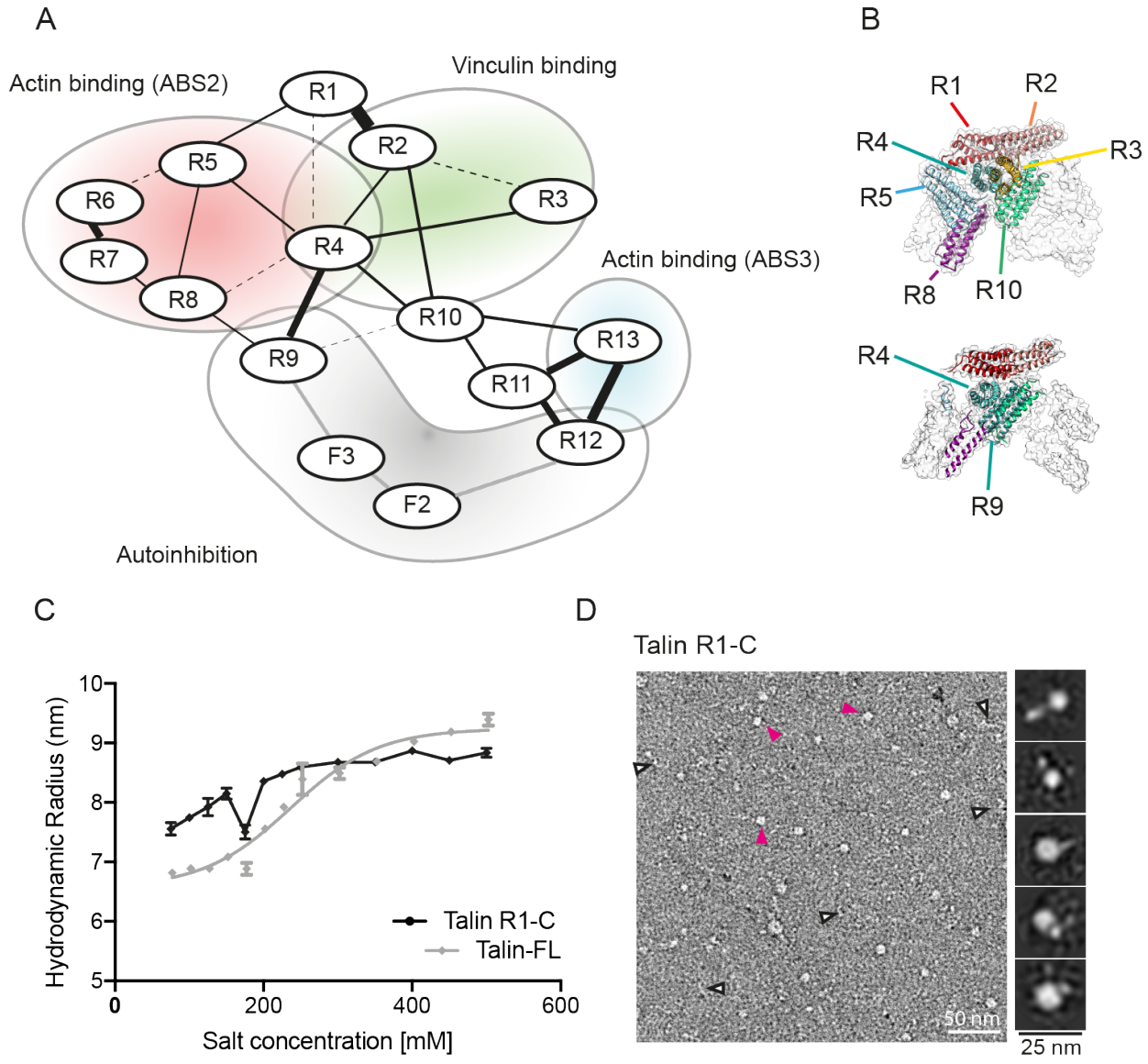

Figure 4. Interdomain interactions of talin

A: Map of talin interdomain interactions derived from the EM structure. Binding domains relevant to this study are colored in red (actin-binding site ABS2), blue (actin-binding site ABS3), and green (vinculin-binding site). Dotted lines indicate positive (i.e. interactions are less not favorable), while solid lines depict negative interaction energies (i.e. domains are interactive) as determined by MD simulations (see STAR methods). The thickness of the lines is proportional to the calculated energies detailed in Figure S5. **B**: Spatial arrangement of the rod domains surrounding the R4 core in two vertical slices through the structure. **C:** DLS measurements of the hydrodynamic radius of R1-C under various salt concentrations in comparison to talin-FL (grey). The R1-C truncation shows a conformational change but it steadily opens up with increasing salt concentration. The size distribution could not be fit to a two-state model. **D**: Negative-stain EM images of talin R1-C at 75 mM KCl. Magenta arrowheads indicate examples of the compact

molecules. White arrowheads indicate open or deformed molecules. 2D averages (right) of the compact entity show globular but featureless averages. Without the FERM domain, R1-C shows mixed population of open and closed architectures.

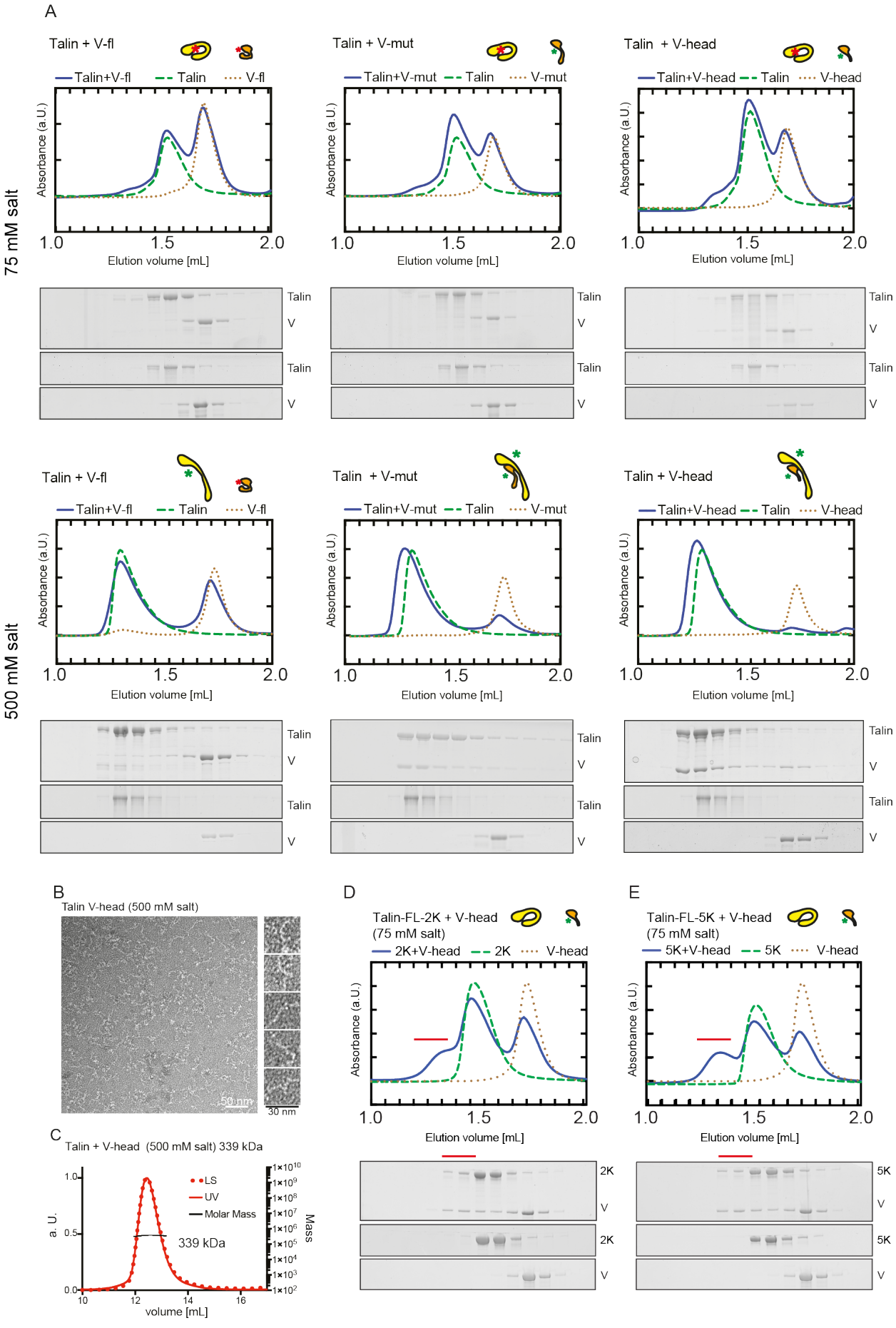
A
75 mM salt
500 mM salt
Talin + V-fl
Talin + V-mut
Talin + V-head
Talin+V-fl
Talin
V-fl
Talin+V-mut
V-mut
Talin+V-head
V-head
Absorbance (a.U.)
Elution volume [mL]
Talin
V
B
Talin V-head (500 mM salt)
50 nm
30 nm
C
Talin + V-head (500 mM salt) 339 kDa
LS
UV
Molar Mass
339 kDa
a. U.
Mass
volume [mL]
D
Talin-FL-2K + V-head
(75 mM salt)
2K+V-head
2K
V-head
2K
V
E
Talin-FL-5K + V-head
(75 mM salt)
5K+V-head
5K
V-head
5K
V

Figure 5. Interaction assays of talin-FL and vinculin under various conditions.

A: Full-length talin and vinculin reconstitution assays using size-exclusion chromatography (SEC). An ionic strength of 75 mM was used for the reconstitution assays shown in the upper panel and 500 mM in the lower panel. SDS-PAGE profiles (talin-vinculin mixture, talin control, vinculin control) of the peaks are shown below the SEC profiles. In order to achieve complex formation, it is necessary that both talin and vinculin employ open formations (bottom-center and bottom-right). V-fl – vinculin full-length, V-mut – vinculin (N773, E775A) mutant, V-head – vinculin head. Minor shoulders at the left side of that talin peaks correspond to the degraded talin without the FERM domain. **B:** Negative-stain EM image of vinculin head bound to open talin at 500 mM KCl. **C:** SEC-multi-angle light-scattering profile of V-head bound to open talin with an calculated molecular weight of 339 kDa, indicating that the complex is made with 1:1 stoichiometry. LS: light scattering, normalized, UV: absorbance. **D**: SEC reconstitution assay of talin-FL-2K mutant and vinculin head at 75 mM salt. **E:** SEC reconstitution assay of talin-FL-5K and vinculin head. The purified proteins have never been exposed to 500 mM salt, which facilitates the opening of talin. The complex formation of these mutants and V-head is observed (indicated by red lines). See also Figure S6-S7.

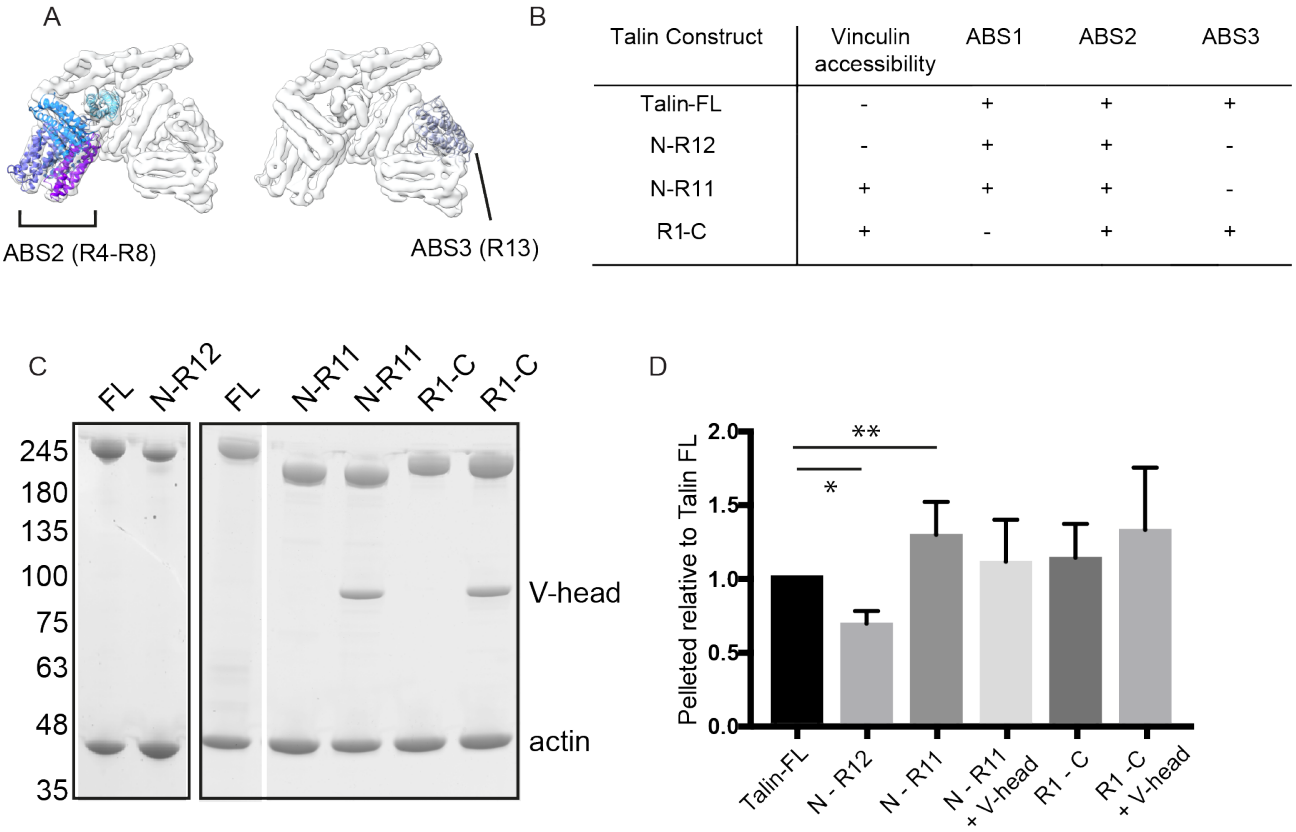

Figure 6. Talin–F-actin binding assay.

A: Scheme of actin-binding domains ABS2 and ABS3 in the context of the autoinhibited talin structure. **B:** Table summarizing tested constructs for F-actin binding and vinculin accessibility of talin in compact conformation (75 mM KCl). **C:** Representative SDS-PAGE analysis of the F-actin co-sedimentation assay with various talin constructs at 75 mM salt. **D:** Quantification of the co-sedimented talin fragments**.** Data are represented as mean ± SD. N-R12 0.68 ± 0.08, N-R11 1.3 ± 0.2, N-R11 + V-head 1.1 ± 0.3, R1-C 1.1 ± 0.2 and R1-C + V-head 1.3 ± 0.4. Differences between talin-FL and N-R12 as well as N-R11 are statistically significant (marked with *), see also Figure S7.

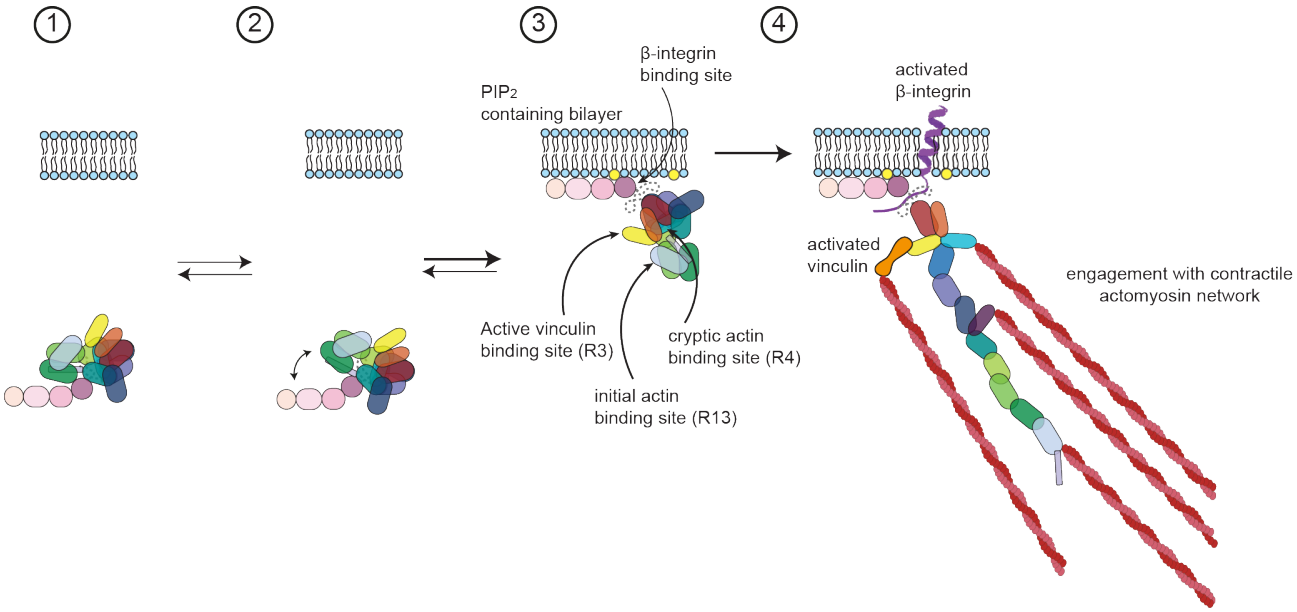

Figure 7. Model of talin activation.

(1) Our structure of talin in the closed form reveals how inactivation is achieved through occlusion of functional sites. Rap1-mediated recruitment of talin to membranes can occurr without breaking the closed formation of talin as the F0 and F1 subdomains are accessible. (2) Our structural analysis also indicated that the closed form of talin is in equilibrium with a semi-opened state due to the instable FERM-lid connection (see Figure S1). (3) Upon binding to the PIP_2-embedded membrane surface, the R12-F2 and R9-F3 interfaces are broken because of competitive interactions with PIP_2 and integrin, respectively (shown in Figure 1). The binding to the integrin tail hinders the F3-rod interaction (Wegener et al., 2007) and releases the rod domains from the FERM head as well as from the plasma membrane. (4) The further opening of the rod domains may require the mechanical aid of actomyosin pulling via the ABS3 and ABS2 actin-binding sites. Vinculin may also take an active role in reinforcing the binding of talin to actin (Humphries et al., 2007).

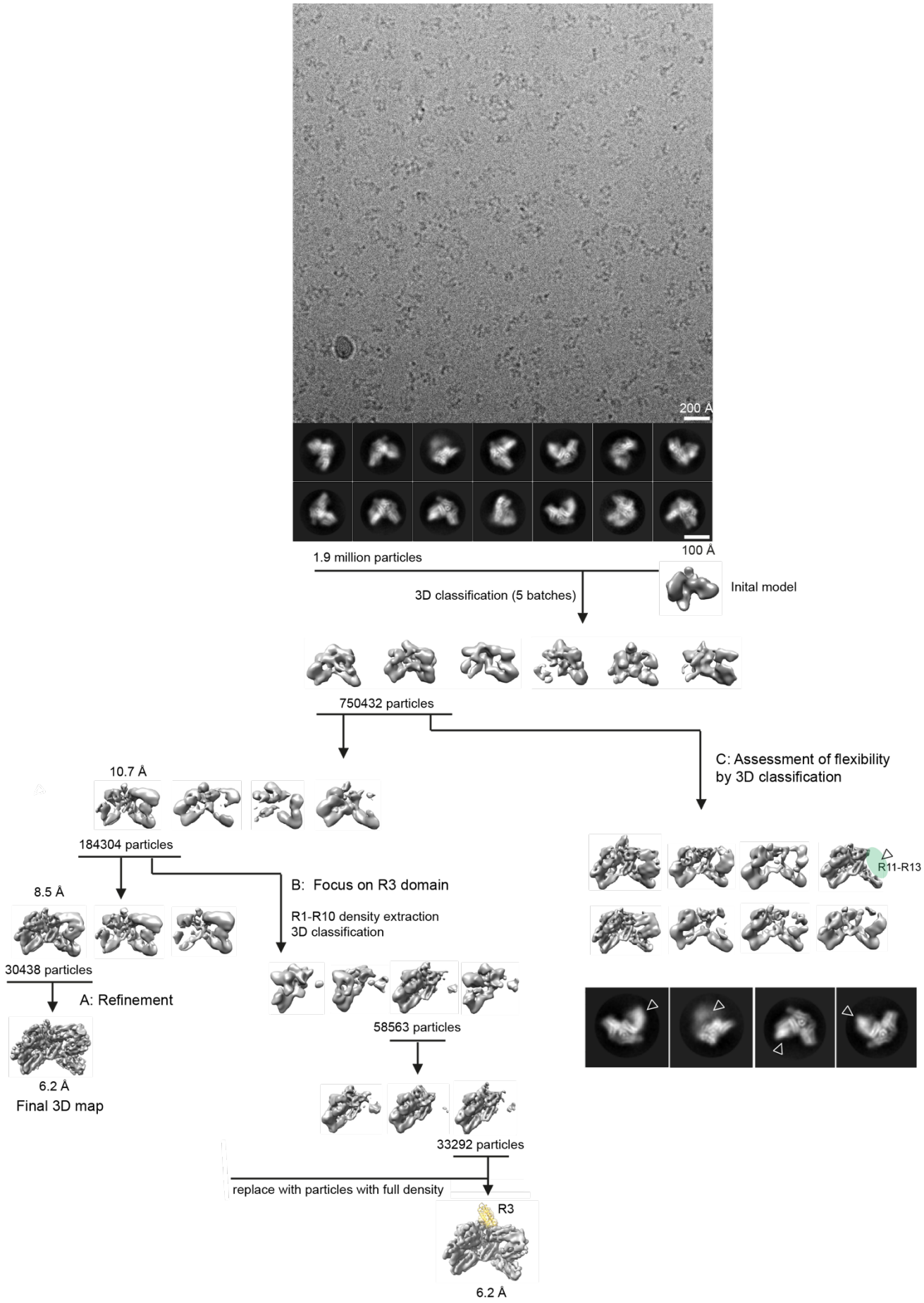

Figure S1: Summary of cryo-EM data processing, related to Figure 1.

Top: Representative cryo-EM image of talin-FL at 75 mM salt with representative 2D averages. **Bottom**: Graphical scheme of image processing. 1.9 million particles were selected out of 2D classifications. Further 3D classifications and refinements facilitated the final model production (**A – left**). To visualize the R3 domain, the core density (R1-R10) was computationally extracted and focused 3D classification of the core density was performed. At the final step of the processing, the alignment parameters were applied to the original particles to visualize the full density **(B – center)**. Yellow density fitted with an available structural model of R3. To assess the flexibility of the autoinhibition pocket consisting of the interface between FERM domain F2-F3 and R12-R13 (lid), extensive 3D classifications were performed, yielding a visualization of the flexible densities of R11-R13 **(C – right)**.

Table S1: Data collection and structure refinement statistics, related to Figure 1.

Data Set	Structure (EMD-4772) (PDB 6R9T)
Data collection statistics	
Microscope	FEI Titan Krios
Detector	Gatan K2 Summit
Grid type	Cu 200 R1.2/1.3
Magnification	130,000
Voltage (kV)	300
Electron dose ($e^-/Å^2$)	76.8
Dose rate (e^-/s/pixel)	8.14
Defocus Range (μm)	-1.0 to -3.0
Number of movie frames	40
Pixel size (Å)	1.06
Number of micrographs	11,007
Number of particles (total)	1,873,975
Number of particles (final map)	30,438
Symmetry imposed	C1
FSC threshold	0.143
Global resolution (Å)	6.2
Local resolution range (Å)	5.5 – 7.9
Refinement statistics	
Particles used for final map	30,438
Map sharpening B factor ($Å^2$)	-309
Number of Residues	
Protein	2185
Number of Atoms	
Protein	16013
Water/Solutes	-
B-factors	
Protein	377
Water/Solutes	-
R.m.s deviations	
Bond lengths (Å)	0.002
Bond angles (°)	0.580
Validation	
MolProbity score	1.57
Clashscore	6.31
Rotamer outliers (%)	1.98
Map correlation coefficient	0.81
Ramachandran Plot	
Preferred (%)	98.6
Allowed (%)	1.4

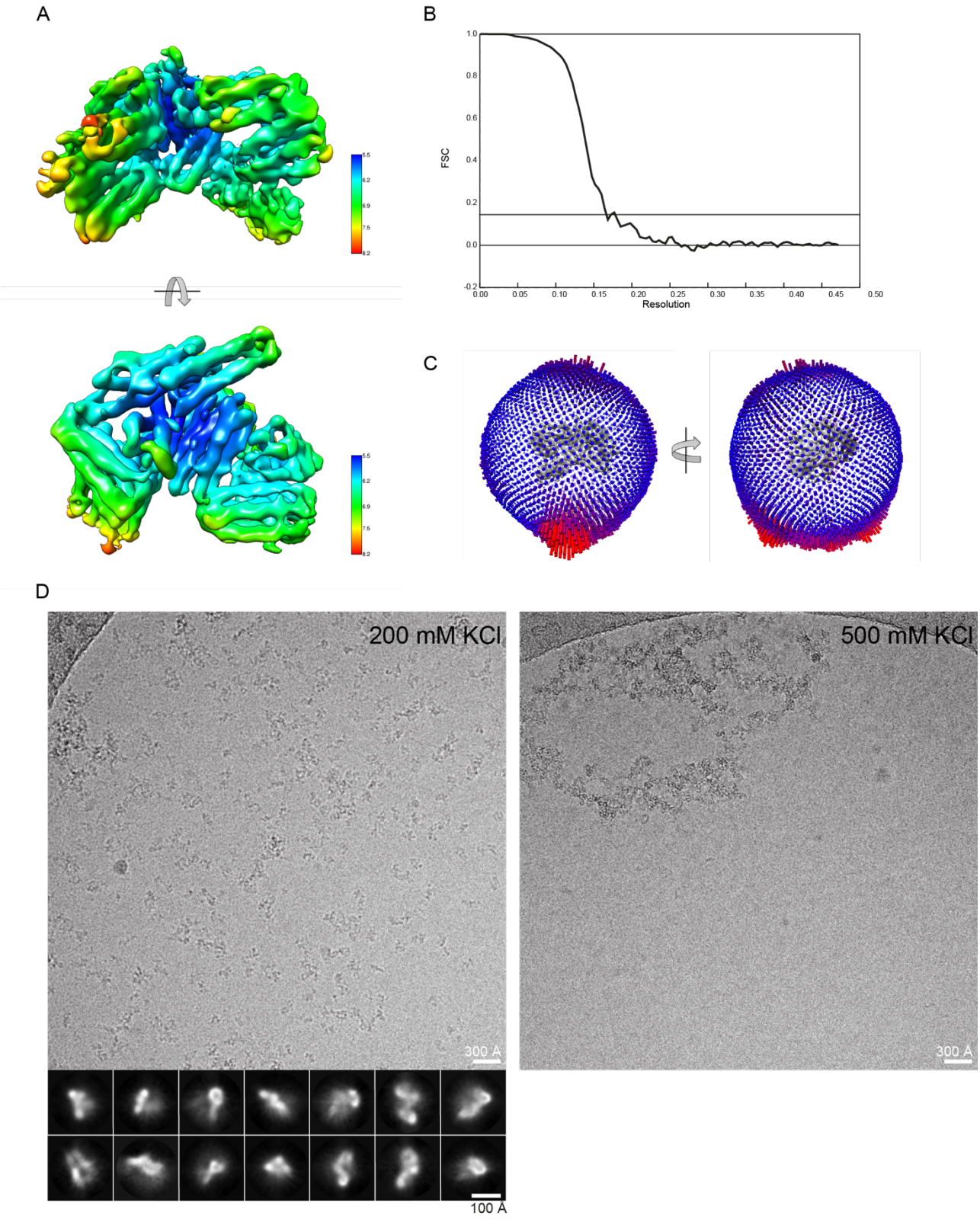

Figure S2: Quality control of cryo-EM data processing, related to Figure 1.

A: Local resolution map of the full-length talin structure, showing a resolution range between 5.5 Å and 7.9 Å. **B:** The Fourier shell correlation (FSC) curve of the full-length

talin structure showing a global resolution of 6.2 Å. The additional line indicates a FSC of 0.143 **C**: Angular distributions of the particle orientations that were incorporated into the final 3D reconstruction. **D**: Cryo-EM images of talin-FL in the presence of 200 mM KCl and 500 mM KCl, showing aggregations presumably due to the talin opening at 500 mM KCl. 2D classifications of talin-FL at 200 mM KCl reveal less robust averages indicating higher structural heterogeneity.

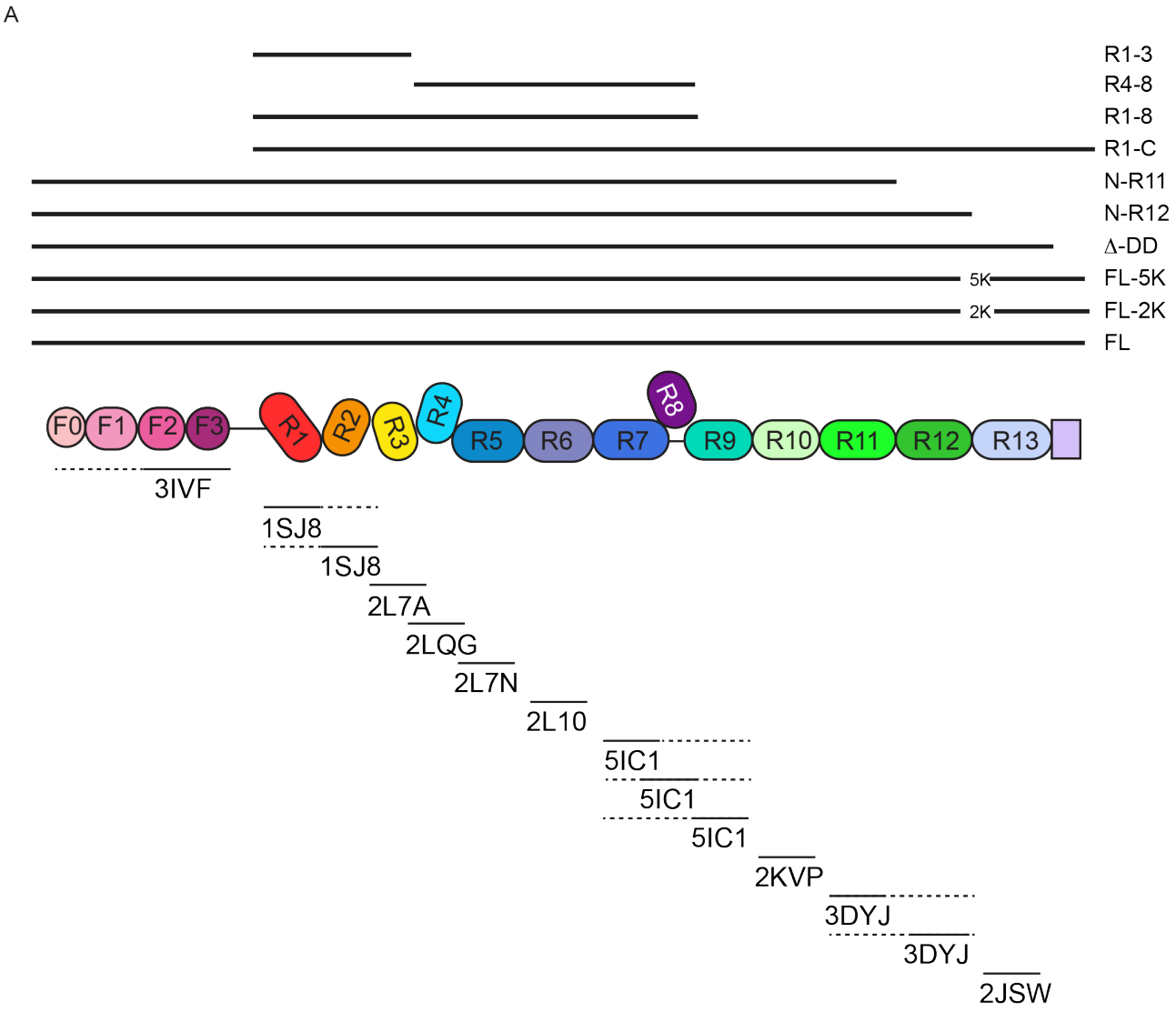

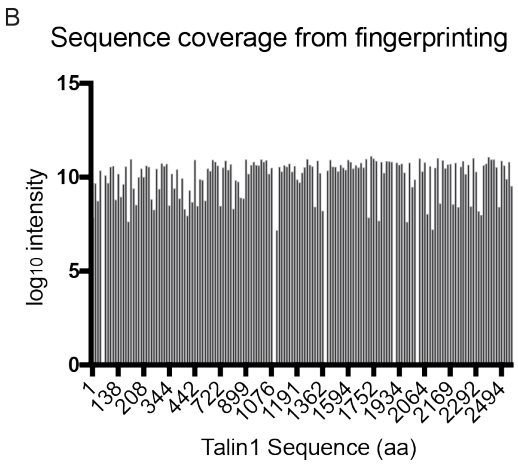

Figure S3: Talin fragments used in this study and sequencing information of full-length talin, related to Figure 1.

A: Scheme of talin fragments used in this study (top) and the structures (PDB codes) that were used as building blocks for the fitting and molecular modelling. For PDBs 3IVF, 1SJ8, 5IC1 and 3DYJ, individual domains are computationally extracted and used independently (see also STAR methods). 2K denotes charge-reversal double mutation E2288K, E2294K and 5K denotes mutations E2288K, E2294K, D2297K, E2299K, D2300K). **B:** Peptide detection of talin-FL by mass spectrometry. The entire sequence of talin (1-2541) is covered, showing no indication of spontaneous cleavage.

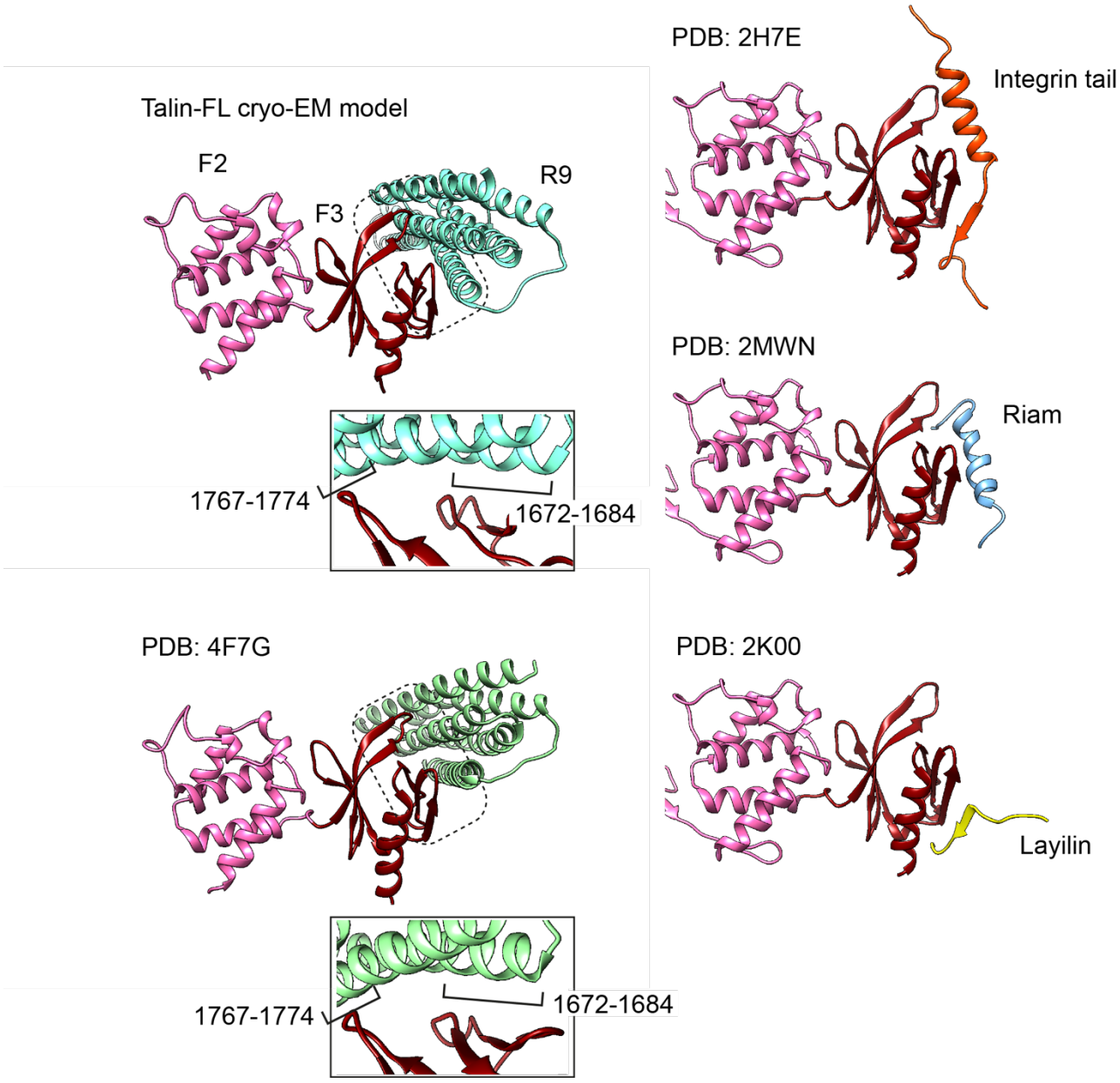

Figure S4: Talin F3-rod binding surfaces obtained from our cryo-EM map in comparison to available structures, related to Figure 1.

Top-left: Our cryo-EM model of the F3-rod binding surface. **Bottom-left:** crystal structure (PDB: 4F7G) of truncated F2-F3 and R9. **Right:** Examples of structures that bind to the talin F3-rod binding surface. From top to bottom: PDB: 4F7G superimposed to 2H7E (Integrin tail), 2MWN (Riam), and 2K00 (Layilin).

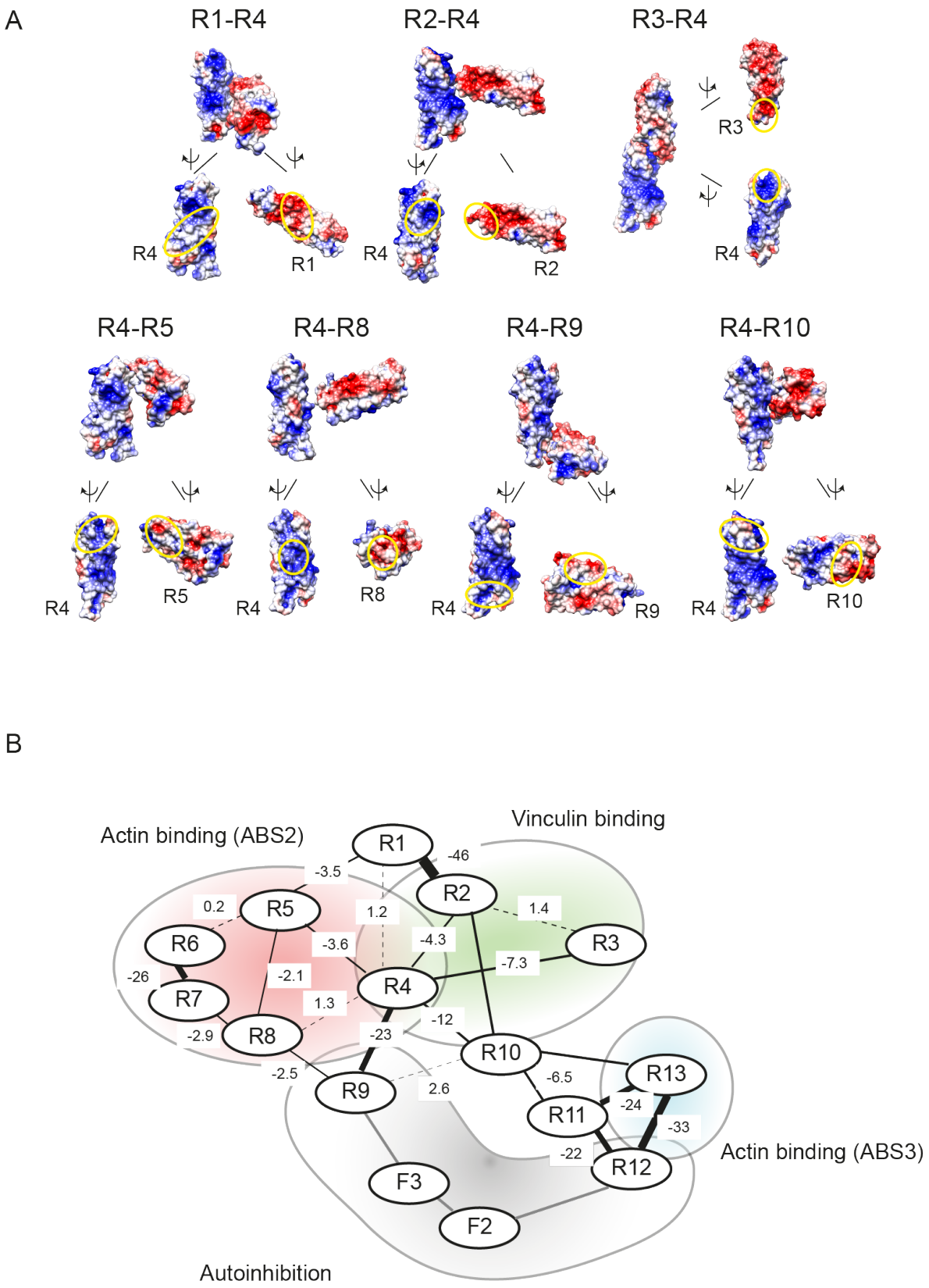

Figure S5: Talin inter-domain interactions, related to Figure 1 and 4.

A: Electrostatic surface potential of individual rod domains surrounding R4 and forming the autoinhibition core. Sites contacting each other are indicated with yellow circles. **B:** Interaction energies calculated by restraint molecular dynamics simulations for major interaction surfaces in the presence of 150 mM salt. Units: kCal/mol. We note that the calculated interaction energies represent enthalpic contributions and do not include the entropic penalties of restricting the large ensemble of open and flexible conformations of talin to a small ensemble of compact conformations seen in the autoinhibited state.

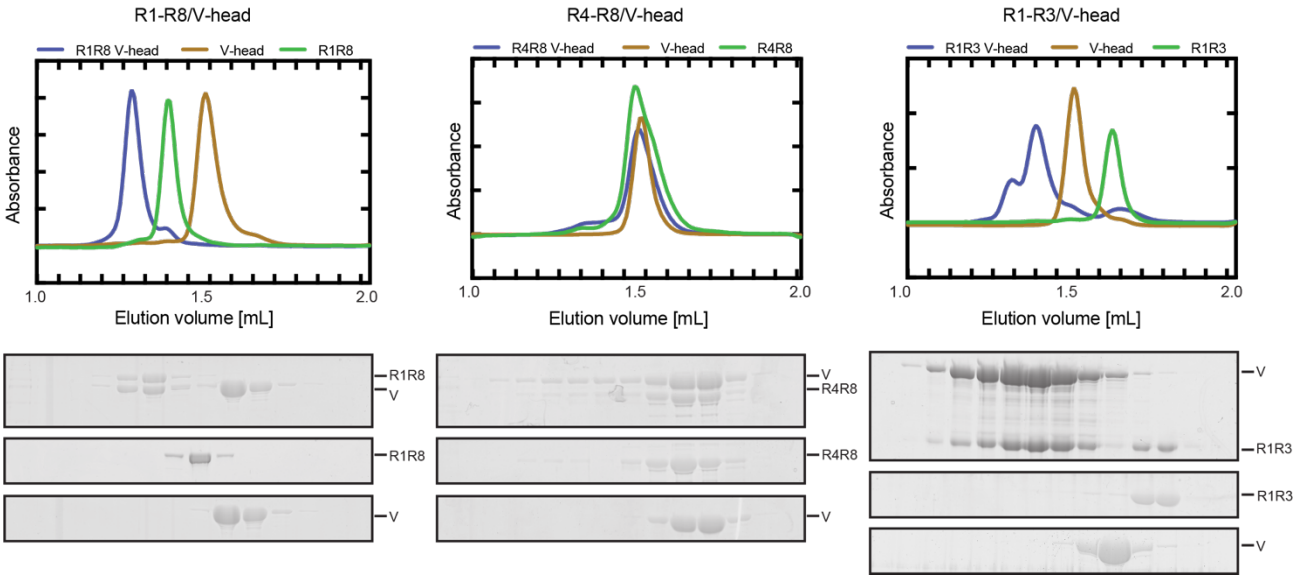

Figure S6: SEC reconstitution assay of various talin rod domains and the vinculin head (V-head) at 75 mM salt, related to Figure 5. The SDS-PAGE analysis corresponds to the profile of the protein mixtures (top), talin control constructs (center), and vinculin head control (bottom), respectively.

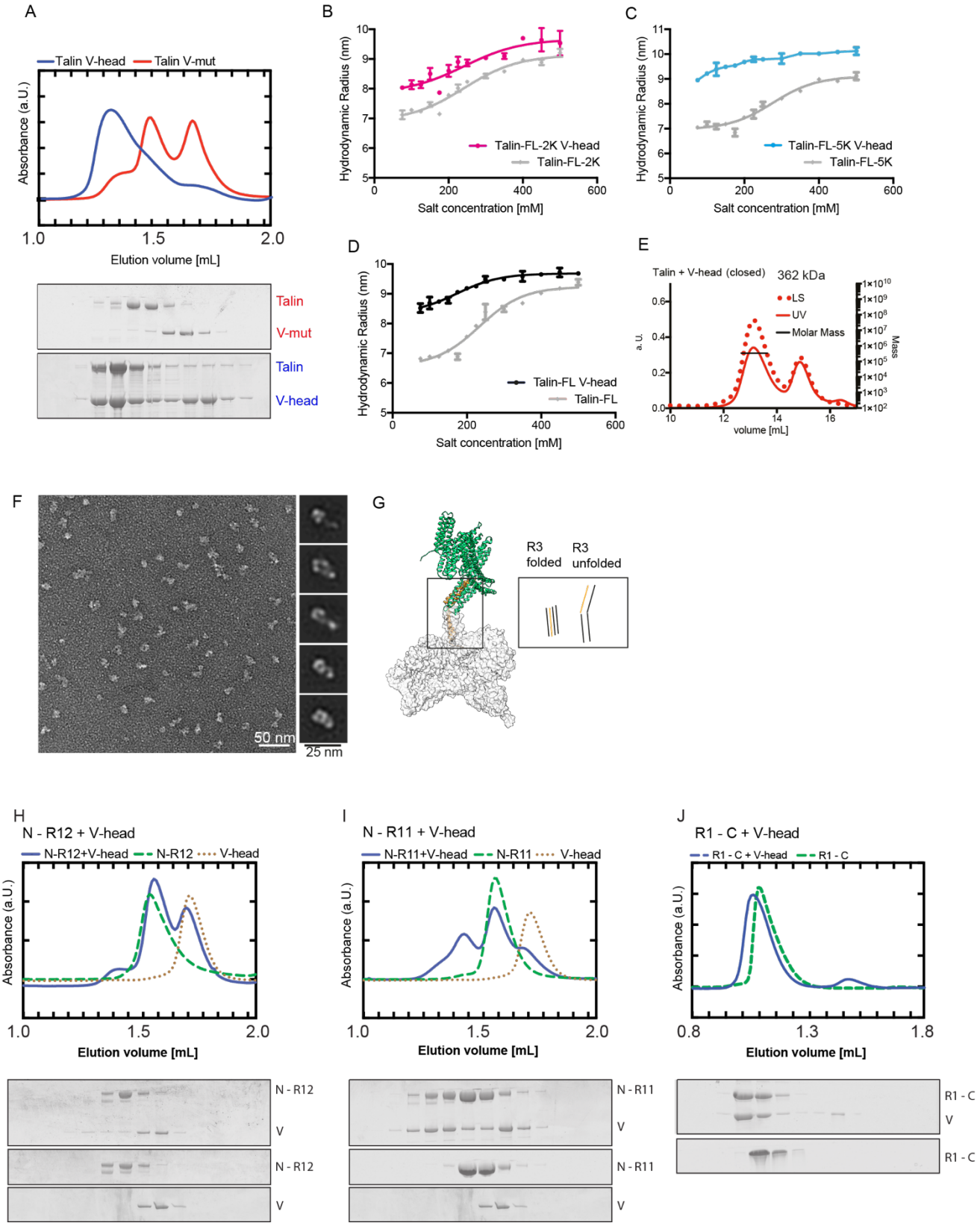

Figure S7: Conformational change of talin in complex with V-head, related to Figure 5 and 6.

A: Size-exclusion chromatography (SEC) profile of talin and vinculin constructs. Reconstitution assays of talin (open conformation) and V-head as well as V-mut were performed at 500 mM salt, and then the complex was assessed by changing the salt concentration to 75 mM. V-head stays in complex with talin (blue), while V-mut dissociates from talin (red). **B-D:** DLS measurements of the hydrodynamic radius of the reconstituted talin constructs (talin-FL, talin-FL-2K and talin-FL-5K) in complex with V-head under various salt concentrations. In comparison to full-length talin constructs alone (shown in grey), the increased size of the sample is observed showing complex formation. A conformational change of talin-V-head complex upon the change of salt concentration is also observed. For the case of talin-FL-5K in complex with V-head, the profile did not fit to a two-state model. **E:** SEC-multi-angle light-scattering profile of the talin (75mM salt, closed) -V-head complex shows a molecular weight of 362 kDa, indicating a 1:1 stoichiometry. LS: light scattering, normalized, UV: absorbance **F:** Negative-stain EM image of the talin-vinculin head complex in closed talin and two-dimensional averages (right), showing a long protrusion from the main globular density. **G:** Molecular modeling of our talin structure (white) with R3 unfolded (yellow) to accommodate the vinculin head density (green). The model was created by combining our cryo-electron microscopy full-length talin structure (white) with available structures of a part of the vinculin head (a.a. 1–258) complexed with talin peptide (a.a. 1944–1969) (PDB: 1RKC, yellow) and the vinculin head (a.a. 259–843) extracted from full-length vinculin (PDB: 1TR2, green). **H-J:** SEC profiles of various talin truncation constructs with V-head at 75 mM salt, showing that the complex formation of talin and V-head occurs only with N-R11 (I) and R1-C (J). N-R12 containing the R12 (lid) does not make a complex with V-head (H). In the reconstitution assay of R1-C + V-head, a Superdex S200 column was used while a Superose 6 was used for the other assays.

Table S2 List of primers and recombinant DNA used in this study, related to STAR methods.

Oligonucleotides		
Primer: talin-FL forward for pCB vector	Eurofins	AAGAAGGAGATATACATATGGT TGCACTTTCACTG
Primer: talin-FL reverse for pCB vector	Eurofins	CAGAGCTTCGAGATGAGCACCT GGTGGTTCTGTTC
Primer: talin-FL forward for pEC vector	Eurofins	CCAGGGGCCCGACTCGAT GGTTGCGCTTTCGCTGAAG
Primer: talin-FL reverse for pEC vector	Eurofins	CAGACCGCCACCGACTGCTTA GTGCTCGTCTCGAAGCTCTG
Primer: talin-R11(2141) reverse for pEC vector	Eurofins	CAGACCGCCACCGACTGCTTG GTGGCCTCATCTTCCACAGCC
Primer: talin-R12(2294) reverse for pEC vector	Eurofins	GCAAAGCACCGGCCTTACTCTG TTCCTTTCATGGCTTCAG
Primer: talin-R13(2482) reverse for pEC vector	Eurofins	CAGACCGCCACCGACTGCTTA TGCAGCTTTCTGGGCCGCC
Primer: talin-R1(482) forward for pEC vector	Eurofins	CCAGGAACAAACCGGCGGCCG AGGACACATGCCACCTC
Primer: talin-R4(913) forward for pEC vector	Eurofins	CCAGGAACAAACCGGCGGCTT GGTGCAGCGCCTGGAG
Primer: talin-R3(912) reverse for pEC vector	Eurofins	CAGACCGCCACCGACTGCTTA CATGCTCCAGGCGCTGC
Primer: talin-R8(1655) reverse for pEC vector	Eurofins	GCAAAGCACCGGCCTTAGGCT TTGTCCCTCATGCTTG
Primer: talin-FL-2K mutagenesis forward	Eurofins	GACCCAGAGGACCCTACTGTC ATTGCT
Primer: talin-FL-5K mutagenesis forward	Eurofins	AAACCAAAGAAACCTACTGTCA TTGCTGAGAATGA
Primer: talin-FL-2K/5K mutagenesis reverse	Eurofins	CACCCATTTTGTTCCTTTCATG GCTTTAGC
Primer: Vinculin-FL forward for pEC vector	Eurofins	CAGGGGCCCGACTCGATGCCA GTGTTTCATACGCGCACG
Primer: Vinculin-FL reverse for pEC vector	Eurofins	GACCGCCACCGACTGCTTACT GGTACCAGGGAGTCTTTC
Primer: V-head reverse for pEC vector	Eurofins	GACCGCCACCGACTGCTTATTC ATCCTTTTCCTCTGG
Recombinant DNA		
pet101-hTln1-His	Gift from Christophe Le Clainche	N/A
pCB-a-bax19-hTln1(1-2541aa)-3C-gfp-his	This study	N/A
pEC-mTln1(1-2541aa)-3C-his	This study	N/A
pCB-a-bax19-mTln1-R1-C(482-2541aa)-3C-mVenus-his	This study	N/A
pEC-mTln1-NtoR12-(1-2294aa)-3C-his	This study	N/A
pEC-mTln1-NtoR11-(1-2141aa)-3C-his	This study	N/A
pCB-a-bax19-mTln1ΔDD-(1-2482aa)-3C-mVenus-his	This study	N/A
pCB-a-bax16-mTln1-R1-R8(482-1655aa)-3C-his	This study	N/A
pCB-a-bax16-mTln1-R1-R3(482-913aa)-3C-his	This study	N/A
pCB-a-bax16-mTln1-R4-R8(914-1655aa)-3C-his	This study	N/A
pEC-mTln1-E2288K/E2294K/D2297K/E2299K/D2300K(5K)-3C-his	This study	N/A
pEC-mTln1-E2288K/E2294K(2K)-3C-his	This study	N/A
pEC-hVcl-3C-His-GST	Subcloned from gift from Carsten Grashoff	N/A
pEC-hVcl-Head-(1-851aa)-3C-His-GST	Subcloned from gift from Carsten Grashoff	N/A
pEC-hVcl-N773A/E775A-3C-His-GST	Subcloned from gift from Carsten Grashoff	N/A

STAR Methods

CONTACT FOR REAGENT AND RESOURCE SHARING

Further information and requests for resources and reagents should be directed to and will be fulfilled by the Lead Contact, Naoko Mizuno (mizuno@biochem.mpg.de).

METHOD DETAILS

Protein purification

Expression constructs of full-length talin1 (talin-FL) were prepared using human talin1 DNA (a gift from Christophe Le Clainche). DNA of talin-FL was amplified using PCR and subcloned into a pCB homemade expression vector with a His tag at the C-terminus for bacterial or mammalian cells. Talin1 was expressed in *E. coli* BL21 (DE3) goldusing ZY auto-induction medium. Cells were lysed by sonication in 50 mM Tris-HCl pH 7.8, 500 mM NaCl, 10 mM imidazole, 1 mM DTT, 5 mM EDTA, purified by nickel-affinity chromatography (complete His-Tag purification column, Roche) and anion exchange (HiTrap Q HP, GE Healthcare). The His-tag was removed using 3C protease and proteins were further purified by size-exclusion chromatography using a Superdex 200 16/600 column (GE Healthcare) in 20 mM HEPES pH 7.8, 75 mM KCl, 0.5 mM ß-Mercaptoethanol and 0.5 mM EDTA and 10% glycerol.

Talin truncation and mutation variants were obtained using mouse talin FL (pLPCXmod-Talin1-Ypet; a gift from Carsten Grashoff,) as a template and cloned into homemade expression vectors (pCB and pEC vectors). Mouse talin constructs used in this study were 1-2482 (talin -ΔDD), 482-2541 (R1-C) 1-2294 (N-R12), 1-2141 (N-R11), 482-1655 (R1-R8), 482-913 (R1-R3), 913-1655 (R4-R8), talin mutant E2288K/E2294K/D2297K/E2299K/D2300K (talin-FL-5K) as well as talin mutant E2288K/E2294K (talin-FL-2K) (see Table S2). The DNA fragments were amplified using PCR and subcloned into a pCB vector containing a cleavable N-terminal Venus-His8-Sumo tag or His tag. Proteins were expressed in *E. coli* BL21 (DE3) gold in ZY auto-induction medium. Talin truncation variants were purified using the same procedure as talin-FL. Tags were removed using 3C or Senp2 protease and proteins were further purified by size-exclusion chromatography using a Superdex 200 16/600 column (GE Healthcare) with 20 mM HEPES pH 7.5, 75 mM NaCl, 0.5 mM EDTA and 0.5 mM ß-Mercaptoethanol.

Vinculin constructs were designed based on a previous report (Cohen et al., 2005) and cloned into homemade pEC vectors containing N-terminal GST-His tag and a 3C-cleavage site. V-head contains a.a. 1-851. Proteins were purified using His-affinity

purification methods and eluted with 500 mM imidazole. Protein fragments were cleaved with 3C-Protease and dialyzed over night against 20 mM HEPES at pH 7.8, 100 mM KCl, 0.5 mM ß-Mercaptoethanol, concentrated and subsequently applied to size-exclusion chromatography (Superdex 200 16/600, GE Healthcare). All purified proteins were stored at −80 °C. Analytical size-exclusion chromatography experiments using talin were performed in 20 mM HEPES at pH 7.8, 0.5 mM ß-Mercaptoethanol, 0.5 mM EDTA either with 75 or 500 mM KCl to test the influence of salt on the conformational change observed under negative-stain EM.

GraFix

The GraFix method was adapted from (Stark, 2010). Talin samples were subjected to a sucrose and glutaraldehyde gradient of 10-30% and 0-0.2%, respectively, in a buffer containing 20 mM HEPES (pH 7.5), 75 mM KCl, 0.5 mM ß-Mercaptoethanol and 0.5 mM EDTA. Gradients were prepared in 2.2 ml ultracentrifuge tubes (open-top polyclear tubes, Seton) using a Gradient Station machine (model ip, Biocomp). 50 uL of talin samples at a concentration of 5 mg/ml (approximately 18.5 uM) were placed on top of the gradients and centrifuged in a TLS55 rotor (Beckman Coulter) at 50 000 rpm, for 6h at 4°C, using an Optima Max-XP ultracentrifuge (Beckman Coulter). 100 uL-Fractions were collected manually from top to bottom and quenched with 100 mM Tris (pH7.5). Fractions containing the monomeric or dimeric talin, as determined by SDS-PAGE were pooled, concentrated, and buffer-exchanged to 20 mM HEPES (pH 7.5), 75 mM KCl, 0.5 mM ß-Mercaptoethanol and 0.5 mM EDTA to remove excess sucrose using Amicon-Ultra, 0.5 ml, 50 MWCO.

Mass spectrometry

The talin-FL sample was diluted in equal volume of buffer containing 2% sodium deoxycholate (SDC), 20 mM TCEP and 80 mM chloroacetamide in 25 mM Tris at pH 8.5 and incubated at 37˚C for 20 min. The sample was then further diluted with LC-MS grade water to reduce the SDC concentration to less than 0.5% and directly digest with 1 µg of trypsin (Promega) overnight. The peptides were then acidified and purified via SDB-SCX StageTips and analysed in a Q Exactive HF mass spectrometer using a 75 min gradient. Raw data were processed using the MaxQuant platform and all identifications were filtered at 1% false discovery rate (FDR).

Negative-stain electron microscopy

For negative-stain EM, homemade carbon-coated grids were prepared and glow discharged before use. 5 µl of sample was applied and incubated for 1 min, blotted, washed twice in two drops of water and stained in 2% uranyl acetate for 1 min. The prepared specimens were visualized with a FEI CM200 with an operating voltage of 160 kV equipped with an Eagle CCD camera with a pixel size of 2.16 Å/pix or with a FEI Tecnai F20 at 200 kV with an Eagle CCD camera with a pixel size of 2.21 Å/pix. For 2D classifications, particles were manually or automatically picked using RELION (Zivanov et al., 2018) and extracted in 276 Å boxes. For shape assessment, 1102 (talin-ΔDD), 1749 (R1-C), 204 (N-R12), 321(N-R11) and 5678 (talin-FL V-head complex, treated with GraFix method for stabilization) particles were selected for reference-free 2D classification using RELION, resulting in 2D class averages. The lengths of open talin were measured using bshow in BSOFT (Heymann and Belnap, 2007). Five images of negatively stained talin were filtered using median filter (n=6) as well as Gaussian filter (sigma=4) to enhance the contrast of the protein densities. Particles showing clear boundaries were manually selected and their contour length was measured using the 'filament' option in BSOFT, facilitating the tracing of elongated, string-like particles. The histogram was created from n=89 samples, and the distribution was fit to normal distribution (average 560 Å, S.D. 170 Å).

Cryo-EM

Samples for cryo-EM were applied to glow-discharged R1.2/1.3 Cu 200 mesh holey carbon grids at a concentration of 0.3 mg/mL in 20 mM HEPES at pH 7.8, 75 mM KCl, 0.5 mM ß-Mercaptoethanol, 0.5 mM EDTA to ensure the compact formation of talin based on the DLS experiment shown in Figure 3D. Under salt concentrations of 200 mM KCl and higher, the compact formation of talin molecule was compromised in the cryo-EM environment, yielding poor 2D averages (Figure S2D). The grids were blotted at ~95% humidity at 4˚C for 4 s and plunged into liquid ethane-propane using a Vitrobot Mark IV (FEI). 11007 micrographs were collected on a Titan Krios (FEI) at 300 kV equipped with a K2 Summit direct electron detector and a quantum energy filter (20 e-V)(Gatan). Micrographs were exposed for 10 s at 7.68 e-/Å2/s (total dose 76.8 e-/Å2) and 40 frames were collected in counting mode (pixel size 1.06 Å/pixel). Defocus was varied between -1 and -3 µm in steps of 0.3 µm. Movies were aligned, gain-normalized and dose-weighted using MotionCor2 (Zheng et al., 2017). Defocus values were determined using GCTF (Zhang, 2016). Particles were automatically picked with Gautomatch using the template-free mode (Gaussian blob with 220 Å diameter), imported to RELION-3 (Zivanov et al., 2018) and extracted in 224 Å-sized boxes. Extracted particles were

applied to 2D classification routine in RELION-3 to remove contaminations. 1,873,975 particles were selected and after removing low quality classes, initial 3D reconstruction was performed using cryoSPARC (Punjani et al., 2017). Using the initial model, 5 batches of 3D classification were performed, yielding several models of a closed talin structure with different completeness of densities. Particles of the most complete model were combined, further aligned and classified. 30,438 particles were selected for the final 3D refinement, yielding a final map with a global resolution of 6.2 Å with up to 5.5 Å resolution in the core of talin using the RELION post-processing routine, using the gold-standard Fourier shell correction (FCS) = 0.143 criterion. In the final map, the R3 domain was only partially resolved. To visualize the R3 domain, flexible densities were computationally subtracted from individual particles using available scheme from RELION-3, and as previously described (Bai et al., 2015), facilitating the focused 3D classification of the core density R1-R10. The particle information and the alignment parameters of the 3D class with the most prominent density of R3 were applied to the original particles that contain the flexible densities (FERM domain and R11-C) and the final map with the R3 domain was obtained. This map was used for the assignment of the R3 domain. Finally, to assess the flexibility of the autoinhibition area in the talin structure, 3D classification was performed to the 750,432 particles obtained from the initial stage of the 3D classification. It was observed that the parts corresponding to R11-R13 exhibited a weaker density compared to the core part (R1-R10) of the structure, detecting high levels of flexibility. Overall, the analysis indicated that the packing of talin-FL is sensitive to its environment, which agrees well with its conformational change observed in our biochemical analysis as well as its cellular function. The graphical summary is depicted in Figure S1.

Molecular fitting and molecular dynamics analysis for flexible fitting

For each of the rod fragments (R1-R13) and the FERM domains, crystal and NMR structures are available. The corresponding PDB entries are 3ivf (FERM domain), 1sj8 (rod domains R1 and R2), 2l7a (R3), 2lqg (R4), 2l10 (R6), 2l7n (R5) 5ic1 (R7, R8, R9), 2kvp (R10), 3dyj (R11, R12), 2jsw (R13). Initially, the structures containing multiple domains (3ivf, 1sj8 and 5ic1) were computationally divided into individual domains. These individual domain structures served as building blocks to build a model of the entire autoinhibited structure of talin (Figure S3).

The R1 rod domain has an asymmetric shape and only one unique well-fitted placement and orientation of this structure in the density could be identified by rigid-body fitting. The C-terminus of the fitted R1 model reaches into a neighboring helical

bundle density in the cryo-EM map, which fitted well with the R2 model. The available structure of R1-R2 complex (1sj8) was independently fitted using the colores program of the Situs package (Chacón and Wriggers, 2002) showing that they matched to each other. This fitting served as a first anchor segment. The resolution of the density was sufficient to clearly distinguish between 4-helix and 5-helix bundle segments in the density. R7 and R8 were readily identified due to the inter-winded helical bundle feature of R7 within R8. Together with the constraint on the maximum linker length to covalently connect consecutive rod-domains it was possible to define placements and also orientations of the subsequent rod domains (R3-R13) in order to fit to the density and at the same time, to allow covalent connection to the previous and subsequent rod-domains. Placements that sterically did not allow connection of consecutive fragments to form a fully connected talin chain were eliminated. Finally, remaining densities, which did not represent a helical bundle arrangement, were assessed. These remaining densities consisted of two globular entities that were identified as F2 and F3 domains due to their secondary structures features. Overall, the fitting was performed independent of any of available structural models showing the inter-domain connections. However, our placements brought the F3 segment in close binding vicinity to the R9 rod-domain. The placement coincided with the crystal structure of F2-F3 in complex with R9 (PDB 4f7g) (within an root-mean square deviation (RMSD) < 0.8 Å).

The resolution of the cyro-EM reconstruction of 6.2 Å together with the sterical constraints to covalently connect domains with smaller linker segments readily allowed the identification of the unique topology for the full chain. However, no cryo-EM densities for the FERM F0 and F1 domains and the DD domain were identified and these parts were not included during model building. Finally, a full covalently connected chain was formed by connecting N- and C-termini of consecutive rod fragments using the Leap module of the Amber16 package (Salomon-Ferrer et al., 2013) in combination with the ff14SB force field (Maier et al., 2015). The disordered connection between FERM F3 and R1 was not included and the F2 and F3 domains were treated as separate proteins not covalently connected to the rod fragments.

The emap/sander module of the Amber16 package was used to perform a flexible fitting and sterical force field optimization (based on the ff14SB force field). In order to keep the structure of each individual template structure (R1-R13 and F2 and F3) close to the corresponding experimental crystal structure distance restraints between backbone atoms within each fragment were included. These restraints kept the secondary structure and the arrangement of secondary structures in each domain to within RMSD < 1 Å from the corresponding experimental domain reference structures.

Connecting loops and side chains were nevertheless fully mobile during flexible fitting. The full start structure was first energy minimized (5000 steps) followed by a Molecular Dynamics (MD) simulation at 300 K (0.5 ns) until no further shift of the mean structure was observed followed by another round of energy minimization. The model was then subjected to manual building and correction in COOT (Emsley et al., 2010)and real-space refinement in PHENIX (Afonine et al., 2018). The final structure fitted well to the cryo-EM density with a correlation coefficient around the model (CC_{mask}) of 0.81 without outliers in the Ramachandran plot (Table S1).

Estimation of interaction energies between talin subunits

The interaction energy between selected pairs of talin fragments (enthalpy) was calculated using the MMPBSA (Molecular Mechanics Poisson Boltzmann Surface Area) approach as implemented in the Amber18 package (Onufriev et al., 2000; Salomon-Ferrer et al., 2013). Pairs of talin subdomains were extracted from the compact talin autoinhibited structure in the same arrangement as observed in the full structure. For each case an ensemble of 250 conformations was generated using short MD simulation (0.1 ns, 300 K) keeping the backbone strongly restraint to the starting placement (allowing shifts < 0.1 Å). The mean domain-domain interaction energy was calculated using the MMPBSA method. It accounts for changes in electrostatic Coulomb interactions, changes in electrostatic solvation (reaction field with the aqueous environment), changes in mean van-der-Waals interactions and nonpolar (hydrophobic) contributions that depend on the buried surface area upon complex formation. In the MMPBSA approach, the change in electrostatic reaction field contributions is calculated by solving the finite-difference Poisson-Boltzmann equation for each structure. The energy of interaction was estimated by subtracting the contributions of each partner from the result of the domain-domain complex for each case. Calculations were performed at a monovalent salt concentration of 0.15 M. We note that the calculated interaction energies represent enthalpic contributions and do not include the entropic penalties of restricting the large ensemble of open and flexible conformations of talin to a small ensemble of compact conformations seen in the autoinhibited state.

F-Actin co-sedimentation assay

Actin was purchased from Hypermol, Germany. Actin was polymerized in 10 mM Tris pH 7.5, 50 mM KCl, 2 mM $MgCl_2$, 0.2 mM $CaCl_2$, 0.2 mM ATP, 0.5 mM DTT for 20 min at RT. Buffer exchange of the samples were performed using Zeba Spin desalting columns (Thermo Scientific). The buffer for all constructs was 20 mM Tris pH 7.5, 75

mM KCl. 2.5 µM talin fragments were incubated with 2.5 µM F-actin for 15 min at RT. The mixture was then ultra-centrifuged at 175 000 x g (TL-100 Ultracentrifuge, Beckmann) for 20 minutes at RT. Pellets were re-suspended to comparable volumes as supernatants with 1x SDS buffer. 6x SDS buffer was added to the supernatant and 10 µl of samples were run on SDS-page and quantified using FIJI (Schindelin et al., 2012).

Analytical size-exclusion chromatography

For analytical size-exclusion chromatography, the buffer exchange of the sample was performed using Zeba Spin desalting columns (Thermo Scientific) to 20 mM HEPES pH 7.5, 75 or 500 mM KCl, and 10 µM of samples were injected to either an analytical Superdex 200i 3.2/300 (for the reconstitutions of R1-C, R1-R3, R4-R8 and R4-R8 and V-head) or Superose 6i 3.2/300 (all other constructs) on an ÄKTAmicro system (GE Healthcare). Fractions were collected, mixed with 6x SDS sample buffer and 10 µl were run on SDS-PAGE.

Dynamic Light-Scattering (DLS)

For measurements of hydrodynamic radius changes, talin-FL, talin N-R11 and talin N-R12 were initially prepared in 20 mM HEPES pH 7.5, 75 mM KCl, 0.5 mM EDTA, 0.5 mM ß-Mercaptoethanol. Further, the samples were diluted to a final concentration of 0.3 mg/ml and final KCl concentrations of 75 – 500 mM (75/100/125/150/175/200/225/250/300/350/400/450/500 mM KCl) in the same buffer in 30 µl wells in a 384-well plate. DLS measurements were performed with a Dynapro Platereader-II Dynamic Light Scattering instrument (Wyatt Technology Corporation) at 20˚C. Samples were independently prepared in triplicates and 20 measurement points per well were taken. The data was analyzed in Dynamic 7.8.1.3 (Wyatt Technology Corporation) and plotted with PRISM (GraphPad). The fitting of the curve was performed using a nonlinear regression fit with a sigmoidal curve.

SEC-MALS

Talin-fl and talin truncations as well as the mixtures of talin and vinculin (1:1 ratio) were prepared in buffer containing 20 mM HEPES, pH 7.5, 75 or 500 mM KCl, 0.5 mM EDTA at 3 mg/ml concentration and 20 µl were run on a Superdex 200 5/150 GL column on an ÄKTAmicro system (GE Healthcare) coupled to a Viscotek TDA302 detector (Malvern, Herrenberg, Germany) in the same buffer. Bovine serum albumin was used as a standard and the refractive index increment (dn/dc) was set to 0.180

ml/g for calculations. Data was analyzed using the OmniSEC 4.5 software (Malvern) and plotted with PRISM (GraphPad).

QUANTIFICATION AND STATISTICAL ANALYSIS

Quantification and statistical analysis related to EM data are integral parts of algorithms and software used.

For DLS analysis, the experiments were performed 3 times independently. The results were averaged and the error bars represent the standard deviations. For the fitting, nonlinear regression fit, sigmoidal curve fitting was applied using the software PRISM (GraphPad).

For F-actin analysis shown in Figure 6, the experiments were performed at least 3 times independently. The talin-FL band was run on the same SDS-PAGE gel as an internal control to standardize the variability of the contrast caused by staining conditions of each SDS-PAGE gels. Therefore, relative quantified values compared to the talin-FL band were used for the analysis. These values were averaged and standard deviations were obtained. Unpaired t-test was used to assess statistical significance.

DATA AND SOFTWARE AVAILABILITY

The cryo-EM map of human talin1 was deposited in the EMDB database with accession code EMD-4772. The flexibly fitted atomic model was deposited in the PDB with accession code 6R9T.

Reference

Afonine, P.V., Poon, B.K., Read, R.J., Sobolev, O.V., Terwilliger, T.C., Urzhumtsev, A., and Adams, P.D. (2018). Real-space refinement in PHENIX for cryo-EM and crystallography. Acta Crystallogr D Struct Biol *74*, 531–544.

Anthis, N.J., Wegener, K.L., Ye, F., Kim, C., Goult, B.T., Lowe, E.D., Vakonakis, I., Bate, N., Critchley, D.R., Ginsberg, M.H., et al. (2009). The structure of an integrin/talin complex reveals the basis of inside-out signal transduction. Embo J *28*, 3623–3632.

Atherton, P., Stutchbury, B., Wang, D.-Y., Jethwa, D., Tsang, R., Meiler-Rodriguez, E., Wang, P., Bate, N., Zent, R., Barsukov, I.L., et al. (2015). Vinculin controls talin engagement with the actomyosin machinery. Nat Commun *6*, 10038.

Austen, K., Ringer, P., Mehlich, A., Chrostek-Grashoff, A., Kluger, C., Klingner, C., Sabass, B., Zent, R., Rief, M., and Grashoff, C. (2015). Extracellular rigidity sensing by talin isoform-specific mechanical linkages. Nat Cell Biol *17*, 1597–1606.

Bachir, A.I., Zareno, J., Moissoglu, K., Plow, E.F., Gratton, E., and Horwitz, A.R. (2014). Integrin-associated complexes form hierarchically with variable stoichiometry in

nascent adhesions. Curr Biol *24*, 1845–1853.

Bai, X.-C., Rajendra, E., Yang, G., Shi, Y., and Scheres, S.H.W. (2015). Sampling the conformational space of the catalytic subunit of human γ-secretase. Elife *4*.

Borgon, R.A., Vonrhein, C., Bricogne, G., Bois, P.R.J., and Izard, T. (2004). Crystal structure of human vinculin. Structure (London, England : 1993) *12*, 1189–1197.

Calderwood, D.A., Campbell, I.D., and Critchley, D.R. (2013). Talins and kindlins: partners in integrin-mediated adhesion. Nat Rev Mol Cell Biol *14*, 503–517.

Carisey, A., Tsang, R., Greiner, A.M., Nijenhuis, N., Heath, N., Nazgiewicz, A., Kemkemer, R., Derby, B., Spatz, J., and Ballestrem, C. (2013). Vinculin regulates the recruitment and release of core focal adhesion proteins in a force-dependent manner. Curr Biol *23*, 271–281.

Case, L.B., Baird, M.A., Shtengel, G., Campbell, S.L., Hess, H.F., Davidson, M.W., and Waterman, C.M. (2015). Molecular mechanism of vinculin activation and nanoscale spatial organization in focal adhesions. Nat Cell Biol *17*, 880–892.

Chacón, P., and Wriggers, W. (2002). Multi-resolution contour-based fitting of macromolecular structures. J. Mol. Biol. *317*, 375–384.

Chinthalapudi, K., Rangarajan, E.S., and Izard, T. (2018). The interaction of talin with the cell membrane is essential for integrin activation and focal adhesion formation. Proc Natl Acad Sci USA *115*, 10339–10344.

Cohen, D.M., Chen, H., Johnson, R.P., Choudhury, B., and Craig, S.W. (2005). Two distinct head-tail interfaces cooperate to suppress activation of vinculin by talin. J Biol Chem *280*, 17109–17117.

Desiniotis, A., and Kyprianou, N. (2011). Significance of talin in cancer progression and metastasis. Int Rev Cell Mol Biol *289*, 117–147.

Di Paolo, G., Pellegrini, L., Letinic, K., Cestra, G., Zoncu, R., Voronov, S., Chang, S., Guo, J., Wenk, M.R., and De Camilli, P. (2002). Recruitment and regulation of phosphatidylinositol phosphate kinase type 1 gamma by the FERM domain of talin. Nature *420*, 85–89.

Elliott, P.R., Goult, B.T., Kopp, P.M., Bate, N., Grossmann, J.G., Roberts, G.C.K., Critchley, D.R., and Barsukov, I.L. (2010). The Structure of the talin head reveals a novel extended conformation of the FERM domain. Structure (London, England : 1993) *18*, 1289–1299.

Ellis, S.J., Goult, B.T., Fairchild, M.J., Harris, N.J., Long, J., Lobo, P., Czerniecki, S., Van Petegem, F., Schöck, F., Peifer, M., et al. (2013). Talin autoinhibition is required for morphogenesis. Curr Biol *23*, 1825–1833.

Emsley, P., Lohkamp, B., Scott, W.G., and Cowtan, K. (2010). Features and development of Coot. Acta Crystallogr. D Biol. Crystallogr. *66*, 486–501.

Fang, K.-P., Dai, W., Ren, Y.-H., Xu, Y.-C., Zhang, S.-M., and Qian, Y.-B. (2016). Both Talin-1 and Talin-2 correlate with malignancy potential of the human hepatocellular carcinoma MHCC-97 L cell. BMC Cancer *16*, 45.

Fillingham, I., Gingras, A.R., Papagrigoriou, E., Patel, B., Emsley, J., Critchley, D.R.,

Roberts, G.C.K., and Barsukov, I.L. (2005). A vinculin binding domain from the talin rod unfolds to form a complex with the vinculin head. Structure (London, England : 1993) *13*, 65–74.

Garcia-Alvarez, B., de Pereda, J.M., Calderwood, D.A., Ulmer, T.S., Critchley, D., Campbell, I.D., Ginsberg, M.H., and Liddington, R.C. (2003). Structural determinants of integrin recognition by talin. Mol Cell *11*, 49–58.

Geiger, B., Spatz, J.P., and Bershadsky, A.D. (2009). Environmental sensing through focal adhesions. Nat Rev Mol Cell Biol *10*, 21–33.

Gingras, A.R., Bate, N., Goult, B.T., Hazelwood, L., Canestrelli, I., Grossmann, J.G., Liu, H., Putz, N.S.M., Roberts, G.C.K., Volkmann, N., et al. (2008). The structure of the C-terminal actin-binding domain of talin. Embo J *27*, 458–469.

Gingras, A.R., Ziegler, W.H., Frank, R., Barsukov, I.L., Roberts, G.C.K., Critchley, D.R., and Emsley, J. (2005). Mapping and consensus sequence identification for multiple vinculin binding sites within the talin rod. J Biol Chem *280*, 37217–37224.

Goldmann, W.H., Bremer, A., Häner, M., Aebi, U., and Isenberg, G. (1994). Native talin is a dumbbell-shaped homodimer when it interacts with actin. J Struct Biol *112*, 3–10.

Goult, B.T., Bouaouina, M., Elliott, P.R., Bate, N., Patel, B., Gingras, A.R., Grossmann, J.G., Roberts, G.C.K., Calderwood, D.A., Critchley, D.R., et al. (2010). Structure of a double ubiquitin-like domain in the talin head: a role in integrin activation. Embo J *29*, 1069–1080.

Goult, B.T., Xu, X.-P., Gingras, A.R., Swift, M., Patel, B., Bate, N., Kopp, P.M., Barsukov, I.L., Critchley, D.R., Volkmann, N., et al. (2013). Structural studies on full-length talin1 reveal a compact auto-inhibited dimer: implications for talin activation. J Struct Biol *184*, 21–32.

Goult, B.T., Yan, J., and Schwartz, M.A. (2018). Talin as a mechanosensitive signaling hub. J Cell Biol.

Haining, A.W.M., Lieberthal, T.J., and Del Río Hernández, A. (2016). Talin: a mechanosensitive molecule in health and disease. Faseb J. *30*, 2073–2085.

Harburger, D.S., and Calderwood, D.A. (2009). Integrin signalling at a glance. J Cell Sci *122*, 159–163.

Hemmings, L., Rees, D.J., Ohanian, V., Bolton, S.J., Gilmore, A.P., Patel, B., Priddle, H., Trevithick, J.E., Hynes, R.O., and Critchley, D.R. (1996). Talin contains three actin-binding sites each of which is adjacent to a vinculin-binding site. J Cell Sci *109 (Pt 11)*, 2715–2726.

Heymann, J.B., and Belnap, D.M. (2007). Bsoft: image processing and molecular modeling for electron microscopy. J Struct Biol *157*, 3–18.

Humphries, J.D., Wang, P., Streuli, C., Geiger, B., Humphries, M.J., and Ballestrem, C. (2007). Vinculin controls focal adhesion formation by direct interactions with talin and actin. J Cell Biol *179*, 1043–1057.

Izard, T., Evans, G., Borgon, R.A., Rush, C.L., Bricogne, G., and Bois, P.R.J. (2004). Vinculin activation by talin through helical bundle conversion. Nature *427*, 171–175.

Johnson, R.P., and Craig, S.W. (1994). An intramolecular association between the head and tail domains of vinculin modulates talin binding. J Biol Chem *269*, 12611–12619.

Kanchanawong, P., Shtengel, G., Pasapera, A.M., Ramko, E.B., Davidson, M.W., Hess, H.F., and Waterman, C.M. (2010). Nanoscale architecture of integrin-based cell adhesions. Nature *468*, 580–584.

Kumar, A., Ouyang, M., Van den Dries, K., McGhee, E.J., Tanaka, K., Anderson, M.D., Groisman, A., Goult, B.T., Anderson, K.I., and Schwartz, M.A. (2016). Talin tension sensor reveals novel features of focal adhesion force transmission and mechanosensitivity. J Cell Biol *213*, 371–383.

Legate, K.R., Wickström, S.A., and Fässler, R. (2009). Genetic and cell biological analysis of integrin outside-in signaling. Genes Dev *23*, 397–418.

Ling, K., Doughman, R.L., Firestone, A.J., Bunce, M.W., and Anderson, R.A. (2002). Type I gamma phosphatidylinositol phosphate kinase targets and regulates focal adhesions. Nature *420*, 89–93.

Liu, J., Wang, Y., Goh, W.I., Goh, H., Baird, M.A., Ruehland, S., Teo, S., Bate, N., Critchley, D.R., Davidson, M.W., et al. (2015). Talin determines the nanoscale architecture of focal adhesions. Proc Natl Acad Sci USA *112*, E4864–E4873.

Maier, J.A., Martinez, C., Kasavajhala, K., Wickstrom, L., Hauser, K.E., and Simmerling, C. (2015). ff14SB: Improving the Accuracy of Protein Side Chain and Backbone Parameters from ff99SB. J Chem Theory Comput *11*, 3696–3713.

Margadant, F., Chew, L.L., Hu, X., Yu, H., Bate, N., Zhang, X., and Sheetz, M. (2011). Mechanotransduction in vivo by repeated talin stretch-relaxation events depends upon vinculin. PLoS Biol *9*, e1001223.

Molony, L., McCaslin, D., Abernethy, J., Paschal, B., and Burridge, K. (1987). Properties of talin from chicken gizzard smooth muscle. J Biol Chem *262*, 7790–7795.

Nieswandt, B., Moser, M., Pleines, I., Varga-Szabo, D., Monkley, S., Critchley, D., and Fässler, R. (2007). Loss of talin1 in platelets abrogates integrin activation, platelet aggregation, and thrombus formation in vitro and in vivo. J. Exp. Med. *204*, 3113–3118.

Onufriev, A., Bashford, D., and Case, D.A. (2000). Modification of the generalized Born model suitable for macromolecules. Journal of Physical Chemistry B *104*, 3712–3720.

Orłowski, A., Kukkurainen, S., Pöyry, A., Rissanen, S., Vattulainen, I., Hytönen, V.P., and Róg, T. (2015). PIP2 and Talin Join Forces to Activate Integrin. J Phys Chem B *119*, 12381–12389.

Papagrigoriou, E., Gingras, A.R., Barsukov, I.L., Bate, N., Fillingham, I.J., Patel, B., Frank, R., Ziegler, W.H., Roberts, G.C.K., Critchley, D.R., et al. (2004). Activation of a vinculin-binding site in the talin rod involves rearrangement of a five-helix bundle. Embo J *23*, 2942–2951.

Parsons, J.T., Horwitz, A.R., and Schwartz, M.A. (2010). Cell adhesion: integrating cytoskeletal dynamics and cellular tension. Nat Rev Mol Cell Biol *11*, 633–643.

Plak, K., Pots, H., Van Haastert, P.J.M., and Kortholt, A. (2016). Direct Interaction between TalinB and Rap1 is necessary for adhesion of Dictyostelium cells. BMC Cell Biol. *17*, 1.

Punjani, A., Rubinstein, J.L., Fleet, D.J., and Brubaker, M.A. (2017). cryoSPARC: algorithms for rapid unsupervised cryo-EM structure determination. Nat. Methods *14*, 290–296.

Rees, D.J., Ades, S.E., Singer, S.J., and Hynes, R.O. (1990). Sequence and domain structure of talin. Nature *347*, 685–689.

Salomon-Ferrer, R., Case, D.A., and Walker, R.C. (2013). An overview of the Amber biomolecular simulation package. Wiley Interdisciplinary Reviews-Computational Molecular Science *3*, 198–210.

Schindelin, J., Arganda-Carreras, I., Frise, E., Kaynig, V., Longair, M., Pietzsch, T., Preibisch, S., Rueden, C., Saalfeld, S., Schmid, B., et al. (2012). Fiji: an open-source platform for biological-image analysis. Nat. Methods *9*, 676–682.

Song, X., Yang, J., Hirbawi, J., Ye, S., Perera, H.D., Goksoy, E., Dwivedi, P., Plow, E.F., Zhang, R., and Qin, J. (2012). A novel membrane-dependent on/off switch mechanism of talin FERM domain at sites of cell adhesion. Cell Res. *22*, 1533–1545.

Stark, H. (2010). GraFix: stabilization of fragile macromolecular complexes for single particle cryo-EM. Meth Enzymol *481*, 109–126.

Sun, Z., Costell, M., and Fässler, R. (2019). Integrin activation by talin, kindlin and mechanical forces. Nat Cell Biol *21*, 25–31.

Tadokoro, S., Shattil, S.J., Eto, K., Tai, V., Liddington, R.C., de Pereda, J.M., Ginsberg, M.H., and Calderwood, D.A. (2003). Talin binding to integrin beta tails: a final common step in integrin activation. Science (New York, NY) *302*, 103–106.

Tanentzapf, G., and Brown, N.H. (2006). An interaction between integrin and the talin FERM domain mediates integrin activation but not linkage to the cytoskeleton. Nat Cell Biol *8*, 601–606.

Wegener, K.L., Basran, J., Bagshaw, C.R., Campbell, I.D., Roberts, G.C.K., Critchley, D.R., and Barsukov, I.L. (2008). Structural basis for the interaction between the cytoplasmic domain of the hyaluronate receptor layilin and the talin F3 subdomain. J. Mol. Biol. *382*, 112–126.

Wegener, K.L., Partridge, A.W., Han, J., Pickford, A.R., Liddington, R.C., Ginsberg, M.H., and Campbell, I.D. (2007). Structural basis of integrin activation by talin. Cell *128*, 171–182.

Winkler, J., Lünsdorf, H., and Jockusch, B.M. (1997). Energy-filtered electron microscopy reveals that talin is a highly flexible protein composed of a series of globular domains. Eur. J. Biochem. *243*, 430–436.

Yang, J., Zhu, L., Zhang, H., Hirbawi, J., Fukuda, K., Dwivedi, P., Liu, J., Byzova, T., Plow, E.F., Wu, J., et al. (2014). Conformational activation of talin by RIAM triggers integrin-mediated cell adhesion. Nat Commun *5*, 5880.

Yao, M., Goult, B.T., Chen, H., Cong, P., Sheetz, M.P., and Yan, J. (2014). Mechanical

activation of vinculin binding to talin locks talin in an unfolded conformation. Sci Rep *4*, 4610.

Zaidel-Bar, R., Ballestrem, C., Kam, Z., and Geiger, B. (2003). Early molecular events in the assembly of matrix adhesions at the leading edge of migrating cells. J Cell Sci *116*, 4605–4613.

Zeiler, M., Moser, M., and Mann, M. (2014). Copy number analysis of the murine platelet proteome spanning the complete abundance range. Mol. Cell Proteomics *13*, 3435–3445.

Zhang, K. (2016). Gctf: Real-time CTF determination and correction. J Struct Biol *193*, 1–12.

Zheng, S.Q., Palovcak, E., Armache, J.-P., Verba, K.A., Cheng, Y., and Agard, D.A. (2017). MotionCor2: anisotropic correction of beam-induced motion for improved cryo-electron microscopy. Nat. Methods *14*, 331–332.

Zhu, L., Yang, J., Bromberger, T., Holly, A., Lu, F., Liu, H., Sun, K., Klapproth, S., Hirbawi, J., Byzova, T.V., et al. (2017). Structure of Rap1b bound to talin reveals a pathway for triggering integrin activation. Nat Commun *8*, 1744.

Zivanov, J., Nakane, T., Forsberg, B.O., Kimanius, D., Hagen, W.J., Lindahl, E., and Scheres, S.H. (2018). New tools for automated high-resolution cryo-EM structure determination in RELION-3. Elife *7*.

5 Manuscript 2

5.1 Kank2 activates talin, reduces force transduction across integrins and induces central adhesion formation

Zhiqi Sun, Hui-Yuan Tseng, Steven Tan, Fabrice Senger, Laetitia Kurzawa, Dirk Dedden, Naoko Mizuno, Anita A. Wasik, Manuel Thery, Alexander R. Dunn and Reinhard Fässler
Nature Cell Biology (2016) vol. 18, 941–953

During my PhD study I was able to support a project of Zhiqi Sun about the role of Kank2 in focal adhesions. The study used a novel integrative adhesome analysis, which combined focal adhesion enrichment with the interactome of the integrin tail and identified the evolutionary conserved Kank family as adhesome components. The study describes that Kank2 localizes around the lateral border of FA and forms a sub-compartment, named the FA-belt in the center of sliding adhesions. There, Kank can directly interact with talin's R7 domain via its conserved N-terminal KN motif and induce both talin's and subsequently integrin's activity. Furthermore Kank binding to talin has a reducing effect on talin's actin binding capabilities, which overall weakens the link between talin and the actomyosin machinery. This leads to reduced integrin-ligand bond strength and can cause slippage between the ligand and integrin. This induces adhesion sliding and lowers the cells migration speed. This study assigns Kank2 with a role as talin activator, which has an additional function in decreasing the talin-actomyosin link to negatively regulate cell migration velocity. My major contribution to this study was the purification of proteins and protein fragments of talin and Kank2 for *in vitro* assays.

nature cell biology

Kank2 activates talin, reduces force transduction across integrins and induces central adhesion formation

Zhiqi Sun[1], Hui-Yuan Tseng[1], Steven Tan[2], Fabrice Senger[3], Laetitia Kurzawa[3], Dirk Dedden[1], Naoko Mizuno[1], Anita A. Wasik[1], Manuel Thery[3], Alexander R. Dunn[2] and Reinhard Fässler[1,4]

Integrin-based adhesions play critical roles in cell migration. Talin activates integrins and flexibly connects integrins to the actomyosin cytoskeleton, thereby serving as a 'molecular clutch' that transmits forces to the extracellular matrix to drive cell migration. Here we identify the evolutionarily conserved Kank protein family as novel components of focal adhesions (FAs). Kank proteins accumulate at the lateral border of FAs, which we term the FA belt, and in central sliding adhesions, where they directly bind the talin rod domain through the Kank amino-terminal (KN) motif and induce talin and integrin activation. In addition, Kank proteins diminish the talin–actomyosin linkage, which curbs force transmission across integrins, leading to reduced integrin–ligand bond strength, slippage between integrin and ligand, central adhesion formation and sliding, and reduced cell migration speed. Our data identify Kank proteins as talin activators that decrease the grip between the integrin–talin complex and actomyosin to regulate cell migration velocity.

Mesenchymal cell migration on the extracellular matrix (ECM) is crucial for embryonic development, wound healing and tumour metastasis. It commences with the formation of a lamellipodium at the cell leading edge, which is stabilized by numerous small and short-lived integrin-containing nascent adhesions (NAs)[1]. As cells migrate, a few NAs mature into larger focal adhesions (FAs) in the lamella, which associate with the actomyosin cytoskeleton and apply traction forces against the ECM necessary to move the cell forward[2].

Integrins are core components of cell–matrix adhesion sites. They are α/β heterodimers that undergo a conformational change before they bind ligands (termed integrin activation), cluster and recruit numerous proteins to their cytoplasmic domains. A hallmark of integrin-mediated adhesion is that the lifetime of integrin–ligand bonds can be flexibly increased when forces are applied to integrins[3]. This property, called force-induced adhesion strengthening, depends on a dynamic association between integrins and F-actin, and is essential for FAs to withstand traction forces that pull the cell forward during cell migration[4]. Consequently, the destabilization of the integrin–F-actin connection or a decline in myosin II activity decreases force transmission across FAs and shortens the lifetime of integrin–ligand bonds, resulting in slippage between integrin and ligand, adhesion sliding, reduced traction forces and a drop in migration speed[5]. The association between integrins and F-actin occurs indirectly through integrin- and/or F-actin-binding proteins such as talin and vinculin[6], which serve as a 'molecular clutch' that couples traction and actin-driven forces in space and time[7–11].

Talin consists of an amino-terminal FERM (protein 4.1, ezrin, radixin, moesin) domain, also called the talin head domain (THD), and a carboxy-terminal rod domain with 13 helical bundles (R1–R13)[12]. The THD binds β-integrin tails and mediates integrin activation. The rod domain contains binding sites for F-actin, vinculin and the Rap1–GTP-interacting adapter molecule (RIAM)[6]. Talin cycles between cytosol, where it remains in an auto-inhibited form[13], and plasma membrane, where it activates integrins and links integrins to F-actin[14,15]. Talin activation can be induced by RIAM binding to the R8 domain[16–18], phosphatidylinositol 4,5-bisphosphate synthesized by a FA-associated splice variant of phosphatidylinositol-4-phosphate 5-kinase type Iγ (PIPKIγ90)[15,19] and the actin retrograde flow, probably by unleashing the talin rod from the THD[20,21]. The cell-type-restricted integrin activation defects in RIAM-deficient mice and normal integrin activation in PIPKIγ90-deficient mice[22–24] suggest that additional talin activators probably exist.

[1]Max Planck Institute of Biochemistry, 82152 Martinsried, Germany. [2]Department of Chemical Engineering, Stanford University, Stanford, California 94305, USA. [3]CytoMorpho Lab, Biosciences & Biotechnology Institute of Grenoble, UMR5168, CEA/INRA/CNRS/Université, 38054 Grenoble-Alpes, Grenoble, France. [4]Correspondence should be addressed to R.F. (e-mail: faessler@biochem.mpg.de)

Received 11 December 2015; accepted 19 July 2016; published online 22 August 2016; DOI: 10.1038/ncb3402

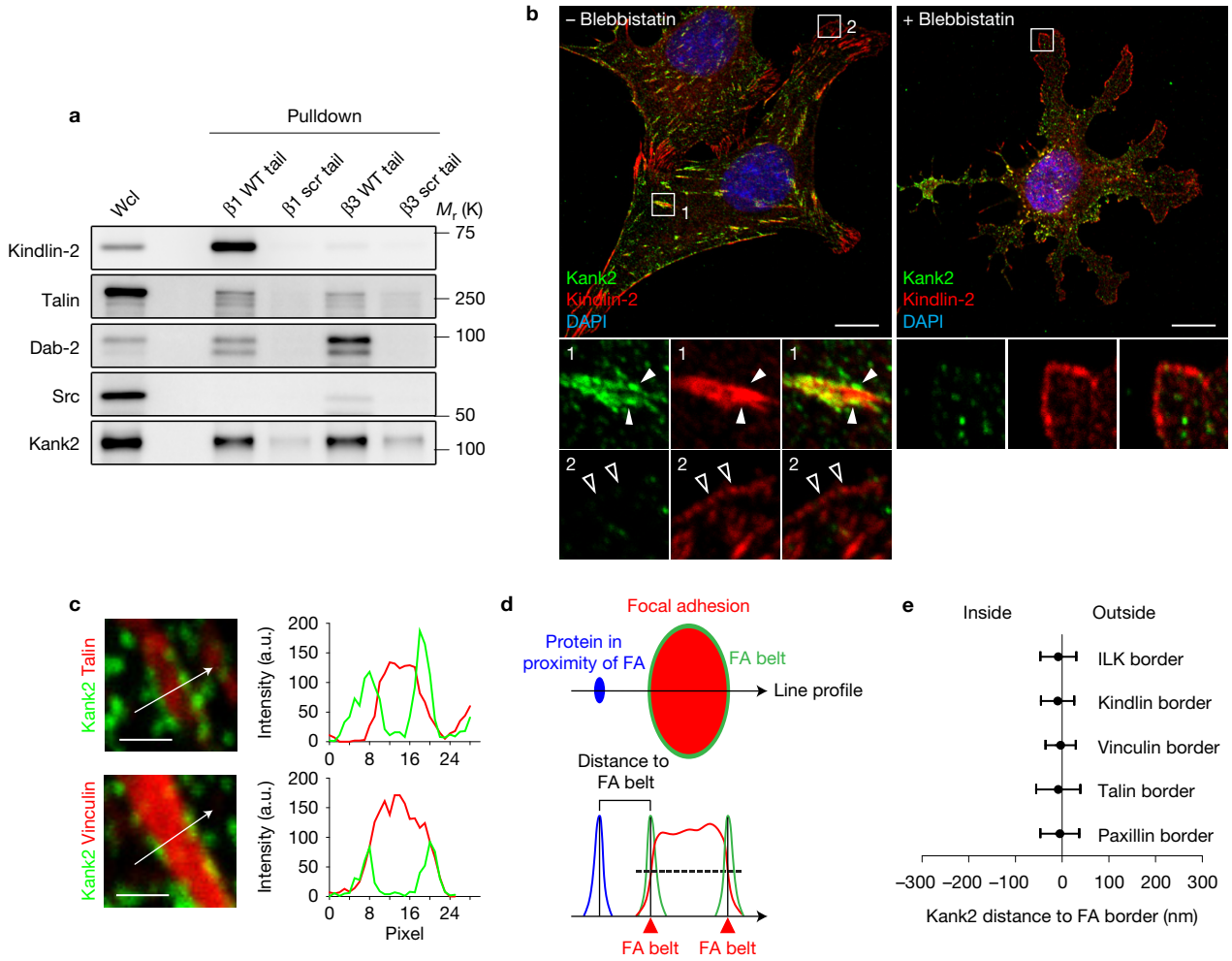

Figure 1 Kank2 is a novel FA protein. (**a**) Western blot showing kindlin-2, talin-1, Dab-2, Src and Kank2 binding to biotinylated β1 and β3 integrin tail peptides. Peptides with scrambled amino-acid sequences (β1 scr tail; β3 scr tail) were used as negative controls. WT, wild type. Wcl, whole cell lysate. (**b**) Mouse fibroblasts seeded on FN for 3 h in the presence or absence of blebbistatin and immunostained for Kank2 (green) and kindlin-2 (red). Full arrowheads indicate Kank2-positive puncta along the FA border; open arrowheads indicate NAs. Scale bar, 10 μm. (**c**) Line profile analysis of cells immunostained for Kank2 and talin or vinculin along depicted line scans. Scale bar, 1 μm. (**d**) Definition of the FA belt at the lateral FA border and the distance from the FA border to proteins in proximity to the FA (outside of FAs) along the depicted line scan. (**e**) Kank2-positive puncta localize to the FA border defined by ILK, kindlin-2, vinculin, talin and paxillin (mean ± s.d.; $n = 8$ FAs for each marker, data pooled from eight cells). Unprocessed original scans of blots are shown in Supplementary Fig. 9.

In the present paper, we identified the evolutionarily conserved Kank protein family as novel FA proteins. They consist of four members (Kank1–4) that are characterized by a Kank N-terminal motif (KN), several central coiled-coil domains and C-terminal ankyrin (Ank) repeats[25]. The single Kank orthologue in worms, VAB19, controls epidermis–muscle attachment[26], neuronal migration[27] and basement membrane remodelling[28]. Mutations in mammalian Kanks have been associated with cerebral palsy type 2, spastic quadriplegia (CPSQ2)[29] and nephrotic syndrome[30]. Kank1 can bind liprin-β1 through a coiled-coil domain and Kif21a through the Ank repeats, and restrict microtubule (MT) outgrowth at the cell cortex and suppress stress fibre formation[31,32]. We report here that Kank2 localizes to the lateral border of FAs (termed the FA belt) and central adhesions, binds the talin rod through the KN motif, promotes talin and integrin activation, and interferes with F-actin binding to the talin rod, which suppresses mechanical force transmission across activated integrins, leading to adhesion sliding and reduced cell migration.

RESULTS

Kank2 is a novel FA protein

To identify novel, β1 integrin tail-associated adhesome proteins, we compared our published FA-enriched proteome (adhesome)[33] with the β1 integrin tail peptide interactome[34] (Supplementary Fig. 1a). Talin, kindlin-2 and the ILK, PINCH, parvin (IPP) complex were enriched in the adhesome and the β1 tail interactome, whereas Dab-2 and SNX17[35], which bind integrin tails during endosomal trafficking, were not enriched in the adhesome. Interestingly, Kank2 was also enriched in the adhesome and β1 tail interactome (Supplementary Fig. 1a). Unlike kindlin-2, which preferentially bound the β1 tail, or Src and Dab-2, which preferentially bound the β3 tail, Kank2 and talin bound β1 and β3 tails equally well (Fig. 1a). Immunostaining

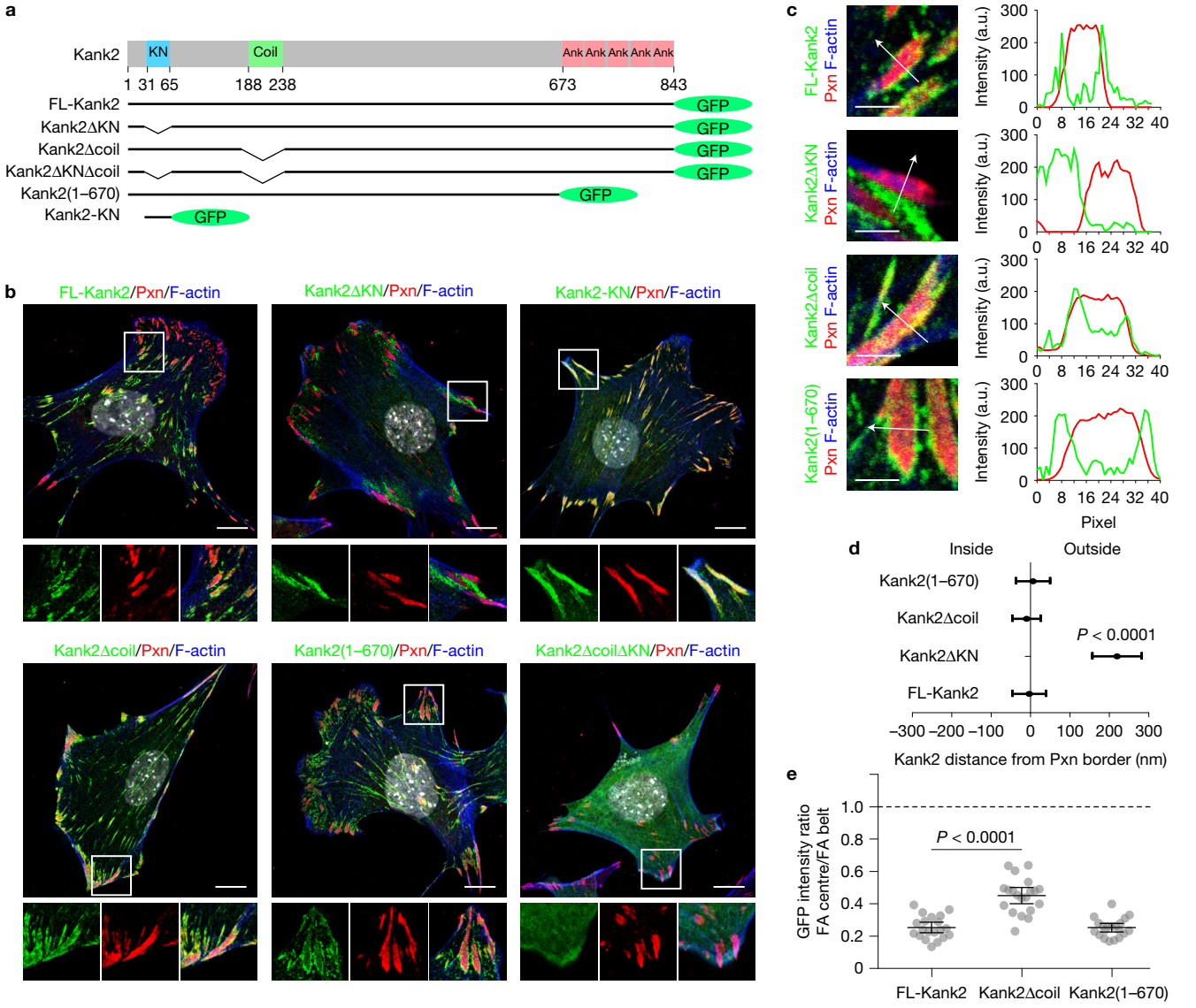

Figure 2 Kank2 is targeted to FAs through the KN motif. (**a**) Domain organization of the Kank2 protein and illustration of GFP-tagged Kank2 truncation/deletion mutants. (**b**) Staining of paxillin (Pxn), F-actin (phalloidin), GFP-tagged Kank2 and DAPI (grey). Scale bar, 10 μm. (**c**) Line profile analysis of GFP-tagged FL-Kank2, Kank2ΔKN, Kank2Δcoil and Kank2(1–670) together with Pxn. Scale bar, 1 μm. (**d**) Line profile quantification of the distance between FL-Kank2, Kank2ΔKN, Kank2Δcoil and Kank2(1–670) to the FA border (mean ± s.d.; $n=8$ FAs for each Kank2 construct, pooled from eight cells; P value calculated using Student's t test). (**e**) Ratios between fluorescence intensities within the FA centre and on the FA belt for FL-Kank2, Kank2Δcoil and Kank2(1–670) (mean ± s.d.; $n=20$ FAs for each Kank2 construct pooled from 10 cells; P value calculated using one-way ANOVA Tukey test).

of fibronectin (FN)-seeded, immortalized mouse fibroblasts revealed that endogenous Kank2 localized to puncta at the outer border of mature kindlin-2- and talin-positive FAs behind the lamella (Fig. 1b, arrowheads, Supplementary Fig. 1c) and to thin, elongated central adhesions (Fig. 1b and Supplementary Fig. 1b), and was absent from NAs and small FAs of the lamella (Fig. 1b, open arrowheads). Blebbistatin-treated cells also lacked Kank2 in kindlin-2-positive NAs of protruding cell membranes (Fig. 1b). The recruitment of Kank2 to the FA border was pronounced in cells cultured on FN-coated crossbow-shaped micropatterns (Supplementary Fig. 1d). Line profile analysis revealed that the Kank2 puncta peaked at the outer FA border, where canonical FA proteins (talin, kindlin-2, ILK, paxillin and vinculin) showed ~50% of their plateau intensity (Fig. 1c–e). We termed this unrecognized FA compartment the 'FA belt'.

Co-immunostaining for β1 and β3 integrins revealed that β3 integrins co-localized with paxillin in the core of mature FAs, whereas total and active (labelled with the activation epitope-reporting 9EG7 antibody) β1 accumulated in FA belts and central adhesions (Supplementary Fig. 1e–g). These data show that mature FAs are surrounded by a Kank2- and β1 integrin-enriched belt.

Kank2 is targeted to FAs through the KN motif

To determine how Kank2 is recruited to the FA belt, we generated green fluorescent protein (GFP)-tagged full length (FL)- Kank2 and

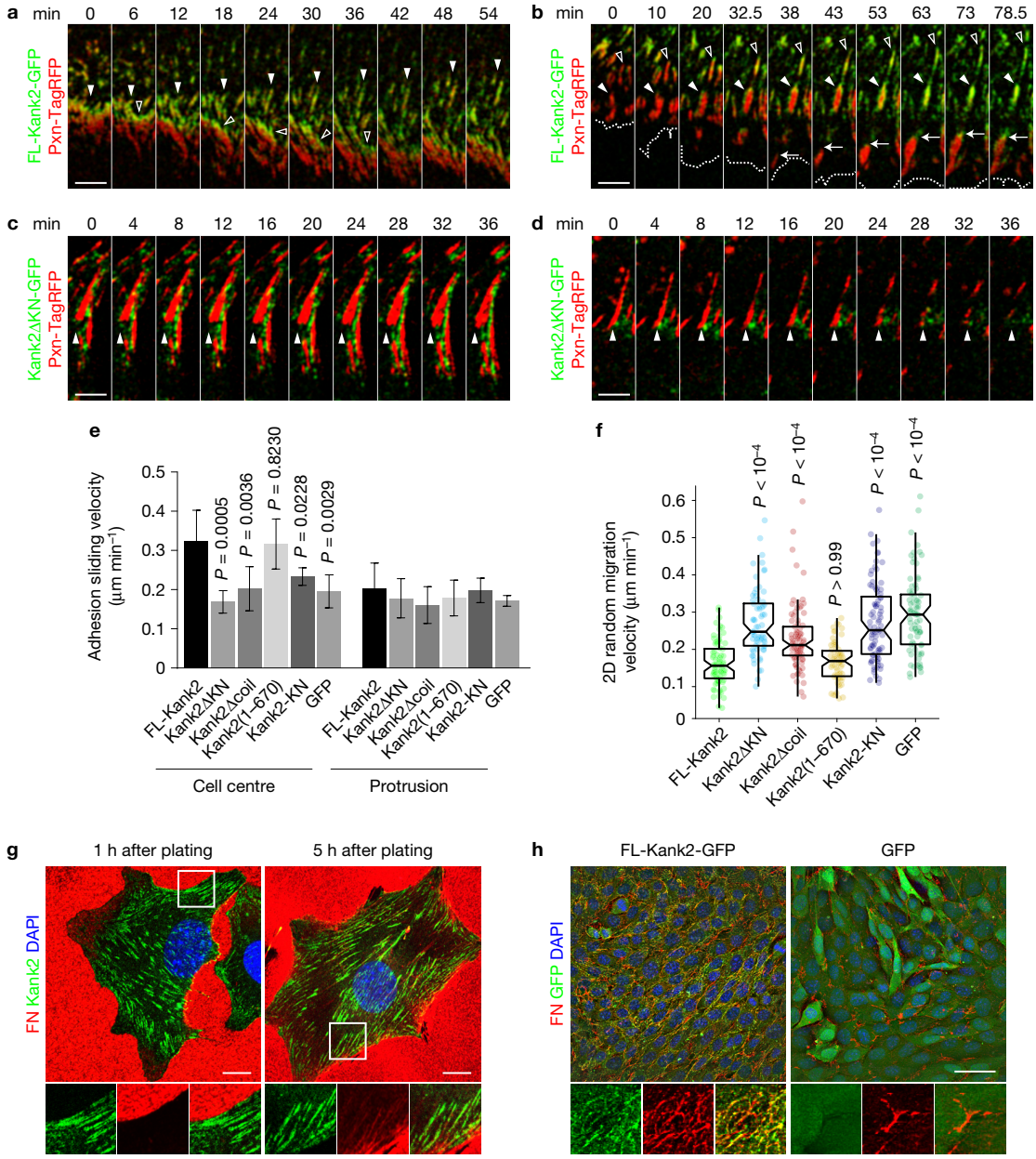

Figure 3 Kank2 curbs cell migration by inducing adhesion sliding. (**a**) Time-lapse images of peripheral FAs in Kank2-depleted fibroblasts stably expressing FL-Kank2-GFP and paxillin-TagRFP (Pxn-TagRFP) 45 min after plating on FN. Arrowheads highlight recruitment of Kank2 to proximal borders of FAs (full arrowheads) and the developing sliding adhesions (open arrowheads). (**b**) Time-lapse images of cells during the migration phase 4 h after plating on FN. Full arrows highlight the recruitment of Kank2-GFP to proximal borders of mature FAs behind the lamella, and open arrowheads highlight the dynamic formation of the Kank2-positive FA belt followed by conversion into thin, elongated sliding adhesions. Dashed lines indicate the cell leading edge. (**c**,**d**) Time-lapse images of peripheral FAs in Kank2-depleted cells stably expressing Kank2ΔKN-GFP and Pxn-TagRFP 45 min after plating on FN. Arrowheads highlight the proximal border of a stable FA (**c**) and disassembling FA (**d**) behind the lamella. Scale bars in **a**–**d**, 5 μm. (**e**) Sliding velocities of central adhesions and FAs from indicated cells (mean ± s.d.; $n=5$ cells pooled from three independent experiments, >400 central adhesions and >100 peripheral adhesions analysed for each condition). (**f**) 2D random migration velocities on FN (dot plot and box plot with median, 95% confidence interval (CI) notch, first–third quantile box and 5th–95th percentile whiskers; n between 60 and 90 cells for each cell line; data aggregated over four independent experiments). P values calculated using one-way ANOVA Tukey test in **e** and Kruskal–Wallis test in **f**. (**g**) Kank2-depleted cells re-expressing FL-Kank2-GFP were plated on FN-coated (10 μg ml^{-1}) coverslips for 1 h or 5 h and immunostained for FN and DAPI. Scale bar, 10 μm. (**h**) Kank2-depleted cells re-expressing FL-Kank2-GFP or GFP control were seeded on FN-coated (10 μg ml^{-1}) coverslips for 12 h at confluence and immunostained for FN and DAPI. Maximal intensity projection of z-stack image series. Scale bar, 50 μm.

deletion constructs of Kank2 lacking evolutionarily conserved domains (Fig. 2a): Kank2ΔKN-GFP lacking the KN motif; Kank2Δcoil-GFP lacking the liprin-β1-binding coiled-coil domain[31]; Kank2(1–670)-GFP lacking the Kif21a-binding Ank repeats[31] and Kank2ΔKNΔcoil-GFP lacking both the KN motif and the coiled-coil domain. The Kank2 constructs were stably expressed in

Kank2-depleted mouse fibroblasts (Supplementary Fig. 2b), which expressed mainly Kank2 (Supplementary Fig. 2a–c).

FL-Kank2-GFP also localized to the belt of paxillin-positive mature FAs and to central adhesions (Fig. 2b). In line with a previous report[31], we also found Kank2 adjacent to FAs in liprin-β1- and ELKS-enriched regions (Supplementary Fig. 3a–c), which capture MT plus ends and promote exocytosis. In contrast, Kank2ΔKN-GFP was absent from FA belts or central adhesions and instead accumulated in liprin-β1- and ELKS-positive regions adjacent to but clearly away from FA belts (Fig. 2b, and Supplementary Fig. 3a,b), as shown by line profile analyses (Fig. 2c,d). Although both Kank2Δcoil-GFP and Kank2(1–670)-GFP showed enrichment on FA belts (Fig. 2b–d), Kank2Δcoil-GFP also penetrated the FA core (Fig. 2e), indicating that the coiled-coil domain contributes to the exclusion of Kank2 from the FA core. Interestingly, Kank2 recruited liprin-β1 through the coiled-coil domain to FA belts, whereas ELKS always localized to the vicinity of the belt (Supplementary Fig. 3a–c). Kank2ΔKNΔcoil-GFP was diffusely distributed throughout the cytosol, whereas the GFP-tagged KN polypeptide completely overlapped with paxillin in all adhesions, including the small, peripheral NAs (Fig. 2b). These results indicate that the KN motif localizes Kank2 to FA belts and central adhesions and that additional protein regions exclude Kank2 from the FA core.

Peptide pulldowns revealed that FL-Kank2-GFP and Kank2-KN-GFP, but not Kank2ΔKN-GFP or GFP, associated with β1 integrin tails (Supplementary Fig. 3d,e). To investigate whether Kank1, Kank3 and Kank4 also localize to the belt, they were tagged with GFP and expressed in Kank2-depleted fibroblasts at similar levels as judged by GFP intensities. Kank1-GFP and Kank3-GFP localized to FA belts, whereas Kank4-GFP associated with FAs with additional cytoplasmic distribution (Supplementary Fig. 3f).

Kank2 inhibits cell migration by inducing adhesion sliding

To unravel how Kank2 is recruited to FA belts, we carried out live cell imaging of paxillin-TagRFP (red fluorescent protein) and Kank2-GFP in Kank2-depleted fibroblasts. During isotropic cell spreading on FN, Kank2-containing puncta were visible in the proximity of FAs. A few minutes after the assembly of radial FAs, Kank2 puncta appeared at their proximal tips pointing to the cell centre, from where Kank2 spread along the FA belt during the following minutes (Supplementary Video 1 and Supplementary Fig. 4a). After cell polarization (45 min after plating), Kank2 puncta continued to accumulate at the proximal border of FAs (Supplementary Video 2 and Fig. 3a), from where Kank2- and paxillin-positive, thin and elongated adhesion structures developed and moved with an average speed of ∼0.3 μm min^{-1} into the cell centre (Supplementary Video 2 and Fig. 3a). In migrating cells (4 h after plating), Kank2-GFP was recruited to the proximal tips of mature FAs and then gradually spread along the FA belt, while it remained absent from NAs in lamellipodia and FAs of the lamella (Supplementary Video 3 and Fig. 3b). The Kank2-positive FA belt formation correlated with the disassembly of the FA cores and the conversion of the FA belts into thin and motile adhesions (Supplementary Video 3 and Fig. 3b). In Kank2ΔKN-GFP-expressing cells, Kank2ΔKN-GFP-positive puncta moved to the proximity of FAs but never entered the FA belt (Supplementary Video 4 and Fig. 3c, closed arrowheads). Moreover, FAs failed to elongate and slide, and the few central adhesions that formed remained stationary (Supplementary Video 4 and Fig. 3c). The stationary FAs in Kank2ΔKN-GFP-expressing cells disassembled behind the lamella (Fig. 3d) with similar rates as in cells expressing FL-Kank2 (Supplementary Video 4 and Supplementary Fig. 4b,c), indicating that adhesion sliding is not caused by adhesion disassembly.

Our data suggest that Kank2 decorates FA belts in a KN-motif-dependent manner and induces the gliding of belts into the cell centre. To confirm that Kank2 induces adhesion motility, we recorded vinculin-mCherry co-expressed in Kank2-depleted fibroblasts with either GFP-tagged FL or mutant Kank2 (Supplementary Videos 5–10). Overlay of 10 sequential colour-coded vinculin-mCherry frames revealed that central adhesions in FL-Kank-GFP- and Kank2(1–670)-expressing cells appeared as rainbows in overlay images due to their significant displacements, whereas central adhesions of cells expressing Kank2ΔKN-GFP, Kank2Δcoil-GFP, KN-GFP or GFP alone were stationary and appeared white in overlay images (Supplementary Fig. 4d). Single-adhesion tracking revealed that central adhesions in FL-Kank2-GFP- and Kank2(1–670)-expressing cells moved with a sliding velocity of ∼0.3 μm min^{-1}, whereas sliding of central adhesions in cells expressing Kank2ΔKN-GFP, Kank2Δcoil-GFP, KN-GFP or GFP alone was slower (Fig. 3e). Furthermore, over 60% of adhesions in FL-Kank2-GFP- and Kank2(1–670)-GFP-expressing cells slid with rates higher than 0.3 μm min^{-1}, whereas the numbers of fast-sliding adhesions were significantly lower in cells expressing Kank2ΔKN-GFP, Kank2Δcoil-GFP, KN-GFP or GFP alone (Supplementary Fig. 4e). Consistent with the absence of Kank2 from adhesions in the protruding front, the sliding velocity of adhesions in protrusion was unaffected by the FL or mutant Kank2 (Fig. 3e).

Adhesion sliding correlates with reduced cell migration speed[7]. Indeed, both Kank2-depleted cell lines showed higher migration velocities when compared with controls (Supplementary Fig. 4f). Furthermore, expression of FL-Kank2-GFP and Kank2(1–670)-GFP but not Kank2ΔKN-GFP, Kank2Δcoil-GFP, KN-GFP or GFP alone in Kank2-depleted fibroblasts decreased migration speed (Fig. 3f). Consistent with the absence of Kank2 from the cell front, cell spreading was unaffected in Kank2-depleted cells or cells expressing Kank2 constructs (Supplementary Fig. 4g).

Centripetal α5β1 integrin translocation was proposed to mediate FN fibrillogenesis[36]. We noticed that Kank2-positive central adhesions formed within 1 h of plating on FN before FN fibrillogenesis occurred, whereas, 5 h after cell seeding, thin FN fibrils, frequently decorated with Kank2, extended from the cell periphery to the cell centre (Fig. 3g). After overnight culture, FL-Kank2-GFP-expressing cells assembled extensive networks of elongated and branched FN fibrils, compared with the few and thickened FN fibrils in GFP-expressing Kank2-depleted cells (Fig. 3h).

Kank2 induces integrin–ligand-bound slippage

Adhesion sliding can be due to ECM cleavage by metalloproteinases (MMPs)[37] or turnover of integrin–ligand complexes[38]. Treatment of FL-Kank2-GFP-expressing cells with the pan-MMP inhibitor Gm6001 did not affect adhesion sliding (Supplementary Fig. 4h). To analyse integrin turnover, we photobleached the C-terminally GFP-tagged α5 integrin (Itga5-GFP) in entire adhesions of Kank2-depleted cells expressing FL-Kank2-mCherry or an empty control

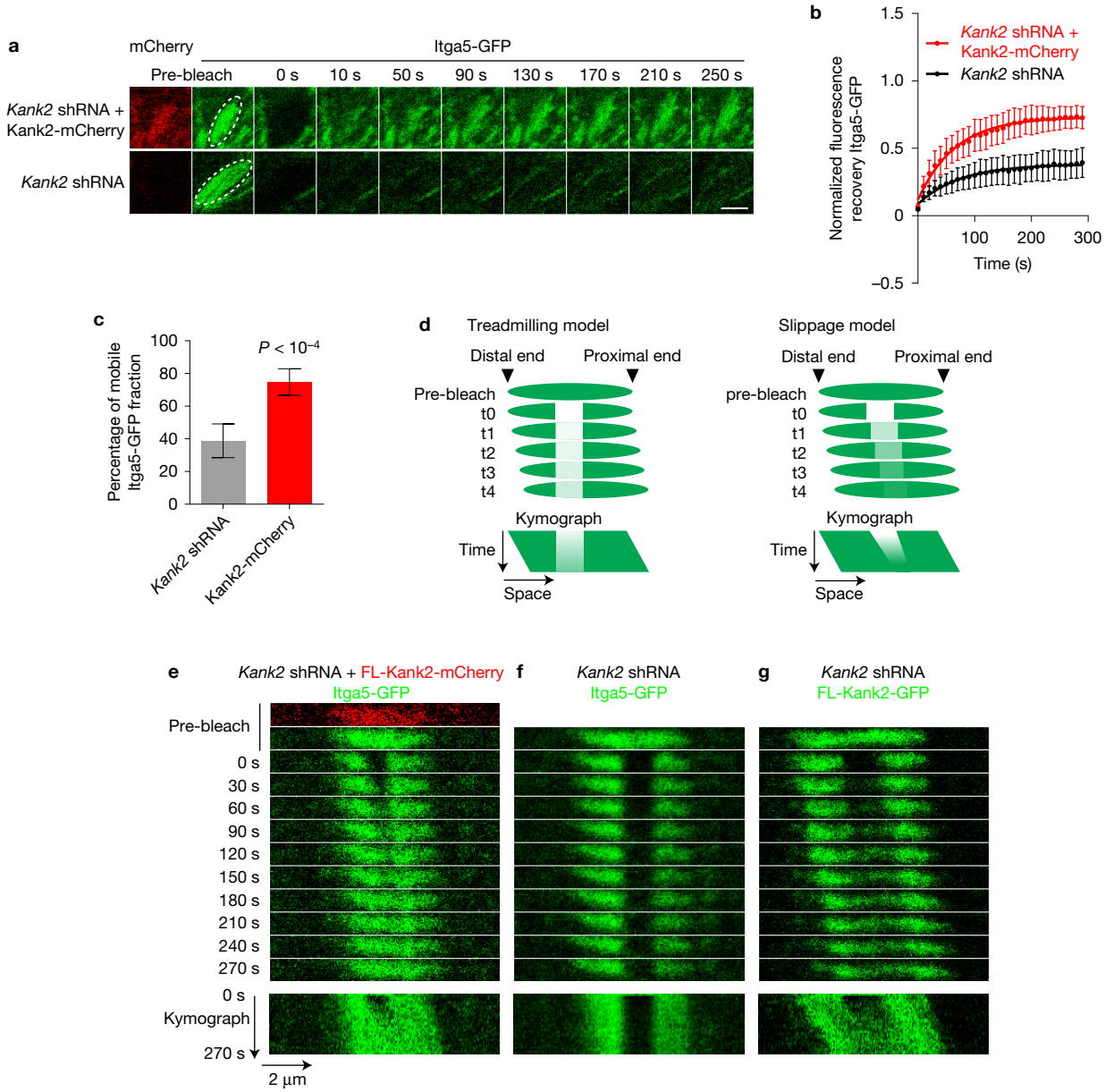

Figure 4 Adhesion sliding occurs at the interface between integrin and ligand. (**a**) Still images from representative time-lapse FRAP experiments with Itga5-GFP in Cherry-tagged FL-Kank2 or empty-vector-expressing fibroblasts. A pre-bleach image shows that Kank2-mCherry and Itga5-GFP co-localized in the region of interest (ROI, white circle). Scale bar, 2 μm (**b**) Fluorescence recovery curves of indicated FRAP experiments. FRAP of Itga5-GFP in central adhesions of Kank2-depleted fibroblasts transduced with either mCherry-tagged FL-Kank2 or empty plasmid. Mean optical intensities in the ROI are normalized to cytosolic background and plotted as percentage of initial intensity before bleaching (mean ± s.d.; $n=8$ independent FRAPs in eight cells for each cell line). Fluorescence recovery curves are fitted to a one-phase association model. (**c**) Mobile Itga5-GFP fractions in bleached adhesions (mean ± s.d.; $n=8$ independent FRAPs in eight cells for each cell line; P value calculated using Students t test). (**d**) Adhesion treadmilling (left) and integrin slippage models predict different experimental results in time-lapse images and kymographs on photobleaching of middle segments in sliding adhesions. (**e**–**g**) Time-lapse images (upper panel) and kymograph (lower panel) of Itga5-GFP (**e**,**f**) or Kank2-GFP (**g**) after photobleaching of the GFP signal in the middle segments of adhesion sites in Kank2-depleted fibroblasts expressing Kank2-mCherry and a low level of Itga5-GFP (**e**), empty plasmid (**f**) or Kank2-GFP (**g**).

plasmid, and found that FL-Kank2 increased the mobile fraction of α5 integrin from about 40% to about 70% (Fig. 4a–c). To distinguish slippage between integrin and ligand from adhesion treadmilling as the cause of adhesion sliding, we photobleached Itga5-GFP in the middle segment of an adhesion and measured GFP recovery. In the case of treadmilling defined by integrin recruitment to the proximal end and release from the distal ends the bleached middle segment should remain stationary (Fig. 4d, left panel), whereas in the case of slippage between integrin and ligand the bleached middle segment should move in the direction of the adhesion sliding, at least during the short time window before integrins are turned over (Fig. 4d, right panel). The experiment revealed

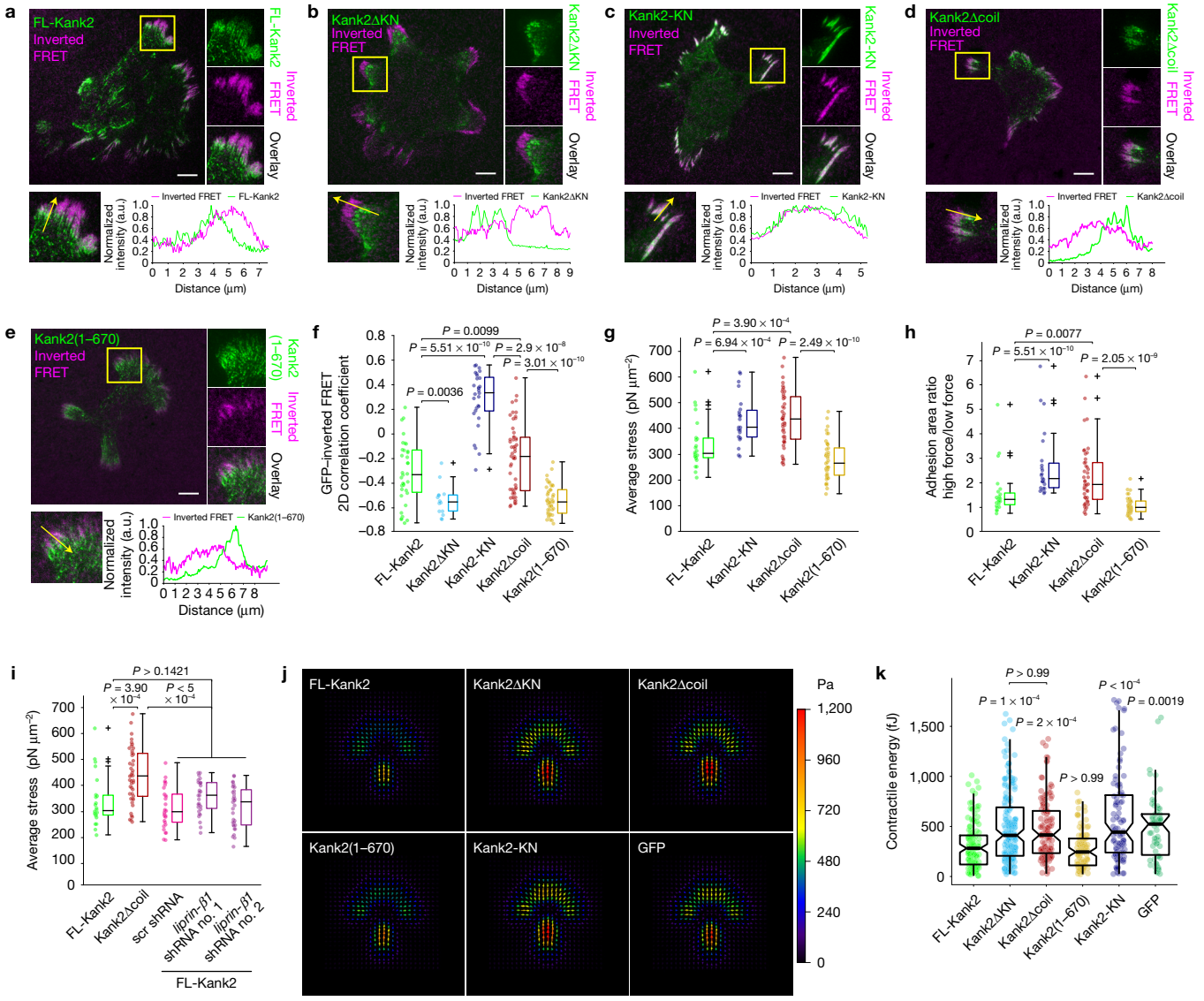

Figure 5 Kank2 impairs force transmission across integrins. (**a**–**e**) GFP and inverted FRET signals in Kank2-depleted cells expressing GFP-tagged FL-Kank2, Kank2ΔKN, Kank2-KN, Kank2Δcoil and Kank2(1–670) seeded on FRET-based RGD tension sensors for 5 h. Split channels of boxed regions are shown on the right-hand side and line profiles of indicated adhesions in the boxed region below. Scale bar, 10 μm. (**f**) 2D correlation coefficient between GFP and inverted FRET signals (dot plot and box plot; FL-Kank2, $n=35$ cells; Kank2ΔKN, $n=14$ cells; Kank2-KN, $n=29$ cells; Kank2Δcoil, $n=45$ cells; Kank2(1–670), $n=42$ cells; data aggregated from three independent experiments for each condition; *P* values were calculated using the Wilcoxon rank sum test; crosses represent outliers). (**g**) Force exerted by adhesions at the cell periphery in cells expressing indicated constructs. (**h**) Ratios between adhesion areas with high tension ($\geq$250 pN μm^{-2}) and adhesion areas with low tension (<250 pN μm^{-2}) were calculated in cells expressing indicated constructs. (**i**) Force exerted by adhesions at the cell periphery in Kank2-depleted cells expressing FL-Kank2 or Kank2Δcoil, or FL-Kank2 together with a scramble (scr) shRNA or two independent shRNAs against liprin-β1 (for **g**–**i**, dot plot and Tukey box plot; FL-Kank2, $n=24$ cells; Kank2-KN, $n=24$ cells; Kank2Δcoil, $n=45$ cells; Kank2(1–670), $n=43$ cells; FL-Kank2 scr shRNA, $n=30$ cells; FL-Kank2 *liprin-β1* shRNA no. 1, $n=31$ cells; FL-Kank2 *liprin-β1* shRNA no. 2, $n=33$ cells; data aggregated from three independent experiments for each condition; *P* values were calculated using the Wilcoxon rank sum test; crosses represent outliers). (**j**) Average traction-force fields of indicated cells on FN-coated micropatterns with 35 kPa rigidity. Arrows indicate force orientation, and colour and length represent local stress magnitude in pascals. (**k**) Contractile energy of individual cells (dot plot and box plot with median, 95% CI notch, first–third quantile box and 5th–95th percentile whiskers; FL-Kank2, $n=125$; Kank2ΔKN, $n=168$; Kank2Δcoil, $n=124$; Kank2(1–670), $n=98$; Kank2-KN, $n=98$; GFP only, $n=62$ cells; data aggregated over three to six independent experiments for each cell line; *P* values calculated using Kruskal–Wallis test).

slippage movement of integrins in Kank2-positive adhesions, but not treadmilling (Fig. 4e). Similarly, photobleaching of FL-Kank2-GFP in the middle segment of a sliding adhesion revealed the same co-sliding of bleached and unbleached areas (Fig. 4g). In contrast, photobleaching of Itga5-GFP in the middle segment of a stationary adhesion in Kank2-depleted cells revealed that neither bleached nor unbleached regions slid (Fig. 4f). These findings indicate that Kank2 destabilizes integrin–ligand complexes, leading to sliding of the Kank2–integrin complex along the ECM and the formation of FN fibrils.

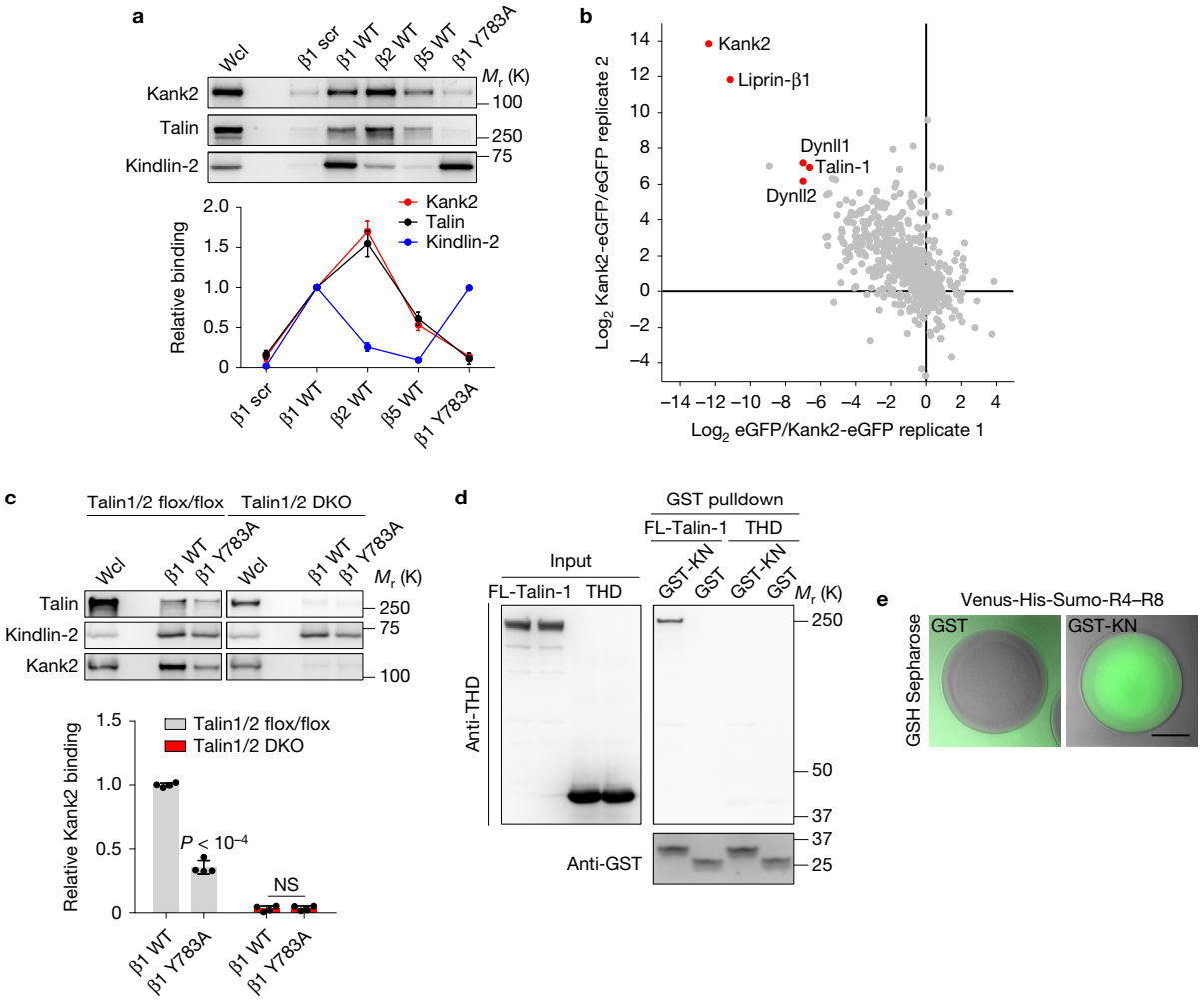

Figure 6 Kank2 directly binds the talin rod. (**a**) Western blot (upper panel) and densitometric analysis (lower panel) of Kank2, kindlin-2 and talin binding to biotinylated wild-type (WT) β1, β2, β5 integrin tails, Y783A-substituted β1 integrin tail (β1 Y783A) and scrambled peptides (β1 scr). Data is illustrated as the mean ± s.d. Wcl, whole cell lysate. (**b**) Scatter plot of label-free quantification (LFQ)-intensity ratios of Kank2-GFP and GFP immunoprecipitates. Specific interactions displaying high Kank2-GFP to GFP and low GFP to Kank2-GFP ratios in two independent replicates are highlighted in red. eGFP, enhanced green fluorescent protein. (**c**) Western blot (upper panel) and densitometric analysis (lower panel) of Kank2, kindlin-2 and talin binding to β1 wild-type and β1 Y783A tails using either talin-1/2 flox/flox or talin-1/2-deficient cells (talin-1/2 double knockout (DKO); mean ± s.d.; $n = 4$ independent pulldown experiments; P values were calculated using Student's t test). NS, not significant. (**d**) Representative GST pulldown of recombinant GST-KN or GST pre-incubated with recombinant talin-1 or THD from two independent experiments. (**e**) Representative epifluorescence images of Venus-His-Sumo-tagged talin R4–R8 domain recruited by GST-KN but not GST control to GSH Sepharose beads from two independent experiments. Scale bar, 5 μm. Source data for **c** can be found in Supplementary Table 2. Unprocessed original scans of blots are shown in Supplementary Fig. 9.

Kank2 suppresses force transmission across integrins

A reduced force transmission across integrins can destabilize integrin–ligand bonds. To test this possibility, we plated fibroblasts expressing GFP-tagged FL-Kank2, Kank2ΔKN, Kank2Δcoil, Kank2(1–670), Kank2-KN or GFP alone on RGD peptides conjugated with a Förster resonance energy transfer (FRET)-based molecular tension sensor, which decreases FRET efficiency under tension[39]. To visualize FRET maps recorded by total internal reflection fluorescence (TIRF) microscopy, we inverted the FRET ratios such that bright signals correspond to low FRET ratios and high traction. We found that FL-Kank2 was enriched at proximal borders of tensioned RGD peptide clusters in the cell periphery and in central adhesions with low inverted FRET signals. In contrast, Kank2ΔKN was absent from tensioned RGD ligand clusters in the periphery and the cell centre, whereas the KN polypeptide overlapped with tensioned RGD clusters in the cell periphery and less frequently in the cell centre (Fig. 5a–c). To determine the coincidence between the GFP-tagged proteins and locally generated tension, we calculated the 2D correlation coefficient between the GFP-tagged proteins and inverted FRET signals and found that tension had a negative correlation with FL-Kank2 (−0.33) and Kank2ΔKN (−0.55) and a positive correlation with the KN polypeptide (0.33; Fig. 5f). Moreover, FL-Kank2 significantly decreased the force at peripheral adhesions when compared with the Kank2-KN (Fig. 5g). Furthermore, the ratios between high- (nominal stress of ≥250 pN μm^{-2}) and low-force- (nominal stress of <250 pN μm^2) bearing adhesion areas were significantly decreased

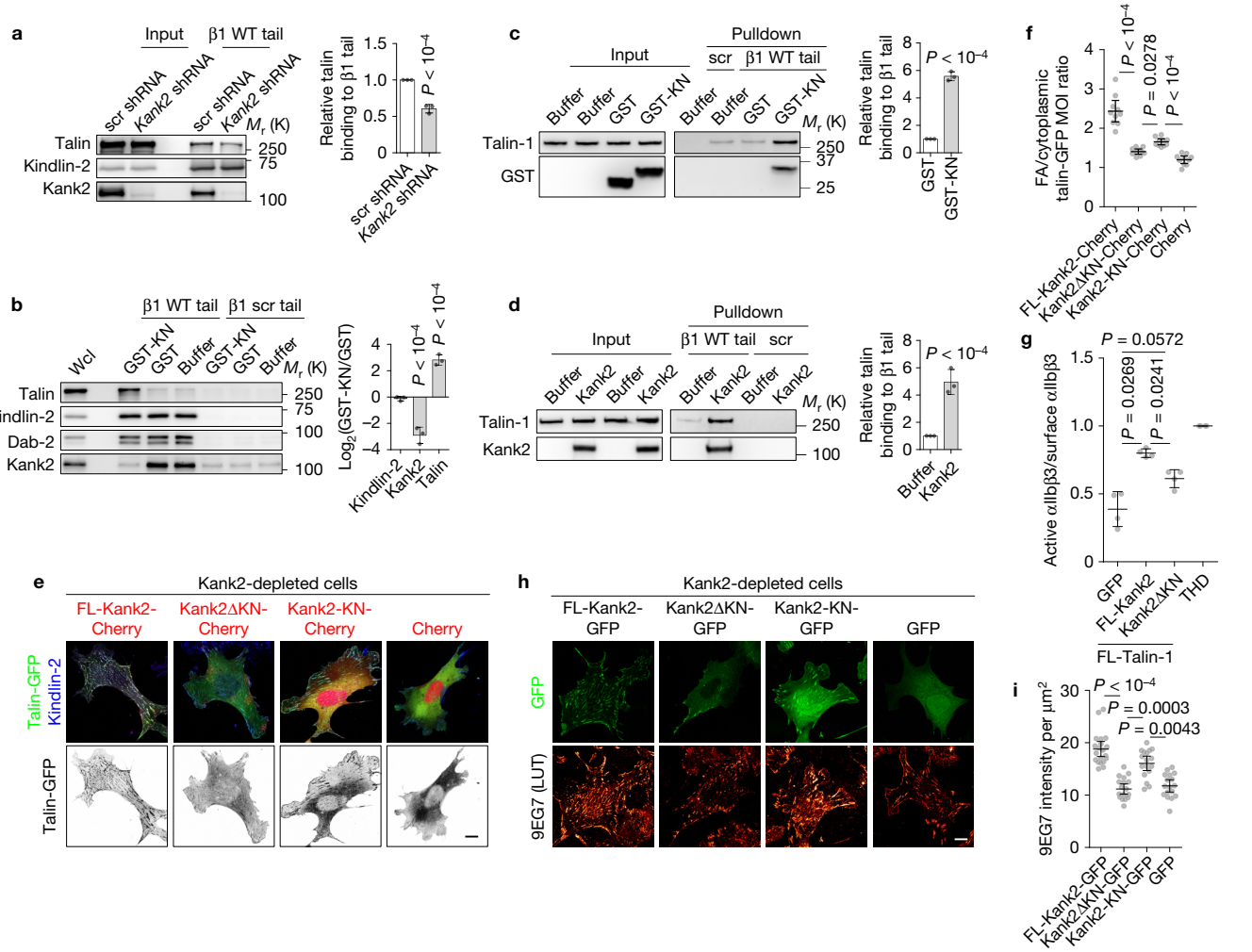

Figure 7 Kank2 induces talin and integrin activation. (**a**) Western blot (left) and densitometric analysis (right) of Kank2, talin and kindlin-2 binding to β1 integrin tail in control (scr shRNA) cells or Kank2-depleted (*Kank2* shRNA) cells (mean ± s.d.; $n = 3$ independent pulldown experiments; *P* values were calculated using Student's *t* test). (**b**) Western blot (left) and densitometric analysis (right) of Kank2, talin, kindlin-2 and Dab-2 binding to β1 integrin tails or scrambled peptide (β1 scr) after addition of recombinant GST-KN or GST (mean ± s.d.; $n = 3$ independent pulldown experiments; *P* values calculated using Student's *t* test). (**c**,**d**) Western blot (left) and densitometric analysis (right) of recombinant talin-1 binding to β1 integrin tail after addition of recombinant GST-KN (**c**) or FL-Kank2 (**d**) (mean ± s.d.; $n = 3$ independent pulldown experiments; *P* values calculated using Student's *t* test). (**e**) Talin-GFP co-expressed with Cherry-tagged FL-Kank2, Kank2ΔKN, Kank2-KN in Kank2-depleted cells and stained for kindlin-2. (**f**) Quantification of talin-1-GFP mean optical intensity (MOI) ratio between kindlin-2-positive adhesion area and kindlin-2-negative cytosolic region in (**e**) (dot plot, mean ± 95% CI; $n = 10$ cells per cell line; *P* values calculated using one-way ANOVA Tukey test). (**g**) Binding of PAC1 antibody reporting active αIIbβ3 integrins normalized to binding of anti-total αIIbβ3 on CHO cells co-expressing talin-1-tagRFP with either Kank2-GFP, Kank2ΔKN-GFP or GFP, or expressing THD only (mean ± s.d.; $n = 4$ independent experiments; *P* values calculated using one-way ANOVA Tukey test). (**h**) Kank2-depleted fibroblasts stably transfected with GFP-tagged FL-Kank2, Kank2ΔKN, Kank2-KN or GFP only (green), seeded on FN and immune-stained with the 9EG7 antibody reporting the exposure of a β1 integrin-specific activation epitope (using orange look-up table (LUT)). (**i**) Signal intensities of 9EG7 staining quantified from (**h**) (dot plot, mean ± 95% CI; $n = 30$ cells per cell line; data aggregated from three independent experiments; *P* values calculated using Kruskal–Wallis test). Scale bars in **e**,**h**, 10 μm. Source data for **a**–**d**,**g** can be found in Supplementary Table 2. Unprocessed original scans of blots are shown in Supplementary Fig. 9.

in FL-Kank2-expressing cells (Fig. 5h), indicating that FL-Kank2 curbs force transmission across adhesion sites. Importantly, deletion of the liprin-β1-binding coiled-coil domain (Kank2Δcoil) but not the deletion of the Kif21a-binding Ank repeats, reduced the negative correlation with the locally generated tension and failed to diminish force transmission across integrins (Fig. 5d–h).

Depletion of liprin-β1 reduced endogenous and overexpressed Kank2 levels (Supplementary Fig. 5a). Although liprin-β1 depletion slightly affected the negative correlation between FL-Kank2-GFP and tension (Supplementary Fig. 5b), force transmission remained unaffected (Fig. 5i and Supplementary Fig. 5c), indicating that the coiled-coil domain in Kank2 regulates force transmission in a liprin-β1-independent manner.

Finally, we confirmed that FL-Kank2 impairs force transmission to ECM-bound integrins with traction-force microscopy (TFM) of our cell lines on FN-coated micropatterns with a rigidity of 35 kPa (ref. 34). In line with the molecular tension sensor experiments, FL-Kank2- and Kank2(1–670)-expressing cells generated significantly

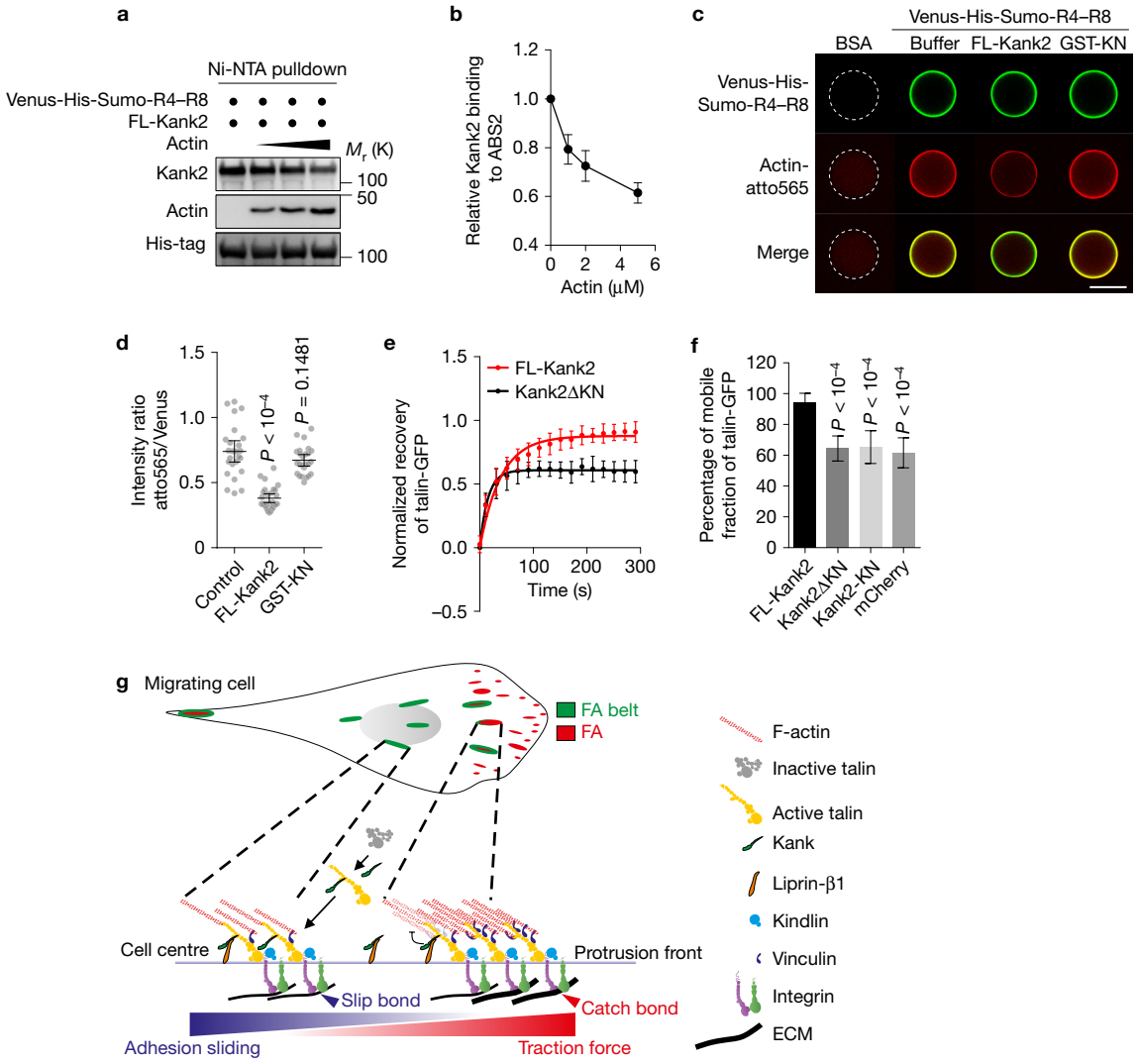

Figure 8 Kank2 decreases F-actin binding to talin-ABS2. (**a**,**b**) Western blot (**a**) and densitometric analysis (**b**) of Kank2 binding to the talin R4–R8 domain in the presence of increasing concentrations of actin (0 μM, 1 μM, 2 μM and 5 μM, mean ± s.d.; $n = 3$ independent pulldown experiments) under polymerization-permissive conditions. (**c**) Representative images of atto565-labelled actin recruited to Ni^{2+}NTA beads coated with bovine serum albumin (BSA) (control) or Venus-His-Sumo-tagged talin R4–R8 domain in the presence of the recombinant GST-KN motif or FL-Kank2 under polymerization-permissive conditions. Scale bar, 100 μm. (**d**) Fluorescence intensity ratios between atto565 and Venus on bead surfaces quantified on the basis of experiments in **c** (dot plot, mean ± 95% CI; $n > 25$ beads per condition; data aggregated from three independent experiments; *P* value calculated using one-way ANOVA Tukey test). (**e**) Fluorescence recovery curves of indicated FRAP experiments. FRAP of talin-1-GFP in central adhesions of Kank2-depleted fibroblasts co-expressing talin-1-GFP and either mCherry-tagged FL-Kank2 or mCherry-tagged Kank2ΔKN. Mean optical intensities in the ROI are normalized to cytosolic background and plotted as percentages of the initial intensity before bleaching (mean ± s.d.). Fluorescence recovery curves are fitted to a one-phase association model. (**f**) Mobile fractions of talin-1-GFP in the bleached adhesions (mean ± s.d.; $n = 10$ independent FRAPs from 10 cells for each condition; *P* value calculated using one-way ANOVA Tukey test). (**g**) Model depicting Kank function in FAs. In migrating cells, Kank2 is absent from adhesion sites of the protrusion front. Behind the lamella, Kank2 is first recruited to the proximal tips of mature FAs, from where it gradually spreads over the entire FA belt. The recruitment of Kank2 to the FA belt is mediated by a direct interaction between the KN motif of Kank2 and the R7 domain in the talin rod. Kank2 displaces F-actin from the talin-ABS2 while simultaneously promoting and/or maintaining talin activation. This dual function of Kank2 permits a partial decoupling of talin-bound, activated integrins from the actomyosin cytoskeleton, leading to diminished force transmission across FAs, reduced traction force, formation of slip bonds between integrins and ligands and the conversion of FA belts into sliding central adhesions. Unprocessed original scans of blots are shown in Supplementary Fig. 9.

less traction force than did cells expressing Kank2ΔKN, Kank2Δcoil, the KN polypeptide or the GFP control (Fig. 5j,k).

Kank2 directly binds the talin rod

To unravel how Kank2 is recruited to the FA belt and suppresses integrin-mediated force transmission, we carried out pulldown experiments with different integrin tail peptides, which revealed that the Kank2-binding profile resembled that of talin but differed from that of kindlin-2 (Fig. 6a). Furthermore, talin-binding-deficient β1 tails (β1 Y783A) pulled down neither Kank2 nor talin, but still kindlin-2 (Fig. 6a), suggesting that talin and Kank2 are co-recruited to integrin tails.

To identify Kank2-interacting proteins that mediate its recruitment to β integrin tails, we immunoprecipitated FL-Kank2-GFP in fibroblasts and determined the interacting proteins by mass spectrometry (MS). Talin-1, dynein light chain isoforms (Dynll1 and Dynll2) and liprin-β1 were identified as binding partners of Kank2 (Fig. 6b). To test whether Kank is recruited to β1 tails in a talin-dependent manner, we carried out β1 tail peptide pulldown in fibroblasts lacking the *Talin-1* and *Talin-2* genes[40] and found that the absence of talin-1 and talin-2 expression abolished Kank2 recruitment to β1 integrin tails (Fig. 6c). Since the FA belt recruitment is KN motif dependent, we purified recombinant glutathione *S*-transferase (GST)-KN, full length talin-1 (FL-talin-1) and the THD (Supplementary Fig. 6a) and carried out GST pulldown experiments, which showed that the GST-KN motif pulled down FL-talin-1 but not the THD (Fig. 6d), indicating that Kank2 binds the talin-1 rod through the KN motif. Expression of different GFP-tagged domains of the talin-1 rod in HEK293 cells followed by co-immunoprecipitation of GST-KN with GFP antibodies revealed that R7R8 domains but not the R8 domain alone associated with the KN polypeptide (Supplementary Fig. 6b). Furthermore, recombinant Venus-tagged talin R4–R8 efficiently bound GST-KN-coupled glutathione beads but not control GST beads (Fig. 6e). These findings indicate that Kank2 directly binds the R7R8 domain of the talin rod through the KN motif.

Kank2 induces talin and β1 integrin activation

The R7R8 domains were shown to bind RIAM, actin and vinculin[41], all of which can induce activation of talin, which in turn binds and activates integrins. To investigate whether Kank2 or KN binding to talin also promotes talin–integrin interactions, we carried out a series of experiments. First, short hairpin RNA (shRNA)-mediated depletion of Kank2 in fibroblasts decreased binding of endogenous talin to β1 integrin tail peptides by about 30% (Fig. 7a), whereas doxycycline-induced expression of FL-Kank2-GFP but not Kank2ΔKN-GFP increased talin binding to β1 integrin tails in a dose-dependent manner (Supplementary Fig. 7a,b). Second, incubation of normal fibroblast lysates with GST-KN or chemically synthesized KN peptide efficiently reduced endogenous Kank2 binding to β1 integrin tail peptides and increased talin binding in a dose-dependent manner, but left kindlin-2 and Dab-2 binding unchanged (Fig. 7b and Supplementary Fig. 7c–e). Third, β1 tails pulled down about five times more recombinant FL-talin in the presence of equal molar GST-KN or recombinant FL-Kank2 (Supplementary Fig. 7f) when compared with GST only (Fig. 7c,d). Fourth, the KN-peptide-mediated activation of FL-talin depended on the THD in full length talin, as it was efficiently blocked by an excess amount of THD domain (Supplementary Fig. 7g,h). Finally, co-expression of talin-GFP and Cherry-tagged FL-Kank2 in Kank2-depleted fibroblasts increased talin-GFP signals in kindlin-2-positive central adhesions and expression of the KN motif promoted talin-GFP localization to peripheral FAs (Fig. 7e,f), whereas Kank2ΔKN- or Cherry-expressing cells had the majority of talin-1-GFP in the cytosol (Fig. 7e,f). Thus Kank2 induces talin activation and binding to integrin β tails.

Since active, integrin-tail-bound talin induces integrin activation, we next tested whether Kank2 promotes integrin activation. The expression of talin-1 together with FL-Kank2-GFP in αIIbβ3-integrin-expressing CHO cells increased binding of the αIIbβ3 integrin activation epitope-reporting PAC1 antibody when compared with cells expressing talin-1 and GFP (Fig. 7g). Importantly, expression of talin-1 and Kank2ΔKN failed to increase PAC1 binding over the talin-1/GFP control (Fig. 7g). Similarly, immunostaining with 9EG7 antibody of FN-adherent Kank2-depleted fibroblasts expressing GFP-tagged FL-Kank2, Kank2ΔKN, Kank2-KN or GFP alone revealed that FL-Kank2-GFP and Kank2-KN-GFP co-localized with active, 9EG7-positive β1 integrins and increased the number of 9EG7-positive adhesion sites, whereas Kank2ΔKN-GFP or GFP alone had no effect on 9EG7 binding (Fig. 7h,i). Altogether, these findings indicate that Kank2 activates talin and integrins in a KN-motif-dependent manner.

Kank2 interferes with F-actin binding to the ABS2 of talin

How does Kank2 binding to talin decrease force transmission across integrins? Kank2 was shown to regulate RhoA and myosin II activities through an association with RhoGDIα in kidney podocytes[30,32]. In contrast to podocytes, however, RhoGDIα was neither identified as a binding partner of FL-Kank2-GFP in the MS-based Kank2 interactome screen nor co-localized with FL-Kank2 in fibroblasts (Supplementary Fig. 8a). Furthermore, similar GTP-bound RhoA and phospho-Ser 19-myosin light chain (pMLC) levels in cells expressing FL-Kank2, Kank2ΔKN, the KN polypeptide or GFP (Supplementary Fig. 8b,c) excluded a role for Kank2 in regulating myosin II activity.

The destabilization of the Talin–F-actin linkage can also decrease force transmission across integrins. Kank2 binds talin in the vicinity of the F-actin-binding site 2 (ABS2). To test whether Kank2 and actin binding to the talin rod is mutually regulated, we incubated recombinant His-tagged talin R4–R8-coated Ni^{2+}-NTA (nitrilotriacetate) beads with FL-Kank2 and actin under polymerization-permissive conditions and observed a dose-dependent inhibition of Kank2 binding to talin R4–R8 by actin (Fig. 8a,b). Consistently, recombinant FL-Kank2 but not GST-KN significantly decreased actin binding to His-tagged talin R4–R8-coated Ni^{2+}-NTA beads (Fig. 8c,d). These results suggest that Kank2 interferes with actin binding to ABS2.

The association of talin with F-actin was shown to immobilize talin in FAs[42,43]. Fluorescence recovery after photobleaching (FRAP) experiments in Kank2-depleted fibroblasts expressing FL-Kank2 or mutant versions of Kank2 showed that FL-Kank2 increased the mobile fraction of talin-GFP from $63.8 \pm 9.0\%$ to $92.4 \pm 7.5\%$ in a 5 min time window (Fig. 8e,f and Supplementary Fig. 8d), whereas neither Kank2ΔKN nor Kank2-KN affected the mobile fraction of talin. These findings confirm that Kank2 destabilizes the talin–F-actin linkage.

DISCUSSION

Kank proteins are defined by a unique KN motif. While a recent study reported that Kank proteins in HeLa cells localize to liprin-β1- and ELKS-containing clusters at the plasma membrane that capture MTs in close proximity to, but always outside FAs[31], we found Kank highly enriched in the β1 integrin tail interactome and the integrin-induced adhesome, pointing to the possibility that Kank proteins also directly function inside FAs. We tested this hypothesis and found that Kank proteins are indeed present in FAs, where they play a dual role: on the one hand they control integrin activity through activating talin, and on the other hand they reduce the talin linkage with the

actomyosin, which leads to reduced force transmission across FAs, increased adhesion sliding and reduced cell migration speed.

Our analysis shows that Kank recruitment to β integrin tails is indirect and occurs through a direct interaction between the KN motif of Kank and the talin R7 domain. The consequence of the Kank–talin interaction is the activation of talin, the binding of the Kank/talin to β integrin tails, integrin activation and integrin–ligand binding. The activation of talin and integrins by Kank is KN motif dependent. In line with this finding, the KN polypeptide is sufficient to induce talin activation and recruitment to β1 integrin tails *in vitro* and to FAs *ex vivo*, and to activate αIIbβ3 and β1 integrins in cells.

Our findings also demonstrate that Kank reduces the cell migration speed by converting FAs at the lamella border into thin and elongated sliding adhesions that glide into the cell centre (Fig. 7). Kank is absent from NAs and becomes recruited to the proximal tip of FAs at the lamella border either by binding to tensed, integrin-bound talin or as a *de novo* assembled Kank2–talin complex. From the proximal FA tips Kank gradually expands around the entire outer FA border, which is followed by the disassembly of the FA core and the gliding of the thin Kank2-positive FA border into the cell centre. We term the outer FA border, to which Kank concentrates during FA conversion, the FA belt. The exclusive localization of the KN-motif-deficient Kank2ΔKN to the previously described liprin-β1- and ELKS-containing clusters and the inability of Kank2ΔKN to induce FA sliding indicate that both FA belt recruitment and FA sliding depend on talin binding. Furthermore, the KN polypeptide also penetrates into the FA centre but fails to induce FA sliding, pointing to the functional importance of additional region(s) in Kank such as the coiled-coil domain.

We also found that Kank binding to talin destabilizes the integrin–actomyosin linkage, leading to decreased force transmission across adhesion sites, which diminishes adhesion strength and traction force, causing integrin–ligand bond slippage, FA sliding and a reduction in migration speed. The destabilization of the integrin–actomyosin linkage occurs with Kank2 binding to the talin rod. Since the KN motif is not sufficient to compete with actin for talin rod binding and for curbing force transmission across integrins, additional region(s) in Kank2 are required to execute these tasks. Such a region could be the coiled-coil domain, whose absence enabled a partial intrusion of the mutant Kank2Δcoil protein into the FA core, impaired the negative correlation with locally produced tension and failed to reduce force transmission across integrins. Mechanistically, the coiled-coil domain could hinder F-actin binding to talin-ABS2 either by oligomerizing Kank2[44] or by recruiting proteins such as liprin-β1. However, the localization of Kank2 to the FA belt and the normal force transduction after liprin-β1 depletion exclude liprin-β1 as potential binding partner of the coiled-coil domain for this function. Alternatively, Kank may bind as-yet-unidentified protein(s) that abrogate(s) talin–integrin tail binding on the FA belt. Such talin binding partners, however, would probably disassemble rather than convert the FA belt into a sliding central adhesion.

The reduced F-actin binding to talin by Kank2 provides a reasonable explanation for the reduced force transmitted across talin–Kank2 complexes to ligand-bound integrins, increased integrin turnover and slippage of integrin ligand bonds, which altogether leads to adhesion sliding and reduced migration speed (Fig. 8g). Consistent with our findings, cells carrying mutations in the ABS2 of talin also show reduced actomyosin coupling to integrin adhesion sites, an increase of the mobile fraction of talin and a decrease of the traction force without affecting cell adhesion or spreading[11]. Kank2 was also shown to bind RhoGDIα, which can potentially inhibit RhoA activity at FA belts and suppress formin-dependent F-actin filament assembly and Rock-mediated myosin II activities[30,32,45]. However, we did not detect RhoGDIα in our MS-based Kank2 interactome or colocalized with Kank2 at FA belts. Furthermore, the normal levels of active RhoA and pMLC in cells expressing FL-Kank2 suggest that RhoA-dependent myosin II activity is not grossly altered, although subtle changes cannot be excluded with our assays.

Kank proteins are also found in liprin-β1- and ELKS-enriched clusters at the plasma membrane where MT plus ends are captured to allow focal exocytosis of MT1-MMP and other cargo[31,46–48], which could also contribute to adhesion sliding and cell migration velocity control. However, Kank2-induced adhesion sliding was not altered when the activities of MMPs were inhibited or MT targeting to FAs was compromised by depleting CLASP[46], indicating that talin–Kank2 complex on FA belts and the ELKS–liprin-β1–Kank2 complex function separately. It is conceivable, however, that Kank proteins coordinate the properties of both compartments and thereby adjust MT dynamics and ECM remodelling with adhesion strengthening. □

METHODS

Methods and any associated references are available in the online version of the paper.

Note: Supplementary Information is available in the online version of the paper

ACKNOWLEDGEMENTS

We thank N. Nagaraj for technical support, and C. Grashoff, O. Rosslier, G. Giannone and R. Böttcher for discussions and reading of the manuscript. The work was supported by the National Institutes of Health R01GM112998 (to A.R.D.), Stanford Graduate Fellowship (to S.T.) and ERC, DFG and Max Planck Society (to R.F.).

AUTHOR CONTRIBUTIONS

Z.S. and R.F. initiated the project, designed the experiments and wrote the paper; Z.S. performed the vast majority of the experiments; H.-Y.T., S.T., F.S., L.K., D.D. and A.A.W. performed experiments; Z.S., S.T., N.M., M.T., A.R.D. and R.F. analysed data; all authors read and approved the manuscript.

COMPETING FINANCIAL INTERESTS

The authors declare no competing financial interests.

Published online at http://dx.doi.org/10.1038/ncb3402
Reprints and permissions information is available online at www.nature.com/reprints

1. Vicente-Manzanares, M. & Horwitz, A. R. Adhesion dynamics at a glance. *J. Cell Sci.* **124,** 3923–3927 (2011).
2. Parsons, J. T., Horwitz, A. R. & Schwartz, M. A. Cell adhesion: integrating cytoskeletal dynamics and cellular tension. *Nat. Rev. Mol. Cell Biol.* **11,** 633–643 (2010).
3. Kong, F., Garcia, A. J., Mould, A. P., Humphries, M. J. & Zhu, C. Demonstration of catch bonds between an integrin and its ligand. *J. Cell Biol.* **185,** 1275–1284 (2009).
4. Hoffman, B. D., Grashoff, C. & Schwartz, M. A. Dynamic molecular processes mediate cellular mechanotransduction. *Nature* **475,** 316–323 (2011).
5. Giannone, G., Mege, R. M. & Thoumine, O. Multi-level molecular clutches in motile cell processes. *Trends Cell Biol.* **19,** 475–486 (2009).
6. Critchley, D. R. Biochemical and structural properties of the integrin-associated cytoskeletal protein talin. *Annu. Rev. Biophys.* **38,** 235–254 (2009).
7. Smilenov, L. B., Mikhailov, A., Pelham, R. J., Marcantonio, E. E. & Gundersen, G. G. Focal adhesion motility revealed in stationary fibroblasts. *Science* **286,** 1172–1174 (1999).
8. Chan, C. E. & Odde, D. J. Traction dynamics of filopodia on compliant substrates. *Science* **322,** 1687–1691 (2008).
9. Austen, K. *et al.* Extracellular rigidity sensing by talin isoform-specific mechanical linkages. *Nat. Cell Biol.* **17,** 1597–1606 (2015).

10. Thievessen, I. *et al.* Vinculin-actin interaction couples actin retrograde flow to focal adhesions, but is dispensable for focal adhesion growth. *J. Cell Biol.* **202,** 163–177 (2013).
11. Atherton, P. *et al.* Vinculin controls talin engagement with the actomyosin machinery. *Nat. Commun.* **6,** 10038 (2015).
12. Calderwood, D. A., Campbell, I. D. & Critchley, D. R. Talins and kindlins: partners in integrin-mediated adhesion. *Nat. Rev. Mol. Cell Biol.* **14,** 503–517 (2013).
13. Goult, B. T. *et al.* Structural studies on full-length talin1 reveal a compact auto-inhibited dimer: implications for talin activation. *J. Struct. Biol.* **184,** 21–32 (2013).
14. Song, X. *et al.* A novel membrane-dependent on/off switch mechanism of talin FERM domain at sites of cell adhesion. *Cell Res.* **22,** 1533–1545 (2012).
15. Goksoy, E. *et al.* Structural basis for the autoinhibition of talin in regulating integrin activation. *Mol. Cell* **31,** 124–133 (2008).
16. Chang, Y. C. *et al.* Structural and mechanistic insights into the recruitment of talin by RIAM in integrin signaling. *Structure* **22,** 1810–1820 (2014).
17. Han, J. *et al.* Reconstructing and deconstructing agonist-induced activation of integrin αIIbβ3. *Curr. Biol.* **16,** 1796–1806 (2006).
18. Lafuente, E. M. *et al.* RIAM, an Ena/VASP and Profilin ligand, interacts with Rap1-GTP and mediates Rap1-induced adhesion. *Dev. Cell* **7,** 585–595 (2004).
19. Legate, K. R. *et al.* Integrin adhesion and force coupling are independently regulated by localized PtdIns(4,5)2 synthesis. *EMBO J.* **30,** 4539–4553 (2011).
20. Comrie, W. A., Babich, A. & Burkhardt, J. K. F-actin flow drives affinity maturation and spatial organization of LFA-1 at the immunological synapse. *J. Cell Biol.* **208,** 475–491 (2015).
21. Case, L. B. & Waterman, C. M. Integration of actin dynamics and cell adhesion by a three-dimensional, mechanosensitive molecular clutch. *Nat. Cell Biol.* **17,** 955–963 (2015).
22. Legate, K. R., Montag, D., Bottcher, R. T., Takahashi, S. & Fassler, R. Comparative phenotypic analysis of the two major splice isoforms of phosphatidylinositol phosphate kinase type Igamma *in vivo*. *J. Cell Sci.* **125,** 5636–5646 (2012).
23. Stritt, S. *et al.* Rap1-GTP-interacting adaptor molecule (RIAM) is dispensable for platelet integrin activation and function in mice. *Blood* **125,** 219–222 (2015).
24. Klapproth, S. *et al.* Loss of the Rap-1 effector RIAM results in leukocyte adhesion deficiency due to impaired β2 integrin function in mice. *Blood* **126,** 2704–2712 (2015).
25. Kakinuma, N., Zhu, Y., Wang, Y., Roy, B. C. & Kiyama, R. Kank proteins: structure, functions and diseases. *Cell. Mol. Life Sci.* **66,** 2651–2659 (2009).
26. Ding, M., Goncharov, A., Jin, Y. & Chisholm., A. D. *C. elegans* ankyrin repeat protein VAB-19 is a component of epidermal attachment structures and is essential for epidermal morphogenesis. *Development* **130,** 5791–5801 (2003).
27. Yang, Y., Lee, W. S., Tang, X. & Wadsworth, W. G. Extracellular matrix regulates UNC-6 (netrin) axon guidance by controlling the direction of intracellular UNC-40 (DCC) outgrowth activity. *PLoS ONE* **9,** e97258 (2014).
28. Ihara, S. *et al.* Basement membrane sliding and targeted adhesion remodels tissue boundaries during uterine-vulval attachment in Caenorhabditis elegans. *Nat. Cell Biol.* **13,** 641–651 (2011).
29. Lerer, I. *et al.* Deletion of the ANKRD15 gene at 9p24.3 causes parent-of-origin-dependent inheritance of familial cerebral palsy. *Human Mol. Genet.* **14,** 3911–3920 (2005).
30. Gee, H. Y. *et al.* KANK deficiency leads to podocyte dysfunction and nephrotic syndrome. *J. Clin. Invest.* **125,** 2375–2384 (2015).
31. van der Vaart, B. *et al.* CFEOM1-associated kinesin KIF21A is a cortical microtubule growth inhibitor. *Dev. Cell* **27,** 145–160 (2013).
32. Kakinuma, N., Roy, B. C., Zhu, Y., Wang, Y. & Kiyama, R. Kank regulates RhoA-dependent formation of actin stress fibers and cell migration via 14-3-3 in PI3K-Akt signaling. *J. Cell Biol.* **181,** 537–549 (2008).
33. Schiller, H. B., Friedel, C. C., Boulegue, C. & Fassler, R. Quantitative proteomics of the integrin adhesome show a myosin II-dependent recruitment of LIM domain proteins. *EMBO Rep.* **12,** 259–266 (2011).
34. Schiller, H. B. *et al.* β1- and αv-class integrins cooperate to regulate myosin II during rigidity sensing of fibronectin-based microenvironments. *Nat. Cell Biol.* **15,** 625–636 (2013).
35. Bottcher, R. T. *et al.* Sorting nexin 17 prevents lysosomal degradation of β1 integrins by binding to the β1-integrin tail. *Nat. Cell Biol.* **14,** 584–592 (2012).
36. Zamir, E. *et al.* Dynamics and segregation of cell-matrix adhesions in cultured fibroblasts. *Nat. Cell Biol.* **2,** 191–196 (2000).
37. Wang, X. *et al.* Integrin Molecular Tension within Motile Focal Adhesions. *Biophys. J.* **109,** 2259–2267 (2015).
38. Ballestrem, C., Hinz, B., Imhof, B. A. & Wehrle-Haller, B. Marching at the front and dragging behind: differential αVβ3-integrin turnover regulates focal adhesion behavior. *J. Cell Biol.* **155,** 1319–1332 (2001).
39. Morimatsu, M., Mekhdjian, A. H., Chang, A. C., Tan, S. J. & Dunn, A. R. Visualizing the interior architecture of focal adhesions with high-resolution traction maps. *Nano. Lett.* **15,** 2220–2228 (2015).
40. Theodosiou, M. *et al.* Kindlin-2 cooperates with talin to activate integrins and induces cell spreading by directly binding paxillin. *Elife* **5,** e10130 (2016).
41. Gingras, A. R. *et al.* Central region of talin has a unique fold that binds vinculin and actin. *J. Biol. Chem.* **285,** 29577–29587 (2010).
42. Himmel, M. *et al.* Control of high affinity interactions in the talin C terminus: how talin domains coordinate protein dynamics in cell adhesions. *J. Biol. Chem.* **284,** 13832–13842 (2009).
43. Rossier, O. *et al.* Integrins β1 and β3 exhibit distinct dynamic nanoscale organizations inside focal adhesions. *Nat. Cell Biol.* **14,** 1057–1067 (2012).
44. Medves, S. *et al.* Multiple oligomerization domains of KANK1-PDGFRβ are required for JAK2-independent hematopoietic cell proliferation and signaling via STAT5 and ERK. *Haematologica* **96,** 1406–1414 (2011).
45. Iskratsch, T. *et al.* FHOD1 is needed for directed forces and adhesion maturation during cell spreading and migration. *Dev. Cell* **27,** 545–559 (2013).
46. Stehbens, S. J. *et al.* CLASPs link focal-adhesion-associated microtubule capture to localized exocytosis and adhesion site turnover. *Nat. Cell Biol.* **16,** 561–573 (2014).
47. Grigoriev, I. *et al.* Rab6 regulates transport and targeting of exocytotic carriers. *Dev. Cell* **13,** 305–314 (2007).
48. Lansbergen, G. *et al.* CLASPs attach microtubule plus ends to the cell cortex through a complex with LL5β. *Dev. Cell* **11,** 21–32 (2006).

DOI: 10.1038/ncb3402

METHODS

Mass spectrometry. To measure Kank1–4 levels in FA-enriched fractions and whole cell lysates, cells were serum-starved for 4 h, plated for 90 min in serum-free medium on FN-coated, BSA-blocked culture dishes, and FAs were isolated[34] for quantitative MS analysis on an LTQ Orbitrap analyser (Thermo Electron). Data were processed using the label-free quantification (LFQ) algorithm embedded in the MaxQuant software[49].

For the MS analysis of anti-GFP pulldowns, the samples were run 1 cm into a 12% SDS–PAGE. The entire lane up to the front was cut into 1 mm × 1 mm slices and subjected to standard in-gel digestions as previously described[50]. Briefly, the gel slices were destained in ethanol followed by sequential reduction and alkylation with 10 mM dithiothreitol (DTT) and 40 mM chloroacetamide (CAA), then dried and incubated with digestion buffer containing 12.5 ng μl^{-1} trypsin in 25 mM Tris buffer (pH 8.5) overnight. Peptides were extracted, purified in StageTips, analysed in an LTQ Orbitrap XL analyser and processed as described above. MS data were further analysed in Perseus and manually annotated for data illustration.

Antibodies. See Supplementary Table 1.

Plasmids, constructs and expression and purification of recombinant proteins. Mouse Kank1 and Kank2 complementary DNAs were cloned into peGFP-N1 vector (Clontech) using XhoI and EcoRI sites, mouse Kank3 using BglII and EcoRI sites and mouse Kank4 using XhoI and AgeI sites. For retrovirus-mediated overexpression, cDNAs of FL-Kank2, Kank2ΔKN lacking amino acids 31–56, Kank2Δcoil lacking amino acids 181–240, Kank2ΔKNΔcoil lacking amino acids 31–56 and 181–240, Kank2(1–670) encoded by amino acids 1–670 and Kank2-KN encoded by amino acids 29–72 were inserted between XhoI and EcoRI sites of the pRetroQ-AcGFP-N1 (Clontech) vector. Expression plasmids for talin-AcGFP and talin-TagRFP were generated from pLPCXmod-Talin1-Ypet (gift from C. Grashoff, Max Planck Institute for Biochemistry) by replacing Ypet with AcGFP or TagRFP-T. The talin rod truncations were inserted between XhoI and EcoRI of the peGFP-N1 vector. The expression plasmid of paxillin-TagRFP was generated by inserting the mouse paxillin cDNA between XhoI and SacI sites of pRetroQ-AcGFP-N1, in which the AcGFP was replaced by TagRFP-T, and the vinculin-mCherry by inserting the mouse vinculin cDNA between NheI and EcoRI sites of the pmCherry-N1 vector.

For stable depletion of Kank2 and liprin-β1 mRNA, two shRNAs targeting 5′-ATACTGTATTCTTGAGTCA-3′ (*Kank2* shRNA no 1) and 5′-AGCCAGAAAGCCAAGCTAC-3′ (*Kank2* shRNA no 2) of the Kank2 3′ untranslated region and two shRNAs targeting 5′-GTGGATTGTTGGAGATGAT-3′ (*liprin-β1* shRNA no 1) and 5′-GAAGCTCAAGTCAACTAAA-3′ (*liprin-β1* shRNA no 2) in the liprin-β1 coding region were cloned into pSuper.Retro.puro or pSuper.Retro.hygro vector (Oligoengine) for retrovirus production. For recombinant Kank2-KN production, the cDNA encoding amino acids 29–72 was cloned between EcoRI and BamHI sites of pGEX-6P1 (GE Healthcare). To produce the THD cDNA was cloned into the pCoofy vector, and to produce FL-talin-1 the pET101-talin-FL construct was used as previously described[51].

The GST-tagged Kank2-KN and GST alone were expressed in BL21 (DE3) overnight at 37 °C. Biomass was lysed in the presence of protease inhibitors (AEBSF-HCl 1 mM, aprotinin 2 μg ml^{-1}, leupeptin 1 μg ml^{-1}, pepstatin 1 μg ml^{-1}) and nuclease (Benzonase) with a high-pressure homogenizer in GST binding buffer (Tris-HCl 50 mM, NaCl 150 mM, EDTA 1 mM, DTT 1 mM, pH 7.5), clarified, incubated with glutathione Sepharose 4 Fast Flow (GE Healthcare) for 3.5 h at 4 °C, washed three times with GST binding buffer and eluted with 50 mM glutathione in glutathione binding buffer. Eluted fractions were desalted (Sephadex G-25 in Hi Prep 26/10) in desalting buffer (50 mM Tris-HCl, 150 mM NaCl, 0.1 mM DTT) and further purified with size-exclusion chromatography (Superdex 75 PC 3.2/30) in desalting buffer.

His-tagged talin-1 production was optimized in BL21 (DE3) on the basis of previously published protocols[51]. The expression was induced with 1 mM isopropylthiogalactoside at 18 °C overnight. After lysis with high-pressure homogenizer in lysis buffer (50 mM Tris-HCl at pH 7.8, 500 mM NaCl, 30 mM imidazole, 1 mM DTT) and clarification of the supernatant, talin-1 was purified by Ni-NTA affinity chromatography (Ni Sepharose High Performance, GE Healthcare) and anion exchange (HiTrap Q HP, GE Healthcare) in MES buffer (20 mM MES at pH 6.3, 1 mM DTT, gradient from 500 mM KCl to 100 mM KCl). The eluted fractions were concentrated (Amicon Ultra-15, molecular weight cutoff 100 kDa) and further purified by size-exclusion chromatography (Superdex 200 10/300 GL, GE Healthcare) in 50 mM Tris-HCl at pH 7.8, 150 mM KCl, 1 mM DTT. Purified fractions were stored in the presence of 50% glycerol at −80 °C.

The THD was produced in *Escherichia coli* Rosetta cells (Merck Millipore). After cell lysis and clarification of the supernatant, the THD was purified by Ni-NTA affinity chromatography (Qiagen), cleaved with SenP2 protease and purified by size-exclusion chromatography (Superdex 200 26/600, GE Healthcare). For the production of recombinant talin R4–R8 domain, mouse talin R4–R8 (corresponding to residues 913–1655) was amplified from pLPCXmod-Talin1-Ypet and subcloned into a vector containing a cleavable N-terminal Venus-His8-Sumo tag (gift from C. Biertümpfel, Max Planck Institute for Biochemistry). Talin R4–R8 was transformed in *E. coli* BL21 (DE3) and expressed with the ZY auto-induction system. Cells were lysed by sonication in 50 mM Tris-HCl at pH 7.8, 500 mM NaCl, 1 mM β-mercaptoethanol, 5 mM EDTA in the presence of protease inhibitor cocktail (Roche) and cleared by centrifugation, and the supernatant was injected into a His-affinity column (Roche), washed with 50 mM Tris-HCl at pH 7.8, 500 mM NaCl, 1 mM β-mercaptoethanol, 5 mM EDTA, 10 mM imidazole and the protein was eluted with 50 mM Tris-HCl at pH 7.8, 500 mM NaCl, 1 mM β-mercaptoethanol, 1 mM EDTA, 500 mM imidazole. Eluted products were further purified using a Superdex 20016/60 column (GE Healthcare) with 20 mM HEPES at pH 7.5, 500 mM NaCl, 1 mM EDTA and 1 mM DTT.

For expression of FL-Kank2, mouse Kank2 was expressed with a cleavable C-terminal 3C-Venus-His8 tag (gift from C. Biertümpfel, Max Planck Institute for Biochemistry) in HEK293S cells. HEK293S cells were grown to 1.5×10^6, transfected with 1 μg plasmid per millilitre of cells and grown for 2 days at 32 °C in the presence of 3.75 μM valproic acid. Cells were lysed by sonication in 50 mM Tris-HCl at pH 7.5, 150 mM NaCl, 3 mM DTT, 1 mM EDTA 1 mM pepstatin, 1 mM AEBSF, 1 mM leupeptin. Soluble fractions were purified by affinity purification, washed (50 mM Tris-HCl at pH 7.5, 1 M NaCl, 3 mM DTT, 1 mM EDTA, 5% glycerol) and eluted by tag cleavage with 3C protease in 50 mM Tris-HCl at pH 7.5, 500 mM NaCl, 3 mM DTT, 1 mM EDTA, 5% glycerol. Proteins were purified using Superdex 200 16/60 column (GE Healthcare) in 20 mM HEPES at pH 7.5, 150 mM KCl, 3 mM DTT, 5% glycerol. All purified proteins were stored at −80 °C.

Viral transduction and transient transfection of cell lines. SV40 large T-immortalized mouse kidney-derived fibroblasts have been previously described[6] and were used to analyse the Kank proteins. For the analysis of integrin α5-GFP turnover, mouse kidney fibroblasts were transduced with lentivirus expressing human integrin α5-GFP, and cells with low expression were FACS-sorted. HEK293 cells were used for GFP pulldown of different talin rod domains. Transient transfections were carried out with Lipofectamine 2000 (Invitrogen) according to the manufacturer's protocol. Transduction of VSV-G pseudotyped retroviral vectors produced by transient transfection of HEK293T were used to generate stable cell lines as previously described[52]. The cell lines used here were not found in the database of commonly misidentified cell lines maintained by ICLAC and NCBI BioSample. The cell lines were tested for mycoplasma contamination and were found to be negative.

Immunoprecipitation and GST pulldown. For immunoprecipitation of GFP-tagged proteins, cells were lysed in M-PER (Thermo Scientific, no 78501) buffer and immunoprecipitated using the μMACS GFP Isolation Kit (Miltenyi Biotec) following the manufacturer's protocol. Elutes were separated in SDS–PAGE for Western blotting or for in-gel digestion and mass spectrometry analysis.

For GST pulldown experiments, recombinant talin-1 and THD, respectively, were re-buffered in GST binding buffer (50 mM Tris-HCl at pH 7.5, 137 mM NaCl, 13 mM KCl, 0.05% Tween-20) with Zebra Desalt Spin Columns (Thermo Scientific). 200 nM GST or GST-Kank2-KN fusion proteins were incubated with 100 nM recombinant talin-1 or 300 nM THD for 30 min at 4 °C and incubated with glutathione Sepharose (GE Healthcare) for another 1.5 h at 4 °C. The resin was washed three times with the GST binding buffer and eluted in ×2 Laemmli buffer at 95 °C for 2 min. Samples were analysed by Western blot using antibodies against THD or GST.

***In vitro* F-actin competition assay.** 24 μM purified alpha skeletal muscle actin (no 8010-01, HYPERMOL) and Atto565-labelled alpha skeletal muscle actin (no 8162-1, HYPERMOL) were polymerized in PolyMix buffer (100 mM KCl, 10 mM imidazole at pH 7.4, 1 mM ATP and 2 mM $MgCl_2$) according to the manufacturer's instructions and stored on ice. The percentage of polymerized actin was estimated to be about 95% by F-actin sedimentation assay at 100,000*g* for 1 h at 25 °C.

To test the effects of F-actin on the interaction between the talin R4–R8 domain and FL-Kank2, 0.4 μM Venus-His-Sumo-tagged R4–R8 domain was incubated with 0.2 μM FL-Kank2 in PolyMix buffer for 1 h on ice before supplementing with 1 μM, 2 μM and 5 μM polymerized actin or empty buffer, and then incubated with Ni^{2+}-NTA beads at 4 °C for 1 h. Beads were washed with PolyMix buffer at 4 °C three times, and bound proteins were analysed by Western blotting.

To visualize actin recruitment onto the talin R4–R8 domain, 5% BSA or 2 μM Venus-His-Sumo-tagged R4–R8 domain were diluted in 30 μl KMEI buffer (50 mM KCl, 10 mM imidazole at pH 7.1, 1 mM EDTA, 2 mM $MgCl_2$) and incubated with Ni^{2+}-NTA beads at 4 °C for 30 min. Then 10 μl buffer (20 mM HEPES at pH 7.5, 150 mM KCl, 3 mM DTT, 5% glycerol) containing 5 μM FL-Kank2, re-buffered 5 μM GST-KN motif or control buffer was added and incubated for 30 min at 4 °C. 10 μl

polymerized Atto565-labelled actin was then added and incubated for 30 min at 4 °C. Before visualization under a confocal microscope, beads were briefly washed twice with ice-cold KMEI buffer and a 20 µl mixture was then injected into a flow chamber made with glass slides and cover slips spaced by one thin layer of Parafilm.

Integrin tail peptide pulldowns. Peptide pulldowns were carried out as previously described[35] with the β1 wild-type cytoplasmic tail peptide (HDRREFAKFEKEKMNAKWDTGENPIYKSAVTTVVNPKYEGK-OH), β1 Y795A tail peptide (HDRREFAKFEKEKMNAKWDTGENPIYKSAVTTVVNPKAEGK-OH), β3 wild-type tail peptide (HDRKEFAKFEEERARAKWDTANNPLYKEATSTFTNITYRGT-OH), β5 wild-type tail peptide (HDRREFAKFQSERSRARYEMASNPLYRKPISTHTVDFAFNKFNKSYNGSVD-OH), β2 wild-type tail peptide (TDLREYRRFEKEKLKSQWNN-DNPLFKSATTTVMNPKFAES-OH) and a scrambled peptide (EYEFEPDKVDTGAKGTKMAKNEKKFRNYTVHNIWESRKVAP-OH).

The tail peptides were synthesized *de novo* with a desthiobiotin on the N-terminus, coupled to Dynabeads MyOne streptavidin C1 (10 mg ml^{-1}, Invitrogen), incubated with cell lysates and after a mild wash with washing buffer containing 137 mM NaCl, 13 mM KCl, 50 mM Tris-HCl at pH 7.4, 0.05% Tween-20, supplemented with 1% BSA and then with M-PER buffer. Bound proteins were eluted in ×2 Laemmli buffer at 95 °C for 5 min.

For the *in vitro* talin activation assay, 10 nM recombinant talin-1 was diluted in the washing buffer and then incubated with 10 nM GST or GST-Kank2-KN together with β1-integrin-tail-peptide-coupled Dynabeads at 4 °C. Beads were washed three times with washing buffer and eluted with ×2 Laemmli buffer at 95 °C for 5 min. The chemically synthesized KN peptide (DPPYSVETPYGYRLDLDFLKYVDDIEKGHTLRRVAVQRRPRLGS) used for talin activation assays was N-terminally acetylated and C-terminally amide-protected. For competition assay between THD and FL-talin in the presence of KN peptide, 10 nM FL-talin-1 was activated with 50 nM chemically synthesized KN peptide and competed with 20 nM and 60 nM THD.

CHO-based αIIbβ3 integrin activation assay. The αIIbβ3 integrin activation was assessed in CHO cells stably expressing human αIIbβ3 integrin (A5 cells)[53] by flow cytometry using the ligand-mimetic antibody PAC1 (BD)[54]. CHO cells were lipofected with 1 µg of plasmids expressing eGFP-tagged Kank2 constructs and/or 3 µg TagRFP-tagged talin-1 or GFP-tagged THD. Cells were trypsinized 24 h after transfection and incubated with the PAC1 antibody (BD) in Tyrode's buffer (pH 7.35) for 30 min on ice, washed and stained with a secondary IgM for 30 min on ice followed by a final wash and staining with a streptavidin-Cy5 for 30 min on ice. PAC1 binding was measured with a FACS Canto, gated for living cells, using 7AAD (Thermo) exclusion as well as GFP–RFP double-positive cells. Total αIIbβ3 integrin surface levels were determined with an anti-αIIb integrin antibody (HIP8, BioLegend). Data evaluation was carried out with the FlowJo software. Surface antigen binding was expressed as geometric mean fluorescence intensity. αIIbβ3 integrin activation levels were defined as the ratio of PAC1 and HIP8 binding in cells positive for eGFP and/or RFP and were normalized with that of the cell expressing THD only.

Polyacrylamide gel micropatterning. Micropatterns were first produced on glass coverslips as previously described[55]. Briefly, 20 mm square glass coverslips were oxidized through oxygen plasma (FEMTO, Diener Electronic) for 10 s at 30 W before incubating with 0.1 mg ml^{-1} poly-L-lysine (PLL)–PEG (polyethylene glycol) (PLL20K-G35-PEG2K, JenKem) in 10 mM HEPES at pH 7.4 for 30 min. After drying, coverslips were exposed to 165 nm UV (UVO-Cleaner, Jelight) through a photomask (Toppan) for 5 min. Then, coverslips were incubated with 20 mg ml^{-1} of FN (FF1141, Sigma) and 20 µg ml^{-1} fluorescently labelled fibrinogen (Alexa Fluor 647 conjugate, no F35200, Invitrogen) in 100 mM sodium bicarbonate solution at pH 8.3 for 30 min.

The polyacrylamide solution was prepared by mixing acrylamide and bis-acrylamide (Sigma) in a respective ratio of 8%/0.264%, resulting in a measured Young's modulus of 35 kPa. The polyacrylamide solution was de-gassed for around 30 min and mixed with passivated fluorescent beads (red fluorescent FluoSpheres carboxylate-modified microspheres, 0.2 µm F8810, Thermo Fisher) by sonication before adding ammonium persulfate and tetramethylethylenediamine. 25 µl of the solution was immediately deposited on the ROI on the photomask and incubated for 21 min under a silanized coverslip. The silanized coverslip was then carefully removed in the presence of sodium bicarbonate and the gels stored overnight at 4 °C in sodium bicarbonate. Coverslips were washed in sterile PBS before seeding the cells and then mounted in a magnetic chamber (Chamlide, LCI) for TFM processing.

Traction-force microscopy and image analysis. Images of cells, beads and patterns were acquired with a confocal spinning disk system (Eclipse Ti-E Nikon inverted microscope) equipped with a CSUX1-A1 Yokogawa confocal head, an Evolve EMCCD camera (Roper Scientific, Princeton Instrument) and a Nikon CFI Plan-APO VC ×60–numerical aperture 1.4 oil immersion objective). The system was controlled by MetaMorph software (Universal Imaging).

TFM and image analysis were carried out as described. All processing was carried out using ImageJ (http://rsb.info.nih.gov/ij). Plugins and macros are available at https://sites.google.com/site/qingzongtseng/tfm. First, bead images are aligned to correct experimental drift. Displacement field was calculated using particle image velocimetry on the basis of a normalized cross-correlation algorithm following an iterative scheme. The final grid size for the displacement fields was 0.267 µm × 0.267 µm. Subsequently, the traction-force field was calculated by means of Fourier transform traction cytometry with a regularization parameter set to 2×10^{-10}.

FN fibrillogenesis assay. Cells were seeded at 90% confluence onto coverslips coated with 10 µg ml^{-1} FN (Calbiochem) at 37 °C and cultured for 12 h in normal culture medium before paraformaldehyde (PFA) fixation and immunostaining.

Immunofluorescence microscopy. For immunostaining, cells were cultured on glass coated with 10 µg ml^{-1} FN (Calbiochem) for 5 h, then fixed with cold methanol:acetone (1:1) for 5 min at −20 °C (for endogenous talin, vinculin and kindlin-2 staining) followed by 15 min rehydration in PBS at room temperature, or with 2% PFA–PBS for 15 min at room temperature (for other immunostaining). PFA-fixed cells were permeabilized when indicated with 0.1% Triton X-100–PBS for 30 min at room temperature. Fixed cells were blocked with 5% BSA in PBS for 1 h at room temperature followed by incubation with the primary antibodies in 5% BSA in PBS overnight at 4 °C and then with secondary antibodies for 1 h at room temperature. Images were collected at room temperature on a Zeiss (Jena) LSM780 confocal laser scanning microscope equipped with a Zeiss Plan-APO ×63–numerical aperture 1.46 oil immersion objective.

Fluorescence recovery after photobleaching. FRAP and fluorescence live cell imaging were carried out on a Zeiss (Jena) LSM780 confocal laser scanning microscope equipped with a Zeiss Plan-APO ×63–numerical aperture 1.46 oil immersion objective with environmental control (5% CO_2 and humidification). Cells were cultured on 10 µg ml^{-1} FN-coated glass-bottom live cell imaging chambers (ibidi). For FRAP experiments, the ROI was bleached with full laser power at 488 nm for 30 iterations and fluorescence recovery was monitored for 5 min with 20 s intervals and 1% laser power for talin-GFP turnover, or was monitored for 5 min with 10 s intervals and 1% laser power for integrin α5-GFP turnover. No significant photobleaching was observed during the post-bleaching phase. FRAP data were extracted with ImageJ. Due to the rapid diffusion of cytosolic talin into the bleached area immediately after bleaching, the mean optical intensity outside adhesion was subtracted from the mean optical intensity in FAs to correct the background. FRAP curves were fitted to a one-phase association model to calculate the mobile fraction.

Confocal microscopy live cell imaging. For confocal microscopy live cell imaging, we used the same microscopic setting as for FRAP. Cells were imaged for the indicated time with 20 s or 30 s intervals with 1–3% laser power depending on the fluorophores. To block MMP activities, cells were plated for 5 h with or without 50 µM GM6001 (no sc-203979, Santa Cruz) before live cell imaging. For data illustration, fluorescent images were background-subtracted and passed through low-pass filters followed by Unsharp Mask in ImageJ.

For the tracking of sliding adhesions, a time lapse of 20 min with 2 min intervals was extracted from the full Supplementary Videos. Raw images were background-subtracted. Single adhesions were identified by thresholding and tracked with the TrackMate plugin in ImageJ. Structures with sizes below 3 pixels (0.04 µm per pixel) were excluded. Adhesion sites with lifetimes above 6 min were tracked to measure their sliding velocities. Average adhesion sliding velocities were calculated on the basis of all analysed adhesions for each cell. For the determination of sliding velocities of central adhesions, vinculin-mCherry-positive adhesions were analysed within 20 µm distance from nuclei in the first frame. For the FAs in the cell protrusions, vinculin-mCherry-positive adhesions were analysed within 10 µm behind the protruding leading edge in the first frame.

Intensity-based immunofluorescence image analysis. For line profile analysis, the fluorescence intensity along a transverse line across elongated FAs was analysed with ImageJ. The pixel position of the intensity peak for the Kank2 puncta was defined as the position of Kank2. Pixel positions corresponding to 50% of the average plateau intensity for conventional adhesion markers were manually annotated.

Kindlin-2 was used to analyse the localization of talin-1-GFP at adhesion sites. GFP intensities outside kindlin-2-positive areas were considered cytosolic. Mean optical intensities of GFP within and outside kindlin-2-positive areas were measured in ImageJ.

For quantification of active β1 integrin levels on the ventral cell surface of adherent cells, PFA-fixed cells were stained with the rat monoclonal antibody 9EG7 without permeabilization. The cellular borders were manually inspected and

DOI: 10.1038/ncb3402

defined. Total intensities corresponding to 9EG7 signals and total cell areas were then measured in ImageJ.

To calculate FA disassembly rates, paxillin-TagRFP intensities during the FA disassembly phase were measured within the ROI with a fixed position that covers the initial FA area. Data were fitted into a one-phase exponential decay function and the decay rate constants were used as FA disassembly rates.

Time-lapse phase contrast video microscopy of 2D random cell migration. Cells were sparsely seeded on a six-well plate coated with 5 μg ml^{-1} FN in the absence of serum for 2 h. Subsequently, cell migration was recorded with a Zeiss Axiovert 200 M equipped with a ×10–numerical aperture 0.3 objective, a motorized stage (Märzhäuser), an environment chamber (EMBL Precision Engineering) and a cooled CCD (charge-coupled device) camera (Roper Scientific) at 37 °C and 5% CO_2 for 6 h with 5 min time intervals. Image acquisition and microscope control were carried out with MetaMorph software (Molecular Devices). The acquired images were analysed using the manual tracking plugin of ImageJ and the Chemotaxis and Migration Tool (ibidi).

RGD tension sensor measurements. The molecular tension sensor was adapted from the sensor previously described[39], with slight modifications to the labelling chemistry. Briefly, the unnatural amino acid used to attach an ATTO647 dye was replaced with a second cysteine to attach an Alexa 647 dye for a higher labelling efficiency. This modified molecular tension sensor still presents the RGD ligand derived from FN and does not change the interactions with the cell. Perfusion chambers were attached to PEGylated coverslips as previously described[39]. Briefly, labelled molecular tension sensor (∼100 nM) was then added to the flow cell and incubated for 30 min, followed by Pluronic F-127 (0.2% w/v) for ∼1 min to prevent nonspecific cell attachment. All the above steps were preceded by a PBS wash to remove excess reagent from the previous step. The cells were then added and incubated for at least 5 h at 37 °C in DMEM high-glucose medium. Images were taken using TIRF microscopy on an inverted microscope (Nikon Ti-E) equipped with an Apo TIRF ×100–numerical aperture 1.49 oil immersion objective (Nikon). Data were acquired at 5 frames per second with either an EMCCD camera (Andor iXon) or an sCMOS camera (Hamamatsu Orca Flash).

For 2D correlation analyses, FL-Kank2-GFP and FRET images were normalized and median filtered to reduce background noise[39]. The channels were then manually thresholded to separate adhesions from the background signal and to create masks for each channel. The pixels from both masks were combined into a single mask, which was applied to the GFP and FRET images. We then used the resulting masked images to calculate the 2D correlation coefficient. Significance was calculated using the Wilcoxon rank sum test.

For comparison of average stress within adhesions between cell lines, the force per pixel was calculated using images of the entire cell taken on the Hamamatsu sCMOS camera. The GFP channel was normalized and processed using a moving boxcar average and thresholding. The adhesions were segmented using a watershed algorithm with a minimum adhesion size of 0.5 μm^2. The average force per μm^2 for adhesions was then calculated with an average sensor density on the basis of previous calibrations[39]. For the adhesion area ratio, each of the pixels from the segmented adhesions was converted to force and the ratio of the number of pixels above 1.25 pN versus below 1.25 pN was calculated. Significance was calculated using the Wilcoxon rank sum test.

RhoA GTPase activity. Indicated cells were serum-starved for 3 h and plated on FN for 1 h in the absence of serum. Active GTP-bound RhoA was affinity purified and detected with the Active Rho Pull-Down and Detection Kit (no 16116, Thermo Scientific) following manufacturer's instructions.

Statistics and reproducibility. Statistical analysis was carried out in GraphPad Prism software (version 5.00, GraphPad Software). Statistical calculations to predetermine required sample size were not carried out. The data sets with data points above 10 were analysed with the D'Agostino and Pearson omnibus normality test. Data sets with normal distributions were analysed with either Student's *t* tests to compare two conditions, or with one-way ANOVA Tukey tests to compare multiple conditions. Data sets that did not follow normal distribution in the normality test or those that should not be considered as normal distribution (for example, TFM measurements) were analysed with a Kruskal–Wallis test (multiple comparison) or Wilcoxon rank sum test (two-sample comparison). In the case of TFM measurements, we carried out outlier identification and data cleaning due to apparent defects in some individual measurements. For data with replicates below 10, we assumed normal distribution on the basis of the appearance of the data and analysed with Student's two-tailed *t* test. Results are depicted as mean ± s.d., mean ± s.e.m. or mean ± 95% CI as indicated in figure legends. All experiments for quantitative analysis were reproduced at least three times.

Data availability. Source data for Figs 6c, 7a–d,g and Supplementary Figs 7b and 8b,c have been provided as Supplementary Table 2. All other data that support the conclusions are available from the authors on request.

49. Cox, J. & Mann, M. MaxQuant enables high peptide identification rates, individualized p.p.b.-range mass accuracies and proteome-wide protein quantification. *Nat. Biotechnol.* **26,** 1367–1372 (2008).
50. Shevchenko, A., Tomas, H., Havlis, J., Olsen, J. V. & Mann, M. In-gel digestion for mass spectrometric characterization of proteins and proteomes. *Nat. Protoc.* **1,** 2856–2860 (2006).
51. Ciobanasu, C., Faivre, B. & LeClainche, C. Actomyosin-dependent formation of the mechanosensitive talin-vinculin complex reinforces actin anchoring. *Nat. Commun.* **5,** 3095 (2014).
52. Pfeifer, A., Kessler, T., Silletti, S., Cheresh, D. A. & Verma, I. M. Suppression of angiogenesis by lentiviral delivery of PEX, a noncatalytic fragment of matrix metalloproteinase 2. *Proc. Natl Acad. Sci. USA* **97,** 12227–12232 (2000).
53. Frojmovic, M. M., O' Toole, T. E., Plow, E. F., Loftus, J. C. & Ginsberg, M. H. Platelet glycoprotein IIb-IIIa (α IIb β 3 integrin) confers fibrinogen- and activation-dependent aggregation on heterologous cells. *Blood* **78,** 369–376 (1991).
54. Shattil, S. J., Hoxie, J. A., Cunningham, M. & Brass, L. F. Changes in the platelet membrane glycoprotein IIb.IIIa complex during platelet activation. *J. Biol. Chem.* **260,** 11107–11114 (1985).
55. Azioune, A., Carpi, N., Tseng, Q., Thery, M. & Piel, M. Protein Micropatterns: a Direct Printing Protocol Using Deep UVs. *Method Cell Biol.* **97,** 133–146 (2010).

DOI: 10.1038/ncb3402

nature cell biology

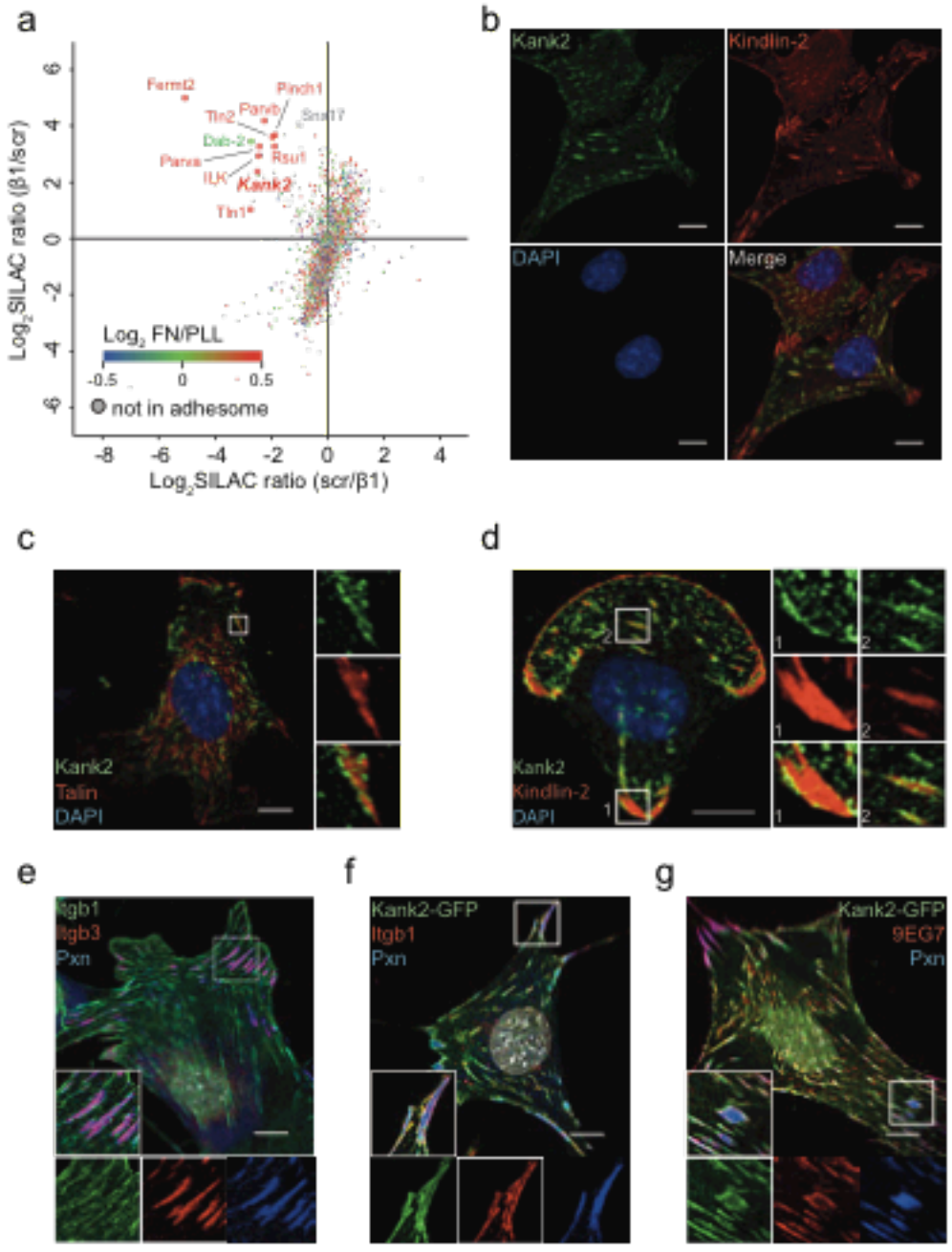

Supplementary Figure 1 (**a**) SILAC ratio plot showing specific β1wt tail interactors with high β1 wt / β1 scr and low β1 scr / β1 wt SILAC ratios in reverse SILAC labeling experiments and with high MS intensities in the FA-enriched proteome of FN-seeded fibroblasts in red. Dab-2 (green) and SNX17 (grey) show a high β1 wt / β1 scr SILAC ration but were absent from the FA-enriched proteome. (**b**) Split channels of Figure 1b. Mouse fibroblasts seeded on FN for 3h and immunostained for Kank2 (green), Kindlin-2 (red) and DAPI (blue). (**c**) Mouse fibroblasts seeded on FN for 3h and immunostained for Kank2 (green), Talin (red) and DAPI (blue). (**d**) Confocal image of immunostained (Kank2, green; Kindlin-2, red; DAPI, blue) wild-type fibroblasts seeded for 3h on a FN-coated micropattern. The boxed areas show Kank2 puncta around paxillin-positive FAs. (**e**) Mouse fibroblasts seeded on FN for 5h and immunostained for β1 integrin (Itgb1, green), β3 integrin (Itgb3, red), Paxillin (Pxn, blue) and DAPI (grey). (**f**,**g**) Mouse fibroblasts expressing Kank2-GFP seeded for 5h on FN and immunostained for β1 integrin (Itgb1, red) or active β1 integrin (9EG7, red), Paxillin (Pxn, blue) and DAPI (grey). Scale bar in **b**-**g**, 10μm.

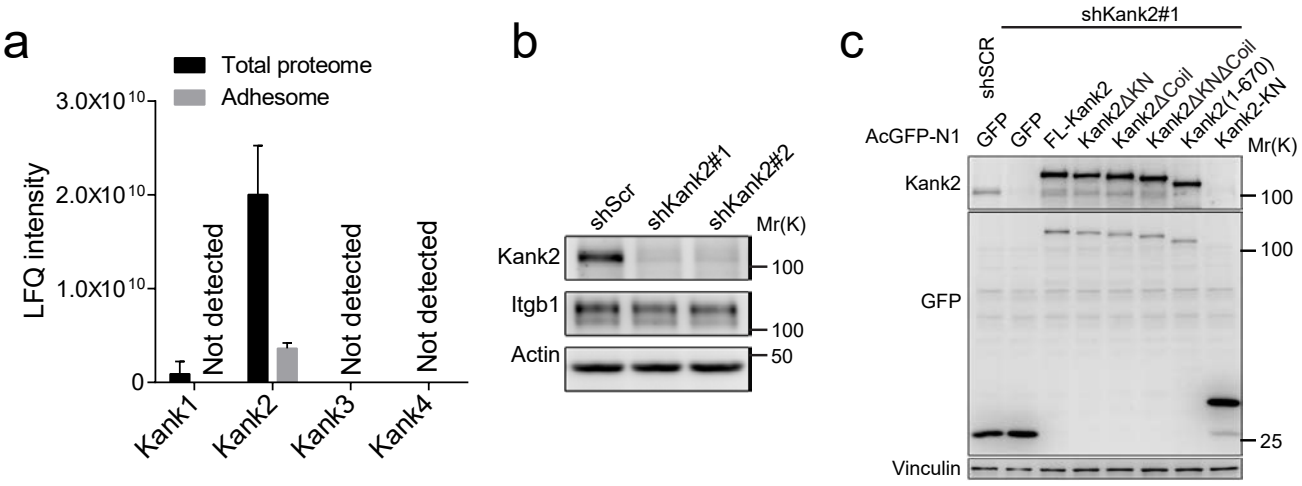

Supplementary Figure 2 (**a**) MS intensities of Kank1-4 in the FA-enriched sub-proteome and total proteome of wild-type mouse kidney fibroblasts (mean ± sd; n = 3 independent MS measurements). (**b**) Western blot analysis of Kank2 and β1 integrin (Itgb1) in cells expressing scrambled (shScr) and Kank2-specific shRNAs. Actin served to control protein loading. (**c**) Western blot analysis of Kank2 before and after shRNA-mediated knockdown using polyclonal anti-Kank2, and of indicated GFP-tagged Kank2 constructs using anti-GFP antibodies, respectively. Vinculin is used as loading control.

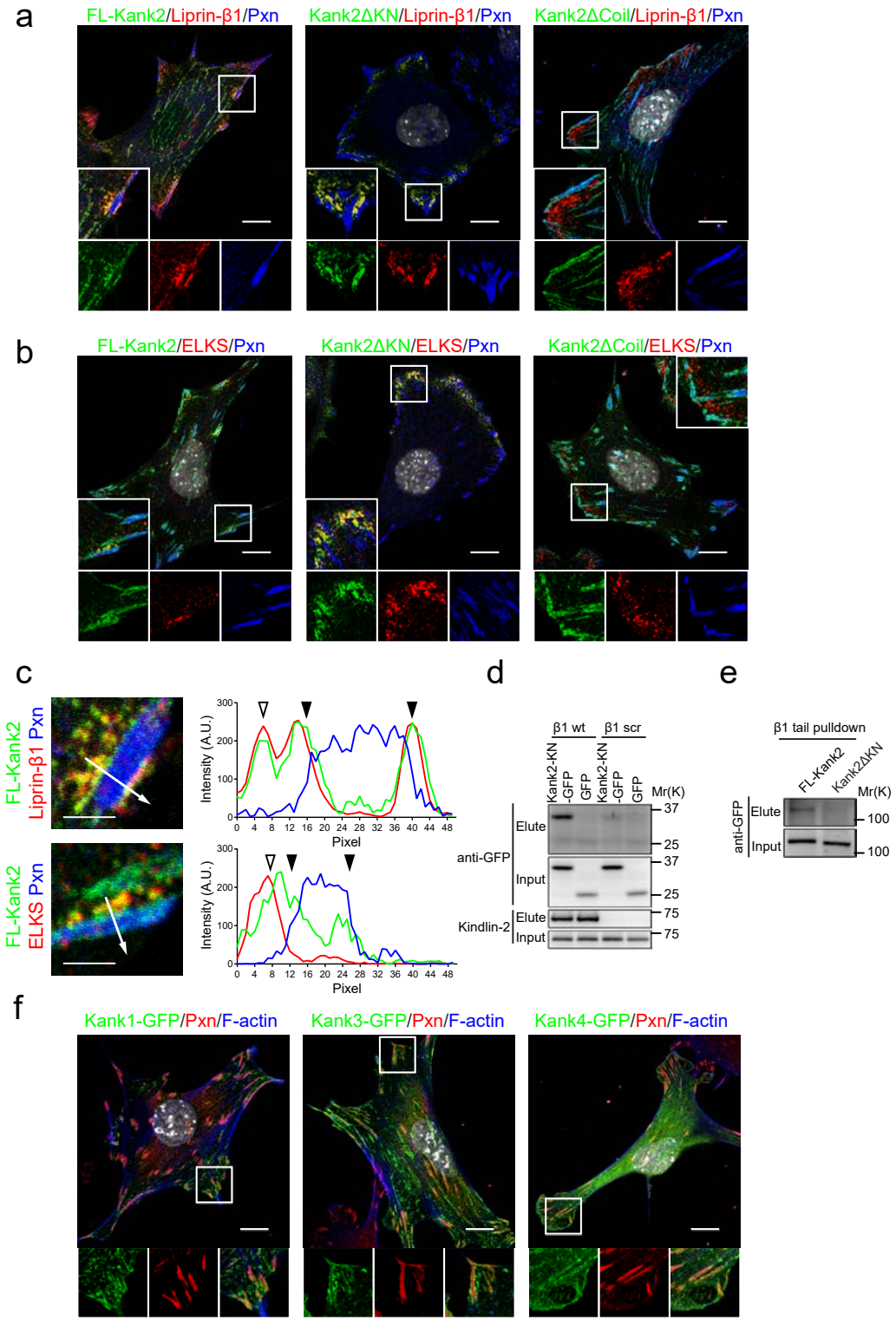

Supplementary Figure 3 (**a**,**b**) Immunofluorescence of GFP-tagged Kank2 constructs (green) co-stained for Liprin-β1 (**a**, red) or ELKS (**b**, red), Paxillin (Pxn; blue) and DAPI (grey). (**c**) Line profile analysis of GFP-tagged FL-Kank2 co-stained with Liprin-β1 and ELKS. Full arrowheads indicate the position of FA belt and open arrowheads indicate Liprin-β1- and ELKS-enriched regions outside the FA belt. Scale bar, 2μm. (**d**,**e**) Western blot testing GFP-tagged Kank-KN (**d**), FL-Kank2 and Kank2ΔKN (**e**) binding to biotinylated β1 integrin tails. FL and mutant Kank2 proteins were detected with the anti-GFP antibody, and Kindlin-2 was used to control the β1 tail pull-down assay. (**f**) GFP-tagged Kank1, Kank3 and Kank4 expressed in Kank2-depleted fibroblasts and co-stained for Paxillin (Pxn; red), F-actin (blue) and DAPI (grey). Scale bars in **a**,**b**,**f**, 10μm.

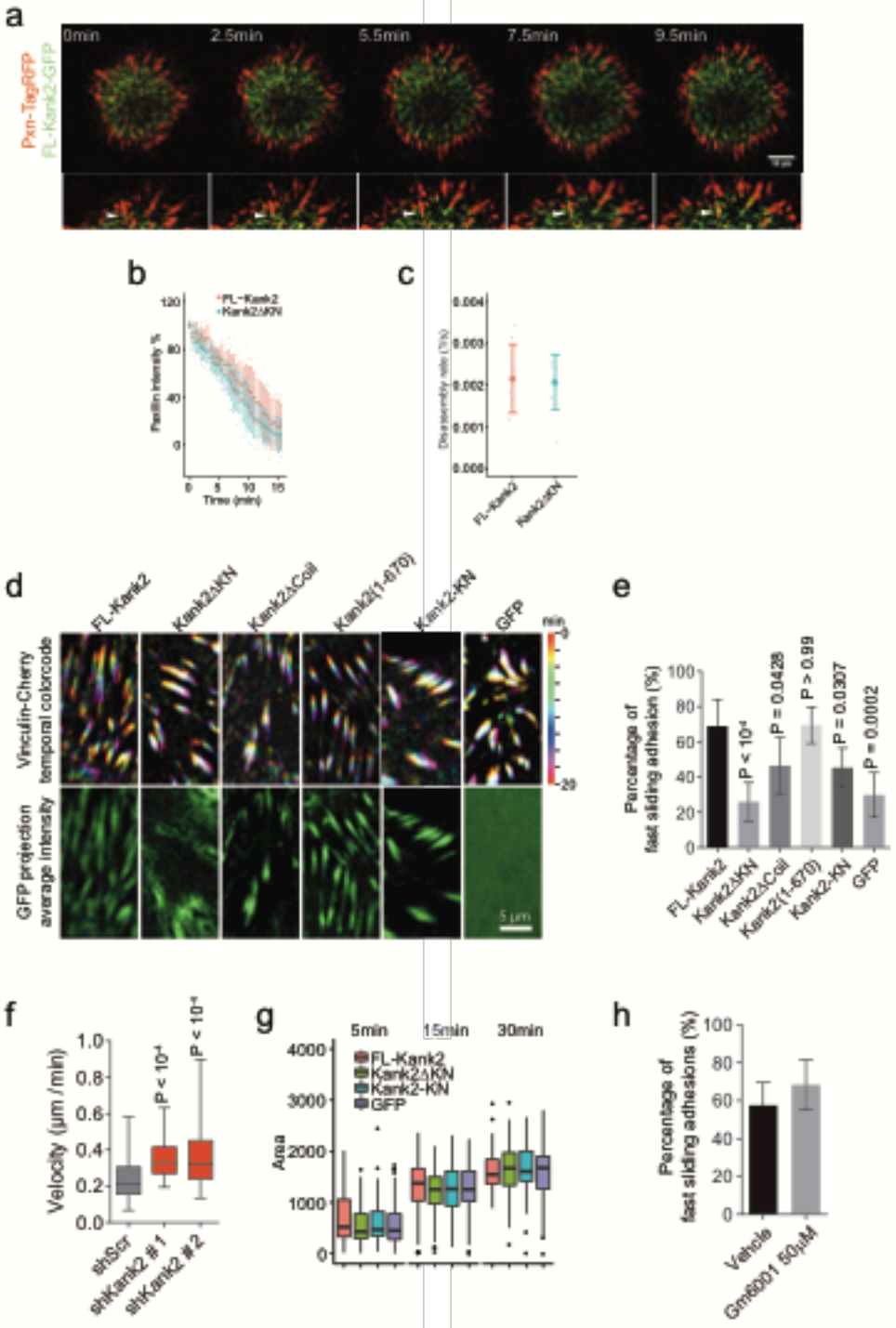

Supplementary Figure 4 (**a**) Time lapse images of cells stably expressing GFP-tagged FL-Kank2 (green) and Paxillin-TagRFP (Pxn-TagRFP; red) during isotropic spreading on FN. Arrow heads indicate Kank2 recruitment to the proximal FA border. (**b**) Normalized Pxn-TagRFP intensities during FA disassembly behind lamella in cells expressing FL-Kank2 (red) or Kank2ΔKN (blue) (mean ± sd; n = 8 cells for FL-Kank2, and n = 10 cells for Kank2ΔKN pooled from 4 independent experiments). (**c**) FA disassembly rates calculated from (**b**) as rate constants in a one-phase exponential decay (mean ± sd). (**d**) Ten overlaid, sequential time lapse images of Vinculin-mCherry in the cell centre temporally color-coded using spectrum look up tables (LUT). Corresponding time lapse images of GFP are shown as projection of average intensity. Scale bar, 5µm. (**e**) Percentage of adhesion sites with sliding velocity above 0.3µm/min in indicated cell lines (mean ± sd, n = 5 cells from 3 independent experiments; *P* values were calculated using one-way ANOVA Tukey test). (**f**) 2-D random migration of indicated cells on FN (box plot with median, 1st-3rd quantile box, minimal to maximal whiskers; shScr, n = 52 cells; shKank2#1, n = 58 cells; shKank2#2, n = 60 cells; data aggregated from 4 independent experiments; *P* values were calculated using Student *t*-test). (**g**) Cell spreading area of indicated cells at different time points (n ≥ 50 cells for each condition). (**h**) Percentage of adhesion sites with sliding velocity above 0.3µm/min in Kank2-depleted fibroblasts stably expressing Paxillin-TagRFP and Kank2-GFP on FN treated with or without 50µM broad spectrum MMP inhibitor Gm6001 for 5h (mean ± sd, n = 5 cells from 3 independent experiments).

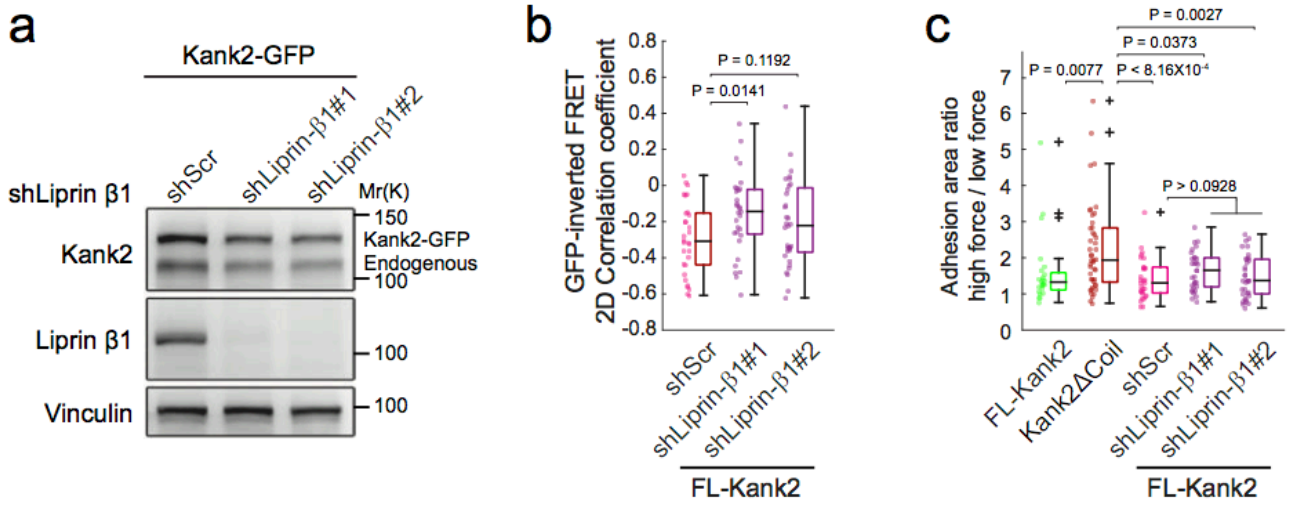

Supplementary Figure 5 (**a**) Western blot analysis of Kank2 and Liprin-β1 in wild-type cells expressing FL-Kank2-GFP together with scrambled (shScr) and two Liprin-β1-specific shRNAs. Vinculin served to control protein loading. (**b**) 2D correlation coefficient between GFP and inverted FRET signals in FL-Kank2-GFP expressing cells before and after Liprin-β1 depletion (dot plot and box plot; FL-Kank2 shScr, n = 30 cells; FL-Kank2 shLiprin-β1#1, n = 31 cells; FL-Kank2 shLiprin-β1#2, n = 33 cells; data aggregated from 3 independent experiments for each condition; *P* values were calculated using the Wilcoxon Rank Sum test). (**c**) Ratio between adhesion area with high tension (≥250pN/μm^2) and adhesion area with low tension (<250pN/μm^2) were calculated in cells expressing indicated constructs (dot plot and box plot; FL-Kank2, n = 24 cells; Kank2ΔCoil, n = 45 cells; FL-Kank2 shScr, n = 30 cells; FL-Kank2 shLiprin-β1#1, n = 31 cells; FL-Kank2 shLiprin-β1#2, n = 33 cells; data aggregated from 3 independent experiments for each condition; *P* values were calculated using the Wilcoxon Rank Sum test).

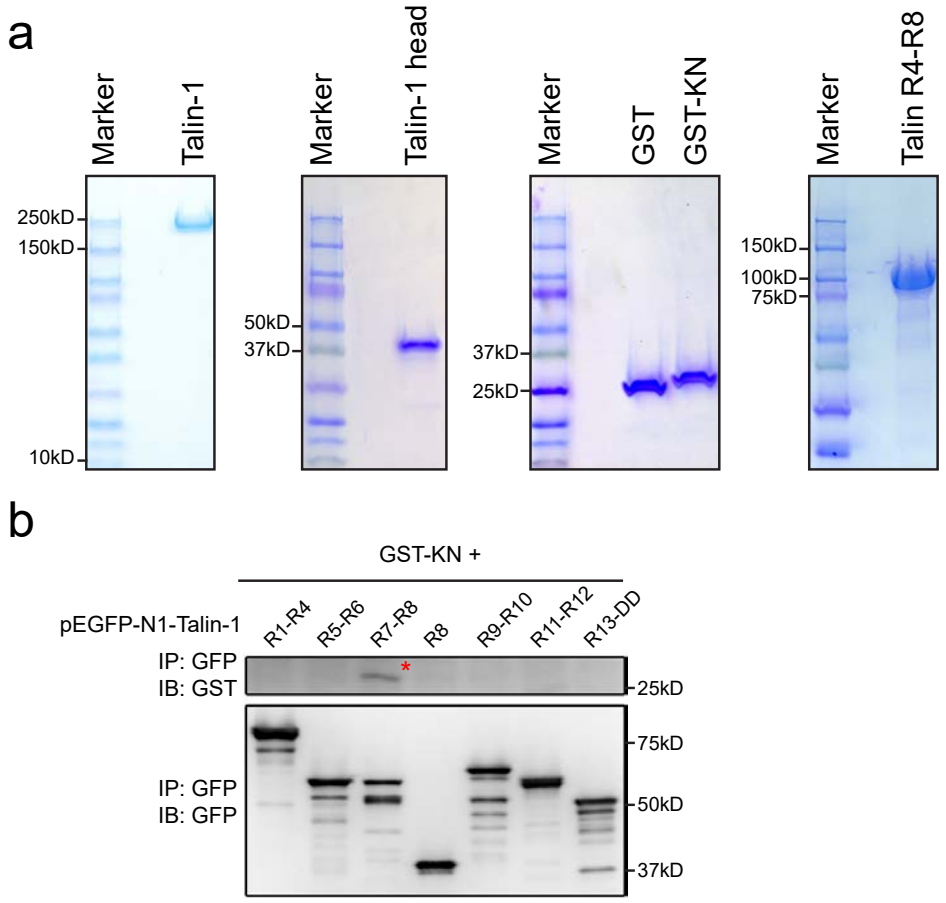

Supplementary Figure 6 (**a**) SDS-PAGE analysis of bacterially expressed and purified FL-Talin-1, Talin head domain (THD), Venus-His-Sumo-tagged Talin R4-R8 domain, GST-KN fusion protein and GST. (**b**) HEK293 cells expressing GFP-tagged Talin rod truncations were lysed, incubated with recombinant GST-KN, immunoprecipitated with anti-GFP antibody and analyzed with Western blot. Red asterisk marks the recombinant GST-KN protein.

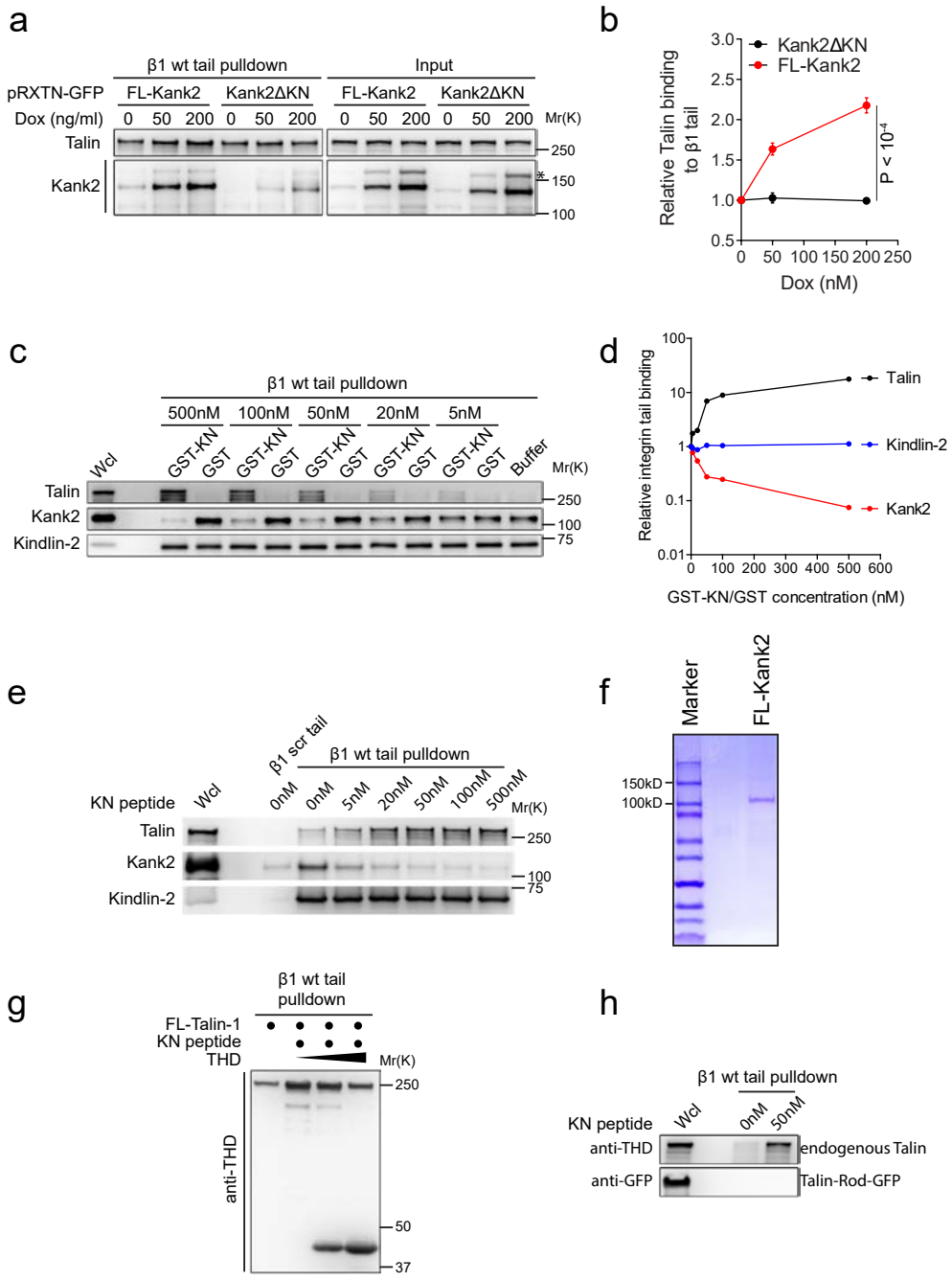

Supplementary Figure 7 (**a**) Western blot and (**b**) densitometry of Talin binding to β1 integrin tails in cells treated with increasing doses of dexamethasone (Dox) to induce expression of either FL-Kank2 or Kank2ΔKN (mean ± sd; n = 3 independent experiments; *P* values were calculated using Student *t*-test). Asterisk marks additional Kank2 bands after transient induction of protein expression, which is likely due to post-translational modification. (**c**,**d**) Representative Western blot (**c**) and densitometry (**d**) of endogenous Kank2, Talin and Kindlin-2 binding to β1 integrin tails in the presence of increasing concentrations of recombinant KN-GST. (**e**) Western blot of endogenous Kank2, Talin and Kindlin-2 binding to β1 integrin tails in the presence of increasing concentrations of chemically synthesized KN peptide. (**f**) SDS-PAGE analysis of FL-Kank2 expressed and purified from HEK293 cells. (**g**) Western blot analysis of recombinant Talin-1 binding to β1 integrin tail in the presence of the KN peptide and increasing concentration of recombinant THD. (**h**) Western blot analysis of β1 integrin tail pull downs of endogenous Talin detected with an antibody recognizing THD in cells overexpressing the GFP-tagged Talin rod domain (Talin-Rod-GFP) in the presence or absence of KN peptide. Source data for panels **b** can be found in Supplementary Table 2.

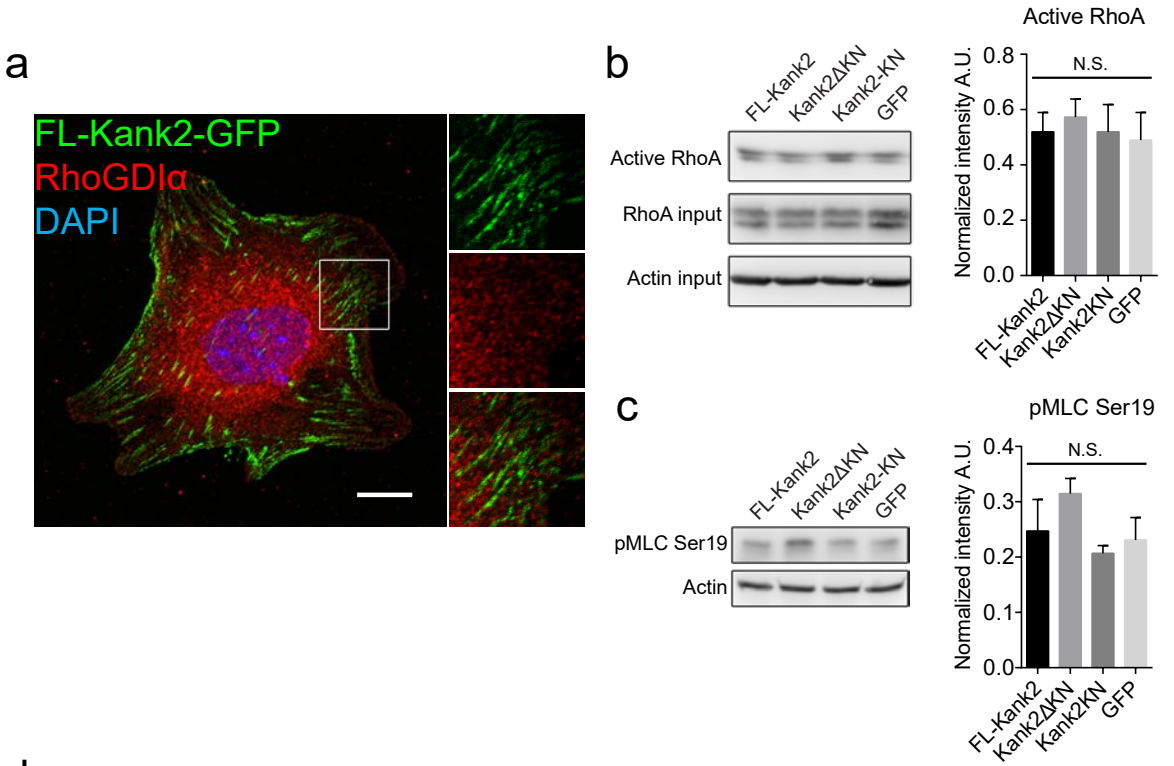

Supplementary Figure 8 (**a**) Immunofluorescence of FL-Kank2-GFP (green) co-stained with endogenous RhoGDIα (red) and DAPI (blue). Scale bar, 10µm. (**b**) Western blot (left) and densitometric (right) analysis of RhoA activation in Kank2-depleted cells expressing indicated Kank2 constructs seeded on FN for 1h (mean ± sd; n = 3 independent experiments; *P* values were calculated using one-way ANOVA Tukey test; N.S., no significance). (**c**) Western blot (left) and densitometric (right) analysis of myosin light chain (MLC) phosphorylation at serine-19 (pMLC-Ser19) in Kank2-depleted cells expressing indicated Kank2 constructs seeded on FN for 1h. Actin was used to control protein loading (mean ± sd; n = 4 independent experiments; *P* values were calculated using one-way ANOVA Tukey test; N.S., no significance). (**d**) Still images from a representative time lapse FRAP experiment of Talin-1-GFP shown in rainbow LUT. Talin-1-GFP was co-expressed with Cherry-tagged FL-Kank2 or Kank2ΔKN, respectively, in Kank2-deplted fibroblasts. Co-localization of Kank2-mCherry and Talin-1-GFP in the region of interest (ROI, red circle) was confirmed in pre-bleached images. Scale bar, 2µm. Source data for panels **b,c** can be found in Supplementary Table 2.

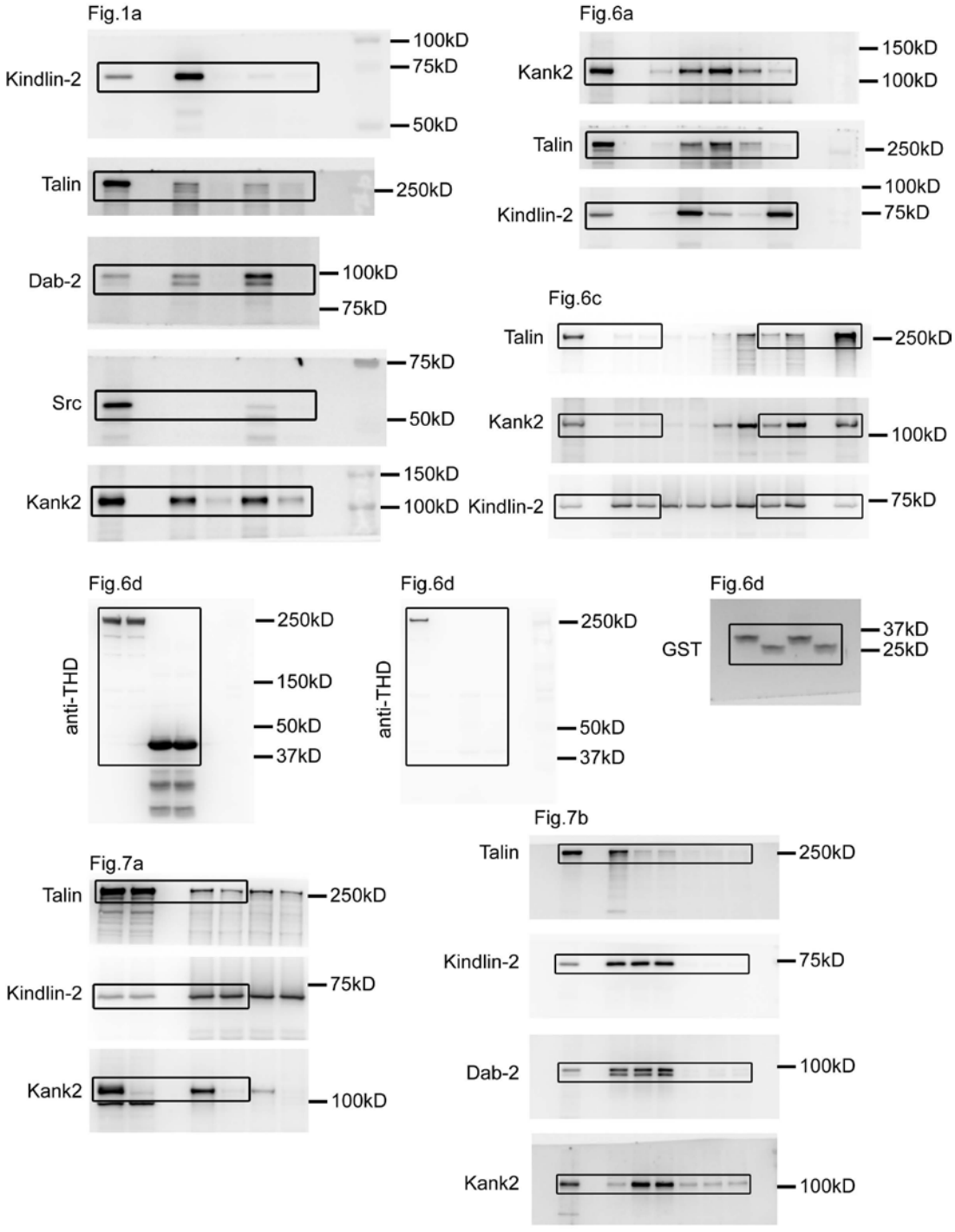

Supplementary Figure 9 Original uncropped Western blots.

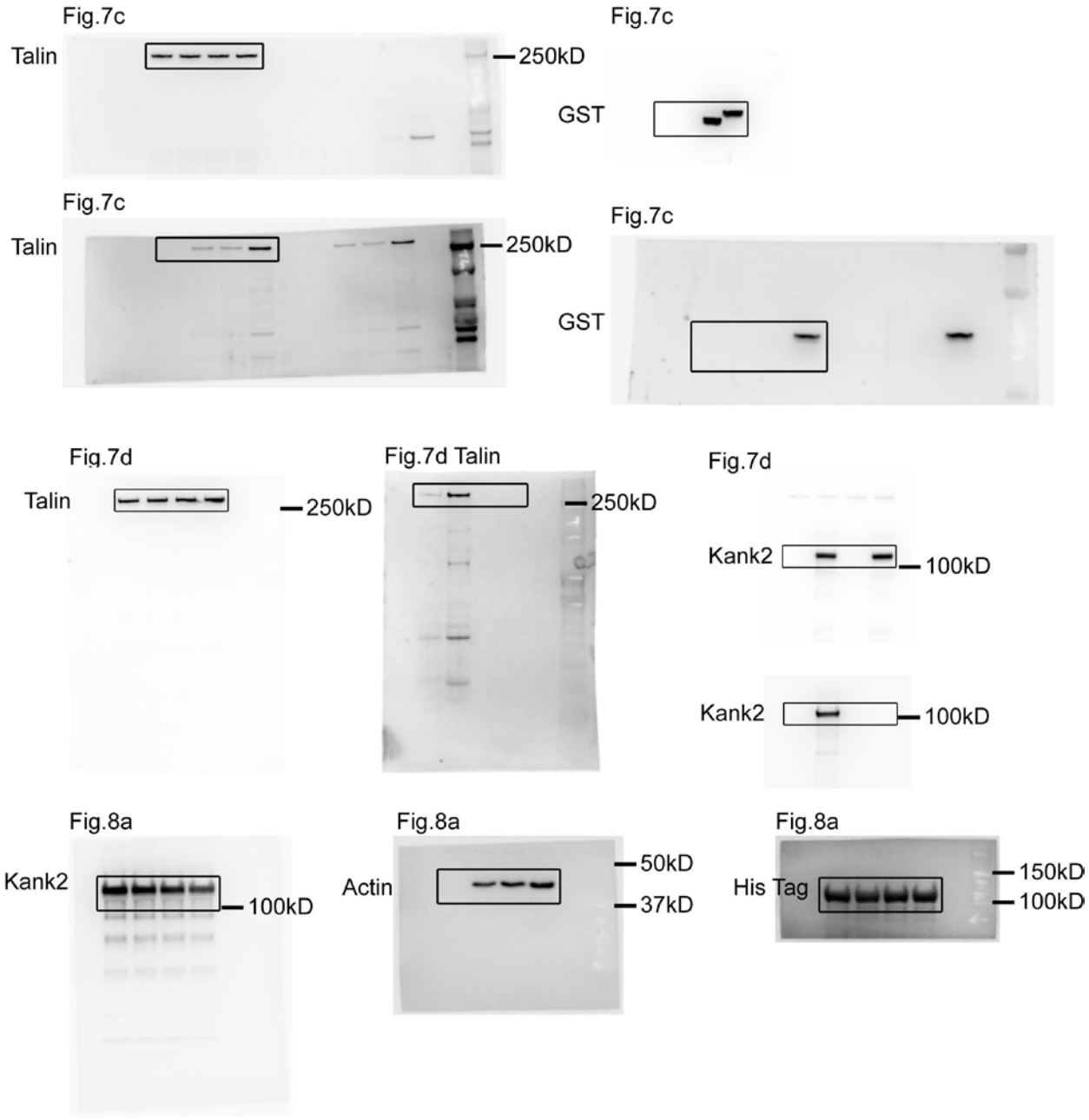

Supplementary Figure 9 continued

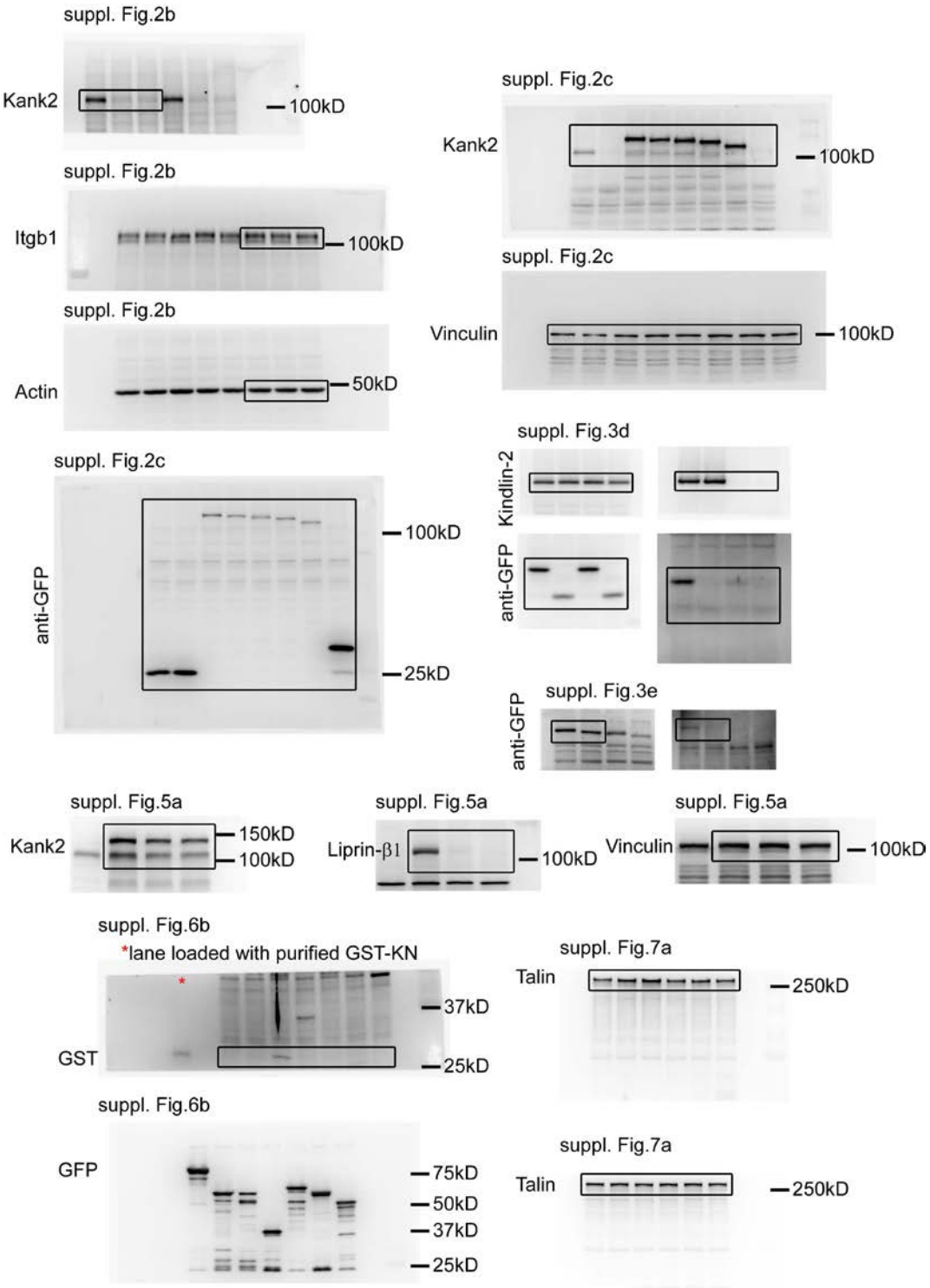

Supplementary Figure 9 continued

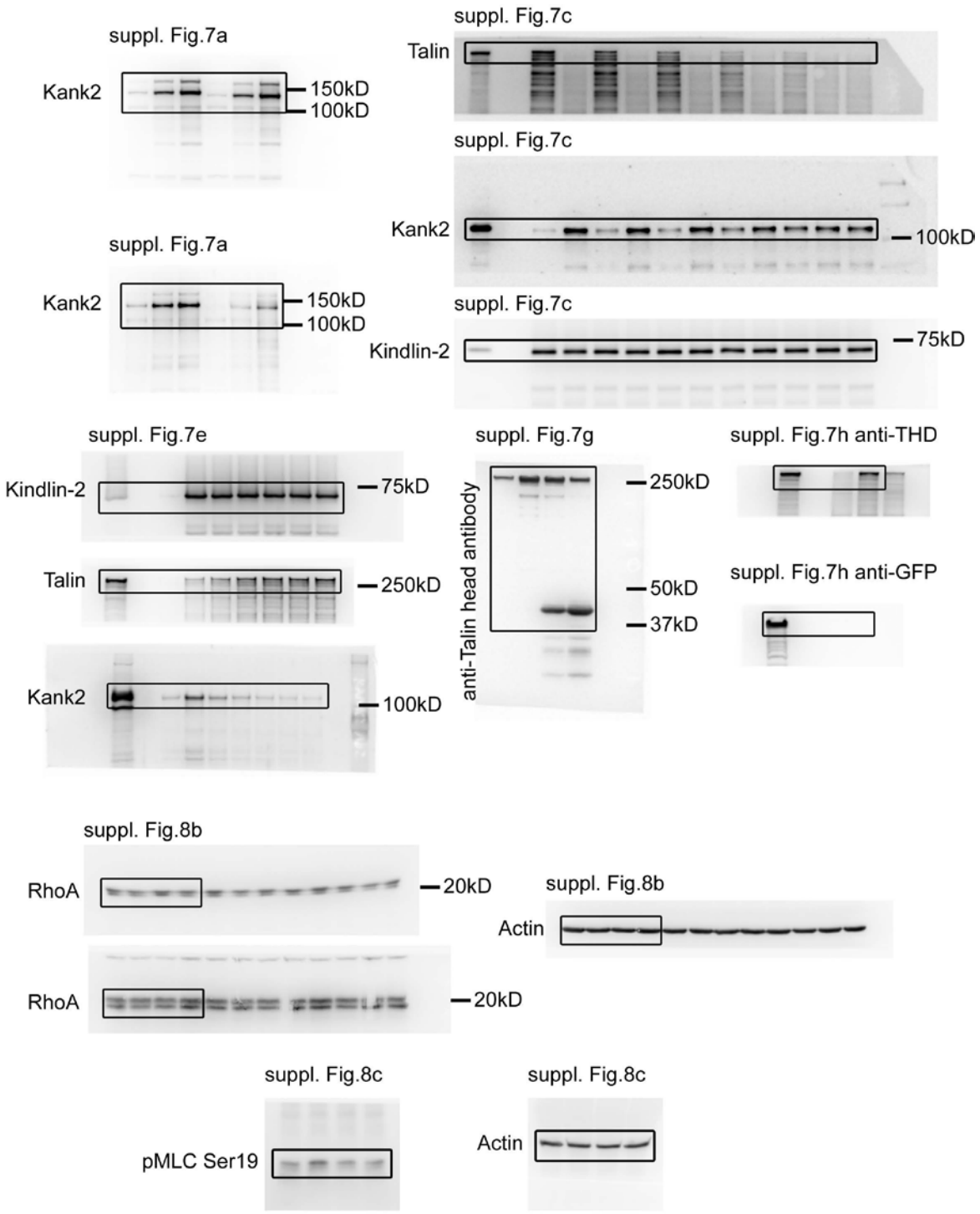

Supplementary Figure 9 continued

6 Outlook

Even though a structure of the autoinhibited talin has been solved in this study, a lot of open questions remain. In this regard, the two elements that could not be placed in the structure, F0/F1 and the dimerization domain, and their role in talin regulation are of high interest.

Positioning the F0/F1 domain of talin's head into the density map resulting from our cryo-EM study was not possible. This is likely due to the unstructured linker between the F0/F1 and F2 domain. It will be interesting to figure out the role in recruitment and activation of these two domains in context with the inhibited structure. An upcoming study shows that the talin head can adopt two conformations through movement of F0/F1, one preventing membrane binding (Goult, unpublished). The mechanism of how talin is recruited to the membrane and how it is activated is not fully understood yet and future studies could help to clarify these events.

Another element that could not be clearly observed within the structure is the dimerization domain of talin. The questions, whether talin forms an inhibited dimer in the cytoplasm and how dimerization influences its inhibition are still open. Future studies of a dimerized inhibited talin might solve these issues.

This study provided evidence that the inhibition of talin is driven by two binding sites: Interactions of F3 with R9 and F2 with R12. The binding interface between F3 and R9 has been studied *in vivo*, by cell and mouse experiments. One study showed that mutation of E1770 to alanine leads to wound healing deficiency (Haage et al., 2018). It is intriguing to perform similar mutation studies in the R12 binding interface *in vivo* to fully understand its implications for talin activation.

Another interesting point to study are talin's many binding partners, such as vinculin, actin, Kank or Rap1. This study showed that some of their interfaces are not accessible in the inhibited state of the talin molecule. To understand the function of talin as mechanosensitive scaffold in adhesions it is vital to uncover the hierarchy of binding events with its partners. It would be interesting to reconstitute a system with talin and different adhesion components *in vitro* to stepwise uncover the events in early adhesion formation. This system would need to include the actin cytoskeleton as well as a membrane with integrin binding sites.

Ultimately, it would be of great interest to structurally characterize an activated/engaged talin in such a reconstituted model system to understand the effects of mechanical tension in focal adhesions.

A lot of studies have been performed to understand talins activation, recruitment and function. Together with this study, it gives us some insight how talin performs its different tasks in the cell. However, future in vitro and in vivo experiments are necessary to fully uncover talin's activation mechanism and the implications it has on cellular processes.

7 References

Anthis, N.J., Wegener, K.L., Critchley, D.R., Campbell, I.D., 2010. Structural Diversity in Integrin/Talin Interactions. Structure/Folding and Design 18, 1654–1666. doi:10.1016/j.str.2010.09.018

Anthis, N.J., Wegener, K.L., Ye, F., Kim, C., Goult, B.T., Lowe, E.D., Vakonakis, I., Bate, N., Critchley, D.R., Ginsberg, M.H., Campbell, I.D., 2009. The structure of an integrin/talin complex reveals the basis of inside-out signal transduction. The EMBO Journal 28, 3623–3632. doi:10.1038/emboj.2009.287

Atherton, P., Ben Stutchbury, Wang, D.-Y., Jethwa, D., Tsang, R., Meiler-Rodriguez, E., Wang, P., Bate, N., Zent, R., Barsukov, I.L., Goult, B.T., Critchley, D.R., Ballestrem, C., 2015. Vinculin controls talin engagement with the actomyosin machinery. Nature Communications 6, 1–12. doi:10.1038/ncomms10038

Austen, K., Ringer, P., Mehlich, A., Chrostek-Grashoff, A., Kluger, C., Klingner, C., Sabass, B., Zent, R., Rief, M., Grashoff, C., 2015. Extracellular rigidity sensing by talin isoform-specific mechanical linkages. Nat Cell Biol 17, 1597–1606. doi:10.1038/ncb3268

Bachir, A.I., Zareno, J., Moissoglu, K., Plow, E.F., Gratton, E., Horwitz, A.R., 2014. Integrin-associated complexes form hierarchically with variable stoichiometry in nascent adhesions. Curr. Biol. 24, 1845–1853. doi:10.1016/j.cub.2014.07.011

Bakolitsa, C., Cohen, D.M., Bankston, L.A., Bobkov, A.A., Cadwell, G.W., Jennings, L., Critchley, D.R., Liddington, S.W.C.R.C., 2004. Structural basis for vinculin activation at sites of cell adhesion. letters to nature 1–4.

Banno A., Goult, B.T., H, L., Bate, N., Critchley, D.R., Ginsberg, M.H., 2012. Subcellular Localization of Talin Is Regulated by Inter-domain Interactions. J. Biol. Chem. 1–15.

Barczyk, M., Carracedo, S., Gullberg, D., 2010. Integrins. Cell Tissue Res. 339, 269–280. doi:10.1007/s00441-009-0834-6

Bays, J.L., DeMali, K.A., 2017. Vinculin in cell–cell and cell–matrix adhesions. Cellular and Molecular Life Sciences 74, 2999–3009. doi:10.1007/s00018-017-2511-3

Benito-Jardón, M., Klapproth, S., Gimeno-LLuch, I., Petzold, T., Bharadwaj, M., Müller, D.J., Zuchtriegel, G., Reichel, C.A., Costell, M., 2017. The fibronectin synergy site re-enforces cell adhesion and mediates a crosstalk between integrin classes. eLife 6, 562. doi:10.7554/eLife.22264

Bhat, M.B., Ma, J., 2002. The transmembrane segment of ryanodine receptor contains an intracellular membrane retention signal for Ca(2+) release channel. J. Biol. Chem. 277, 8597–8601. doi:10.1074/jbc.M107609200

Bledzka, K., Bialkowska, K., Sossey-Alaoui, K., Vaynberg, J., Pluskota, E., Qin, J., Plow, E.F., 2016. Kindlin-2 directly binds actin and regulates integrin outside-in signaling. J Cell Biol 213, 97–108. doi:10.1083/jcb.201501006

Bouaouina, M., Lad, Y., Calderwood, D.A., 2008. The N-terminal domains of talin cooperate with the phosphotyrosine binding-like domain to activate beta1 and beta3 integrins. J. Biol. Chem. 283, 6118–6125. doi:10.1074/jbc.M709527200

Bouchet, B.P., Gough, R.E., Ammon, Y.-C., van de Willige, D., Post, H., Jacquemet, G., Altelaar, A.M., Heck, A.J., Goult, B.T., Akhmanova, A., 2016. Talin-KANK1 interaction controls the recruitment of cortical microtubule stabilizing complexes to focal adhesions. eLife 5, 1–23. doi:10.7554/eLife.18124

Böttcher, R.T., Veelders, M., Rombaut, P., Faix, J., Theodosiou, M., Stradal, T.E., Rottner, K., Zent, R., Herzog, F., Fässler, R., 2017. Kindlin-2 recruits paxillin and Arp2/3 to promote membrane protrusions during initial cell spreading. J Cell Biol 216, 3785–3798. doi:10.1083/jcb.201701176

Brakebusch, C., Fässler, R., 2003. The integrin-actin connection, an eternal love affair. The EMBO Journal 22, 2324–2333. doi:10.1093/emboj/cdg245

Brilot, A.F., Chen, J.Z., Cheng, A., Pan, J., Harrison, S.C., Potter, C.S., Carragher, B., Henderson, R., Grigorieff, N., 2012. Beam-induced motion of vitrified specimen on

holey carbon film. Journal of Structural Biology 177, 630–637. doi:10.1016/j.jsb.2012.02.003
Bromberger, T., Klapproth, S., Rohwedder, I., Zhu, L., Mittmann, L., Reichel, C.A., Sperandio, M., Qin, J., Moser, M., 2018. Direct Rap1/Talin1 interaction regulates platelet and neutrophil integrin activity in mice. Blood 132, 2754–2762. doi:10.1182/blood-2018-04-846766
Burridge, K., Connell, L., 1983. Talin: A cytoskeletal component concentrated in adhesion plaques and other sites of actin-membrane interaction. Cytoskeleton 3, 405–417. doi:10.1002/cm.970030509
Calderwood, D.A., Fujioka, Y., de Pereda, J.M., Garcia-Alvarez, B., Nakamoto, T., Margolis, B., McGlade, C.J., Liddington, R.C., Ginsberg, M.H., 2003. Integrin beta cytoplasmic domain interactions with phosphotyrosine-binding domains: a structural prototype for diversity in integrin signaling. Proc Natl Acad Sci USA 100, 2272–2277. doi:10.1073/pnas.262791999
Calderwood, D.A., Yan, B., de Pereda, J.M., Alvarez, B.G., Fujioka, Y., Liddington, R.C., Ginsberg, M.H., 2002. The phosphotyrosine binding-like domain of talin activates integrins. J. Biol. Chem. 277, 21749–21758. doi:10.1074/jbc.M111996200
Calderwood, D.A., Zent, R., Grant, R., Rees, D.J., Hynes, R.O., Ginsberg, M.H., 1999. The Talin head domain binds to integrin beta subunit cytoplasmic tails and regulates integrin activation. J. Biol. Chem. 274, 28071–28074. doi:10.1074/jbc.274.40.28071
Campbell, I.D., Humphries, M.J., 2011. Integrin structure, activation, and interactions. Cold Spring Harb Perspect Biol 3, a004994–a004994. doi:10.1101/cshperspect.a004994
Carisey, A., Ballestrem, C., 2010. Vinculin, an adapter protein in control of cell adhesion signalling. European Journal of Cell Biology 90, 157–163. doi:10.1016/j.ejcb.2010.06.007
Carisey, A., Tsang, R., Greiner, A.M., Nijenhuis, N., Heath, N., Nazgiewicz, A., Kemkemer, R., Derby, B., Spatz, J., Ballestrem, C., 2013a. Vinculin regulates the recruitment and release of core focal adhesion proteins in a force-dependent manner. Curr. Biol. 23, 271–281. doi:10.1016/j.cub.2013.01.009
Case, L.B., Baird, M.A., Shtengel, G., Campbell, S.L., Hess, H.F., Davidson, M.W., Waterman, C.M., 2015. Molecular mechanism of vinculin activation and nanoscale spatial organization in focal adhesions. Nat Cell Biol 17, 880–892. doi:10.1038/ncb3180
Case, L.B., Waterman, C.M., 2015. Integration of actin dynamics and cell adhesion by a three-dimensional, mechanosensitive molecular clutch. Nat Cell Biol 17, 955–963. doi:10.1038/ncb3191
Cavalcanti-Adam, E.A., Volberg, T., Micoulet, A., Kessler, H., Geiger, B., Spatz, J.P., 2007. Cell Spreading and Focal Adhesion Dynamics Are Regulated by Spacing of Integrin Ligands. Biophysj 92, 2964–2974. doi:10.1529/biophysj.106.089730
Chan, C.E., Odde, D.J., 2008. Traction Dynamics of Filopodia on Compliant Substrates. Science 322, 1687.
Changede, R., Xu, X., Margadant, F., Sheetz, M.P., 2015. Nascent Integrin Adhesions Form on All Matrix Rigidities after Integrin Activation. Dev. Cell 35, 614–621. doi:10.1016/j.devcel.2015.11.001
Chen, H., Cohen, D.M., Choudhury, D.M., Kioka, N., Craig, S.W., 2005. Spatial distribution and functional significance of activated vinculin in living cells. J Cell Biol 169, 459–470. doi:10.1083/jcb.200410100
Chen, W., Lou, J., Zhu, C., 2010. Forcing switch from short- to intermediate- and long-lived states of the alphaA domain generates LFA-1/ICAM-1 catch bonds. J. Biol. Chem. 285, 35967–35978. doi:10.1074/jbc.M110.155770
Chinthalapudi, K., Rangarajan, E.S., Izard, T., 2018a. The interaction of talin with the cell membrane is essential for integrin activation and focal adhesion formation. Proc. Natl. Acad. Sci. U.S.A. 115, 10339–10344. doi:10.1073/pnas.1806275115
Choi, C.K., Vicente-Manzanares, M., Zareno, J., Whitmore, L.A., Mogilner, A., Horwitz, A.R.,

2008. Actin and alpha-actinin orchestrate the assembly and maturation of nascent adhesions in a myosin II motor-independent manner. Nat Cell Biol 10, 1039–1050. doi:10.1038/ncb1763

Choi, C.K., Zareno, J., Digman, M.A., Gratton, E., Horwitz, A.R., 2011. Cross-Correlated Fluctuation Analysis Reveals Phosphorylation-Regulated Paxillin-FAK Complexes in Nascent Adhesions. Biophysj 100, 583–592. doi:10.1016/j.bpj.2010.12.3719

Chung, J.-H., Kim, H.M., 2017. The Nobel Prize in Chemistry 2017: High-Resolution Cryo-Electron Microscopy. AM 47, 218–222. doi:10.9729/AM.2017.47.4.218

Ciobanasu, C., Wang, H., Henriot, V., Mathieu, C., Fente, A., Csillag, S., Vigouroux, C., Faivre, B., Le Clainche, C., 2018. Integrin-bound talin head inhibits actin filament barbed-end elongation. J. Biol. Chem. 293, 2586–2596. doi:10.1074/jbc.M117.808204

Cohen, D.M., Chen, H., Johnson, R.P., Choudhury, B., Craig, S.W., 2005. Two Distinct Head-Tail Interfaces Cooperate to Suppress Activation of Vinculin by Talin. J. Biol. Chem. 280, 17109–17117. doi:10.1074/jbc.M414704200

Cormier, A., Campbell, M.G., Ito, S., Wu, S., Lou, J., Marks, J., Baron, J.L., Nishimura, S.L., Cheng, Y., 2018. Cryo-EM structure of the αvβ8 integrin reveals a mechanism for stabilizing integrin extension. Nat. Struct. Mol. Biol. 25, 698–704. doi:10.1038/s41594-018-0093-x

Dang, I., Gorelik, R., Sousa-Blin, C., Derivery, E., Guérin, C., Linkner, J., Nemethova, M., Dumortier, J.G., Giger, F.A., Chipysheva, T.A., Ermilova, V.D., Vacher, S., Campanacci, V., Herrada, I., Planson, A.-G., Fetics, S., Henriot, V., David, V., Oguievetskaia, K., Lakisic, G., Pierre, F., Steffen, A., Boyreau, A., Peyriéras, N., Rottner, K., Zinn-Justin, S., Cherfils, J., Bièche, I., Alexandrova, A.Y., David, N.B., Small, J.V., Faix, J., Blanchoin, L., Gautreau, A., 2013. Inhibitory signalling to the Arp2/3 complex steers cell migration. Nature 503, 281–284. doi:10.1038/nature12611

de Pereda, J.M., Wegener, K.L., Santelli, E., Bate, N., Ginsberg, M.H., Critchley, D.R., Campbell, I.D., Liddington, R.C., 2005. Structural Basis for Phosphatidylinositol Phosphate Kinase Type Iγ Binding to Talin at Focal Adhesions. J. Biol. Chem. 280, 8381–8386.

De Rosier, D.J., Klug, A., 1968. Reconstruction of three dimensional structures from electron micrographs. Nature 217, 130–134.

del Rio, A., Perez-Jimenez, R., Liu, R., Roca-Cusachs, P., Fernandez, J.M., Sheetz, M.P., 2009a. Stretching single talin rod molecules activates vinculin binding. Science 323, 638–641. doi:10.1126/science.1162912

DeMali, K.A., Barlow, C.A., Burridge, K., 2002. Recruitment of the Arp2/3 complex to vinculin: coupling membrane protrusion to matrix adhesion. J Cell Biol 159, 881–891. doi:10.1083/jcb.200206043

Di Paolo, G., Pellegrini, L., Letinic, K., Cestra, G., Zoncu, R., Voronov, S., Chang, S., Guo, J., Wenk, M.R., De Camilli, P., 2002. Recruitment and regulation of phosphatidylinositol phosphate kinase type 1γ by the FERM domain of talin. Nature 420, 85–89.

Diez, G., List, F., Smith, J., Ziegler, W.H., Goldmann, W.H., 2008. Direct evidence of vinculin tail–lipid membrane interaction in beta-sheet conformation. Biochem. Biophys. Res. Commun. 373, 69–73. doi:10.1016/j.bbrc.2008.05.182

Dubochet, J., Lepault, R., Berriman, A., Homo, J.C., 1982. Electron microscopy of frozen water and aqueous solutions. Journal of Microscopy 1–19.

Elliott, P.R., Goult, B.T., Kopp, P.M., Bate, N., Grossmann, J.G., Roberts, G.C.K., Critchley, D.R., Barsukov, I.L., 2010. The Structure of the Talin Head Reveals a Novel Extended Conformation of the FERM Domain. Structure/Folding and Design 18, 1289–1299. doi:10.1016/j.str.2010.07.011

Ellis, S.J., Pines, M., Fairchild, M.J., Tanentzapf, G., 2011. In vivo functional analysis reveals specific roles for the integrin-binding sites of talin. J Cell Sci 124, 1844–1856. doi:10.1242/jcs.083337

Elosegui-Artola, A., Oria, R., Chen, Y., Kosmalska, A., Pérez-González, C., Castro, N., Zhu, C., Trepat, X., Roca-Cusachs, P., n.d. Mechanical regulation of a molecular clutch defines

force transmission and transduction in response to matrix rigidity. Nat Cell Biol 18, 540 EP –.
Engler, A.J., Sen, S., Sweeney, H.L., Discher, D.E., 2006. Matrix elasticity directs stem cell lineage specification. Cell 126, 677–689. doi:10.1016/j.cell.2006.06.044
Ezratty, E.J., Bertaux, C., Marcantonio, E.E., Gundersen, G.G., 2009. Clathrin mediates integrin endocytosis for focal adhesion disassembly in migrating cells. J Cell Biol 187, 733–747. doi:10.1083/jcb.200904054
Ezratty, E.J., Partridge, M.A., Gundersen, G.G., 2005. Microtubule-induced focal adhesion disassembly is mediated by dynamin and focal adhesion kinase. Nat Cell Biol 7, 581–590. doi:10.1038/ncb1262
Franco, S.J., Rodgers, M.A., Perrin, B.J., Han, J., Bennin, D.A., Critchley, D.R., Huttenlocher, A., 2004. Calpain-mediated proteolysis of talin regulates adhesion dynamics. Nat Cell Biol 6, 977–983. doi:10.1038/ncb1175
Friedland, J.C., Lee, M.H., Boettiger, D., 2009. Mechanically activated integrin switch controls alpha5beta1 function. Science 323, 642–644. doi:10.1126/science.1168441
Fukuda, K., Bledzka, K., Yang, J., Perera, H.D., Plow, E.F., Qin, J., 2014. Molecular basis of kindlin-2 binding to integrin-linked kinase pseudokinase for regulating cell adhesion. J. Biol. Chem. 289, 28363–28375. doi:10.1074/jbc.M114.596692
Gardel, M.L., Schneider, I.C., Aratyn-Schaus, Y., Waterman, C.M., 2010. Mechanical Integration of Actin and Adhesion Dynamics in Cell Migration. Annu. Rev. Cell Dev. Biol. 26, 315–333. doi:10.1146/annurev.cellbio.011209.122036
Gee, H.Y., Zhang, F., Ashraf, S., Kohl, S., Sadowski, C.E., Vega-Warner, V., Zhou, W., Lovric, S., Fang, H., Nettleton, M., Zhu, J.-Y., Hoefele, J., Weber, L.T., Podracka, L., Boor, A., Fehrenbach, H., Innis, J.W., Washburn, J., Levy, S., Lifton, R.P., Otto, E.A., Han, Z., Hildebrandt, F., 2015. KANK deficiency leads to podocyte dysfunction and nephrotic syndrome. J. Clin. Invest. 125, 2375–2384. doi:10.1172/JCI79504
Geiger, B., 1979. A 130K Protein from Chicken Gizzard: Its Localization at the Termini of Microfilament Bundles in Cultured. Cell 1–13.
Geiger, B., Tokuyasu, K.T., Dutton, A.H., Singer, S.J., 1980. Vinculin, an intracellular protein localized at specialized sites where microfilament bundles terminate at cell membranes. Proc Natl Acad Sci USA 77, 4127–4131. doi:10.1073/pnas.77.7.4127
Gingras, A.R., Bate, N., Goult, B.T., Hazelwood, L., Canestrelli, I., Grossmann, J.G., Liu, H., Putz, N.S.M., Roberts, G.C.K., Volkmann, N., Hanein, D., Barsukov, I.L., Critchley, D.R., 2008. The structure of the C-terminal actin-binding domain of talin. The EMBO Journal 27, 458–469. doi:10.1038/sj.emboj.7601965
Gingras, A.R., Bate, N., Goult, B.T., Patel, B., Kopp, P.M., Emsley, J., Barsukov, I.L., Roberts, G.C.K., Critchley, D.R., 2010a. Central region of talin has a unique fold that binds vinculin and actin. J. Biol. Chem. 285, 29577–29587. doi:10.1074/jbc.M109.095455
Gingras, A.R., Lagarrigue, F., Cuevas, M.N., Valadez, A.J., Zorovich, M., McLaughlin, W., Lopez-Ramirez, M.A., Seban, N., Ley, K., Kiosses, W.B., Ginsberg, M.H., 2019. Rap1 binding and a lipid-dependent helix in talin F1 domain promote integrin activation in tandem. J Cell Biol 78, jcb.201810061–11. doi:10.1083/jcb.201810061
Gingras, A.R., Ziegler, W.H., Frank, R., Barsukov, I.L., Roberts, G.C.K., Critchley, D.R., Emsley, J., 2005. Mapping and consensus sequence identification for multiple vinculin binding sites within the talin rod. J. Biol. Chem. 280, 37217–37224. doi:10.1074/jbc.M508060200
Goksoy, E., Ma, Y.-Q., Wang, X., Kong, X., Perera, D., Plow, E.F., Qin, J., 2008. Structural Basis for the Autoinhibition of Talin in Regulating Integrin Activation. Molecular Cell 31, 124–133. doi:10.1016/j.molcel.2008.06.011
Goldmann, W.H., Isenberg, G., 1991. Kinetic determination of talin-actin binding. Biochem. Biophys. Res. Commun. 178, 718–723.
Golji, J., Mofrad, M.R.K., 2014. The talin dimer structure orientation is mechanically regulated. Biophys. J. 107, 1802–1809. doi:10.1016/j.bpj.2014.08.038
Golji, J., Mofrad, M.R.K., 2010. A Molecular Dynamics Investigation of Vinculin Activation.

Biophysj 99, 1073–1081. doi:10.1016/j.bpj.2010.05.024
Golji, J., Wendorff, T., Mofrad, M.R.K., 2012. Phosphorylation Primes Vinculin for Activation. Biophysj 102, 2022–2030. doi:10.1016/j.bpj.2012.01.062
Gough, R.E., Goult, B.T., 2018a. The tale of two talins - two isoforms to fine-tune integrin signalling. FEBS Lett 592, 2108–2125. doi:10.1002/1873-3468.13081
Goult, B.T., Bouaouina, M., Elliott, P.R., Bate, N., Patel, B., Gingras, A.R., Grossmann, J.G., Roberts, G.C.K., Calderwood, D.A., Critchley, D.R., Barsukov, I.L., 2010b. Structure of a double ubiquitin-like domain in the talin head: a role in integrin activation. EMBO J 29, 1069.
Goult, B.T., Xu, X.-P., Gingras, A.R., Swift, M., Patel, B., Bate, N., Kopp, P.M., Barsukov, I.L., Critchley, D.R., Volkmann, N., Hanein, D., 2013a. Structural studies on full-length talin1 reveal a compact auto-inhibited dimer: Implications for talin activation. Journal of Structural Biology 184, 21–32. doi:10.1016/j.jsb.2013.05.014
Goult, B.T., Yan, J., Schwartz, M.A., 2018. Talin as a mechanosensitive signaling hub. J Cell Biol 217, 3776–3784. doi:10.1083/jcb.201808061
Goult, B.T., Zacharchenko, T., Bate, N., Tsang, R., Hey, F., Gingras, A.R., Elliott, P.R., Roberts, G.C.K., Ballestrem, C., Critchley, D.R., Barsukov, I.L., 2013b. RIAM and vinculin binding to talin are mutually exclusive and regulate adhesion assembly and turnover. J. Biol. Chem. 288, 8238–8249. doi:10.1074/jbc.M112.438119
Grashoff, C., Hoffman, B.D., Brenner, M.D., Zhou, R., Parsons, M., Yang, M.T., McLean, M.A., Sligar, S.G., Chen, C.S., Ha, T., Schwartz, M.A., 2010. Measuring mechanical tension across vinculin reveals regulation of focal adhesion dynamics. Nature 466, 263–266. doi:10.1038/nature09198
Gunawan, M., Venkatesan, N., Loh, J.T., Wong, J.F., Berger, H., Neo, W.H., Li, L.Y.J., La Win, M.K., Yau, Y.H., Guo, T., See, P.C.E., Yamazaki, S., Chin, K.C., Gingras, A.R., Shochat, S.G., Ng, L.G., Sze, S.K., Ginhoux, F., Su, I.-H., 2015. The methyltransferase Ezh2 controls cell adhesion and migration through direct methylation of the extranuclear regulatory protein talin. Nat. Immunol. 16, 505–516. doi:10.1038/ni.3125
Haage, A., Goodwin, K., Whitewood, A., Camp, D., Bogutz, A., Turner, C.T., Granville, D.J., Lefebvre, L., Plotnikov, S., Goult, B.T., Tanentzapf, G., 2018. Talin Autoinhibition Regulates Cell-ECM Adhesion Dynamics and Wound Healing In Vivo. CellReports 25, 2401–2416.e5. doi:10.1016/j.celrep.2018.10.098
Harburger, D.S., Bouaouina, M., Calderwood, D.A., 2009. Kindlin-1 and -2 directly bind the C-terminal region of beta integrin cytoplasmic tails and exert integrin-specific activation effects. J. Biol. Chem. 284, 11485–11497. doi:10.1074/jbc.M809233200
Hemmings, L., Rees, D.J., Ohanian, V., Bolton, S.J., Gilmore, A.P., Patel, B., Priddle, H., Trevithick, J.E., Hynes, R.O., Critchley, D.R., 1996. Talin contains three actin-binding sites each of which is adjacent to a vinculin-binding site. J Cell Sci 109 (Pt 11), 2715–2726.
Hensley, M.R., Cui, Z., Chua, R.F.M., Simpson, S., Shammas, N.L., Yang, J.-Y., Leung, Y.F., Zhang, G., 2016. Evolutionary and developmental analysis reveals KANK genes were co-opted for vertebrate vascular development. Sci Rep 6, 27816. doi:10.1038/srep27816
Horton, E.R., Byron, A., Askari, J.A., Ng, D.H.J., Millon-Frémillon, A., Robertson, J., Koper, E.J., Paul, N.R., Warwood, S., Knight, D., Humphries, J.D., Humphries, M.J., 2015. Definition of a consensus integrin adhesome and its dynamics during adhesion complex assembly and disassembly. Nat Cell Biol 17, 1577–1587. doi:10.1038/ncb3257
Horton, E.R., Humphries, J.D., James, J., Jones, M.C., Askari, J.A., Humphries, M.J., 2016. The integrin adhesome network at a glance. J Cell Sci 129, 4159–4163. doi:10.1242/jcs.192054
Horwitz, A., Duggan, K., Buck, C., Beckerle, M.C., Burridge, K., 1986. Interaction of plasma membrane fibronectin receptor with talin—a transmembrane linkage. Nature 320, 531–533. doi:10.1038/320531a0

Hu, S., Tee, Y.-H., Kabla, A., Zaidel-Bar, R., Bershadsky, A., Hersen, P., 2015. Structured illumination microscopy reveals focal adhesions are composed of linear subunits. Cytoskeleton (Hoboken) 72, 235–245. doi:10.1002/cm.21223

Hughes, P.E., O'Toole, T.E., Ylänne, J., Shattil, S.J., Ginsberg, M.H., 1995. The conserved membrane-proximal region of an integrin cytoplasmic domain specifies ligand binding affinity. J. Biol. Chem. 270, 12411–12417.

Humphries, J.D., Byron, A., Bass, M.D., Craig, S.E., Pinney, J.W., Knight, D., Humphries, M.J., 2009. Proteomic analysis of integrin-associated complexes identifies RCC2 as a dual regulator of Rac1 and Arf6. Sci Signal 2, ra51–ra51. doi:10.1126/scisignal.2000396

Hynes, R.O., 1987. Integrins: A family of cell surface receptors. Cell 48, 549–554.

Izard, T., Evans, G., Borgon, R.A., Rush, C.L., Bricogne, G., Bois, P.R.J., 2004. Vinculin activation by talin through helical bundle conversion. Nature 427, 171–175. doi:10.1038/nature02281

J, H., Monkley, S.J., Critchley, D.R., Petrich, B.G., 2011. Talin-dependent integrin activation is required for fibrin clot retraction by platelets. Blood 1–5. doi:10.1182/blood

Jannie, K.M., Ellerbroek, S.M., Zhou, D.W., Chen, S., Crompton, D.J., García, A.J., DeMali, K.A., 2015. Vinculin-dependent actin bundling regulates cell migration and traction forces. Biochem. J. 465, 383–393. doi:10.1042/BJ20140872

Johnson, M.S., Lu, N., Denessiouk, K., Heino, J., Gullberg, D., 2009. Integrins during evolution: evolutionary trees and model organisms. Biochim. Biophys. Acta 1788, 779–789. doi:10.1016/j.bbamem.2008.12.013

Kalli AC., Campbell, I.D., Marc, S., 2011. Multiscale simulations suggest a mechanism for integrin inside-out activation. PNAS 1–6. doi:10.1073/pnas.1104505108

Kanchanawong, P., Shtengel, G., Pasapera, A.M., Ramko, E.B., Davidson, M.W., Hess, H.F., Waterman, C.M., 2010. Nanoscale architecture of integrin-based cell adhesions. Nature 468, 580–584. doi:10.1038/nature09621

Klapholz, B., Brown, N.H., 2017. Talin – the master of integrin adhesions. J Cell Sci 130, 2435–2446. doi:10.1242/jcs.190991

Klapholz, B., Herbert, S.L., Wellmann, J., Johnson, R., Parsons, M., Brown, N.H., 2015. Alternative mechanisms for talin to mediate integrin function. Curr. Biol. 25, 847–857. doi:10.1016/j.cub.2015.01.043

Kopp, P.M., Bate, N., Hansen, T.M., BRINDLE, N.P.J., Praekelt, U., Debrand, E., Coleman, S., Mazzeo, D., Goult, B.T., Gingras, A.R., Pritchard, C.A., Critchley, D.R., Monkley, S.J., 2010a. Studies on the morphology and spreading of human endothelial cells define key inter- and intramolecular interactions for talin1. European Journal of Cell Biology 89, 661–673. doi:10.1016/j.ejcb.2010.05.003

Kumar, A., Anderson, K.L., Swift, M.F., Hanein, D., Volkmann, N., Schwartz, M.A., 2018. Local Tension on Talin in Focal Adhesions Correlates with F-Actin Alignment at the Nanometer Scale. Biophysj 115, 1569–1579. doi:10.1016/j.bpj.2018.08.045

Kumar, A., Ouyang, M., Van den Dries, K., McGhee, E.J., Tanaka, K., Anderson, M.D., Groisman, A., Goult, B.T., Anderson, K.I., Schwartz, M.A., 2016. Correction: Talin tension sensor reveals novel features of focal adhesion force transmission and mechanosensitivity. J Cell Biol 214, 231–231. doi:10.1083/jcb.20151001207062016c

Kuo, J.-C., Han, X., Hsiao, C.-T., Yates, J.R., III, Waterman, C.M., 2011. Analysis of the myosin-II-responsive focal adhesion proteome reveals a role for β-Pix in negative regulation of focal adhesion maturation. Nat Cell Biol 13, 383–9. doi:10.1038/ncb2216

Lagarrigue, F., Kim, C., Ginsberg, M.H., 2016. The Rap1-RIAM-talin axis of integrin activation and blood cell function. Blood 128, 479–487. doi:10.1182/blood-2015-12-638700

Larson, R.S., Corbi, A.L., Berman, L., Springer, T., 1989. Primary structure of the leukocyte function-associated molecule-1 alpha subunit: an integrin with an embedded domain defining a protein superfamily. J Cell Biol 108, 703.

Lau, T.-L., Kim, C., Ginsberg, M.H., Ulmer, T.S., 2009. The structure of the integrin αIIbβ3 transmembrane complex explains integrin transmembrane signalling. The EMBO Journal 1–11. doi:10.1038/emboj.2009.63

Le Clainche, C., Dwivedi, S.P., Didry, D., Carlier, M.-F., 2010. Vinculin is a dually regulated actin filament barbed end-capping and side-binding protein. J. Biol. Chem. 285, 23420–23432. doi:10.1074/jbc.M110.102830

Lee, H.-S., Bellin, R.M., Walker, D.L., Patel, B., Powers, P., Liu, H., Garcia-Alvarez, B., de Pereda, J.M., Liddington, R.C., Volkmann, N., Hanein, D., Critchley, D.R., Robson, R.M., 2004. Characterization of an Actin-binding Site within the Talin FERM Domain. Journal of Molecular Biology 343, 771–784. doi:10.1016/j.jmb.2004.08.069

Lee, H.-S., Lim, C.J., Puzon-McLaughlin, W., Shattil, S.J., Ginsberg, M.H., 2009. RIAM activates integrins by linking talin to ras GTPase membrane-targeting sequences. J. Biol. Chem. 284, 5119–5127. doi:10.1074/jbc.M807117200

Lee, J.O., Rieu, P., Arnaout, M.A., Liddington, R., 1995. Crystal structure of the A domain from the alpha subunit of integrin CR3 (CD11b/CD18). Cell 80, 631–638.

Lefort, C.T., Rossaint, J., Moser, M., Petrich, B.G., Zarbock, A., Monkley, S.J., Critchley, D.R., Ginsberg, M.H., Fassler, R., Ley, K., 2012. Distinct roles for talin-1 and kindlin-3 in LFA-1 extension and affinity regulation. Blood 119, 4275–4282. doi:10.1182/blood-2011-08-373118

Legate, K.R., Fässler, R., 2009. Mechanisms that regulate adaptor binding to beta-integrin cytoplasmic tails. J Cell Sci 122, 187–198. doi:10.1242/jcs.041624

Legate, K.R., Takahashi, S., Bonakdar, N., Ben Fabry, Boettiger, D., Zent, R., ssler, R.F.A., 2011. Integrin adhesion and force coupling are independently regulated by localized PtdIns(4,5)2 synthesis. The EMBO Journal 1–16. doi:10.1038/emboj.2011.332

Lewellyn, L., Cetera, M., Horne-Badovinac, S., 2013. Misshapen decreases integrin levels to promote epithelial motility and planar polarity in Drosophila. J Cell Biol 200, 721–729. doi:10.1083/jcb.201209129

Li, C.-C., Kuo, J.-C., Waterman, C.M., Kiyama, R., Moss, J., Vaughan, M., 2011. Effects of brefeldin A-inhibited guanine nucleotide-exchange (BIG) 1 and KANK1 proteins on cell polarity and directed migration during wound healing. Proc. Natl. Acad. Sci. U.S.A. 108, 19228–19233. doi:10.1073/pnas.1117011108

Li, G., Du, X., Vass, W.C., Papageorge, A.G., Lowy, D.R., Qian, X., 2011. Full activity of the deleted in liver cancer 1 (DLC1) tumor suppressor depends on an LD-like motif that binds talin and focal adhesion kinase (FAK). Proc. Natl. Acad. Sci. U.S.A. 108, 17129–17134. doi:10.1073/pnas.1112122108

Li, H., Deng, Y., Sun, K., Yang, H., Liu, J., Wang, M., Zhang, Z., Lin, J., Wu, C., Wei, Z., Yu, C., 2017. Structural basis of kindlin-mediated integrin recognition and activation. Proc Natl Acad Sci USA 114, 9349–9354. doi:10.1073/pnas.1703064114

Li, J., Springer, T.A., 2017. Integrin extension enables ultrasensitive regulation by cytoskeletal force. Proc. Natl. Acad. Sci. U.S.A. 114, 4685–4690. doi:10.1073/pnas.1704171114

Li, X., Mooney, P., Zheng, S., Booth, C.R., Braunfeld, M.B., Gubbens, S., Agard, D.A., Cheng, Y., 2013. Electron counting and beam-induced motion correction enable near-atomic-resolution single-particle cryo-EM. Nat Methods 10, 584–590. doi:10.1038/nmeth.2472

Liu, J., Wang, Y., Goh, W.I., Goh, H., Baird, M.A., Ruehland, S., Teo, S., Bate, N., Critchley, D.R., Davidson, M.W., Kanchanawong, P., 2015. Talin determines the nanoscale architecture of focal adhesions. Proc Natl Acad Sci USA 112, E4864–E4873. doi:10.1073/pnas.1512025112

Loveland, A.B., Demo, G., Grigorieff, N., Korostelev, A.A., 2017. Ensemble cryo-EM elucidates the mechanism of translation fidelity. Nature 546, 113–117. doi:10.1038/nature22397

Luo, B.-H., Carman, C.V., Springer, T.A., 2007a. Structural basis of integrin regulation and signaling. Annu. Rev. Immunol. 25, 619–647.

doi:10.1146/annurev.immunol.25.022106.141618
Luo, B.-H., Carman, C.V., Takagi, J., Springer, T.A., 2005. Disrupting integrin transmembrane domain heterodimerization increases ligand binding affinity, not valency or clustering. Proc Natl Acad Sci USA 102, 3679–3684. doi:10.1073/pnas.0409440102
Margadant, F., Chew, L.L., Hu, X., Yu, H., Bate, N., Zhang, X., Sheetz, M., 2011. Mechanotransduction In Vivo by Repeated Talin Stretch-Relaxation Events Depends upon Vinculin. PLOS Biology 9, e1001223. doi:10.1371/journal.pbio.1001223
Matus, D.Q., Chang, E., Makohon-Moore, S.C., Hagedorn, M.A., Chi, Q., Sherwood, D.R., 2014. Cell division and targeted cell cycle arrest opens and stabilizes basement membrane gaps. Nature Communications 5, 4184. doi:10.1038/ncomms5184
Mitchison, T., Kirschner, M., 1988. Cytoskeletal dynamics and nerve growth. Neuron 1, 761–772.
Monkley, S.J., Pritchard, C.A., Critchley, D.R., 2001b. Analysis of the Mammalian Talin2 Gene TLN2. Biochem. Biophys. Res. Commun. 286, 880–885. doi:10.1006/bbrc.2001.5497
Monkley, S.J., Zhou, X.H., Kinston, S.J., Giblett, S.M., Hemmings, L., Priddle, H., Brown, J.E., Pritchard, C.A., Critchley, D.R., Fassler, R., 2000. Disruption of the talin gene arrests mouse development at the gastrulation stage. Dev. Dyn. 219, 560–574. doi:10.1002/1097-0177
Montanez, E., Ussar, S., Schifferer, M., Bösl, M., Zent, R., Moser, M., Fässler, R., 2008. Kindlin-2 controls bidirectional signaling of integrins. Genes Dev. 22, 1325–1330. doi:10.1101/gad.469408
Moore, T.I., Aaron, J., Chew, T.-L., Springer, T.A., 2018. Measuring Integrin Conformational Change on the Cell Surface with Super-Resolution Microscopy. CellReports 22, 1903–1912. doi:10.1016/j.celrep.2018.01.062
Moser, M., Bauer, M., Schmid, S., Ruppert, R., Schmidt, S., Sixt, M., Wang, H.-V., Sperandio, M., Fässler, R., 2009. Kindlin-3 is required for beta2 integrin-mediated leukocyte adhesion to endothelial cells. Nat. Med. 15, 300–305. doi:10.1038/nm.1921
Moser, M., Nieswandt, B., Ussar, S., Pozgajova, M., Fässler, R., 2008. Kindlin-3 is essential for integrin activation and platelet aggregation. Nat. Med. 14, 325–330. doi:10.1038/nm1722
Muguruma, M., Matsumura, S., Fukazawa, T., 1990. Direct interactions between talin and actin. Biochem. Biophys. Res. Commun. 171, 1217–1223.
Nakane, T., Kimanius, D., Lindahl, E., Scheres, S.H., 2018. Characterisation of molecular motions in cryo-EM single-particle data by multi-body refinement in RELION. eLife 7, 1485. doi:10.7554/eLife.36861
Nordenfelt, P., Moore, T.I., Mehta, S.B., Kalappurakkal, J.M., Swaminathan, V., Koga, N., Lambert, T.J., Baker, D., Waters, J.C., Oldenbourg, R., Tani, T., Mayor, S., Waterman, C.M., Springer, T.A., 2017. Direction of actin flow dictates integrin LFA-1 orientation during leukocyte migration. Nature Communications 8, 2047. doi:10.1038/s41467-017-01848-y
Partridge, A.W., Liu, S., Kim, S., Bowie, J.U., Ginsberg, M.H., 2005. Transmembrane domain helix packing stabilizes integrin alphaIIbbeta3 in the low affinity state. J. Biol. Chem. 280, 7294–7300. doi:10.1074/jbc.M412701200
Paszek, M.J., DuFort, C.C., Rubashkin, M.G., Davidson, M.W., Thorn, K.S., Liphardt, J.T., Weaver, V.M., n.d. Scanning angle interference microscopy reveals cell dynamics at the nanoscale. Nat Methods 9, 825 EP –.
Petrich, B.G., Marchese, P., Ruggeri, Z.M., Spiess, S., Weichert, R.A.M., Ye, F., Tiedt, R., Skoda, R.C., Monkley, S.J., Critchley, D.R., Ginsberg, M.H., 2007. Talin is required for integrin-mediated platelet function in hemostasis and thrombosis. J Exp Med 204, 3103–3111. doi:10.1084/jem.20071800
Goult B, Zacharchenko T, Bate N, Tsang R, Hey F, Gingras A, Elliot P, Roberts G, Ballestrem C., Critchley D., Barsukov I. RIAM and Vinculin Binding to Talin Are

Mutually Exclusive and Regulate Adhesion Assembly and Turnover, 2013. RIAM and Vinculin Binding to Talin Are Mutually Exclusive and Regulate Adhesion Assembly and Turnover 1–29.

Roca-Cusachs, P., del Rio, A., Puklin-Faucher, E., Gauthier, N.C., Biais, N., Sheetz, M.P., 2013. Integrin-dependent force transmission to the extracellular matrix by α-actinin triggers adhesion maturation. PNAS 1–10. doi:10.1073/pnas.1220723110/-/DCSupplemental

Rossier, O., Octeau, V., Sibarita, J.-B., Leduc, C., Tessier, B., Nair, D., Gatterdam, V., Destaing, O., Albigès-Rizo, C., Tampé, R., Cognet, L., Choquet, D., Lounis, B., Giannone, G., 2012. Integrins β1 and β3 exhibit distinct dynamic nanoscale organizations inside focal adhesions. Nat Cell Biol 14, 1057–1067. doi:10.1038/ncb2588

Roy, B.C., Kakinuma, N., Kiyama, R., 2009. Kank attenuates actin remodeling by preventing interaction between IRSp53 and Rac1. J Cell Biol 184, 253–267. doi:10.1083/jcb.200805147

Ruskin, R.S., Yu, Z., Grigorieff, N., 2013. Quantitative characterization of electron detectors for transmission electron microscopy. Journal of Structural Biology 184, 385–393. doi:10.1016/j.jsb.2013.10.016

Santala, P., Heino, J., 1991. Regulation of integrin-type cell adhesion receptors by cytokines. J. Biol. Chem. 266, 23505–23509.

Sarkar, S., Roy, B.C., Hatano, N., Aoyagi, T., Gohji, K., Kiyama, R., 2002. A novel ankyrin repeat-containing gene (Kank) located at 9p24 is a growth suppressor of renal cell carcinoma. J. Biol. Chem. 277, 36585–36591. doi:10.1074/jbc.M204244200

Sawada, Y., Tamada, M., Dubin-Thaler, B.J., Cherniavskaya, O., Sakai, R., Tanaka, S., Sheetz, M.P., 2006. Force sensing by mechanical extension of the Src family kinase substrate p130Cas. Cell 127, 1015–1026. doi:10.1016/j.cell.2006.09.044

Scheres, S.H., 2014. Beam-induced motion correction for sub-megadalton cryo-EM particles. eLife 3, e03665. doi:10.7554/eLife.03665

Schiemer, J., Bohm, A., Lin, L., Merrill-Skoloff, G., Flaumenhaft, R., Huang, J.-S., Le Breton, G.C., Chishti, A.H., 2016. Gα 13Switch Region 2 Relieves Talin Autoinhibition to Activate αIIbβ3 Integrin. J. Biol. Chem. 291, 26598–26612. doi:10.1074/jbc.M116.747279

Schibata A., Chen L., Nagai R., Ishidate F., Chada R., Miwa., Naruse K., Shirai Y., Fujiwara T., Kusumi A., 2013. Rac1 Recruitment to the Archipelago Structure of the Focal Adhesion through the Fluid Membrane as Revealed by Single-Molecule Analysis 1–17. doi:10.1002/cm.21097)

Schiller, H.B., Fässler, R., 2013. Mechanosensitivity and compositional dynamics of cell–matrix adhesions. Nature Publishing Group 14, 509–519. doi:10.1038/embor.2013.49

Schmidt, J.M.E.A., 1999. Interaction of Talin with Actin: Sensitive Modulation of Filament Crosslinking Activity 1–12.

Schoen, I., Pruitt, B.L., Vogel, V., 2013. The Yin-Yang of Rigidity Sensing: How Forces and Mechanical Properties Regulate the Cellular Response to Materials. Annu. Rev. Mater. Res. 43, 589–618. doi:10.1146/annurev-matsci-062910-100407

Sen, M., Yuki, K., Springer, T.A., 2013. An internal ligand-bound, metastable state of a leukocyte integrin, αXβ2. J Cell Biol 203, 629–642. doi:10.1083/jcb.201308083

Shen, K., Tolbert, C.E., Guilluy, C., Swaminathan, V.S., Berginski, M.E., Burridge, K., Superfine, R., Campbell, S.L., 2011. The vinculin C-terminal hairpin mediates F-actin bundle formation, focal adhesion, and cell mechanical properties. J. Biol. Chem. 286, 45103–45115. doi:10.1074/jbc.M111.244293

Smilenov, L.B., Mikhailov, A., Pelham, R.J., Marcantonio, E.E., Gundersen, G.G., 1999. Focal adhesion motility revealed in stationary fibroblasts. Science 286, 1172–1174.

Song, X., Yang, J., Hirbawi, J., Ye, S., Perera, H.D., Goksoy, E., Dwivedi, P., Plow, E.F., Zhang, R., Qin, J., 2012a. A novel membrane-dependent on/off switch mechanism of talin FERM domain at sites of cell adhesion. Nature Publishing Group 22, 1533–1545.

doi:10.1038/cr.2012.97
Spiess, M., Hernandez-Varas, P., Oddone, A., Olofsson, H., Blom, H., Waithe, D., Lock, J.G., Lakadamyali, M., Strömblad, S., 2018. Active and inactive β1 integrins segregate into distinct nanoclusters in focal adhesions. J Cell Biol 217, 1929–1940. doi:10.1083/jcb.201707075
Springer, T.A., Dustin, M.L., 2012. Integrin inside-out signaling and the immunological synapse. Current Opinion in Cell Biology 24, 107–115. doi:10.1016/j.ceb.2011.10.004
Springer, T.A., Zhu, J., Xiao, T., 2008. Structural basis for distinctive recognition of fibrinogen gammaC peptide by the platelet integrin alphaIIbbeta3. J Cell Biol 182, 791–800. doi:10.1083/jcb.200801146
Stehbens, S.J., Paszek, M., Pemble, H., Ettinger, A., Gierke, S., Wittmann, T., 2014. CLASPs link focal-adhesion-associated microtubule capture to localized exocytosis and adhesion site turnover. Nat Cell Biol 16, 561–573. doi:10.1038/ncb2975
Strohmeyer, N., Bharadwaj, M., Costell, M., Fässler, R., Müller, D.J., 2017. Fibronectin-bound α5β1 integrins sense load and signal to reinforce adhesion in less than a second. Nat Mater 16, 1262–1270. doi:10.1038/nmat5023
Sun, N., Critchley, D.R., Paulin, D., Li, Z., Robson, R.M., 2008. Identification of a repeated domain within mammalian α-synemin that interacts directly with talin. Experimental Cell Research 314, 1839–1849. doi:10.1016/j.yexcr.2008.01.034
Sun, Z., Costell, M., Fässler, R., 2018. Integrin activation by talin, kindlin and mechanical forces. Nat Cell Biol 1–7. doi:10.1038/s41556-018-0234-9
Sun, Z., Tseng, H.-Y., Tan, S., Senger, F., Kurzawa, L., Dedden, D., Mizuno, N., Wasik, A.A., Thery, M., Dunn, A.R., Fässler, R., 2016. Kank2 activates talin, reduces force transduction across integrins and induces central adhesion formation. Nat Cell Biol 18, 941–953. doi:10.1038/ncb3402
Suzuki, J.-I., Roy, B.C., Ogaeri, T., Kakinuma, N., Kiyama, R., 2017. Depletion of tumor suppressor Kank1 induces centrosomal amplification via hyperactivation of RhoA. Experimental Cell Research 353, 79–87. doi:10.1016/j.yexcr.2017.03.006
Swaminathan, V., Waterman, C.M., n.d. The molecular clutch model for mechanotransduction evolves. Nat Cell Biol 18, 459 EP –.
Tadokoro, S., Shattil, S.J., Eto, K., Tai, V., Liddington, R.C., de Pereda, J.M., Ginsberg, M.H., Calderwood, D.A., 2003. Talin binding to integrin beta tails: a final common step in integrin activation. Science 302, 103–106. doi:10.1126/science.1086652
Takagi, J., Petre, B.M., Walz, T., Springer, T.A., 2002. Global conformational rearrangements in integrin extracellular domains in outside-in and inside-out signaling. Cell 110, 599–511.
Tamkun, J.W., DeSimone, D.W., Fonda, D., Patel, R.S., Buck, C., Horwitz, A.F., Hynes, R.O., 1986. Structure of integrin, a glycoprotein involved in the transmembrane linkage between fibronectin and actin. Cell 46, 271–282. doi:10.1016/0092-8674(86)90744-0
Teckchandani, A., Cooper, J.A., 2016. The ubiquitin-proteasome system regulates focal adhesions at the leading edge of migrating cells. eLife 5, 1295. doi:10.7554/eLife.17440
Tepass, U., 2009. FERM proteins in animal morphogenesis. Current Opinion in Genetics & Development 19, 357–367. doi:10.1016/j.gde.2009.05.006
Theodosiou, M., Widmaier, M., Böttcher, R.T., Rognoni, E., Veelders, M., Bharadwaj, M., Lambacher, A., Austen, K., Müller, D.J., Zent, R., Fässler, R., 2016. Kindlin-2 cooperates with talin to activate integrins and induces cell spreading by directly binding paxillin. eLife 5, e10130. doi:10.7554/eLife.10130
Thievessen, I., Thompson, P.M., Berlemont, S., Plevock, K.M., Plotnikov, S.V., Zemljic-Harpf, A., Ross, R.S., Davidson, M.W., Danuser, G., Campbell, S.L., Waterman, C.M., 2013. Vinculin-actin interaction couples actin retrograde flow to focal adhesions, but is dispensable for focal adhesion growth. J Cell Biol 202, 163–177.

doi:10.1083/jcb.201303129
Ussar, S., Moser, M., Widmaier, M., Rognoni, E., Harrer, C., Genzel-Boroviczeny, O., Fässler, R., 2008. Loss of Kindlin-1 causes skin atrophy and lethal neonatal intestinal epithelial dysfunction. PLoS Genet. 4, e1000289. doi:10.1371/journal.pgen.1000289
van der Vaart, B., van Riel, W.E., Doodhi, H., Kevenaar, J.T., Katrukha, E.A., Gumy, L., Bouchet, B.P., Grigoriev, I., Spangler, S.A., Yu, K.L., Wulf, P.S., Wu, J., Lansbergen, G., van Battum, E.Y., Pasterkamp, R.J., Mimori-Kiyosue, Y., Demmers, J., Olieric, N., Maly, I.V., Hoogenraad, C.C., Akhmanova, A., 2013. CFEOM1-associated kinesin KIF21A is a cortical microtubule growth inhibitor. Dev. Cell 27, 145–160. doi:10.1016/j.devcel.2013.09.010
Vicente-Manzanares, M., Choi, C.K., Horwitz, A.R., 2009. Integrins in cell migration--the actin connection. J Cell Sci 122, 199–206. doi:10.1242/jcs.018564
Vitorino, P., Yeung, S., Crow, A., Bakke, J., Smyczek, T., West, K., McNamara, E., Eastham-Anderson, J., Gould, S., Harris, S.F., Ndubaku, C., Ye, W., 2015. MAP4K4 regulates integrin-FERM binding to control endothelial cell motility. Nature 519, 425–430. doi:10.1038/nature14323
Wang, J.-H., 2012. Pull and push: talin activation for integrin signaling. Cell Res. 22, 1512–1514. doi:10.1038/cr.2012.103
Webb, D.J., Donais, K., Whitmore, L.A., Thomas, S.M., Turner, C.E., Parsons, J.T., Horwitz, A.F., 2004. FAK-Src signalling through paxillin, ERK and MLCK regulates adhesion disassembly. Nat Cell Biol 6, 154–161. doi:10.1038/ncb1094
Wen, K.-K., Rubenstein, P.A., DeMali, K.A., 2009. Vinculin nucleates actin polymerization and modifies actin filament structure. J. Biol. Chem. 284, 30463–30473. doi:10.1074/jbc.M109.021295
Winkler, J., Lünsdorf, H., Jockusch, B.M., 1997. Energy-Filtered Electron Microscopy Reveals that Talin is a Highly Flexible Protein Composed of a Series of Globular Domains. Eur J Biochem 243, 430–436. doi:10.1111/j.1432-1033.1997.0430a.x
Winograd-Katz, S.E., Fässler, R., Geiger, B., Legate, K.R., 2014. The integrin adhesome: from genes and proteins to human disease. Nat. Rev. Mol. Cell Biol. 15, 273–288. doi:10.1038/nrm3769
Wirth, V.F., List, F., Diez, G., Goldmann, W.H., 2010. Vinculinâ€™s C-terminal region facilitates phospholipid membrane insertion. Biochem. Biophys. Res. Commun. 398, 433–437. doi:10.1016/j.bbrc.2010.06.094
Wiseman, P.W., Brown, C.M., Webb, D.J., Hebert, B., Johnson, N.L., Squier, J.A., Ellisman, M.H., Horwitz, A.F., 2004. Spatial mapping of integrin interactions and dynamics during cell migration by image correlation microscopy. J Cell Sci 117, 5521–5534. doi:10.1242/jcs.01416
Xia, S., Kanchanawong, P., 2017. Nanoscale mechanobiology of cell adhesions. Seminars in Cell and Developmental Biology 71, 53–67. doi:10.1016/j.semcdb.2017.07.029
Xiao, T., Takagi, J., Coller, B.S., Wang, J.-H., Springer, T.A., 2004. Structural basis for allostery in integrins and binding to fibrinogen-mimetic therapeutics. Nature 432, 59–67. doi:10.1038/nature02976
Xiong, J.P., Stehle, T., Diefenbach, B., Zhang, R., Dunker, R., Scott, D.L., Joachimiak, A., Goodman, S.L., Arnaout, M.A., 2001. Crystal structure of the extracellular segment of integrin alpha Vbeta3. Science 294, 339–345. doi:10.1126/science.1064535
Xiong, J.P., Stehle, T., Goodman, S.L., Arnaout, M.A., 2003. Integrins, cations and ligands: making the connection. J. Thromb. Haemost. 1, 1642–1654.
Yao, M., Goult, B.T., Klapholz, B., Hu, X., Toseland, C.P., Guo, Y., Cong, P., Sheetz, M.P., Yan, J., 2016. The mechanical response of talin. Nature Communications 7, 1–11. doi:10.1038/ncomms11966
Ye, F., Hu, G., Taylor, D., Ratnikov, B., Bobkov, A.A., McLean, M.A., Sligar, S.G., Taylor, K.A., Ginsberg, M.H., 2010. Recreation of the terminal events in physiological integrin activation. J Cell Biol 188, 157–173. doi:10.1083/jcb.200908045
Zaidel-Bar, R., Milo, R., Kam, Z., Geiger, B., 2007. A paxillin tyrosine phosphorylation

switch regulates the assembly and form of cell-matrix adhesions. J Cell Sci 120, 137–148. doi:10.1242/jcs.03314

Zemljic-Harpf, A.E., Miller, J.C., Henderson, S.A., Wright, A.T., Manso, A.M., Elsherif, L., Dalton, N.D., Thor, A.K., Perkins, G.A., McCulloch, A.D., Ross, R.S., 2007. Cardiac-myocyte-specific excision of the vinculin gene disrupts cellular junctions, causing sudden death or dilated cardiomyopathy. Mol. Cell. Biol. 27, 7522–7537. doi:10.1128/MCB.00728-07

Zhang, X., Jiang, G., Cai, Y., Monkley, S.J., Critchley, D.R., Sheetz, M.P., 2008. Talin depletion reveals independence of initial cell spreading from integrin activation and traction. Nat Cell Biol 10, 1062–1068. doi:10.1038/ncb1765

Zhou, Y., Dang, J., Chang, K.-Y., Yau, E., Aza-Blanc, P., Moscat, J., Rana, T.M., 2016. miR-1298 Inhibits Mutant KRAS-Driven Tumor Growth by Repressing FAK and LAMB3. Cancer Res. 76, 5777–5787. doi:10.1158/0008-5472.CAN-15-2936

Zhu, J., Zhu, J., Springer, T.A., 2013. Complete integrin headpiece opening in eight steps. J Cell Biol 201, 1053–1068. doi:10.1083/jcb.201212037

Zhu, L., Yang, J., Bromberger, T., Holly, A., Lu, F., Liu, H., Sun, K., Klapproth, S., Hirbawi, J., Byzova, T.V., Plow, E.F., Moser, M., Qin, J., 2017. Structure of Rap1b bound to talin reveals a pathway for triggering integrin activation. Nature Communications 1–11. doi:10.1038/s41467-017-01822-8

8 Acknowledgements

First of all, I would like to express my deep gratitude to my PhD supervisor Naoko Mizuno. She offered me the opportunity to work on this project and provided me with a great research environment that offered me freedom and the opportunity to reach my scientific goals. I appreciate her support and guidance in scientific questions and her trust in me as scientist.

Furthermore, I would like to thank my thesis advisor Reinhard Fässler for his guidance and support in scientific questions. He taught me how to put my work into perspective and inspired me through his knowledge and open-minded discussions. He helped me to immerse into the field and to grow as a scientist.

I would like to thank Elena Conti as a member of my thesis advisory committee and a department leader, for providing excellent research infrastructure, great advice and giving me support during my PhD time. Extended thanks also go to Andreas Bausch as member of my thesis advisory committee.

My gratitude goes to all the people that helped me during my scientific studies. The 'Crystalization Facility', 'Biochemisty Core Facility' and 'Electron Microscopy Facility' for their excellent technical setups and scientific support. I thank Zhiqi Sun for a fruitful collaboration. Martin Zachariae for providing valuable data for my studies. Christian Biertuempfel for supporting me with valuable insights and data. Rajan Prabu for software support and technical discussions. Wolfgang Baumeister for providing access to his microcopy infrastructure and Juergen Plitzko and Guenter Pfeiffer for their technical support.

I want to thank my past and present labmembers Steffi, Nirakar, Chris, Charlotte, Hanna, Sven, Iosune, Qianmin, Wolfgang, Julia and Ines. Thanks for supporting me and for accepting my stubbornness and moods. They, together with members of the Biertuempfel and Lorentzen groups, especially Giulia and Shun-Shiao, made the lab a great place during and after working hours. Extended thanks go to the people of Conti department for providing great atmosphere as well as scientific discussion, here special thanks go to Jana for her support during challenging times.

Finally, and most importantly, I want to thank my parents and family. Without their love, understanding and continuous support, this thesis would not have been impossible.